



**A Study of the Characteristics of Graphene Oxide Films
Irradiated by an Nd:YVO₄ Nanosecond Pulse Laser to form
Reduced Graphene Oxide**

being a thesis submitted in fulfilment of the
requirements for the degree of
Doctor of Philosophy

University of Hull

by

Jonathan Matthew Saul

May 2019

For my wife Zoë

With special thanks to my parents Adrian and Valerie Saul

Acknowledgements

Thanks are extended to Dr Chris Walton for all his advice and supervision and also to Dr Neil Kemp for all his help.

I would also like to thank Lloyd Glanville at the University of Hull for his help, Dr Graham Hickman at Nottingham Trent University and Dr Mark Isaccs for help with XPS data collection at the EPSRC National Facility for XPS (HarwellXPS), operated by Cardiff University and UCL, under contract No. PR16195.

I also acknowledge support from the Air Force Research Laboratory, UES, Inc., the Air Force Office of Scientific Research (C. C. Perry. via FA9550-13-1-0040).

Abstract

In recent years considerable research focus has been directed to graphene like materials that display properties that are similar to the excellent physical, chemical and mechanical characteristics of graphene. In this respect, one major research area is the reduction of graphene oxide (GO) and especially the laser reduction of graphene oxide.

The main aim of this thesis was to develop, construct and test an experimental system to create laser reduced graphene oxide films, and to classify the degree of reduction by measured changes in the surface characteristics, conductivity and resistance, and chemical composition of the surface. The objective was to achieve laser reduced graphene oxide with optimum high-quality graphene like features.

A system was developed using an Nd:YVO₄ laser with wavelength 1064nm and was successfully used to create reduced graphene oxide with the findings compared, with some success, to theoretical predictions and those of other researchers.

Many researchers have completed major experimental programmes that involve time consuming, expensive and repetitive tests where systematic and incremental changes are made to a large number of variables to establish the optimum characteristics of the degree of reduction. To avoid such repeat testing a primary objective of the thesis was to develop a system that yielded the optimum information from a single test. Such an experimental setup was successfully developed, and the resultant pattern of reduced graphene oxide was termed a z-scan.

The z-scan pattern was created by a range of fluence values which ranged from below the threshold value to create reduction through to those that caused full ablation of the surface. Good agreement was observed between the experimental results and the predicted pattern of the damage threshold which was observed at a fluence of 13.8 mJcm⁻². To better

understand the quality of the reduced GO at points over the surface of the z-scan a further series of tests with large area irradiated surfaces at different fluence values were completed.

The roughness of these irradiated large area samples was independent of fluence but was enhanced by an order of magnitude when compared to that measured for GO. The conductivity of the irradiated sample was shown to increase with increase in laser fluence in an almost linear way.

Raman spectra demonstrated the usual D, G and 2D peaks and, in line with other researchers the reduction was interpreted by the ID/IG and I2D/IG ratios. As fluence was increased the relationship between the ID/IG ratio had an overall downward trend in the range 1.21 to 0.75 with a flattening of the relationship at 0.75 corresponding to a fluence circa 35 mJcm⁻². Examination of the I2D/IG ratio showed that there was a gradual increase from a value of 0.23 to 0.31 but in this case with a saturation value at a fluence circa 32 mJcm⁻². Hence it was concluded that a fluence in the range 32 mJcm⁻² to 35 mJcm⁻² resulted in the optimum reduction of the GO. Similarly, the XPS results recorded a significant change in the carbon and oxygen species in the GO and rGO. The oxygen content was shown to reduce significantly at a fluence of ~35 mJcm⁻² with a flattening off at higher values of fluence to a constant value. A corresponding increase in the C-C carbon occurred and the carbon/oxygen peak ratio increased significantly in the range 29.1 mJcm⁻² to 36.5 mJcm⁻² with an overall increase from 3.5 at a fluence of 21.8 mJcm⁻² to 13 at a fluence of 46.0. These results confirm that at a fluence in the range 30 – 35 mJcm⁻² the degree of reduction is sufficient to transform the carbon and oxygen species with the reduced GO having graphene like characteristics.

Temperature changes were also identified as a major factor to influence the reduction process and a temperature model, based on the theory of Yakovlev et al., 2019, has been described. The model predicted significantly high values at the centre of the laser beam but there was a rapid reduction in temperature in a radial direction away from the centre. Good

agreement was observed between the predicted temperature and the boundary of reduced GO of the z-scan which was shown to occur at a temperature of circa 210 °C.

Tests were also completed to establish the wettability of the irradiated surface and it was observed that the wettability contact angle increased with increase in laser fluence. Values increased in an almost linear way, but values increased from 46 ° for GO to a maximum value of 84 ° for the rGO. These values compare well with the results of other researcher who have used similar irradiated surfaces. As the surface roughness was independent of fluence the increases in contact angle were attributed to the changes in the chemistry of the surface. Based on the outputs of the surface chemistry analysis for optimum reduction at a fluence in the range 32 mJcm⁻² to 36 mJcm⁻² the corresponding contact angle was circa 80°.

In summary it was concluded that the experimental facility successfully met the overall aim of the thesis and provided an efficient and reliable one step technique to establish the optimum range of laser fluence to create good quality rGO, supported by physical, electrical and chemical results.

Contents	Page Number
Chapter 1: Introduction	1
1.1 General Background on Graphene	1
1.2 Brief Summary of Research using Lasers to Reduce Graphene Oxide	3
1.3 Aims and Objectives	4
1.4 Details of Thesis Contents	5
Chapter 2: Literature review of Recent Research Advances in the Reduction and Application of Reduced Graphene Oxide.	6
2.1 Introduction	6
2.2 Scientific Context and Structure of Graphene, Graphite and Graphene Oxide.	7
2.2.1 <i>Graphene</i>	7
2.2.2 <i>Graphite</i>	8
2.2.3 <i>Graphite Oxide</i>	9
2.2.4 <i>Graphene Oxide</i>	9
2.2.5 <i>Reduced Graphene Oxide (rGO)</i>	10
2.3 Routes for the Reduction of Graphene Oxide to Reduced Graphene Oxide.	10
2.3.1 <i>Chemical Reduction</i>	10
2.3.2 <i>Thermal Reduction</i>	11
2.3.3 <i>Photo Reduction</i>	11
2.4 Laser Systems	12
2.4.1 <i>Laser Wavelength</i>	13
2.4.2 <i>Pulse Duration, Repetition Frequency, Time Period and Pulse Energy</i>	14
2.4.3 <i>Laser Intensity</i>	14
2.4.4 <i>Laser Power, Irradiance and Fluence</i>	14
2.4.5 <i>Sample Movement</i>	16
2.4.6 <i>Beam Energy Profile</i>	16
2.5 Characterisation of the Degree of Reduction	18
2.5.1 <i>Surface Profiling and Roughness</i>	20

2.5.2	<i>Conductance/Resistance changes</i>	20
2.5.3	<i>Raman Spectroscopy</i>	21
2.5.4	<i>X-ray Photoelectron Spectroscopy</i>	25
2.5.5	<i>Scanning Electron Microscopy</i>	27
2.5.6	<i>Powder X-ray Diffraction</i>	27
2.5.7	<i>Changes in Wettability</i>	28
2.5.8	<i>Importance of Temperature</i>	28
2.5.9	<i>Summary of the Measurement Techniques used in this thesis</i>	29
2.6	Summary Overview of Prior Research	29
2.6.1	<i>Parameter Studies</i>	29
2.6.2	<i>Direct Laser Writing</i>	30
2.6.3	<i>Inert Conditions</i>	31
2.6.4	<i>GO in Solution</i>	32
2.6.5	<i>Devices</i>	32
2.6.6	<i>Comments Related to Thesis Objectives</i>	34
2.7	Types of Laser used and their Operational Characteristics	34
2.8	Fuller Review of Selected Papers Relevant to the Thesis	38
2.8.1	<i>Surface Characteristics and Conductivity</i>	39
2.8.1.1	- Studies highlighting an increase in layer thickness	39
2.8.1.2	- Roughness changes	42
2.8.1.3	- Height highlighting a reduction in layer thickness	44
2.8.1.4	- Irradiated line width	45
2.8.1.5	- Fluence changes	49
2.8.1.6	- Repetition frequency	49
2.8.1.7	- Changes in laser wavelength	50
2.8.1.8	- 3D structures	50
2.8.2	<i>Raman Spectroscopy and XPS</i>	53
2.8.2.1	- Important early studies	53
2.8.2.2	- Studies with multiple lasers	54
2.8.2.3	- Studies with changes to the power/energy per pulse/fluence and scanning speed.	59
2.8.2.4	- Studies with changes to exposure duration	67
2.8.2.5	- Studies using two beam laser interference	68
2.8.2.6	- Thermal considerations	69
2.8.2.7	- Temporal evolution	69
2.8.2.8	- Multi photon absorption	70
2.8.2.9	- Summary Table of Raman Spectra and XPS results of other researchers	71
2.9	Influence of Temperature on the Reduction Process	75

2.9.1	<i>Photon Interaction with Matter and Photochemical and Photothermal Reduction</i>	75
2.9.2	<i>Review of Previous Literature on Temperature Modelling</i>	78
2.10	Literature Associated with the Wettability of Reduced GO Surfaces	80
2.11	Identified Knowledge Gaps Leading to Thesis Aims and Objectives	85
Chapter 3: Theory		91
3.1	Z-Scan Theory	91
3.2	Temperature Modelling	96
Chapter 4: Experimental systems and methods		100
4.1.1	<i>Lens</i>	100
4.1.2	<i>Details of Laser</i>	101
4.1.3	<i>Optical Microscopy</i>	101
4.1.4	<i>Stages</i>	102
4.1.5	<i>Glass Substrates</i>	102
4.1.6	<i>Preparation of Graphene Oxide Films</i>	102
4.1.7	<i>Surface Profiler</i>	103
4.1.8	<i>Scanning Electron Microscope</i>	104
4.1.9	<i>Raman Spectroscopy</i>	105
4.1.10	<i>X-ray Photoelectron Spectroscopy</i>	106
4.1.11	<i>Wettability</i>	106
Chapter 5: Results and Analysis		107
5.1	Initial System Characterisation	107
5.1.1	<i>Uncertainty Calculation</i>	107
5.1.2	<i>Laser Characteristics</i>	107
5.1.3	<i>Characteristics of the GO Layer</i>	112
5.2	Reduction of GO	114
5.2.1	<i>Creation of rGO Spots</i>	115
5.2.2	<i>rGO Tracks at Different Fluence</i>	116
5.2.3	<i>Translation Speed</i>	117
5.3	Z-Scan Methodology and Experimental System	118

5.3.1	<i>Experimental Z-Scan</i>	119
5.3.2	<i>Measurements using Surface Profiler</i>	122
5.3.3	<i>Comparison of Experimental Results with Theoretical Distribution</i>	124
5.3.4	<i>Discussion of Surface Characteristics of Other Researchers</i>	126
5.3.5	<i>Assessment of Z-Scan Degree of Reduction using Raman Spectroscopy</i>	131
5.4	Large Area Results	133
5.4.1	<i>Surface Profile Measurements.</i>	134
5.4.2	<i>Conductivity Measurements</i>	136
5.5	Raman Spectroscopy and XPS	138
5.5.1	<i>Raman Spectroscopy</i>	138
5.5.2	<i>Discussion of Raman Spectroscopy Results of Other Researchers</i>	142
5.5.3	<i>XPS Analysis</i>	152
5.5.4	<i>Discussion of XPS Results of Other Researchers</i>	158
5.6	Results of Wettability Testing	159
5.6.1	<i>Relationship Between Wettability and Surface Roughness</i>	161
5.6.2	<i>Comparison of Wettability Results with Other Researchers</i>	162
5.7	Results of Temperature Modelling	163
5.7.1	<i>Results from Model Predictions of Temperature</i>	163
5.7.2	<i>Review of Temperature Modelling Outputs Identified in the Literature</i>	165
5.8	Summary Comment Related to the Research of Others	170
	Chapter 6: Conclusions and Further Work	171
	References	176
	Appendix I	I
	Appendix II	II

List of Figures

Chapter 1

Figure 1.1 Some techniques for graphene production	2
--	---

Chapter 2

Figure 2.1 Hexagonal lattice structure of graphene.	8
Figure 2.2 Structure of graphene and graphite	8
Figure 2.3. Chemical structure of graphene oxide	9
Figure 2.4 Typical set up of a laser system	13
Figure 2.5 Power-time characteristics of laser pulses	15
Figure 2.6 Overlapping of laser spot with movement in the x direction	16
Figure 2.7 Spatial distribution of Gaussian laser beam showing intensity profile	17
Figure 2.8 Characteristics of Gaussian Laser Beam showing the Rayleigh length (Z_r) as a function of the beam waist (ω_0)	18
Figure 2.9 Laser irradiated spots due to an increase in fluence from left to right and the consequent change in spot size	19
Figure 2.10 Typical I/V plots for ohmic materials	21
Figure 2.11 Typical Raman Spectra for GO and rGO after irradiation with ns, fs and continuous wave lasers, after Arul <i>et al.</i> , 2016, © Elsevier	23
Figure 2.12 Typical XPS Spectra of GO	26
Figure 2.13 Application technologies using rGO	33
Figure 2.14 Jablonski diagrams show electron states and possible electron transitions between each state	76
Figure 2.15 Droplets on solid surface with value of contact angle defining hydrophobic, neutral, hydrophilic and perfect wettability	81
Figure 2.16 Single droplet on a solid substrate showing balanced solid/liquid, solid/gas and liquid/gas forces and values of contact angle classifying wettability	82
Figure 2.17 Plot of Raman ID/IG values as a function of the number of overlapping pulses and Fluence, after Arul <i>et al.</i> , 2016, © Elsevier	89
Figure 2.18 Grey scale degree of reduction of irradiated sample squares as a function of spot velocity and laser frequency, after Evalshin <i>et al.</i> , 2018, © WILEY	89

Chapter 3

Figure 3.1 Schematic representation of zone of influence of overlapping spots as a sample is moved through a laser beam in the x and z directions	91
Figure 3.2 Typical z-scan pattern created when a sample is translated through a gaussian laser beam in the x and z directions simultaneously	93
Figure 3.3 3D representation of the predicted fluence produced during a typical z-scan	95

Chapter 4

Figure 4.1 – Experimental system	100
----------------------------------	-----

Figure 4.2 - Advanced Optical Technology Nd:YVO ₄ laser and control unit. (Photonics Media, 1999)	101
Figure 4.3 - Lamellae structure of GO after being drop cast from aqueous solution onto glass substrate.	103
Figure 4.4 - BRUKER Dektak XT surface profiler (Bruker, 2014)	104
Figure 4.5-Thermo Fisher Scientific DXR II Raman spectrometer (ThermoFisher, 2019)	105
Figure 4.6 - CAG 100 contact angle goniometer	106
Chapter 5	
Figure 5.1 - Relationship between Diode Wavelength and Temperature.	108
Figure 5.2 – Diode output power as a function of input current at 5, 10 and 20 kHz pulse repetition frequencies.	109
Figure 5.3 – Relationship between the average diode output power and wavelength as a function of input current	109
Figure 5.4 - Spectral response of pump diode.	111
Figure 5.5 - Wavelength Output of Nd:YVO ₄ laser	111
Figure 5.6 - Ablation diameter as a function of the vertical distance from the objective lens	111
Figure 5.7 – Surface profiles of GO thickness across the sample at ambient temperature. M denotes mean value	112
Figure 5.8 - Surface profiles of GO thickness across the sample after annealing. M denotes mean value.	113
Figure 5.9. Relationship between thickness of the GO layer and temperature.	114
Figure 5.10. Irradiated spots on Graphene Oxide after 1000 Pulses at Different Fluences. 200x Magnification	116
Figure 5.11. Tracks with Different Fluence at Constant Scanning Speed 3.0 mms ⁻¹ . 200x Magnification with the scale line representing 100 μm	116
Figure 5.12 - Tracks Created at Different Translation Speeds after Irradiation at 10kHz Pulse Repetition Frequency and 35mJcm ⁻² . 200x Magnification, Scale line represents 100μm	118
Figure 5.13. One half of a typical optical micrograph of z-scan (2 mms ⁻¹ , 10 Hz), 50x magnification	119
Figure 5.14 (a) - SEM image of z-scan at z = 0 with 1mm scale bar	120
Figure 5.14 (b) - SEM image of z-scan at z = 0 with 10 μm scale bar	121
Figure 5.15. SEM image at the location, point B, Figure 5.16, where the damage radius is a maximum with ρ _{max} equal to 100 μm and the z distance of 760 μm.	121
Figure 5.16 (a-d). Surface profiles showing the depth and expansion of the GO surface at different locations in the x direction from ω ₀ with a) 0.3 mm, b) 0.6 mm c) 0.9 mm, d) 1.2mm.	122
Figure 5.17 - 3D surface profile of z-scan	123
Figure 5.18 – Surface profile along the x axis at r=0 of z-scan.	124
Figure 5.19 Predicted distribution of fluence with experimental limit of	125

damage plotted as the white line at 13.8 mJcm^{-2} .	
Figure 5.20 Irradiated tracks after Yung et al., 2013. X axis is 'Distance along layer μm ', Y axis is Layer thickness nm. © AIP Publishing	127
Figure 5.21 Changes in irradiated spot size with laser power and corresponding change in surface profile due to irradiation, after Kang et al., (2018) Elsevier ©	128
Figure 5.22 – Decrease in irradiated GO thickness as a function of energy density, after Wan et al., 2019. Elsevier ©	129
Figure 5.23 - Effect of laser power on rGO thickness showing three regions of reduction, after (Deng et al, 2016) Elsevier ©	130
Figure 5.24 - Raman spectroscopy applied horizontally to the sample at location B from Figure 5.16	131
Figure 5.25 - Ratio of D and G peak intensities for Raman spectra at different positions across the z-scan. Fluence values at each displacement value are given in Table 5.2.	132
Figure 5.26 – Typical surface profile of drop-cast GO prior to irradiation. Displacement describes the distance across the sample	135
Figure 5.27 – Typical surface profile of a GO sample after irradiation at a fluence of 41.1 mJcm^{-2} . Displacement describes the distance across the sample	135
Figure 5.28 – Surface roughness of GO sample after raster irradiation showing roughness both parallel and perpendicular to the raster direction	136
Figure 5.29 – Conductivity as a function of laser fluence	137
Figure 5.30 – Raman spectroscopy results showing D, G and 2D peaks of samples irradiated at fluence values in the range 23.9 mJcm^{-2} to 41.1 mJcm^{-2} .	139
Figure 5.31 - Peak integral ratio of D and G Raman peaks corresponding to irradiation over the fluence range 23.9 mJcm^{-2} to 41.1 mJcm^{-2} .	139
Figure 5.32 - Peak integral ratio for I2D/IG corresponding to irradiated samples at fluence values in the range 23.9 mJcm^{-2} to 41.1 mJcm^{-2} .	141
Figure 5.33 ID/IG peak intensity ratio for ns laser, after Arul et al., (2016). ©Elsevier	142
Figure 5.34 - I2D/IG for ns laser, after Arul et al., (2016). ©Elsevier	143
Figure 5.35 - Relationship between degree of reduction, laser frequency and spot velocity after Evlashin et al (2018). ©WILEY (2018)	144
Figure 5.36 ID/IG ratio, I2D/IG ratio and resistance measurements as a function of laser energy per pulse, after Bobinskiy et al (2017) ©Elsevier	145
Figure 5.37 Results of ID/IG ratio after Wan et al., 2019. ©Elsevier	147
Figure 5.38 2D representation of ID/IG ratio results, after Wan et al., 2019. ©Elsevier	147
Figure 5.39 Raman spectra as a function of pulse number, after Kymakis et al., 2013 and Petridis et al., 2013. ©WILEY 2013	148
Figure 5.40 (a) Irradiated images at different pulse numbers, (b) Corresponding Raman spectra and (c) ID/IG ratios	151

from the Raman data after Li <i>et al</i> (2014) ©Optical Society of America	
Figure 5.41 - XPS spectra of a GO sample used in the study	153
Figure 5.42 - XPS spectra of rGO after irradiation with a laser fluence of 21.8 mJcm ⁻²	153
Figure 5.43 - XPS spectra of rGO after irradiation with a laser fluence of 29.1 mJcm ⁻² .	154
Figure 5.44 - XPS spectra of rGO after irradiation with a laser fluence of 56.1 mJcm ⁻² .	154
Figure 5.45 – XPS spectra of the C-C sp ² hybridisation	155
Figure 5.46 - XPS spectra of the C-C sp ³ hybridisation	156
Figure 5.47 - XPS spectra of the oxygen species	156
Figure 5.48 – Relationship between the oxygen species peak and fluence	157
Figure 5.49 – Relationship between the Carbon/Oxygen peak ratios as a function of fluence	158
Figure 5.50 – Results of repeated tests to assess the relationship between contact angle and line spacing.	160
Figure 5.51 Relationship between contact angle and fluence	160
Figure 5.52 – Surface roughness of GO sample after raster irradiation showing roughness both parallel and perpendicular to the raster direction (repeat of Figure 5.37)	161
Figure 5.53 (a) Superhydrophobic grid surface and (b) resultant contact angle after Jiang <i>et al.</i> , 2014. ©WILEY (2014)	163
Figure 5.54 Predicted temperature on the surface of the GO with 1064 nm wavelength, 4.6 ns pulse duration and 10 kHz PRF	164
Figure 5.55 Distribution of temperature in the z-direction on the centreline of the sample	165
Figure 5.56 Predicted temperature distribution in a GO layer on a PET substrate, after Kymakis <i>et al.</i> , 2013 ©Elsevier.	166
Figure 5.57 Predicted temperature distribution as a function of the number of GO layers, after Zhou <i>et al.</i> , 2010 ©WILEY (2010)	167
Figure 5.58 Temperature predictions in GO as a function of the radius from the laser beam centre, after Evlashin <i>et al.</i> , 2018 ©WILEY (2018)	168
Figure 5.59 Temperature predictions in GO at a power of 50 mW highlighting the changes through the layer depth (1) representing the surface and (6) at 1200 nm after Trusovas <i>et al</i> (2013) ©Elsevier.	169

List of Tables

Chapter 2

Table 2.1 Lasers and operating parameters used in prior research	36
Table 2.2 Summary of resistivity and conductivity results of other researchers	52
Table 2.3 Summary of Raman Spectroscopy results of other researchers	72
Table 2.4 Summary of XPS results of other researchers	74

Chapter 3

Table 3.1 Parameter values for application into the temperature model	99
---	----

Chapter 5

Table 5.1 Fluence values corresponding to displacement from $z = 0$	133
---	-----

Chapter 1: Introduction

1.1 General Background on Graphene

Graphene is a single 2D carbon layer of the graphite structure and is a flat monolayer of sp^2 carbon atoms tightly packed into a two-dimensional (2D) honeycomb lattice. To fabricate single sheet graphene, it is required that the Van der Waals attraction between the first and second layers must be overcome without disturbing the subsequent layers. Novoselov *et al.*, 2004, were the first to produce free standing graphene films using mechanical exfoliation where adhesive tape was used to peel off layers of graphitic crystal flakes which were subsequently rubbed against an oxidised silicon surface. This resulted in the fabrication of a single thickness layer of graphene - world breaking research – with the result that major international new research was stimulated. Such free-standing graphene films have exceptional thermal, electrical and mechanical properties including ultrahigh carrier mobility, optical transmittance, high conductivity, flexibility and excellent stability, see Geim and Novoselev, 2007. It is also chemically inert and has low cost. Hence graphene is an excellent material for applications in electronics, ophthalmics and quantum electrodynamics, Novoselov *et al.*, 2012.

Excellent early reviews of the development of graphene were presented by Allen, *et al.*, 2010, and Obeng and Srinivasan, 2011, but since that time there has been a prolific increase in research activity. This has involved major research on the techniques for graphene production, of a better understanding of the properties and characteristics of graphene and the application of graphene in a multitude of applications. Production techniques of graphene are ever increasing and some of the techniques are shown in Figure 1.1.

Many of these techniques are expensive, time consuming or environmentally challenging and have difficulties associated with the fabrication of high-quality large area graphene. Many researchers have focussed their attention on the application of graphene oxide (GO) and its modification to replicate the characteristics of graphene.



Figure 1.1 Some techniques for graphene production

Graphene oxide has insulating characteristics primarily due to the prevalence of the oxygen containing groups and this, together with the fact that the GO surface may contain defects, make GO an unsuitable material for many electronic applications. Reducing the oxygen containing groups in GO results in the restoration of a graphene like lattice which is accompanied by the conversion of sp^3 to sp^2 carbon hybridisations and results in a return to a material with graphene-like properties, for example, improved conductivity.

Several techniques have been employed to reduce graphene oxide (GO) but the 3 primary routes for reduction are *chemical, thermal and photoreduction*. These are discussed more fully in Chapter 2. The ***topic of this thesis is the photothermal reduction of GO using an Nd:YVO₄ laser.***

1.2 Brief Summary of Research using Lasers to Reduce Graphene Oxide

Early research was completed by Zhang *et al.*, 2010, Zhou *et al.*, 2010, Subrahmanyam *et al.*, 2010, and Kumar, Subrahmanyam and Rao, 2011, who clearly demonstrated that the laser irradiation system had a significant influence on the surface morphology and the chemical composition of the rGO and that such changes could be tuned by controlling the laser characteristics and thickness of the GO layers. Studies included an examination of the resultant features and changes in the thickness of the irradiated layer, Arul el al., 2015, Deng *et al.*, 2016, squares, channels and grids of the irradiated pattern, Evlashin *et al.*, 2018, Jiang *et al.*, 2014, Wan *et al.*, 2019, Zhang *et al.*, 2013, flexible patterning, Bobrinetskiy *et al.*, 2016, Guo *et al.*, 2014, Kang *et al.*, 2018, defects, Sokolov *et al.*, 2013, temperature, Lazauskas *et al.*, 2014, conductivity Tao *et al.*, 2012, Yung *et al.*, 2013, and multi photon absorption, Li *et al.*, 2014. An extremely important feature of these studies is that the pattern size and the chemical structure of the pattern of rGO may be precisely and accurately controlled by the intensity and scanning rate of the laser irradiation. However, to establish the most preferable (optimum) reduction parameters in each of these studies it has been required to complete a vast number of tests. This stimulated the concept of the thesis to develop a methodology that would allow an examination of the reduction degree, from no damage to full ablation of the GO surface, using only one experiment. To develop such a methodology the author had the idea to move a GO sample on a glass substrate, in both the horizontal and vertical planes, across a fixed laser beam. As the sample moves in the horizontal and vertical directions, the vertical distance between the laser beam and the sample will change and this results in a change in the spot size, and hence fluence. This results in a pattern of reduction which has been termed a z-scan.

1.3 Aims and Objectives

The main aim of the thesis was to develop, construct and test an experimental system to create laser reduced graphene oxide films, and to classify the degree of reduction by measured changes in the surface characteristics, conductivity and resistance and chemical composition of the surface with a view to finding the characteristics at which the resultant GO contained high quality graphene like features.

Many researchers have completed major experimental programmes that involve time consuming, expensive and repetitive tests where systematic and incremental changes are made to a large number of variables to establish the optimum characteristics of the degree of reduction. A primary objective of the thesis was to develop the experimental system in such a way that the same information may be derived from a single test. The objective was to develop a pattern of reduced GO in the GO film surface that encompassed the complete range of outcomes, from no damage below the threshold fluence to complete ablation. The resultant pattern of reduction was termed a 'z-scan'.

Subsequently, to estimate the fluence at all points in the z-scan pattern using theoretical predictions and to compare the theory predicted values with those observed in the experimental programme.

Once the maximum range of fluence values, from threshold to ablation, had been established, a further objective was to devise and complete a series of studies using large areas of reduced graphene oxide. Here, the fluence outputs from the z-scan methodology were used to prepare large areas of reduced GO for the maximum range of fluence values. It is proposed to use the results of these studies to refine and confirm the characteristics of the degree of reduction within the z-scan pattern.

Surface coatings may be manufactured with reduced GO and the study provided a further opportunity to evaluate the characteristics of the large area irradiated surfaces in terms of the relationship between wettability, roughness and the surface chemistry of the surface.

As photothermal reduction of GO is very much temperature dependent, an aim of the study was to develop a mathematical model to describe the temperature changes associated with the z-scan methodology and to compare predictions with the observed pattern of reduction and the reported findings from the temperature models of other researchers.

1.4 Details of Thesis Contents

Following this introductory chapter, Chapter 2 presents an overview of the current literature on the reduction and application of GO by laser irradiation but with a special emphasis on the reduction of GO thin films, as this is the topic of this thesis.

Chapter 3 presents the theoretical considerations given to the z-scan and temperature modelling aspects of the research. Details of the layout of the experimental system, the equipment used, and its mode of operation are presented in Chapter 4. The results and analysis of these tests is included in Chapter 5 which has been split into 4 sections. Section 5.1 describes the details involved with the characterisation of the laser used within the system, Section 5.2 describes the application of the experimental system to create irradiated spots and stripes in a GO surface, whilst Section 5.3 describes the measurements made to establish the characteristics of the z-scan and how these compare to the theoretical predictions and the results of other researchers followed by Section 5.4 which describes the results from the large area tests. These tests utilise the outputs from the z-scan to create large area reduced graphene oxide at different fluence values, which are analysed for changes in the physical and chemical parameters as a function of changes in the laser fluence. Where appropriate, the results of other researchers are discussed. Chapter 6 presents the conclusions of the research and presents details of potential further work identified by the author.

Chapter 2: Literature review of Recent Research Advances in the Reduction and Application of Reduced Graphene Oxide.

2.1 Introduction

This Chapter presents details of the scientific context associated with the expansive use and application of graphene and graphene oxide, and of the way in which graphene oxide may be reduced to create a material with graphene like properties. A focus has been made on the science and technology associated with the laser reduction of graphene oxide as this is the topic of the thesis. The review highlights that the many different types of laser have been used in previous studies and that the laser used in this study, a Nd:YVO₄ pulsed laser with wavelength 1064 nm and 4.6 ns pulse duration, compliments this range of lasers. A large section of the Chapter concentrates on the previously completed research on how these lasers have been used to create reduced graphene oxide with the emphasis placed on the laser reduction of graphene oxide films. Some details of the reduction of graphite oxide and graphene oxide in solution have been included as these have been used to support the interpretation of the results obtained by the author, presented in Chapter 5 of the thesis. Due to the prolific volume of research, especially that associated with the application of graphene oxide, the review has highlighted that many different lasers, experimental methodologies and analysis techniques have been utilised. The Chapter has been divided into the following Sections:

- 2.2 Scientific context and structure of graphene, graphite and graphene oxide.
- 2.3 Routes for the reduction of graphene oxide to reduced graphene oxide
- 2.4 Laser systems
- 2.5 Characterisation of the degree of reduction
- 2.6 Summary overview of prior research

- 2.7 Types of laser used and their operational characteristics
- 2.8 Fuller review of selected papers relevant to the thesis
- 2.9 Influence of temperature on the reduction process
- 2.10 Literature associated with the wettability of reduced GO surfaces
- 2.11 Identified knowledge gaps leading to thesis aims and objectives

2.2 Scientific Context and Structure of Graphene, Graphite and Graphene Oxide

Many researchers have focussed their attention on the application of graphene oxide (GO) and its modification to replicate the characteristics of graphene. Graphene Oxide is easily produced by the sonication of graphite oxide, which is cheap, readily available and easily prepared from GO solution to thin layer films of GO. The chemical structure of graphene, graphite oxide and graphene oxide are shown in Figures 2.1 to 2.3.

2.2.1 Graphene

As stated earlier, graphene is a carbon nanomaterial and is a planar 2D hexagonal honeycomb crystal lattice of sp^2 bonded carbon atoms, as shown in Figure 2.1. The lattice is one atom thick and this, together with the sp^2 hybridisation and atomic thickness of 0.345 nm results in a material with the highest known strength and excellent electrical, optical and thermal properties. The length between the carbon atoms in the hexagonal ring is circa 0.142 nm.

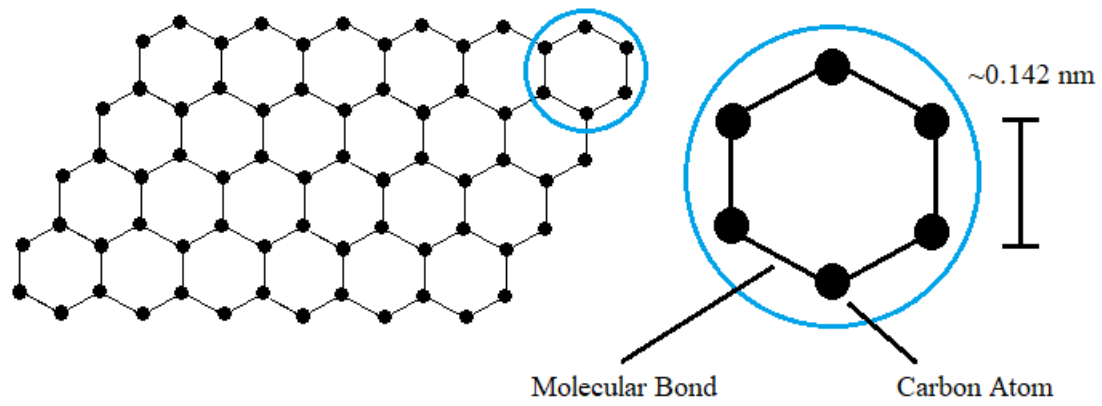


Figure 2.1 Hexagonal lattice structure of graphene.

2.2.2 Graphite

Graphite is a stack of graphene layers held weakly together, as illustrated in Figure 2.2.

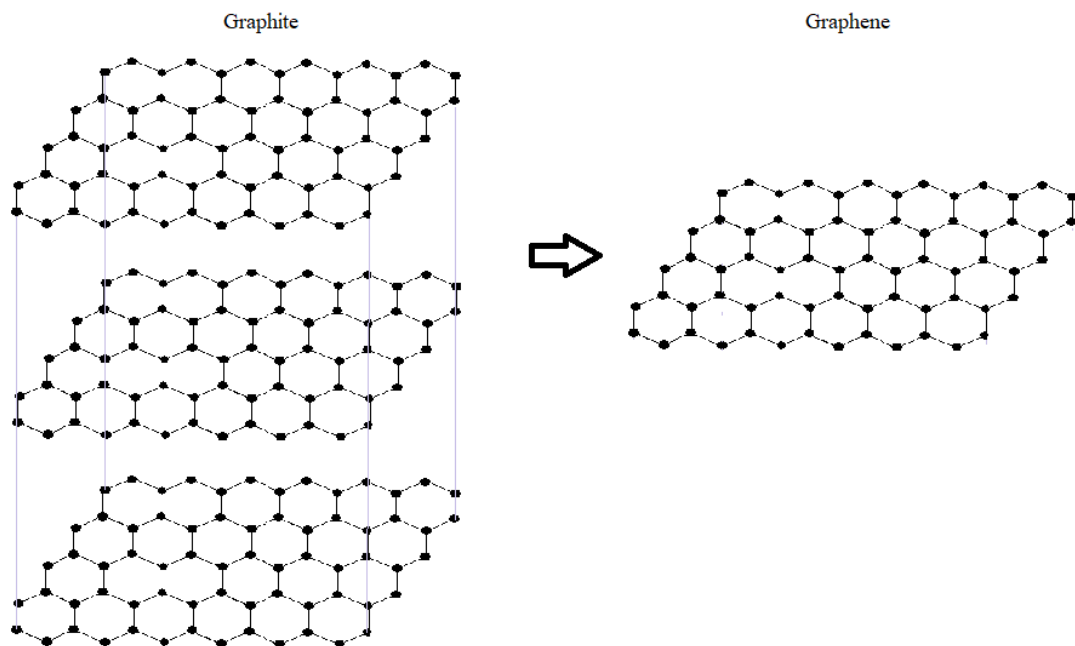


Figure 2.2 Structure of graphene and graphite

2.2.3 Graphite Oxide

Graphite oxide is obtained by treating **graphite** with strong oxidizers and, in the past, the most common method of production has been the Hummers Method where graphite is treated with a mixture of sulphuric acid, sodium nitrate and potassium permanganate. Graphite oxide has a layer structure similar to that of graphite but the spacing between layers is much larger (up to 2 times) and more irregular. This disrupts the sp^2 bonding network with the result that graphite oxide becomes an insulator. Because of this larger spacing between layers, graphite oxide is hydrophilic and is easily formed into a solution when mixed with water.

2.2.4 Graphene Oxide

When fully oxidised compounds of graphite oxide are dispersed in water the solution becomes graphene oxide and the chemical structure of graphene oxide is shown in Figure 2.3.

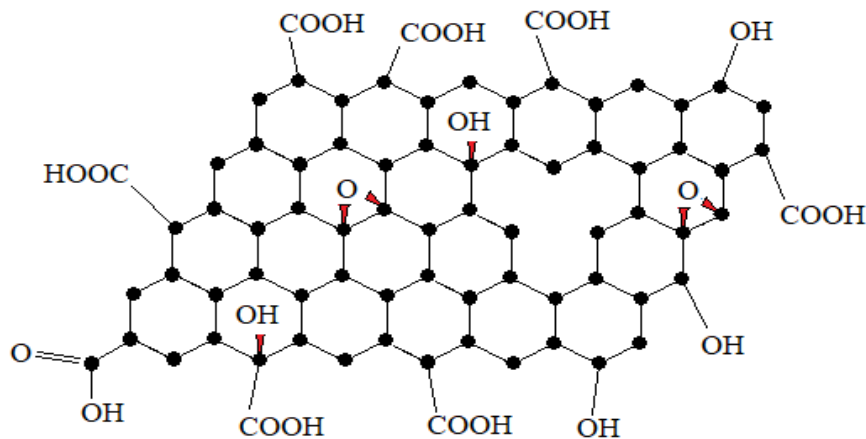


Figure 2.3. Chemical structure of graphene oxide

The structure includes the presence of the sp^2 hybridised carbon-carbon bonds, sp^3 hybridised carbon-carbon bonds, epoxide/hydroxyl carbon-oxygen bonds, carbonyl carbon=oxygenn bonds and carboxyl COOH bonds. The distributions of these bonds describe the footprint of the graphene oxide which has insulating characteristics. This is due to the prevalence of the oxygen containing groups and this, together with the fact that the GO surface may contain defects, make GO an unsuitable material for many electronic applications. By removing the oxygen containing groups from GO results in the restoration of the graphene like lattice with the reduced GO, termed rGO, accompanied by the conversion of sp^3 to sp^2 carbon hybridisations and a return to graphene-like properties, for example, improved conductivity and reduced resistance.

2.2.5 Reduced Graphene Oxide (rGO)

When graphene oxide is photo-reduced to reduced graphene oxide, the degree of reduction is highlighted by changes in the surface characteristics, conductivity and resistance and chemical composition. The degree of reduction is key to the quality of the reduced graphene oxide and many techniques are used to assess the physical and chemical characteristics of rGO. These have been discussed in Section 2.5 of this chapter.

2.3 Routes for the Reduction of Graphene Oxide to Reduced Graphene Oxide

Several reduction techniques have been employed to reduce graphene oxide (GO) to reduced graphene oxide (rGO). There are 3 primary routes for reduction: **chemical, thermal and photoreduction**.

2.3.1 Chemical Reduction

Chemical reduction, as detailed for example by Yang *et al.*, 2009, Eda and Chhowalla, 2010, Gao *et al.*, 2009, make use of a chemical reducing reagent, for example, hydrazine, to de-oxygenise the GO. These methods are environmentally unfriendly as they produce volumes

of toxic waste and result in surface contamination which is often not conducive for device fabrication.

2.3.2 Thermal Reduction

Such techniques usually involve high temperature thermal annealing with temperatures greater than 1000°C, see for example, Gao *et al.*, 2009, Ju *et al.*, 2010, with the GO frequently held in inert atmospheres. This results in high energy waste and has the disadvantage that the high temperature is incompatible with device fabrication, notably the provision of suitable substrates, especially flexible substrates. More recently microwaves have been used to thermally reduce GO, see Voiry *et al.*, 2016.

Both chemical and thermal reduction techniques also present difficulties associated with the control of the degree of oxygen removal and in the precise patterning of micro-structures.

2.3.3 Photo Reduction

Photoreduction is the deoxygenation of GO using photo induced techniques which include photothermal reduction and photochemical reduction, see Pei and Cheng, 2011, Zhang *et al.*, 2010, Kumar *et al.*, 2017, Wan *et al.*, 2018. Photoreduction of GO has distinct advantages over both chemical and thermal reduction as the processes are highly efficient and low cost. Techniques include catalysts, sunlight, camera flash, lamps, microwaves and lasers. They also offer the opportunity to control the level of photoinduced reduction, for example by controlling the characteristics of the camera flash or the wavelength, power, pulse duration etc of the laser. It is also possible to use masks to expose the desired area or to directly control the position of the laser or sample to irradiate complex patterns of reduced GO. It is also feasible to photo reduce GO on flexible substrates, thereby assisting the opportunity for the fabrication of flexible electronics.

The mechanisms of photo reduction have been reported widely and essentially fall into three categories: **photochemical** reduction, see Mukherjee *et al.*, 2012, in which the photo-generated electron–hole pairs provide the mechanism for the removal of OCGs, leading to the restoration of sp^2 domains, **photothermal** reduction, see Zhou *et al.*, 2010, Strong *et al.*, 2012, El Kady *et al.*, 2012, and the third category a combination of both **photochemical and photothermal** reduction occurring within the same process, see Sokolov *et al.*, 2013, Pedritis *et al.*, 2013, Zhang *et al.*, 2010. Kymakis *et al.*, 2013 and 2014, Arul *et al.*, 2016., Bobrinetskiy *et al.*, 2017 and Evlashin *et al.*, 2016.

Smirnov *et al.*, 2011, observed that the threshold for transition between the photochemical and photothermal processes occurred at a photon energy of 3.2 eV. The value of 3.2 eV effectively corresponds to a laser wavelength of 390nm and hence treatment by a laser with a wavelength smaller than 390nm would mainly undergo a photochemical process, whereas for lasers with wavelengths larger than 390nm, the reduction process is mainly photothermal. Hence, photochemical processes tend to occur using lasers with short wavelength and ultrashort pulse widths. In this thesis a laser with a wavelength of 1064 nm was used and hence the focus of the study is on the **photothermal reduction** of GO films.

2.4 Laser Systems

A large number of different types of laser may be used in the reduction process and each laser is defined by its wavelength, pulse repetition frequency, pulse duration and power. A typical set-up of a laser system is shown in Figure 2.4.

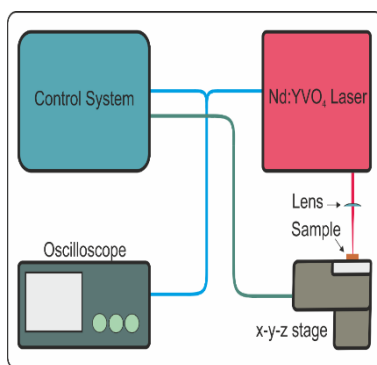


Figure 2.4 Typical set up of a laser system

The control system is used to precisely move a sample to a desired location and simultaneously turn the laser on at a desired frequency. The laser is used to produce coherent beam of light which is focussed by an objective lens onto the GO sample. This results in a spot of irradiated area the diameter (D) of which is governed by the characteristics of the objective lens and the distance from the lens to the sample surface.

2.4.1 Laser Wavelength

Laser wavelengths range from ultra-violet to far-infrared where;

Ultra Violet	10 – 400 nm	Visible	400 – 750 nm
Near Infrared	750 – 1500 nm	Mid Infrared	1500– 4000 nm
Far Infrared	4000 – 10^6 nm		

The frequency of the laser radiation determines whether the light may be reflected, absorbed or transmitted through the sample. High frequency radiation, for example ultraviolet lasers, have a photon energy which is sufficiently high to create photochemical effects (see Section 2.3.3) due to the breaking of chemical bonds.

2.4.2 *Pulse Duration, Repetition Frequency, Time Period and Pulse Energy*

Pulse duration is the full width half maximum time interval of the pulse and lasers used commonly have pulse durations in the nanosecond (ns) and femtosecond (fs) range, although some work has been completed using picosecond (ps) lasers. Continuous wave lasers are not pulsed but are used in constant operation.

Pulse repetition frequency is the repetition frequency at which the laser operates or number of laser pulses per second, measured in Hz.

The **time period** is defined as $1/\text{Pulse Repetition Frequency}$ and is the amount of time between each pulse.

The **pulse energy** is the energy contained within one laser pulse and can be measured directly or calculated knowing it is equal to the average power divided by the pulse repetition frequency.

2.4.3 *Laser Intensity*

The laser intensity can be measured in multiple different ways which describe how the energy of a laser beam is distributed in time and space.

2.4.4 *Laser Power, Irradiance and Fluence*

The power-time relationship of a pulsed laser is shown schematically in Figure 2.5. Power is measured in Watts or Joules per second and can be described in two ways, **peak power** and **average power**.

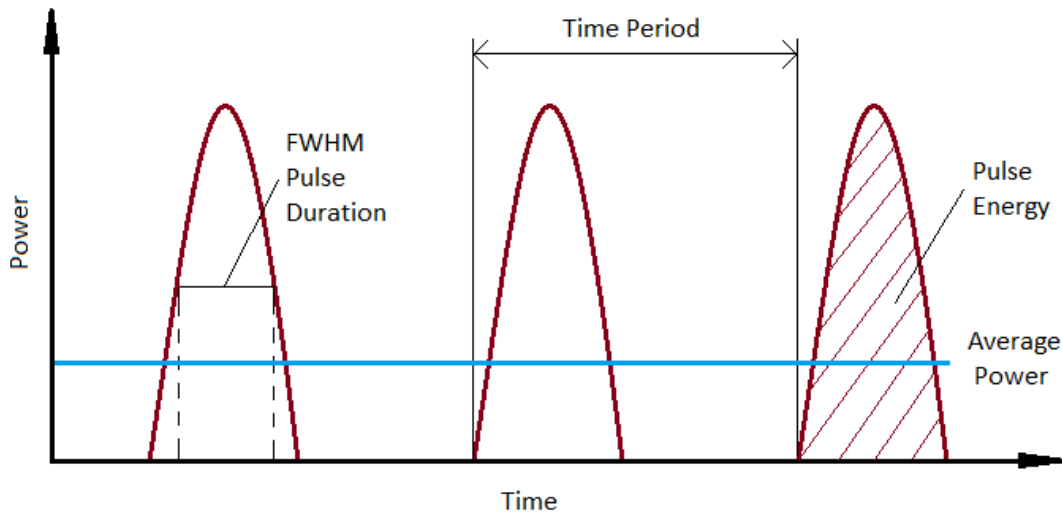


Figure 2.5 Power-time characteristics of laser pulses

Peak power is defined as the pulse energy divided by the full width half maximum pulse duration.

Average Power is defined as the pulse energy divided by the time period.

Irradiance is defined as the laser power divided by the irradiated area and is measured in Watts per unit area. This is a very effective unit for measurement as it includes information about the total energy per unit time over a given area.

Fluence is the laser pulse energy at the sample surface divided by the irradiated area and is sometimes called the energy density. Historically this form of characterisation has been used extensively to describe laser systems and is the most common way to describe laser intensity in the scientific community. The fluence can be controlled by changing either the pulse energy present on a surface, which can be achieved via attenuation of the beam, or by changing the area of that pulse which can be done simply by changing the distance of a sample to a lens placed in the beam path.

2.4.5 Sample Movement

Movement of a sample in the beam propagation direction or z-direction will result in a change of the spot size and therefore a change in fluence. Movement in the x or y direction results in a translation of the spot over the sample surface which will result in an irradiated track in the GO surface. The degree of reduction is governed by the laser fluence, scan speed and pulse rate of the laser as there will be a number of overlapping pulses that contribute to the total amount of energy supplied to a particular point. A schematic of the process is shown in Figure 2.6 and it is important to understand the impact on the average fluence and overall dose at a particular point on the surface when there is relative movement between the sample and the laser beam. This is of particular relevance to this thesis and further details are presented in Section 3.1.

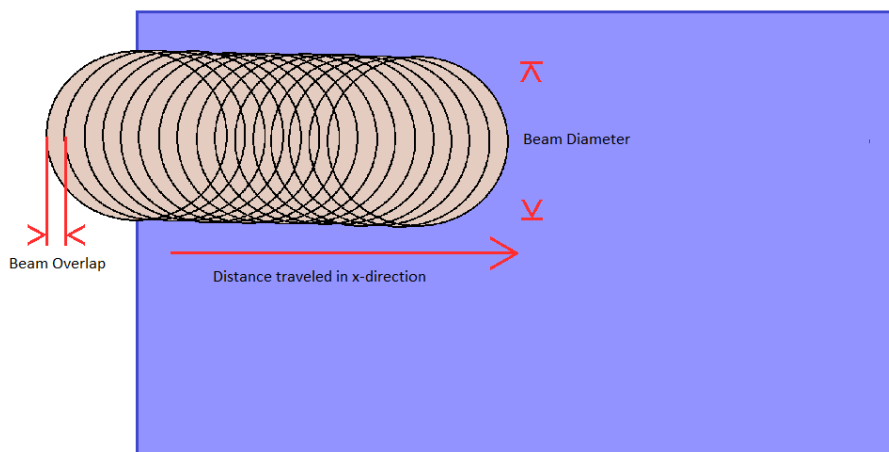


Figure 2.6 Overlapping of laser spot with movement in the x direction

2.4.6 Beam Energy Profile

The spatial beam profile of a laser beam is typically a Gaussian distribution, see Figure 2.7, and therefore there is a higher intensity at the centre of the beam.

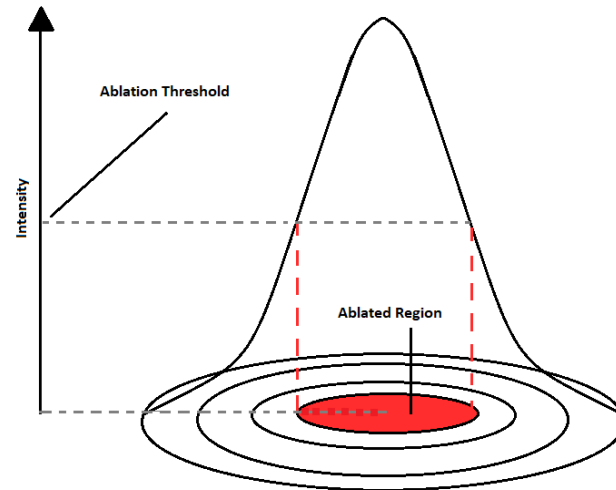


Figure 2.7 Spatial distribution of Gaussian laser beam showing intensity profile

The formula for this beam distribution is shown as equation 2.1.

$$I(r) = I_0 \left(\frac{-2r^2}{\omega_0^2} \right) \quad \text{eqn 2.1}$$

When a circular beam like that shown in Figure 1.8 is focused through a lens the beam width will reduce in size to a minimum beam waist known as (ω_0) at the focal length of the lens (f). After the beam has travelled a distance known as the Rayleigh length (Z_r) its cross sectional area will be double that of (ω_0) . These parameters can be seen in Figure 2.8 and calculation for the Rayleigh length is shown in equation 2.2.

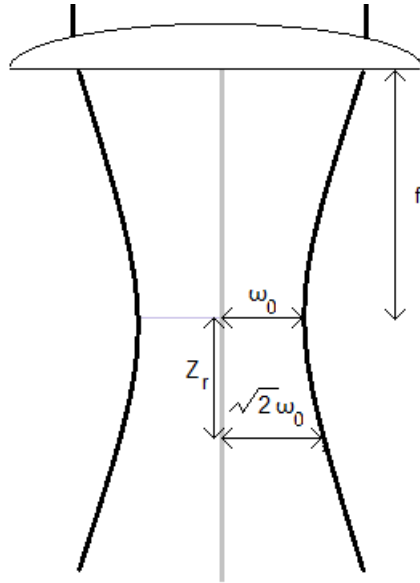


Figure 2.8 Characteristics of Gaussian Laser Beam showing the Rayleigh length (Z_r) as a function of the beam waist (ω_0)

$$Z_r = \frac{\pi \omega_0^2}{\lambda} \quad \text{eqn 2.2}$$

In this study an Nd:YVO₄ laser with a pulsed Gaussian beam of wavelength 1064nm, pulse repetition rate 10kHz and a pulse duration of 4.8ns was used to irradiate films of graphene oxide on glass substrates. Equations 2.1 and 2.2 have subsequently been used to describe the distribution of the fluence of the laser beam on the GO surface.

2.5 Characterisation of the Degree of Reduction

When graphene oxide is photo-reduced to reduced graphene oxide, the degree of reduction is highlighted by changes in the surface characteristics, conductivity and resistance and chemical composition of the surface. To illustrate the impact of laser irradiation on GO films, Figure 2.9 presents an illustrative image obtained using the experimental system developed by the author, to highlight a series of irradiated spots in a GO surface following irradiation at different values of fluence, shown above each Figure. The fluence was changed by adjusting the vertical distance between the sample

surface and the lens of the laser and this resulted in a change in the spot size due to the Gaussian beam distribution of the beam. The spot sizes are also listed in Figure 2.9.

Fluence mJcm^{-2}	46	51	57	64	74	84
Spot diameter μm	184	179	163	157	140	131



Pristine GO (a) (b) (c) (d) (e) (f) (g)

Figure 2.9 Laser irradiated spots due to an increase in fluence from left to right and the consequent change in spot size

These results are more fully described in Section 5.2.1 but serve to illustrate the changes that occur when a GO surface is irradiated at different values of fluence. The colour change, see Li et al., 2014, reflects a difference in the degree of reduction from that of the pristine GO film prior to irradiation with no damage (a), through partial reduction (b), complete reduction (c) and partial to full ablation (d) – (g). The following terms are used to describe the damage and ablation:

Damage threshold – the fluence at which damage first occurs

Ablation threshold – the fluence at which the GO is fully ablated

Values of fluence between the damage and ablation thresholds result in a degree of reduction as a function of the laser fluence. At each fluence it is important to fully quantify the changes in the surface characteristics and the resultant chemical transitions that occur within the GO film as these define the degree of GO reduction to rGO. Several techniques are commonly used to classify the degree of rGO reduction, and these include:

2.5.1 Surface Profiling and Roughness

Many researchers have highlighted that the laser irradiation of GO results in changes to the surface characteristics and hence roughness of the irradiated surface. Hence for each of the experiments the author completed a series of profile measurements of the surface prior to and following the laser irradiation of the GO surface. These are discussed more fully in Section 5.4.1.

2.5.2 Conductance/Resistance changes

The electrical resistance of a material is a measure of its opposition to the flow of electric current. The inverse quantity is electrical conductance i.e. how easily the electric current is able to pass through the material. The SI unit of electrical resistance is the ohm (Ω), while electrical conductance is measured in Siemens (S). The resistance R of a given material depends primarily on the resistivity of the material (ρ), its length and cross section. The resistance R of a conductor of uniform cross section, therefore, can be computed as:

$$R = \rho \frac{l}{A} \quad \text{eqn 2.3}$$

where l is the length of the material, A is the cross-sectional area and ρ is the electrical resistivity of the material. The resistivity can also be calculated if a value for the resistance of a material of known area and length can be obtained.

$$\rho = R \frac{A}{l} \quad \text{eqn 2.4}$$

The conductivity of a material σ is inversely proportional to the resistivity;

$$\sigma = \frac{1}{\rho} \quad \text{eqn 2.5}$$

Most researchers have measured the conductivity/resistivity using the relationship between current and voltage in the form of I/V plots. Two techniques have been shown to commonly be used in the literature: the 2-point probe method see Bobrinetskiy *et al.*, 2017, Kumar *et al.*, 2011, Strong *et al.*, 2012, Wan *et al.*, 2019, and the 4-point probe method see Battacharjya *et al.*, 2018, Gao 2011., Ghoniem *et al.*, 2016, Huang *et al.*, 2011, Sokolov *et al.*, 2013. In this study a 2-point probe was used and, in this method, two electrodes are inserted into the surface of the GO/rGO and the relationship between the input voltage and current between the 2 electrodes is measured. For materials that are ohmic the relationship is a straight line, as shown in Figure 2.10.

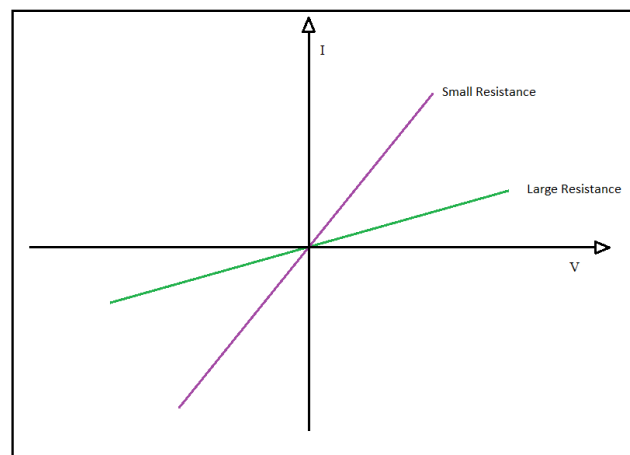


Figure 2.10 Typical I/V plots for ohmic materials

The slope of the graph is subsequently used to assess the resistance and conductivity of the material, with the proviso that the distance and cross-sectional area between the electrodes is known. For GO and rGO previous researchers have reported a wide range of conductivity and resistance results, see Table 2.2, with the results from this study presented in Section 5.4.2 of the thesis.

2.5.3 Raman Spectroscopy

Raman Spectroscopy is a non-destructive chemical analysis technique which is based on the interaction of light with the chemical bonds of the material. The Indian physicist, C V Raman,

discovered that molecules scatter light from a high intensity monochromatic source, such as a laser, and that most of the scattered light has the same wavelength as the incident light. (termed Rayleigh scattering). However, Raman observed that a very small portion of the light may be scattered with different wavelengths, termed Raman Scattering. This is attributed to photons (particles of light) exchanging part of their energy with the molecular vibrations in the material and that the change in energy depends on the frequency of vibration of the molecules which are in turn dependent the masses of the atoms involved and the strength of the bonds between them. Hence the chemical structure of the material governs the Raman scattering and by detecting the scattered light it is possible to relate this not only to the chemical structure but also to the phase, crystallinity and molecular interactions within the material.

The Raman scattered light has a spectrum that shows the relationship between the wavelength (frequency) of the scattered light and its intensity. This contains a number of peaks corresponding to different wavelengths and each peak corresponds to a specific molecular bond vibration or group of vibrations. These peaks are commonly referred to as bands.

In general, Raman spectra highlight three major Raman peaks around 1350 cm^{-1} (D band), 1580 cm^{-1} (G band), and 2700 cm^{-1} (2D band). Several researchers have completed comprehensive studies to interpret the Raman spectra for graphene, graphite, graphene oxide and reduced graphene oxide, see Ferrari *et al.*, 2006, Cancado *et al.*, 2006, Ferrari *et al.*, 2007, Tuinistra and Koenig, 2007, Kudin *et al.*, 2008, Cancado *et al.*, 2011, Lucchese *et al.*, 2010, Ferrari and Basko, 2013 and Diez Betriu *et al.*, 2013. A typical Raman spectra is shown in Figure 2.11. This highlights the D, G and 2D-bands. The D-band is due to first order scattering by zone-boundary phonons caused by disorder or defects in the sp^2 carbon, such as point defects, subdomain boundaries, and edges. This band is largely silent in graphene like structures, but it gains intensity in the spectrum when there are defects in the surface layers of the film, Cancado *et al.*, 2011. The G-band appears in graphene, GO and rGO and reflects first order scattering from an in-plane, E_{2g} phonon mode of sp^2 domains. It is usual to

normalize the Raman spectra to the G band such that comparisons of the relative intensities of the other bands in the spectra may be made. The 2D-band corresponds to the first overtone of the D band and appears in the spectrum at a wavenumber of $\sim 2700\text{ cm}^{-1}$ when the sp^2 rings are present. It originates from a double resonance process and is inextricably linked to the electronic band structure of graphene, and changes as graphene's band structure changes, Ferrari and Basko, 2013. The 2D band is largely absent in GO due to the presence of oxygen containing groups which result in a reduced number of sp^2 hybridised carbons but the laser reduction of GO results in a translation of the carbon lattice with the return to a the more graphene-like, sp^2 structure. This results in an increase in the 2D Raman intensity.

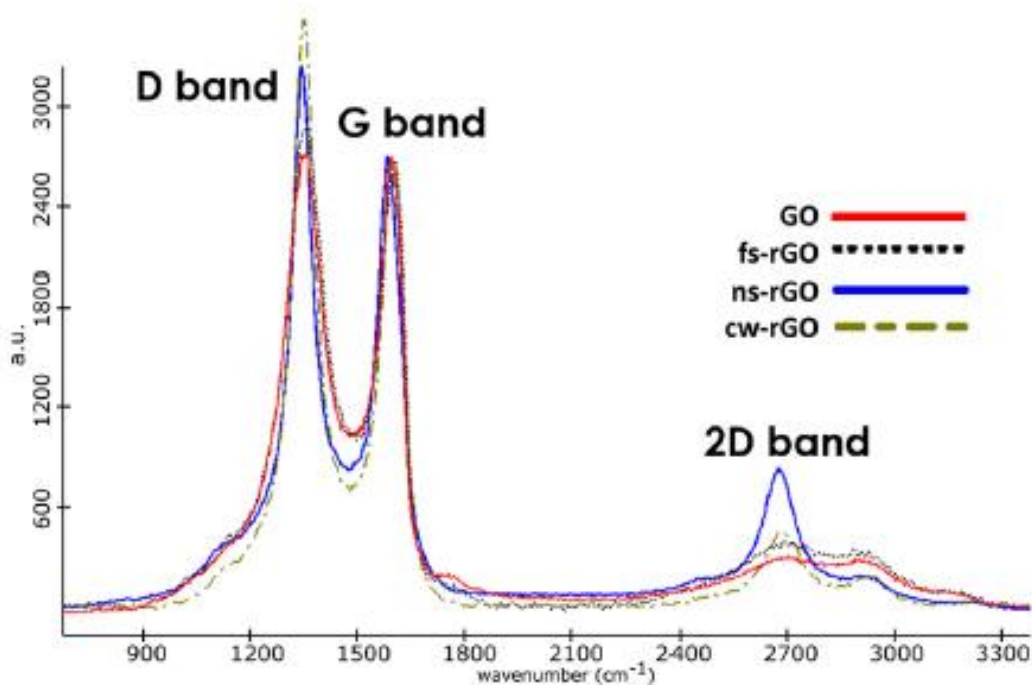


Figure 2.11 Typical Raman Spectra for GO and rGO after irradiation with ns, fs and continuous wave lasers, after Arul *et al.*, 2016, © Elsevier

To interpret differences in the Raman spectra from one material to another the values of the $I(D)/I(G)$ and $I(2D)/I(G)$ ratios are widely used to provide structural information about the graphene films, Trusovas *et al.*, 2016. A decrease in the $I(D)/I(G)$ ratio reflects a reduction in the number of defects and an increase in the crystalline size, an increased D peak intensity and a

narrowing of the G band together with an increase in the I2D/IG ratio reflect the restoration of sp²-hybridized carbon-carbon bonds in the lattice structure and the presence of a fewer number of graphene layers. To assess the narrowing of the spectra reference is made to the full width half maximum (FWHM) of each peak. Hence, for reduced GO the optimum Raman results are a low ID/IG to reflect few defects and a high I2D/IG to reflect the conversion of sp³ to sp² carbon species.

Tuinistra and Koenig, 2007, were the first to observe that the ratio of the D to G intensities varied inversely with the crystallite size, L_a , where:

$$\frac{I(D)}{I(G)} = \frac{C(\lambda)}{L_a} \quad \text{eqn 2.6}$$

and L_a is equal to ~ 4.4 nm when C is equal to 488 nm.

This led to the development of the equation

$$L_a = (1.8 \times 10^{-9})\lambda^4 \left(\frac{I(D)}{I(G)}\right)^{-1} \quad \text{eqn 2.7}$$

where λ is the excitation wavelength, ID is the peak intensity of the D band, and IG is the peak intensity of the G band.

This equation was subsequently modified by Cancado *et al.*, 2006, and Lucchese *et al.*, 2010, to take account of the integrated area of the D and G peaks, where:

$$L_a = (2.4 \times 10^{-9})\lambda^4 \left(\frac{I(D)}{I(G)}\right)^{-1} \quad \text{eqn 2.8}$$

and ID is the integrated intensity of the D band, and IG is the integrated intensity of the G band.

Equation 2.8 has commonly been used by many researchers and has also been used by the author.

Details of the way in which these identifiers have been used by other researchers is described much more fully in Section 2.8.2 and further details are presented in the results discussion of Chapter 5, Sections 5.5.1 and 5.5.2. A description of the Raman instrumentation used in this study is presented in Chapter 4, Section 4.1.9.

2.5.4 X-ray Photoelectron Spectroscopy

X-ray photoelectron spectroscopy (XPS) is a quantitative spectroscopic technique that measures the elements (surface chemistry) that exist within the surface of a material (usually the first 10nm) and of the way in which they are bonded. The material is irradiated with a beam of X-rays which results in the release of a number of photo emitted electrons from the surface. The kinetic energy of these electrons is measured, and these describe a footprint of the surface chemistry of the material. XPS is used to identify and quantity individual elements, identify contamination of the surface, establish empirical formula in the form of integer ratios of the atoms in the chemical compounds and provide details of the local bonding of atoms.

The electron binding energy of each of the emitted electrons can be determined by using equation 2.9:

$$E_{binding} = E_{photon} - (E_{kinetic} + \phi) \quad \text{eqn 2.9}$$

where $E_{binding}$ is the binding energy (BE) of the electron, E_{photon} is the energy of the X-ray photons being used, $E_{kinetic}$ is the kinetic energy of the electron as measured by the instrument and ϕ is the work function dependent on both the spectrometer and the material. This equation is essentially a conservation of energy equation. Hence by knowing the characteristics of the instruments it is possible to calculate the binding energy for each individual element.

Typical outputs from XPS are shown in Figure 2.12

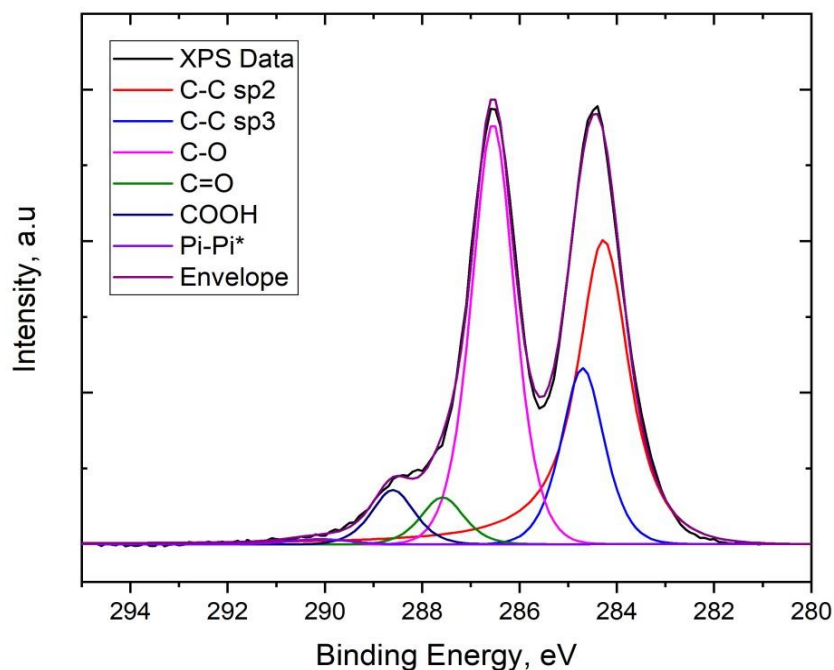


Figure 2.12 Typical XPS Spectra of GO

The XPS data in Figure 2.12 may be deconvoluted to provide information about the chemical bonds in the GO surface. These show the distributions of the sp^2 hybridised carbon-carbon bonds (C-C sp^2) centred on 284.5 eV, the sp^3 hybridised carbon-carbon bonds (C-C sp^3) centred on 285 eV, epoxide/hydroxyl carbon-oxygen bonds (C-O) at 286.6 eV, carbonyl carbon=oxygen bonds (C=O) at 287.6 eV and carboxyl (COOH) at 286.6 eV. Figure 2.12 also shows that distributions may be observed for the COOH and $\pi - \pi^*$ but these have not been commonly used in the assessment of rGO. Following laser irradiation changes to the intensity and shape of these distributions gives a measure of the degree of reduction. Such reduction is usually classified as the changes in the Carbon to Oxygen atomic ratio $C/O_{at}\%$ and the changes in the area under each curve of the chemical bonds, expressed as a percentage.

Previous researchers who have used XPS to examine the quality of GO and rGO have expressed their results using plots of the relative intensity of each element versus binding energy. Fuller details of this research are presented in Section 2.8.2. In this study a similar approach has been adopted with the use of XPS to monitor the changes in carbon and oxygen surface chemistry before and after laser irradiation. The instrumentation used and its application is described in Chapter 4 with the results discussed and compared to those of other researchers in Section 5.5.4 of the thesis.

2.5.5 Scanning Electron Microscopy

A scanning electron microscope (SEM) scans the sample surface with a focussed beam of electrons which interact with atoms in the sample. This results in secondary electrons being emitted from the atoms excited by the electron beam which are detected by the SEM. The electron beam is very narrow but with a large depth of field and, when the beam is rastered over the sample area, an image is produced which has a characteristic three-dimensional appearance, usually at single nano-meter resolution. Interpretation of these images yields details of the topography and make-up of the sample.

Again, many researchers have used SEM to study the changes in the topography characteristics when GO has been irradiated and details of these studies, together with the results of SEM analysis by the author, are presented in Section 5.3.1 of this thesis.

2.5.6 Powder X-ray Diffraction

Some authors have presented results using powder X-ray diffraction (PXRD) in which the material to be analysed is crushed into a powder and homogenised. The technique is primarily used for phase identification of crystalline materials. The result only relates to the bulk sample and it is not possible to select individual locations of a sample where the quality of reduction degree is desired. Due to this reason PXRD has not been studied as part of this thesis.

2.5.7 Changes in Wettability

Wettability may be defined as the propensity of a liquid to spread on a solid surface. The shape of the liquid surface is governed by gravity and the cohesion and surface tension forces which balance to achieve an equilibrium state. This corresponds to the minimum energy state governed by the three forces. The wettability of the surface may be defined by the contact angle (θ) made between the liquid surface and the solid surface and the resultant minimum energy state. The contact angle is governed by the characteristics of the liquid and the roughness of the solid surface and may be described as hydrophobic ($\theta > 90^\circ$), neutral ($\theta = 90^\circ$), hydrophilic ($\theta < 90^\circ$) and perfect ($\theta = 180^\circ$). Hence, in the application of surface coatings, it is desirable to create as near perfect wettability as possible and hence much research has concentrated on the creation of hydrophilic states. Attempts have been made, see Furio *et al.*, 2017, Jiang *et al.*, 2014, Zhang *et al.*, 2012, to examine the wettability of laser reduced rGO and these have highlighted significant improvements in the value of the contact angle for a range of rGO surfaces. Tests were therefore completed to assess the wettability characteristics of the rGO produced in this thesis, see Section 4.1.11, and to assess the changes in rGO wettability with laser fluence and surface roughness, see Section 5.6.

2.5.8 Importance of Temperature

Clearly, the reduction process has been shown to be temperature dependent and several researchers have attempted to develop temperature models to better understand the reduction process, see Kymakis *et al.*, 2013, Zhou *et al.*, 2010, Deng *et al.*, 2016, Evlashin *et al.*, 2018 and Trusovas *et al.*, 2013. These have met with limited success and are more fully discussed in Section 2.9. Subsequently, the author attempted to develop a temperature model to describe the z-scan methodology. The theory behind the z-scan and the temperature model is described in Chapter 3 together with the thesis outcomes and comparison of the research of others in Section 5.7.

2.5.9 Summary of the Measurement Techniques used in this thesis

Based on the review of literature and the above discussion the following measurement techniques were used: Surface Profiling and Roughness, Conductivity/Resistivity, Raman Spectroscopy, XPS and SEM. In addition, as described above, the wettability, classified by the contact angle of a water droplet on the irradiated surface, has been measured.

2.6 Summary Overview of Prior Research

Further to the introduction presented in Section 1.2, a further a series of review papers, Zhang *et al.*, 2013, El-Kady and Kaner, 2014, Sugioka *et al.*, 2014, Jang *et al.*, 2016, Singh, *et al.*, 2016, Trusovas *et al.*, 2016, Kumar *et al.*, 2017, Liu *et al.*, 2017, Wan *et al.*, 2018, Wang *et al.*, 2018, have highlighted the prolific and expansive nature of the application, synthesis, reduction and micro-patterning of graphene oxide (GO). This research has been extensively reviewed and has been used to form the basis of the research completed in this thesis.

2.6.1 Parameter Studies

The research of Zhang *et al.*, 2010, using a pulsed laser, and Zhou *et al.*, 2010, who used a continuous wave laser, paved the way for the environmentally friendly, low cost and controllable reduction of GO using lasers. This early research has led to a large number of fundamental studies that have examined the reduction of GO films and GO solutions for a range of environmental and experimental conditions. For example, different lasers types were studied by Arul *et al.*, 2016, (continuous wave, pulsed ns and pulsed fs) and Kymakis *et al.*, 2014, (pulsed fs and ns), with studies under ambient and inert conditions, see Sokolov *et al.*, 2010. Examples of studies have addressed laser power, He *et al.*, 2016, energy per laser pulse, Bobrinetskiy *et al.*, 2017, repetition rate, Kang *et al.*, 2018, exposure duration, Chen *et al.*, 2014, and scanning speed, Wan *et al.*, 2018. The effect of layer thickness on the resultant changes in conductivity was studied by Tao *et al.*, 2011, whilst a major study with over 8000 tests was completed by Evlashin *et al.*, 2018, who highlighted the relationship between the

degree of reduction and all of the latter variables. Optimum reduction was expressed as a function of Energy Fluence, which combines measures of pulse frequency, pulse energy, the velocity of the laser spot and the spot diameter. To establish the parameters for optimum reduction, all these studies used all or some of the analysis techniques outlined in Section 2.5. Much fuller details of the outcomes of this research have been presented in Section 2.8 which highlights that the majority of these researchers completed a large number of tests. In most cases a large volume of systematic and incremental changes were made to a large number of variables, including the nature of the GO, the laser characteristics and their operational modes, to establish the optimum physical and chemical structure of the rGO for each potential application. Such tests are extremely time consuming and expensive. The need for a less onerous, speedy and novel way to establish this range of optimum parameters has stimulated one of the primary aims of the thesis; the creation of the z-scan methodology.

2.6.2 Direct Laser Writing

Laser direct writing techniques have been commonly exploited in the patterning of GO films and surfaces. Precise fs laser patterning of GO was reported by Zhang *et al*, 2010 b, who created unique three-dimensional shapes with high fabricating accuracy and spatial resolution. One significant approach is laser scribing. El-Kady and Kaner, 2014, presented an excellent summary of the research undertaken using laser scribing techniques and presented their own research to illustrate how such technology may be implemented to develop high-performance and flexible graphene-based electrochemical capacitors, El-Kady *et al.*, 2013, and high-power graphene micro-supercapacitors for flexible and on-chip energy storage, El-Kady and Kaner, 2013. Strong *et al.*, 2012, presented early research using a LightScribe DVD for the reduction and subsequent expansion and exfoliation and fine patterning of graphite oxide. The resultant reduced GO was of relatively poor quality and contained a number of defects. However, the porous surface was not only conducive to the creation of a flexible all organic NO₂ gas sensor but also as a scaffold for the successful growth of platinum nanoparticles. Similarly, Tian *et al.*, 2014 a,b, has been a prolific researcher to use laser scribed

rGO to create strain sensors, flexible resistive random access memory and pressure sensors with high sensitivity.

Lightscribe approaches were also adopted by Arul *et al.*, 2016, in his comparison of three different types of laser performance and by Deng *et al.*, 2016, who showed the flexibility of the approach to reduce GO on a number of arbitrary surfaces, for example a piece of genko leaf, a resin spectacle lens, a feather dress and a butterfly wing. Other substrates have also been used, Das *et al.*, 2016, created 3D nanostructures from inkjet printed reduced GO on cellulose based paper, Han *et al.*, 2015, used UV radiation on graphene oxide papers for bioinspired actuators whilst photo paper was used by Li *et al.*, 2015, to create laser scribed micro-supercapacitors.

2.6.3 Inert Conditions

To avoid the presence of oxygen on the samples several researchers have completed studies in inert atmospheres. Sokolov *et al.*, 2010, used a 532 nm laser in both continuous wave and pulsed mode and a 355 nm wavelength laser in pulsed mode to study the reduction of graphite oxide in air and a nitrogen atmosphere, and an 248 nm excimer laser with samples in a vacuum and in a nitrogen atmosphere. They concluded that the quality of graphene produced in high vacuum was slightly better than that produced in a N₂ background gas. A controllable nitrogen atmosphere with the application of picosecond laser was used to study layers of graphite oxide was mixed with Congo red dye, Trusovas *et al.*, 2012, whilst a novel methodology for the reduction of freestanding graphite oxide (GO) sheet by picosecond pulse laser direct writing in liquid nitrogen and nitrogen gas was reported by Guan *et al.*, 2016. They observed the frozen rGO showed a better ordered crack free structure with less defects and a better electron supercapacitor performance. Bhattacharjya *et al.*, 2018 created an inert gas N₂ atmosphere and used a CO₂ laser to produce a binder-free and self-standing electrode for symmetric supercapacitor cell whilst Petridis *et al.*, 2013, used a vacuum chamber to maintain inert conditions for transistor development. Guo *et al.*, 2014 reported the simultaneous reduction and heteroatom N-doping of GO by femtosecond laser direct writing (FsLDW) in an

NH₃ atmosphere. Complex micropatterns of N-doped and reduced GO (NRGO) were successfully produced and were used to create end bottom-gate n-type FETs.

2.6.4 GO in Solution

The reduction of GO solutions have also been studied in detail. Huang *et al.*, 2011, Spano *et al.*, 2014 and Muttaqin *et al.*, 2017, reported the reduction of GO solutions, observed by colour changes from a brownish yellow to black, as a function of controllable laser parameters. They confirmed that UV light, visible light and fs lasers may be used in the reduction process. The reduction of GO films and GO in solution was studied by Yang and Bock, 2016, who confirmed that the resultant rGO materials using both techniques were appropriate for use in device fabrication. In contrast, Ibrahim *et al.*, 2016, used a femtosecond laser to convert an ultrahigh concentration of aqueous graphene oxide solution into a reduced graphene oxide gel. The laser was focused on the air/solution interface which resulted in the vaporisation of water and the removal of the oxygen containing groups. The resultant gel, termed 'femtogel', and was used to create rGO gel films suitable for device fabrication. Nanostructures from ribbons to quantum dots were produced by the reduction of a GO solution by Lin *et al.*, 2015, whilst Petridis *et al.*, 2013, Stylianakis *et al.*, 2014 and Mukherjee *et al.*, 2012, respectively developed organic photovoltaic devices, organic solar cells and high powered anodes for lithium-ion batteries.

2.6.5 Devices

Other studies have completed a range of tests to establish the optimum parameters for rGO which are specifically targeted to proof of concept applications and device fabrication. A summary of the range of applications is shown in Figure 2.13

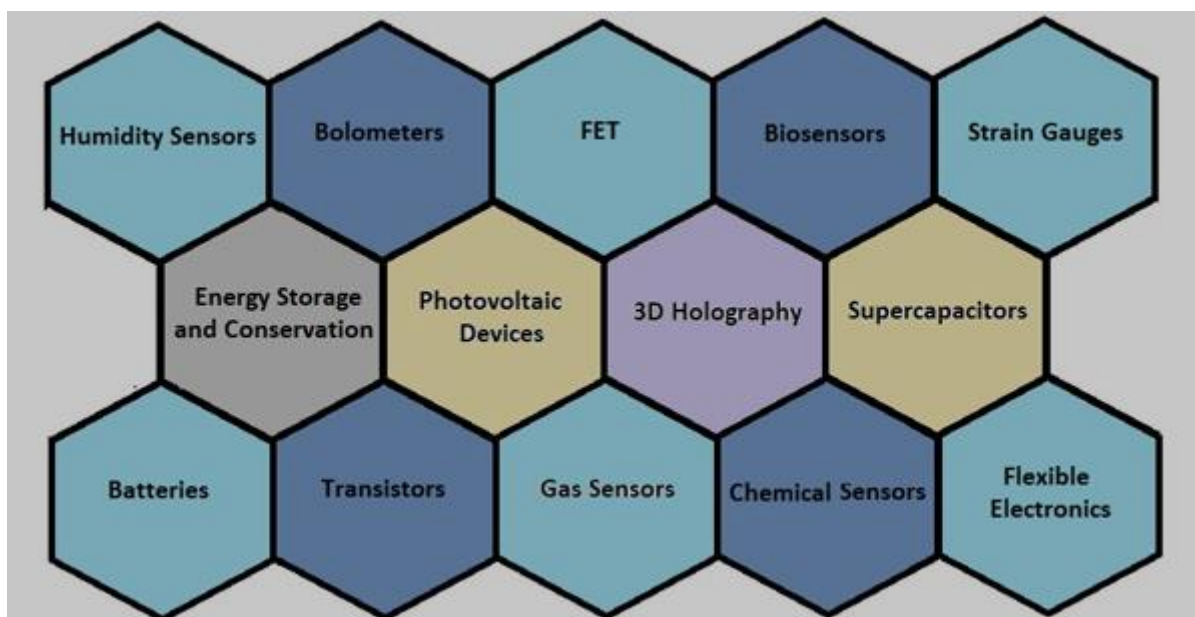


Figure 2.13 Application technologies using rGO

Major elements of research have been completed by Kymakis and co-workers on the application of laser reduced GO films and solutions, see Kymakis *et al.*, 2013, Konios *et al.*, 2015, and Petridis *et al.*, 2013, who researched flexible organic photovoltaic cells, Kymakis *et al.*, 2014 flexible large area optoelectronics, Petridis *et al.*, 2013, field effect transistors, Viskadourous *et al.*, 2014, field emission cathodes and Stylianakis *et al.*, 2014, tunable bandgaps for organic solar cells. Other similar studies were completed by Yin *et al.*, 2010, who used flexible reduced graphene oxide films as transparent electrodes in OPD devices, Guo *et al.*, 2012a, bandgap tailoring, Yung *et al.*, 2013, patterned rGO transparent circuits on GO film, Zheng *et al.*, 2017, rGO within functional photonic devices and Guo *et al.*, 2012b, who developed a two-beam laser interference technique to profile the GO/rGO surface for the production of flexible humidity sensing devices. Li *et al.*, 2015, produced three-dimensional holographic images using athermally reduced graphene oxide. The application of GO and reduced GO has stimulated a multitude of supercapacitors, see Gao *et al.*, 2011, El-Kady *et al.*, 2012, Hu *et al.*, 2014, Kumar *et al.*, 2016, Ghoniem *et al.*, 2016, Yang and Bock, 2016 and Bhattacharjya *et al.*, 2018. Evlashin *et al.*, 2016, Jiang *et al.*, 2016 studied bolometers whilst energy conversion, energy storage, and environmental and biosensing devices were reported

by Tahir *et al.*, 2016, Liu *et al.*, 2017 and Thekkakara *et al.*, 2015. Several other review papers have presented excellent descriptions of this previous work, see Kumar 2013, Kumar *et al.*, 2017, Singh *et al.*, 2016, Sugioka *et al.*, 2014, Trusovas *et al.*, 2016, Zhao *et al.*, 2016 and Wan *et al.*, 2018.

2.6.6 *Comments Related to Thesis Objectives*

The above studies extensively show the versatility of GO and rGO but it is stressed that each of these publications has required, prior to the proof of concept stage of device development, a study of the properties/characteristics of the reduced GO, for example, oxygen modulation, changes in conductivity etc, to establish the optimum performance of the trial device. Again, this emphasises the need to establish the optimum degree of reduction that is appropriate for each device and here the adoption of the z-scan approach developed as part of this thesis, could offer considerable potential benefit in the search for optimum reduction.

In summary, this overview has attempted to encompass the majority of publications in the literature that are in some way relevant to this thesis. However, due to the sheer volume of this research, the following sections of the thesis only describe the most relevant aspects of the literature that have a focus on the characteristics and properties of laser reduced GO films. Studies that have used GO solutions, doping or publications where the emphasis has been on device development and not the basic properties of GO films have not been discussed in detail.

2.7 Types of laser used and their operational characteristics.

A wide range of lasers are available and to illustrate the scale of the different types of lasers used in the reduction of GO films, a comprehensive literature review has been completed and reference is made to Table 2.1. This outlines the details of the types of lasers, their characteristics and the mode of operation used by each individual team of researchers, arranged in alphabetical order.

Table 2.1 highlights the vast range in the type of laser and their operational characteristics that have been used by previous researchers. Both continuous wave lasers and pulsed lasers have been extensively used and a range of different wavelengths, pulse durations, repetition rates and powers have been utilised to create reduced graphene oxide. The set-up of the laser system determines the beam spot size, and this, together with the scan speed determine the size and shape of the irradiated surface. To classify the degree of reduction of this surface reference has commonly been made to laser Fluence, sometimes termed the energy density. Fluence is defined as the laser pulse energy at the sample surface divided by the irradiated area. Other parameters, such as laser power, the energy per unit pulse, or derived parameters such as Energy Fluence (Evlashin 2018) have been used. Where appropriate, the range in the values of fluence and these other variables have been included in Table 2.1.

Table 2.1 Lasers and operating parameters used in prior research

Lead Author	Wavelength nm	Pulse Duration	Frequency	Fluence /	Power	Spot Size	Scan Speed/
Arul <i>et al.</i> , 2016	780 CW LS DVD					15 x 15mm	
Bhattachariya <i>et al.</i> 2018	CO ₂ 10.6µm				9 – 15W	0.5mm	10 -500mms ⁻¹
Bobrinetski <i>et al.</i> 2017	SatsumaHP2 515nm	280fs	500kHz	7–60 nJ range	20µJ max ≥2µJ used	≤ 5 µm	5-100mms ⁻¹
Chen <i>et al</i> 2014	800nm	120fs	80MHz		3mW – 8mW		
Deng <i>et al.</i> 2016	650nm				Low 1.1 to 11.5mW		
Evlashin <i>et al.</i> , 2016	1064 nm Fibre	20ns	10kHz	4 – 28 Jcm ⁻²		50 µm	Overlapping ~3
Evlashin <i>et al.</i> , 2018	1064 nm Fibre	4 – 200ns	1.6 – 1000kHz	0.1 – 100Jcm ⁻²		30 µm	20mms ⁻¹ - 10cms ⁻¹
Furio <i>et al.</i> , 2017	UV Light				300 W		
Ghoniem <i>et al.</i> , 2016	CO ₂				2.0W		
Guo <i>et al.</i> , 2012 a	Nd:YAG	10ns			– 0.3W		
Guo <i>et al.</i> , 2012 b	780ns	120fs	80MHz		8 – 23mW		
He <i>et al.</i> , 2016	780ns	120fs	80MHz				Exposure time 300µs
Huang <i>et al.</i> , 2011	Excimer 248nm	20ns	5Hz		200mJ		Exposure time 5 mins
Jiang <i>et al.</i> , 2016	Nd:YAG 355nm	10ns	10Hz		0.4W	9mm	
Kang <i>et al.</i> ,2018	795nm CW					35µm	10-100µms ⁻¹
Konios <i>et al.</i> , 2016	Excimer 248 nm	0.5 ps	1 Hz	0.4 Jcm ⁻²		0.02 mm ²	
Kumar <i>et al.</i> , 2016	355 nm	20ns			130 – 376 mW	20 µm	0.5 – 5 mms ⁻¹
Kymakis <i>et al.</i> , 2013	800 nm	100fs	1kHz and 80 MHz	3.5 – 35 mJcm ⁻²	1 – 10mW	170µm	
Kymakis <i>et al.</i> , 2014	800n	100fs	1kHz and 80 MHz	3.5 – 35 mJcm ⁻²	1 – 10mW	170µm	
Lasauskas <i>et al.</i> , 2014	Lightscribe 788nm				5mW		
Li <i>et al.</i> , 2014	750 and 830nm	120ns	10kHz	Pulse energy 1.4µJ	10 – 90 mW	30µm x 30µm	
Lin <i>et al.</i> , 2015	415nm	10ns	10kHz	2.58 Jcm ⁻²			
Liu <i>et al.</i> , 2016	800nm	120fs					
Longo <i>et al.</i> , 2017	CW 532nm				20mW		Exposure time 5 mins

Oh <i>et al.</i> , 2012	CW 976 nm				500 – 1000 mW	10 – 50 mm ⁻¹	
Petridis <i>et al.</i> , 2013	KrF Excimer 248 nm	20 ns	1 Hz	10 – 80 mJcm ⁻¹			10 – 1200 pulses
Sokolov <i>et al.</i> , 2010	532 CW						
Sokolov <i>et al.</i> , 2013	KrF Excimer 248 nm	25 ns	1 Hz	60 – 400mJcm ⁻¹		1.8 x 1.98mm	
Spano <i>et al.</i> , 2014	Nd:YAG 532nm	5ns	10Hz	0.32Jcm ⁻²		28mm	Exposure time 15 – 300 mins
Strong <i>et al.</i> , 2012	788nm			5mW			
Tao <i>et al.</i> , 2011	CW Diode 532 nm	CW			12 mW		
Teoh <i>et al.</i> , 2012	532nm				5 – 80 mW	1 μm	
Trusovas <i>et al.</i> , 2013	1064nm	10ps	100kHz	48 - 320 mJcm ⁻¹	7 - 50 mW	20μm	5 – 10 mms ⁻¹
Wan <i>et al.</i> , 2019	780nm	70fs	50MHz	1.9 – 8.3 mJcm ⁻¹	3 – 13 mW	2μm	
Yang <i>et al.</i> , 2016	KrF Excimer 248nm		10 Hz		300 – 530 mJ		
Yang <i>et al.</i> , 2018	UV pulsed 355nm	28ns	100kHz	0.153–0.525 mJcm ⁻¹		60 x 60 mm	50 mms ⁻¹
Yung <i>et al.</i> , 2013	Excimer 248nm	20ns	1Hz	65 -75 mJcm ⁻¹		40nm	200μms ⁻¹
Zhang <i>et al.</i> , 2010	790 nm	120fs	80MHz		0.5 – 3.5 mW	55nm	Exposure time 600μs
Zhou <i>et al.</i> , 2010	663nm			3.4 x 10 ⁻⁹ Wm ⁻²	80 W	3μm	15μms ⁻¹

Table 2.1 (cont) Lasers and operating parameters used in prior research

The following ranges in values were observed:

Wavelength – these range from a wide use of UV Excimer and CO₂ lasers with wavelengths in the range 248 nm to 10.6 μm, through to 1064 nm in the near infrared region.

Pulse Durations: nanosecond, femtosecond and picosecond laser pulse durations have been used.

Frequency – these range from 1 Hz to 80 MHz.

Power – 1.1 mW to 300W

Spot size – 40 nm to 15 mm

Fluence 0.15 mJcm⁻² to 100 Jcm⁻²

Scanning speed 10 μms⁻¹ to 10 cm⁻¹

Exposure time 600μs to 7 hours.

The laser selected for this study was an Nd:YVO₄ laser with 1064 nm wavelength, 4.6 ns pulse duration and frequency 10 kHz, and, by examination of Table 2.1, it can be seen that the combination of these three parameters is different, in some way, to those used by other researchers. Hence the use of this laser, applied to reduce GO films, complimented the existing bank of laser applications detailed in Table 2.1 and provided the opportunity to extend the knowledge base on the laser reduction of GO. This has provided a new avenue of research and the creation of new knowledge, the results of which may be compared to those of other researchers which is one of the aims of the thesis.

2.8 Fuller Review of Selected Papers Relevant to the Thesis

In addition to the large range of lasers used in the previous studies, each individual team of researchers have used some, or all, of the analysis techniques outlined in Section 2.5 to

classify the degree of GO reduction. These relate to a fundamental understanding of the relationship between the characteristics of the GO films, the operational characteristics of the laser and the resultant properties and characteristics of the irradiated GO. In this thesis, the author has used surface profiling, conductivity/resistance measurement, Raman Spectroscopy, X-Ray photoelectron spectroscopy and wettability changes as the analysis techniques to classify the degree of GO film reduction and hence a detailed examination of the results of other researchers that have used these techniques has been made. These are detailed in Sections 2.8.1 which specifically addresses the research on surface characteristics and conductivity changes whilst Section 2.8.2 reports on the Raman and XPS results.

2.8.1 Surface Characteristics and Conductivity

The change in the surface characteristics of irradiated GO, and the subsequent change in conductivity, has been used by many researchers to partially describe the degree of GO reduction. Of particular relevance is the way in which the thickness and roughness of the GO films change with different sources of irradiation and the consequent impact on the resistance/conductivity of the irradiated surface. In some studies, the film has been shown to expand whilst in others the irradiated surface is reduced in thickness. The expansion/reduction process is very much a function of the characteristics of the laser used and a review of the findings of previous researchers is now presented.

2.8.1.1 - Studies highlighting an increase in layer thickness

Expanded surface structures were observed by Cote *et al*, 2009, who reported the flash reduction of GO and by Mukherjee *et al*, 2012, who observed a unique “open-pore” structure due to photothermal reduction. Similarly, expanded structures have been observed by a host of researchers using a standard LightScribe DVD optical drive with 788 nm laser wavelength. Strong *et al.*, 2012, examined the reduction of graphite oxide films. The power of the laser was changed to give different measures of the laser intensity which was subsequently interpreted as grey scale images of different degrees of rGO reduction. The number of times

the laser was scanned over the same section of the surface was also monitored. It was observed that both laser intensity and the number of passes over the surface significantly influenced the characteristics of the resultant rGO and in respect of conductivity the sheet resistance was observed to reduce with increase in laser intensity and to reduce when the number of passes was increased. The optimum reduced resistance was observed at the highest power and the largest number of passes and was reduced from a value greater than $20 \text{ M}\Omega\text{sq}^{-1}$ to $80 \text{ }\Omega\text{sq}^{-1}$ for the reduced graphite oxide. The latter resistance corresponded to a conductivity of 1650 S m^{-1} .

As part of a study that examined the reduction of GO using 3 different thermal treatments, Lazauskas *et al.*, 2014, used a Lightscribe DVD laser 788 nm wavelength and 5 mW maximum power. The initial thickness of the GO layer was 1200 nm and at low power the layer was observed to expand and at higher power the surface contained visual cracks which were attributed to the intensive evaporation of volatile solids. The surface structure was observed to be highly porous which could be attributed to the drastic expansion that occurs due to the removal of the oxygen containing groups (OCGs). They concluded that the expanded surface offered considerable potential for the development of sensors. Similarly, Trusovas *et al.*, 2013, who used a 1064 nm wavelength, 10 ps pulse rate and 100 kHz repetition rate, power in the range 7 mW to 50 mW and scanning speed in the range 5 mms^{-1} to 100 mms^{-1} , showed that the initial thickness of the GO layers was observed to expand as a function of increased fluence. At the higher values of fluence they also observed that crack like structures appeared in the expanded surface and these were attributed to the intensive evaporation of volatile solids. In terms of expansion magnitude, Sokolov *et al.*, 2013, using an ns KrF excimer laser with wavelength 248 nm, observed an increase in the order of $3.2 \text{ }\mu\text{m}$.

Kymakis *et al.*, 2013, Petridis *et al.*, 2013, and Kymakis *et al.*, 2014, completed a large series of tests using 3 lasers to measure the reduction characteristics of GO films with thickness in the range 4.5 to 29 nm on 15 mm square PET substrates. The lasers used were a Ti:Sapphire laser with wavelength 800 nm, 100 fs pulses, repetition rate of 1 kHz and output power in the range of 1.0–10 mW corresponding to fluences of $3.5\text{--}35 \text{ mJcm}^{-2}$. This laser was used to assess

changes in fluence with a constant number of pulses. To investigate the repetition rate effect on the reduction process, a femtosecond (fs) laser with wavelength 800 nm, 100 fs pulse duration and 80-MHz repetition rate was used with a KrF excimer laser of 248 nm, 30-ns pulse duration, and 10-Hz used to assess the effect of pulse duration. The results presented an array of reduction values covering a large range of laser parameters. They showed that the roughness of the GO surface was increased by irradiation and, for areas of large rGO, produced by repeated scanning across the substrate, SEM and AFM highlighted confirmed that the roughness of the rGO was consistent, apart from when partial ablation occurred at power greater than 5.5 mW. A large number of tests were completed to establish the best conductive films through optimum tuning of laser parameters and the thickness of the GO layer. Films of thickness between 4.5 nm to 20.1 nm were tested. The threshold fluence required to reduce the sheet resistance using the fs laser was 3.5 mJcm^{-2} (corresponding to 1 mW output power). The sheet resistance was observed to be a function of laser power and the number of pulses per spot. A film thickness of 20.1 nm and laser power of 5.5 mW were subsequently used to highlight changes in resistance and conductivity due to an increase in the number of pulses in the range 1 – 300 per spot. This resulted in a rapid and large decrease in sheet resistance over the range 1 to 20 pulses ($1000 \text{ k}\Omega\text{sq}^{-1}$ to circa $20 \text{ k}\Omega\text{cm}^{-1}$) with a more gradual reduction prior to saturation at circa 100 pulses (circa $0.7 \text{ k}\Omega\text{cm}^{-1}$). Similarly for a film thickness of 20.1 nm and pulse number 100 the sheet resistance was shown to decrease with laser power from $1200 \text{ k}\Omega\text{cm}^{-1}$ to circa $10 \text{ k}\Omega\text{cm}^{-1}$ at a power of 5.5 mW. An increase in the pulse repetition rate from 1 Hz to 80 MHz (20.1 nm, 100 fs, 100 pulses) resulted in a lower sheet resistance for the same laser power.

Using a KrF excimer laser (243 nm, 20 ns and 1Hz, with pulse numbers in range 10 to 1200, and different fluences) the reduction efficiency was confirmed to be a function of the laser parameters. The threshold of reduction, defined by the lowest fluence to create an increase in conductivity, was circa $10\text{-}15 \text{ mJcm}^{-2}$. It was concluded that by the careful selection of laser parameters (laser energy and number of pulses) the sheet resistance may be reduced by more than 3 orders of magnitude with a corresponding increase in conductivity.

A large range of surface characteristics due to changes in laser power were reported by Deng *et al* (2016). They used an fs, 650 nm laser and increased the laser power from low, through medium to high laser power (low power range 1.1 to 11.5 mW), medium laser power (71 to 116 mW), and high laser power (>172 mW). They observed three distinct regions of reduction which they termed growth, transition and etch regions corresponding to the increase in power. At low power the thickness of the rGO layer increased almost linearly (growth region) and formed a loosely stacked structure. The transition region (medium power) defined a gradual reduction in the thickness of the irradiated surface, attributed to a combination of thickness growth and a reduction in thickness caused by a layer by layer gasification of oxygen, whilst at high laser power the GO layer was completely ablated with the gasification of both oxygen and carbon species. Conductivity and resistance measurements confirmed the observation of the three distinct zones of reduction.

2.8.1.2 - Roughness changes

Three different types of low wavelength lasers were used by Arul *et al.*, 2016, to study the photoreduction of GO to rGO under constant ambient conditions: a CW, 788 nm laser (LightScribe DVD drive), a nanosecond (ns) UV laser (248 nm, 5 ns pulse duration, 500 Hz repetition rate) with fluences in the range 48 mJcm^{-2} to 240 mJcm^{-2} and pulse rates in the range 2 to 50 and a femtosecond (fs) laser (800 nm, 100 fs pulse duration, 1 kHz) at fluences in the range 47 mJcm^{-2} to 968 mJcm^{-2} (1.17 to $24.2 \mu\text{J pulse}^{-1}$) with pulse repetition rate in the range 2 to 50. The ns laser was shown to create rGO with optimum graphene like characteristics whilst the CW laser resulted in the largest damage to the GO surface. The thickness of the GO layers prior to irradiation ranged from 20 to 25 μm and had a relatively featureless surface with slight ripples and a roughness 1.0 to 1.7 μm . Following irradiation, the roughness of the surface was increased. The femtosecond laser resulted in small, irregular (<10 μm diameter) nodules with ripples superimposed on the nodules whilst the ns and CW lasers created nodules (<10 μm diameter) and of the order of 10 μm or slightly larger respectively. The fluence threshold for the GO surface using UV nanosecond pulsed laser ablation (248 nm, 5 ns) was reported as circa 10 mJcm^{-2} .

Increased roughness was also observed by Ibrahim *et al.*, 2016, who, using an fs 800 nm wavelength laser, showed an increase in roughness from 12 nm to 25.3 nm upon irradiation.

Konios *et al.*, 2015, used an excimer laser with wavelength 248 nm, fluence $\approx 0.4 \text{ Jcm}^{-2}$, beam size 0.02 mm^2 , pulse width 0.5 ps, repetition rate 1 Hz, to reduce GO and showed that the initial rGO had a relatively homogeneous and smooth surface with a root mean-square roughness value of 1.59 nm. Following irradiation, the rms roughness was increased to 6.99 nm which was attributed to the loss of oxygen groups. Grids of irradiated rGO were fabricated and the resistance was observed to be a function of the periodicity of the surface ranging from $0.281 \text{ k}\Omega\text{sq}^{-1}$ for the chemically modified rGO through to $405 \text{ k}\Omega\text{sq}^{-1}$ for a periodicity of $550 \mu\text{m}$ and $2850 \text{ k}\Omega\text{sq}^{-1}$ when the periodicity was reduced to $213 \mu\text{m}$. These values highlight that a major increase in the conductivity of GO is afforded by incorporating a grid of irradiated lines into the surface.

An interesting study was completed by Longo *et al.*, 2017, who used graphite nanoplatelets in a modified Hummers method to produce GO with higher reaction yield and faster kinetics. This was placed on PET substrates and irradiated using a continuous wave Nd:YVO₄ laser emitting at 532 nm with 20 mW for 5 min. Uniquely they recorded the temporal evolution of GO reduction during the laser treatment and they concluded reduction process was mainly due to dehydration of the GO layers. The GO surface was observed to contain a series of variously orientated ripples, but these were not observed on the reduced surface. Irradiated racks of different width were fabricated in the GO by controlling the spot size of the laser by changing the distance between the GO surface and the focussing optics, and, for example, following irradiation of a $50 \mu\text{m}$ wide strip irradiated at a laser power of 20 mW for a duration of 5 mins showed that the resistance was reduced from $7 \times 10^8 \text{ k}\Omega\text{sq}^{-1}$ (GO) to $2.9 \text{ k}\Omega\text{sq}^{-1}$, indicating a controllable conductivity of the rGO track. In contrast, Yang and Bock, 2016, used a KrF excimer laser (248 nm) using 300 mJ or 530 mJ beam energies at a 10 Hz repetition rate for either 1 or 2 h to examine the reduction of GO solutions. They reported that that the surface of the reduced GO was randomly aggregated, crumpled and disordered. However, the

conductivity of the reduced GO was increased to a value 1738 Sm^{-1} corresponding to a resistance value of $0.64 \text{ }\Omega\text{cm}^{-2}$.

Substrate temperature studies were completed by Teoh *et al.*, 2011. They irradiated spin coated GO layers of thickness of 20 nm to 60 nm using a laser with wavelength 532 nm, spot size 1 μm and laser power in the range 5 mW to 80 mW. The substrate was heated from an initial temperature of 22°C to temperatures in the range 30 to 100 °C. The roughness of the surface was a function of laser power and at 80 °C the roughness increased rapidly from circa 5 nm to 30 nm over the power range 10 mW to 20 mW and then reduced to a value of circa 10 nm over the range 30 to 50 mW. The sharp rise was attributed to physical damage with more defective sites whilst the reduction was due to annealing at the higher laser power. Samples were sonicated and this resulted in the removal of some or all of the rGO and GO as a function of laser power and temperature. A unique matrix of results was presented, termed a scientific guide, and this was divided into four regions, namely, positive development where both the rGO and GO remained after sonication, negative development where only the rGO remained, partial development where only some of the rGO remained, and unsuccessful development with either the complete removal of both rGO and GO or the non-creation of rGO. The matrix was used to establish criteria for reduction, and they used a series of laser irradiation, sonication, and spin-coating steps to create a 3D multi layered structure with micro-patterning.

2.8.1.3 – Studies highlighting a reduction in layer thickness

In contrast Chen *et al.*, 2014, observed uniform and continuous patterns of reduced thickness rGO using an fs laser 800 nm, wavelength, 120 fs pulse width, 80 MHz repetition rate, exposure durations 500 μs to 900 μs and power 3 mW and 8 mW. The thickness of the GO film was circa 60 nm and for a track width circa 1 nm the track depth was circa 50 nm following irradiation. They explained this reduction by the removal of the oxygen containing groups from the GO sheets and laser induced ablation. Further they concluded that the reduction process was both photochemical and photothermal and involved a combination of electron

excitation, the electron–hole (e–h) recombination induced thermal effect and the possible occurrence of two-photon or multi-photon absorption.

The surface morphology of 43 nm thick GO films was studied by He *et al.*, 2016, who observed that the GO surface contained wrinkles which were smoothed by irradiation using an fs 780 nm laser. They showed that the sunken depth in a 34 μm wide channel was a function of laser power with the depth increasing from 12 nm at 4 mW to 19 nm at 8 mW. The change in sunken depth was attributed to mass loss of OCGs and the emission of carbon species from the GO films. Similar patterns in the flattening of the irregular GO surface into a smoother rGO surface were observed by Bobrinetskiy *et al.*, 2017, who used an fs laser, 515 nm and spot size 5 μm on 0.5 μm thick graphene oxide films.

Yung *et al.*, 2013, used a 248 nm excimer laser, 20 ns pulse width, 1 Hz and 200 μms^{-1} scan speed) to irradiate tracks and circuits in spun cast GO on glass substrates. The spot size was circa 10 μm x 10 μm with a range of energy density 60 mJcm^{-2} to 190 mJcm^{-2} . The majority of tests were completed with a fluence in the range 65 mJcm^{-2} to 75 mJcm^{-2} . The thickness of the GO layer was circa 40 nm and the ablated (sunken) depth in 10 μm wide tracks was between 18 nm and 25 nm with a mean roughness of 0.54 nm. The edges of the tracks were much rougher attributed to steep temperature change accompanied by violent photothermal effects. Resistance measurements identified three zones as a function of the laser fluence defined by a large drop by a factor of circa 10^4 orders of magnitude between 65 mJcm^{-2} and 75 mJcm^{-2} , a slight increase in resistance between 100 mJcm^{-2} and 160 mJcm^{-2} and a subsequent saturation above 160 mJcm^{-2} . The lowest resistance 1×10^{-3} $\text{M}\Omega$ was observed at a fluence of 110 mJcm^{-2} with a corresponding high conductivity 1.3×10^4 Sm^{-1} at 110 mJcm^{-2} .

2.8.1.4 – Irradiated Line Width

Zhang *et al.*, 2010, completed a comprehensive series of tests to examine the relationship between channel width and irradiated channel sunken depth in a 55 nm thick GO film when irradiated with an fs laser with 790 nm wavelength, 120 fs pulse width, 80 MHz repetition

rate, 600 μs exposure duration and a 100 nm scanning step length. Irradiated channel widths in the range 1.5 μm to 500 nm resulted in a sunken surface with corresponding depths of 35 nm and 25 nm respectively. The sunken surface was attributed to the loss of mass and as a result of the rearrangement of atoms in photothermal reduction.

Measurements of conductivity and resistivity showed that these parameters were a function of laser power and in general the higher the laser power, the higher the conductivity, and the lower the resistivity. The highest conductivity was $2.56 \times 10^4 \text{ Sm}^{-1}$ and the lowest resistivity $3.91 \times 10^{-5} \text{ }\Omega\text{m}$ at a laser output power of 3.0 mW. Current voltage curves showed an approximate linear dependence between voltage and current, indicating stable conductivity.

A continuous wave diode laser (wavelength 663 nm, maximum output power of 80 mW ($3.4 \times 10^9 \text{ Wm}^{-2}$ laser density at the sample surface), scan rate $15 \mu\text{ms}^{-1}$ and beam diameter 3 μm) was used by Zhou *et al.*, 2010, to generate micropatterns (grooves and rectangular grids) of rGO in GO layers. The process was heavily dependent on the number of GO layers. Each layer of GO was 1.5 nm thick. For 3 layers there was no observed irradiation, for 5 layers only partial irradiation and for 6 layers or more the laser was effective in irradiating a channel in the GO. The thickness of the layer was 9 nm and the depth of irradiated channel was about 4.5 nm (equivalent to 3 layers). The conductivity of the rGO channel was 1.1 Sm^{-1} . In summary they showed that the layer thickness of GO and the type of substrate material were critical in the laser irradiation process and they concluded that laser absorption and the rate of heat dissipation were important factors. Hence the transfer of heat into the layer was key and outlined an important need for temperature modelling. Similarly, Tao *et al.*, 2012, used a CW diode 532 nm laser to create 20 μm channels in 32 nm and 16 nm thick GO. Following irradiation at a power of 12 W the sunken depth in 1 nm wide irradiated channel was 16 nm whilst at a power of 6W the sunken depth in a 15 nm thick layer of GO was 5 nm. The sunken depth was attributed to partial oxidative burning and photothermal reduction and, as the thickness to the irradiated layer was shown not to decrease with repeats of irradiation of the same channel it was concluded that the laser absorption and rate of heat dissipation is thickness dependent. This thickness dependency highlighted that a minimum of 5 GO layers

were required to observe changes in the surface structure and conductivity. The conductivity of the rGO channels was measured to increase by at least 2 orders of magnitude from circa 0.012 μS to circa 2.82 μS over the range 0 to 0.1 volts. The conductivity increase was observed to be a linear function of the irradiated channel width and repeated scanning of the same channel initially increased the conductivity of the irradiated area but this was subsequently saturated at a conductivity of $\sim 36 \text{ Scm}^{-1}$. Raman and XPS concluded that partial oxidative burning combined with photothermal reduction were the underlying mechanisms for the enhancement of the conductivity after laser irradiation of the GO film.

Wan *et al.*, 2019, examined the laser reduction of GO on glass substrates when changes to the laser power and scanning speed of the laser. The thickness of the GO films was 110 nm and an fs pulse laser with 780 nm centre wavelength, 70 fs pulse width, 50 MHz repetition rate and spot size of 2 μm diameter was used to irradiate an array of rectangular spots each with different power and scanning speed. Power ranged from 3 to 13 mW (corresponding fluence 1.9 to 8.3 mJcm^{-2}) with the range of scanning speed 0.1 to 5 μms^{-1} . The thickness of GO layer was 110 nm. They observed that the thickness of the GO layer was reduced by the irradiation and was a function of the laser scanning speed and energy density. Following irradiation, the sunken depth was observed to increase as a function of laser energy density. At a value of 7 $\text{mJ}\mu\text{m}^{-2}$ the sunken depth was 22 nm which increased to 77 nm at an energy density of 37.5 $\text{mJ}\mu\text{m}^{-2}$ above which the sunken depth was almost constant upto the experimental limit of 65 $\text{mJ}\mu\text{m}^{-2}$. Independently, for the same laser power, the scanning speed was observed to influence the sunken depth, with an increase in depth at a lower scan speed. The change in depth was attributed to mass loss and laser ablation.

Similarly, the conductivity of the laser irradiated GO was observed to be a function of scanning speed and laser energy density. The GO used in the study had a conductivity of $1 \times 10^{-3} \text{ Sm}^{-1}$ and was increased in the range 19 Sm^{-1} (5 μms^{-1}) to 45.5 Sm^{-1} (1 μms^{-1}) at the different scanning speeds. The latter result represents a 4 order of magnitude increase in the conductivity due to laser irradiation.

Oh *et al.*, 2012, reported on the development of a Laser Induced Backward Transfer (LIBT) technique to establish patterns of graphene and rGO directly transferred from GO layers onto PET substrates. They used a continuous wave laser with wavelength 976 nm, power in the range 500 to 1000 mW and scan rate in the range 10 mms⁻¹ to 50 mms⁻¹. A minimum power of 600 mW was required to create a continuous pattern of rGO and tests were completed to examine the relationship between the width of an irradiated line in the rGO and the laser output power and the scan speed. The line width was increased with an increase in output power (circa 205 to 320 μm at 700 mW) and the line width reduced for an increase in the scan rate (circa 380 to 210 μm at scan rate 30 mms⁻¹). SEM images were used to clearly highlight the changes in width. This was as expected as the heat produced by laser absorption is proportional to the laser power and the interaction time and hence wider patterns were expected at higher power or lower scanning speed. The sheet resistance of the rGO was circa 70 Ωsq^{-1} which confirmed effective reduction.

Kumar *et al.*, 2016, used free standing 35 mm diameter and circa 2.2 μm thick films of GO on a moveable stage to fabricate a micro-supercapacitor by direct laser writing. They used an Nd:YVO₄ pulsed laser with wavelength 355 nm, pulse duration 20 ns, 20 μm minimum spot size and 20 W maximum power to create lines of reduced GO between electrodes. Patterns were created at a fixed laser power of 244 mW and scanning speeds in the range 0.5 to 5 mms⁻¹ and with changes to the laser power in the range 130 to 376 mW at a fixed scan speed of 2.5 mms⁻¹. They showed that the reduction process was a function of both parameters. At lower laser scan speeds (≤ 1 mms⁻¹), strong ablation of the GO film occurred with an enlarged and irregular surface pattern in the GO whilst at high scan speeds there was insufficient thermal energy and only partial reduction of the GO was observed. From 1.5 to 5 mms⁻¹, the width of the irradiated line gradually decreased and the optimized laser speed for patterning and reduction was 2.5 mms⁻¹ with corresponding line width 100 μm . By similar observation, there was a uniform reduction in line width with increase in laser power and the optimum power for the reduction of a 2.2 μm film was 244 mW. Above a power above 344 mW the onset of ablation resulted in an abrupt increase in line width caused by lateral heat dissipation.

Resistance (conductivity) values were measured using a two-point probe and the I/V curves for the rGO highlighted a linear dependence between I and V, pointing to Ohmic behaviour. The GO films had high insulating behaviour and high resistance circa $5 \times 10^6 \Omega\text{cm}^{-1}$. The conductivity of the rGO film gradually increased from a value of circa 0.25 Sm^{-1} at a scan speed of 0.5 mms^{-1} to a local maxima of circa 5.5 Sm^{-1} (resistance circa $0.1 \times 10 \Omega\text{cm}^{-1}$) at a scan speed of 2.5 mms^{-1} . At higher scan speeds the conductivity was reduced.

2.8.1.5 - Fluence changes

Yang *et al.*, 2018, investigated the laser reduction of GO powders using a pulsed UV laser with 355 nm wavelength at 5 fluences (0.153, 0.255, 0.357, 0.438 and 0.525 mJcm^{-2}). The pulse repetition rate, scan speed and number of irradiated cycles were fixed at 100 kHz, 50 mms^{-1} , and 10 respectively. The electrical resistance for the GO powders was 280 M Ω and this was reduced on irradiation to 18.2 M Ω at a fluence of 0.153 mJcm^{-2} and further reduced to a value of 2.67 M Ω at a fluence 0.423 mJcm^{-2} . Above this fluence value the GO powders were ablated, and the resistance rapidly increased to a value of 80.3 M Ω at a fluence of 0.525 mJcm^{-2} . Correspondingly recorded changes in surface area mimicked the changes in resistance but in reverse.

2.8.1.6 - Repetition frequency

Two different lasers were used by Kang *et al.*, 2018, to irradiate commercial 170 nm thick graphene oxide (GO) films on glass substrates: a Ti:sapphire laser with wavelength 795 nm operated both in continuous-wave (CW) mode and in pulsed mode (11 MHz repetition rate, and 300-fs pulse duration) and a Ti:sapphire laser with wavelength 794 nm operated at three repetition rates (76 MHz, 10 kHz and 250 kHz) and three pulse durations (125 fs, 180 fs and 400 fs). Different focal length lenses were used to maintain an almost constant spot size. Based on changes in transmission and resistance the degree of reduction was observed for changes in laser fluence and the pulse repetition rate. They observed two patterns of material behaviour as the laser power was increased. The first was due to the absorbed laser energy

creating graphene like layers and the second due to the thinning of layers due to a smaller interlayer distance as the layer becomes more graphene like. Minimum transmission was used to determine the threshold power which was different for each laser. The resistivity at 10 kHz was $6.3 \pm 1.8 \times 10^4 \Omega \text{ sq}^{-1}$ which corresponded to a conductivity of $1.5 \pm 0.5 \text{ Sm}^{-1}$. The CW and the pulsed laser operated at 11 MHz also resulted in reduced resistance by at least 4 orders of magnitude compared to GO. They concluded that kHz pulse trains were more effective for GO reduction than MHz pulse trains or a continuous wave laser.

2.8.1.7 - Changes in laser wavelength

Guo *et al.*, 2014 developed an fs laser system with wavelengths of 750 and 830 nm, instantaneous peak power 400 μJ per pulse, average power 4W, pulse duration 90 fs and repetition rate 10 kHz to create 2D freeform patterns of reduced and ablated GO in 3 – 5 μm thick films. Pulse numbers of 750 and 830 and 1000 were used to irradiate 30 μm by 30 μm squares in the GO film. They observed that the laser with 750 nm wavelength was far more efficient at reducing and ablating the GO. They explained the reduction process as system induced multi-photon absorption (MPA).

2.8.1.8 - 3D structures

The surface structure of reduced GO has been carefully modulated by the use of different lasers and the control of laser parameters to create 3D surfaces and images. Li *et al.*, 2015 used an fs-pulsed laser with wavelength of 800 nm, repetition rate of 1 KHz, pulse width 100 fs and beam width 0.55 μm to create full colour holographic images by subwavelength-scale multilevel optical index modulation. Senyuk *et al.*, 2015, also fabricated three-dimensional functional solid microstructures of reduced graphene oxide using a pulsed near-infrared laser for application in colloids and optoelectronics, whilst Lin *et al.*, 2015, used a pulsed laser (415 nm, 10 Hz, 10 ns) with high fluence, circa 2.58 Jcm^{-2} , to produce GO nanostructures with different shapes including quantum dots (lateral dimension less than 100 nm), nano-ribbons and nanoflakes (squares, rectangles, triangles, hexagons and disks). The surface of rGO was

also used by Lee *et al.*, 2011, to create biocompatible scaffolds for human mesenchymal stem cells.

Section 2.8.1 has highlighted that a large volume of research has been associated with the measurement of surface characteristics and conductivity of the reduced GO as many of the applications rely on the knowledge of these parameters. Table 2.2 highlights a summary of findings of other researchers.

Table 2.2 Summary of resistivity and conductivity results of other researchers

Lead Author	Conductivity
Arul <i>et al.</i> , 2016	2016, no conductivity measurements taken
Bhattacharjya <i>et al.</i> 2018	2018, Between 5 and 15 Ωsq^{-1}
Bobrinetski <i>et al.</i> 2017	Sheet resistance in range 200 – 1200 Ω/sq with minimum 200 Ω/sq in the pulse energy range 35 – 45nJ and 10-25 pulses per μm .
Chen <i>et al.</i> 2014	I/V plots function of laser intensity and exposure duration, Lowest resistance at 900 μs 7.68 x 10 ⁴ Ω and largest at 500 μs = 6.49 x 10 ⁵ Ω .
Deng <i>et al.</i> 2016	GO 160 μm , Low 2.2k Ω , Medium 763 Ω , High 20k Ω (ablated)
Evlashin <i>et al.</i> , 2016	2016 20-100 W/mK
Evlashin <i>et al.</i> , 2018	2018 Lowest resistance 60 Ωsq^{-1}
Furio <i>et al.</i> , 2017	69.2 M Ωsq^{-1} , 14.08 k Ωsq^{-1}
Ghoniem <i>et al.</i> , 2016	rGO 273 Sm^{-1}
Guo <i>et al.</i> , 2012 a	2012 2 Beam. Ohmic I/V plots. Resistance reduced with increased laser power
Guo <i>et al.</i> , 2012 b	2012 Bandgap Ohmic relationship as above
He <i>et al.</i> , 2016	2016
Huang <i>et al.</i> , 2011	2011 Resistance rGO 53.8k Ωsq^{-1} . Conductivity rGO 1.8 x 10 ⁴ Sm^{-1} .
Jiang <i>et al.</i> , 2016	2016 2 Beam Ohmic I/V TBLI more conductive
Kang <i>et al.</i> , 2018	2018 Resistivity at 10kHz 6.3 \pm 1.8 x 10 ⁴ Ωsq^{-1} , which is 5 orders of magnitude less than GO. The corresponding conductivity is Cond 1.5 \pm 0.5 Sm^{-1} . CW and 11MHz also reduced resistance significantly by at least 4 orders of magnitude,
Konios <i>et al.</i> , 2016	2015 no conductivity taken
Kumar <i>et al.</i> , 2016	2016 GO – 5x10 ⁶ Ωcm^{-2} rGO 5 Scm^{-1}
Kymakis <i>et al.</i> , 2013	2016 Conductivity increased by 2 orders of magnitude for a small increase in power (0-4mW). At 5.5 mW a layer thickness 20.1 nm showed large decrease in sheet resistance over the range 1 to 20 pulses from 1000 k Ωsq^{-1} to 20 k Ωsq^{-1} to a minimum of circa 0.7 k Ωsq^{-1} . For a layer thickness 4.5 nm sheet resistance 18 k Ωsq^{-1}
Kymakis <i>et al.</i> , 2014	2014 no conductivity taken
Lasauskas <i>et al.</i> , 2014	2014 no conductivity taken
Li <i>et al.</i> , 2014	2015 no conductivity taken
Lin <i>et al.</i> , 2015	2016 The resistance of the RGO micropatterns further depends on the width and film thickness. Highest conductivity 2.56 x 10 ⁻⁴ at 3mW (range 1 x 10 ⁻³ at 1mW, 5 x 10 ⁻³ at 2mW) Lowest resistance 3.91 x 10 ⁻⁵ Ωm at 3mW. High at 1mW 1.1 x 10 ⁻³ Ωm .
Liu <i>et al.</i> , 2016	2017 – 2.9 k Ωsq^{-1}
Longo <i>et al.</i> , 2017	2012 - 70 Ωsq^{-1}
Oh <i>et al.</i> , 2012	2013 by increasing N, the conductivity of the GO channel progressively improves by more than three orders of magnitude. Corresponding reduction in resistance.
Petridis <i>et al.</i> , 2013	100 – 500 Ωsq^{-1}
Sokolov <i>et al.</i> , 2010	No conductivity taken
Sokolov <i>et al.</i> , 2013	I/V curve for GO nonlinear with conductivity values between 8.07 10 ⁻⁴ to 5.42 10 ⁻³ S m^{-1} . Linear for rGO with conductivity value largely increased to 2.35 10 ³ S m^{-1} . From Kang 1.73 8x10 ³ Sm^{-1}
Spano <i>et al.</i> , 2014	2011 Conductivity function of channel width – linear increase circa 7.3 Sm^{-1} . (6mW, layer 16nm, sunken depth 5nm). Conductivity function of repeated scanning with saturation at 36 Sm^{-1} after 5 scans (6mW, 8nm layer). Conductivity of films 32nm thick had sunken depth 15nm with conductivity 38.3 Scm^{-1} . Laser absorption and rate of heat dissipation is thickness dependent.
Strong <i>et al.</i> , 2012	2012 No conductivity results
Tao <i>et al.</i> , 2011	2013 No conductivity results.
Teoh <i>et al.</i> , 2012	2019 Conductivity of the laser irradiated GO was observed to be a function of scanning speed and laser energy density. The GO used in the study had a conductivity of 1 x 10 ⁻³ Sm^{-1} and was increased in the range 19 Sm^{-1} (5 μms^{-1}) to 45.5 Sm^{-1} (1 μms^{-1}) at the different scanning speeds. The latter result represents a 4 order of magnitude increase in the conductivity due to laser irradiation.
Trusovas <i>et al.</i> , 2013	2016 Conductivity 1738 Sm^{-1} , Resistance 0.64 Ωcm^{-2}
Wan <i>et al.</i> , 2019	2018 18.2 to 0.267 M Ω
Yang <i>et al.</i> , 2016	2013 Three zones defined change in resistance – following little change upto 60 mJcm ⁻² a large drop by factor of circa 10 ⁴ orders of magnitude between 65 mJcm ⁻² and 75 mJcm ⁻² was observed which highlights reduction threshold circa 70 mJcm ⁻² . Greater than 100 mJcm ⁻² C-C bonds break which results in an increase of resistance

	as the GO is ablated and the new surface layers of GO create additional resistance. Above 160 mJcm ⁻² there is a tradeoff between ablation and the newly generated GO with little change in resistance. Highest conductivity 1.3 10 ⁴ Sm ⁻¹ at 110 mJcm ⁻² with corresponding resistance circa 1 x 10 ⁻³ MΩ.
Yang <i>et al.</i> , 2018	2010 . Strong dependency on output power. Higher the laser power the higher the conductivity and the lower the resistance.Highest conductivity was 2.56×10 ⁴ Sm ⁻¹ and the lowest resistivity 3.91×10 ⁻⁵ Ωm at a laser output power of 3.0mW.
Yung <i>et al.</i> , 2013	2010 Go insulating rGO 1.1 Sm ⁻¹

The above discussion has highlighted that many factors influence the surface characteristics of laser irradiated GO. Hence, in this thesis, due consideration has been given to the measurement of surface roughness, change in thickness and change in conductivity of the laser reduced GO samples.

2.8.2 Raman Spectroscopy and XPS

The review of literature has highlighted that both Raman Spectroscopy and X-Ray Photoelectron Spectroscopy have been extensively used in the interpretation of the quality and degree of laser reduction. Many researchers have highlighted that the two analysis techniques are mutually complimentary as they provide a more definitive verification of the reduction of rGO and cross reference between the two sets of results has been commonly made. This section of the thesis has presented a discussion of the literature outputs for both Raman and XPS, either in combination or as an individual analysis technique.

2.8.2.1 - Important early studies

The first reported studies on the reduction of GO were made by Zhang *et al.*, 2010, and Zhou *et al.*, 2010. Zhang *et al.*, 2010, used an fs laser with 790 nm wavelength, 120 fs pulse width, 80 MHz repetition rate, 600 μs exposure duration and a 100 nm scanning step length, to construct patterns of reduced GO between two gold electrodes. The thickness of the GO film was circa 55 nm and line widths in the range 1.5 μm to 500 nm were irradiated.

Raman spectra analysis of GO the films showed D and G peaks at 1354 and 1599 cm⁻¹ respectively. Irradiation resulted in a slightly more peaked distribution but there was no observed band shift in the two spectra. The ID/IG ratio increased from a value of 0.83 (GO) to

0.89 (rGO), caused by a decrease in the size of reduced and patterned graphene domains. X-ray photoelectron spectroscopy (XPS) showed that after reduction the O1's peak intensity was significantly decreased with the content of the carbon not bound to oxygen increased from 44% (GO) to circa 61% rGO).

In contrast, Zhou *et al.*, 2010, used a continuous wave diode laser (wavelength 663 nm, maximum output power of 80 mW ($3.4 \times 10^9 \text{ Wm}^{-2}$ laser density at the sample surface), scan rate $15 \mu\text{ms}^{-1}$ and beam diameter $3 \mu\text{m}$) to generate micropatterns (grooves and rectangular grids) of rGO in GO layers. Raman analysis showed that, following irradiation, there was no band shift, the intensities of both the D and G peaks were reduced but with little change in the shape of the bands or the ID/IG ratio. The I(D)/IG ratio was greater than unity for both the GO and rGO. The peak intensities were also found to be a linear function of the number of layers.

2.8.2.2 - Studies with multiple lasers

Three different lasers were used by Arul *et al.*, 2016, to study the photoreduction of GO to rGO under constant ambient conditions 20°C and 30% relative humidity. The GO films were placed on PET substrates. The lasers used were a CW, 788 nm laser (LightScribe DVD drive) with 6 passes used to form multiple 15 mm by 15 mm square samples, a Nanosecond (ns) UV laser (248 nm, 5 ns pulse duration, 2 to 50 pulse rate, 500 Hz repetition rate) to generate $5 \mu\text{m}$ by $5 \mu\text{m}$ squares for a range of fluence 48 mJcm^{-2} to 240 mJcm^{-2} . and a femtosecond (fs) laser (800 nm, 100 fs pulse duration, 1 kHz) to create $50 \mu\text{m}$ by $50 \mu\text{m}$ square spots at fluences in the range 47 mJcm^{-2} to 968 mJcm^{-2} (1.17 to $24.2 \mu\text{J pulse}^{-1}$) with pulse repetition rate in the range 2 to 50.

The Raman results showed that the D, G and 2D peaks were a function of the fluence and pulse repetition rate for the ns and CW lasers but not for the fs laser. The ID/IG peak was observed to increase for all laser types (from 1.0 (GO) to 1.1 ns and fs and 1.3CW) indicating the presence of defects but with the CW laser creating a larger surface damage. The ratio of

I2D/IG showed that the fs laser did not result in the transformation from sp^3 to sp^2 as the value of the ratio remained the same as that for GO. For the CW laser there was a slight increase in the ratio and for the ns laser the ratio was a factor of 6 times greater than that for GO. The optimum ns parameters to create the highest I2D/IG ratio were 0.12 mJcm^{-2} with 40 overlapping pulses.

The XPS results confirmed that all three laser types removed oxygen from the surface layers but that only the CW and ns lasers reduced the oxygen associated with epoxides and hydroxyls. This suggested that only these two lasers were able to convert the sp^3 to a more graphene like sp^2 lattice.

Arul *et al.*, 2016, proposed that their findings could be explained by reference to a 2-stage process – a photochemical stage and a heat generation stage. It is known, see Sugiota *et al.*, 2014, that fs laser pulses are much less effective when compared to ns lasers at depositing heat in materials and hence the fs laser creates a photochemical removal of oxygen from the surface whereas the ns laser creates a photochemical reduction and a thermal transformation of the carbon lattice to a planar, hexagonal sp^2 conjugated, graphene-like layer. Similarly, the CW laser also created a thermal reaction in the layer but because of the lower fluence and wavelength, the thermal energy change, and hence transformation was not as high. In summary, they concluded that the photochemical reduction of GO is not thermally mediated, but that the structural reorganization from sp^3 to sp^2 required heat deposition into the material.

The role of fs and ns lasers was also studied by Kymakis *et al.*, 2013, Petridis *et al.*, 2013 and Kymakis *et al.*, 2014, who examined the potential of rGO films for application as transparent electrodes in organic photovoltaics (OPV) and for large area optoelectronics. These papers used the same data derived from experiments on the laser reduction of spin coated GO films on PET substrates in air at room temperature. The initial laser was a Ti:Sapphire pulsed laser, 800 nm, 100 fs, 1 kHz and power 1 to 10 mW giving a fluence of 3.5 to 35 mJcm^{-2} . Initial tests showed that as the fluence was increased a series of irradiated spots in the GO were observed

to gradually darken in colour, thereby highlighting a gradual increase in the reduction to rGO. Subsequent tests were also completed using the same laser but operated at 80 MHz to assess the effect of repetition rate and a KrF Excimer laser, 248 nm, 30 ns and 10 Hz to assess the impact of changes to the pulse duration. For each laser the range of fluence was the same at 3.5 mJcm^{-2} to 35 mJcm^{-2} .

Using the ns laser with a 20.1 nm thick layer of GO, as the pulse number increased, Raman spectra showed the D and G peaks reduced in intensity (explained as potential oxidative burning or reduction of interlayer spacing due to removal of oxygenating groups and water), the FWHM for the D and G peaks narrowed (attributed to the re-establishment of the sp^2 carbons and reduction in structural defects within the basal plane of the rGO) but with no appreciable band shift. The D over G peak intensity ratio, $I_{\text{D}}/I_{\text{G}}$, increased rapidly from a value of 0.79 for GO to a value circa 0.96 - 1.0 after 120 pulses. Further increases in the pulse number upto 1200 pulses resulted in a slight overall increase to maximum value circa 1.05. In contrast, for the fs laser (5.5 mW, fs 100 and 20.1 nm) the $I_{\text{D}}/I_{\text{G}}$ ratio was shown to reduce for pulse numbers up to 100 (due to non-thermal reduction) with a subsequent increase to a peak value at circa 0.85 corresponding to 400 pulses, attributed thermal reduction. Hence the pulse duration has a significant influence on the ratio of $I_{\text{D}}/I_{\text{G}}$ which is due to the thermal mechanisms associated with fs and ns pulses. XPS measurements of the GO and rGO surfaces before and after irradiation indicated with the C1's having 3 peaks that correspond to carbon atoms in different functional groups. The non-oxygenated ring C, the C in C-O bands and carboxylate carbon C=O. The carbon content bonded to oxygen was observed to change from 61% to 16%, thereby confirming that most of the oxygen groups were removed. The mechanisms of oxygen removal were attributed to 2 processes: 1) non thermal electronic excitation in the first hundreds of femtoseconds where the C-O electronic bonding near the top of the valence band is significantly weakened (electrons excited from bonding to antibonding states resulting in oxygen removal, and 2) electron-hole (e-h) recombination occurs during the fs pulse and heat reduction of GO dominates the oxygen removal.

They suggested that the narrowing of both the D and G peaks resulted from the creation of more sp^2 carbons to a more graphene like structure. An increase in the ID/IG ratio indicated a disordering of graphite but an ordering of the amorphous carbon structure. Hence the I(D)/(IG) ratio should increase with increasing ordering. The ID/IG ratio was used to predict the average distance between defects, and, using the equation of Lucchese *et al* 2010, Kymakis *et al*, 2013. showed that the distance between defects increased from 10 to 11 nm. This suggested that there was a limit in GO lattice ordering and consequent oxygen removal.

Two different lasers were used by Kang *et al.*, 2018, to irradiate commercial 170 nm thick graphene oxide (GO) films on glass substrates: a Ti:sapphire laser with wavelength 795 nm operated both in continuous-wave (CW) mode or in pulsed mode (11 MHz repetition rate, and 300-fs pulse duration) and a Ti:sapphire laser with wavelength 794 nm operated at three repetition rates (76 MHz, 10 kHz and 250 kHz) and three pulse durations (125 fs, 180 fs and 400 fs). Different focal length lenses were used to maintain an almost constant spot size. No Raman data was presented, and they observed that the resolution of the XPS instrumentation was too low apart from being able to detect a reduction in oxygen. Their main findings related to changes in conductivity as reported above. Continuous wave and ns lasers were used by Sokolov *et al.*, 2010. The continuous-wave laser had a 532 nm wavelength and pulsed lasers with 532 nm and 355 nm wavelength were used to irradiate graphite oxide in air and in N_2 gas. Raman spectroscopy showed that the I2D/IG ratios vary with laser power, wavelength and background gas. An I2D/IG ratio of ~ 0.17 was obtained using continuous-wave excitation in a N_2 background.

Comparison of the Raman spectra for the CW 532 nm beam in the presence of ambient air and N_2 gas showed that the 2D band was enhanced, the G band narrowed, and the D band was nearly removed. The pulsed 532 and 355 nm laser irradiation in N_2 showed the formation of the 2D band and a narrowing of the G band. The D band feature appeared not to change with an increase in wavelength. Examination of the D and 2D peak intensity ratios ID/I2D, a ratio not commonly used in the literature, showed that when using the 355 nm laser, the 2D band was produced at the lowest powers, with a range of ratio values reducing from 2 to 1

and remaining almost constant as the power was increased to the highest power. The 2D band did not appear until the power was 5 mJ per pulse which corresponds to circa 2.8 MWcm⁻². The differences were explained in terms of electron hole plasmas. Single-photon-mediated valence-to-conduction band transitions are excited at 355 nm but at 532 nm at least two photons are required to exceed the band gap and hence a multiphoton process was required to create a similar electron-hole plasma.

Further studies to examine the reduction of graphite oxide in a vacuum chamber with high (10⁻⁶ Torr) and low vacuum (10² Torr) and an environment of flowing high purity N₂ gas were reported by Sokolov *et al.*, 2013. They used a 248 nm excimer laser (25 ns pulse width, 1 Hz, fluence between 60 and 400 mJcm⁻²) to reduce the graphite oxide films. The laser was used to produce a spot size (1.8 by 1.98 mm) and single lines were irradiated for a range of laser characteristics. Raman spectroscopy recorded the characteristic D peak at 1351cm⁻¹ and G peak at 1590 cm⁻¹. The 2D peak was less in evidence. On irradiation, the intensity of D peak was reduced significantly, the G peak was reduced and a 2D peak was observed at 2672 cm⁻¹.

For GO, XPS showed that the initial oxygen concentration was 29% and that the C/O ratio was 2.43 (calculated using the areas under the C1 and O1 peaks). After irradiation, the oxygen content decreased to 3% and the C/O ratio increased to 40. Curve fitting of the C1's spectra showed that the oxygen components were removed with a major increase in the C – C peak which confirmed the dominance of sp² hybridised carbon. The results confirmed graphene formation. Further evidence of the transition from GO to rGO was given by reference to the distance between defects. Using the equation after Cancado *et al.*, 2006, the values of L_D increased from 18.2 nm to 31.5 nm upon irradiation, thereby confirming a transition of the GO to a more ordered state with fewer defects. This was taken as confirmation that the GO had reduced to rGO.

2.8.2.3 - Studies with changes to the power/energy per pulse/fluence and scanning speed.

Many researchers have studied the impact of ns and fs lasers when changes to the power/energy per pulse/fluence and scanning speed have been made. These have involved major studies with systematic and incremental changes made to the variables studied. For example, Bobrinetskiy *et al.*, 2017, used a femtosecond laser to study the reduction of 0.5 μm thick graphene oxide films on a 100 μm thick PET substrate. The femtosecond laser and optics system had a maximum pulse energy of 20 μJ (maximum of 2 μJ used so as not to damage the substrate), wavelength 515 nm, 280 fs pulse length, 500 kHz. repetition rate and spot size under 5 μm . The fs laser was used to create a grid of irradiated squares at 5 nm spacing with different values of energy per pulse (7 – 60 nJ) and scanning speeds (5 – 100 mms^{-1}). This resulted in the completion of a large number of tests and Raman spectroscopy measurements showed that the ratio of the intensity peaks ID/IG and I2D/IG were a function of both energy per pulse and scanning speed, with the ID/IG ratio increasing and decreasing within the range 1.04 to 0.78 and I2D/IG ratio in the range 0.1 to 0.40. 2D plots of the results were interpreted to yield three distinct zones of reduction as a function of the energy per pulse and these were defined as a function of the reduction mechanism: photoreduction (Zone 1), photothermal (zone 3) and a combination of the two (Zone 2). An fs laser was also used by Wan *et al.*, 2019, who examined the laser reduction of GO on glass substrates when changes were made to the laser power and scanning speed of the laser. The thickness of the GO films was 110 nm and an fs pulse laser with 780 nm centre wavelength, 70 fs pulse width, 50 MHz repetition rate and spot size of 2 μm diameter was used to irradiate an array of rectangular spots each with different power and scanning speed. Power ranged from 3 to 13 mW (corresponding fluence 1.93 mJcm^{-2} to 8.3 mJcm^{-2}) with the range of scanning speed 0.1 to 5 μms^{-1} .

XPS showed the presence of carbon C1's and oxygen O1's and as the laser power was increased the intensity of the C1's increased significantly whilst O1's peak decreased which indicated a loss of oxygen atoms. The atomic carbon to oxygen ratios (C/O), calculated from the area of the peaks of C1's and O1's spectra, increased from 2.46 for GO to 3.35 when irradiated at 13 mW. A clear relationship was established between the C/O ratio and laser

power with the decrease in the percentage of oxygen circa 5.2% at 3 mW with a similar value at 10 mW but rising to 13.3% at 13 mW.

The XPS spectra were deconvoluted into 5 main peaks corresponding to the sp^2 hybridized carbon (C-C sp^2 284.5 eV), sp^3 hybridized carbon (C-C sp^3 285 eV), epoxide/hydroxyl (C-O 286.6 eV), carbonyl (C=O 287.6 eV), and carboxyl (COOH 288.6 eV). This enabled a review of the change in sp^2 carbon bonds to sp^3 carbon and a 3 mW laser power was sufficient to convert circa 21% of sp^3 to sp^2 with the value rising to 22.8% at 13 mW.

Raman spectra showed typical D and G bands at 1355 cm^{-1} and 1604 cm^{-1} respectively. The G band peak was considerably lower than the D band peak and the ratio of ID/IG, which describes a measure of the disorder in the graphene structure, ranged from 1.37 to 1.13. The ratio of ID/IG was, in general, observed to reduce for an increase in laser power and to increase with an increase in scanning speed. The authors also used energy density $\text{mJ}\mu\text{m}^{-2}$ (laser power/(scanning speed x track width)) to highlight also that the ratio of ID/IG reduced with increased energy density. At higher values of energy density, the ratio tended to a constant value circa 1.15.

The irradiation at the reported laser powers and scanning speed did not result in the development of a 2D peak at the expected 2700 cm^{-1} . Such a peak is due to second order of zone-boundary phonons. The results suggested that the 780 nm fs laser reduction was localized, and that the reduction was insufficient to create large planar sheets of graphene.

Trusovas *et al.*, 2013, used a 1064 nm wavelength, 10 ps pulse rate and 100 kHz repetition rate to examine the reduction of GO for changes in laser power in the range 7 mW to 50 mW and scanning speed in the range 5 mms^{-1} to 100 mms^{-1} . For a spot diameter $20\ \mu\text{m}$ the corresponding fluence was 48 mJcm^{-2} to 320 mJcm^{-2} . As the fluence was increased the D band intensity increased and the D and G bands narrowed with a shift in intensity to a shorter wavelength. A 2D band appeared at 30 mW and increased in intensity to 50 mW. The optimum reduction was observed at a scanning speed of 30 mms^{-1} at a power of 50 mW. By

tuning the power and the scanning speed it was possible to create lines irradiated at the same laser dose. The D, G, 2D peaks were observed to be a function of the laser dose.

The largest study by far was completed by Evlashin *et al.*, 2018, who used an ns fibre pulsed infrared laser of wavelength 1064 nm to reduce GO to rGO in ambient conditions. They completed over 8000 tests to examine the relationship between laser pulse duration (4 – 200 ns), laser pulse frequency (1.6 to 1000 kHz), average laser fluence (0.1 – 100 Jcm⁻¹ and laser scanning beam speed in the range 20 to 10000 mms⁻¹. The results of this study are discussed more fully in Chapter 5 but in summary, the Raman spectra showed the ID/IG ratio was 1.03 for GO and 0.22 for rGO and the I2D/IG ratio was 0.50 for rGO. Using the empirical expression, after Concado *et al.*, 2006, they estimated crystallite sizes of 28 nm for GO and 88 nm for rGO. The latter value, together with the low ID/IG ratio and the high I2D/IG ratio for rGO, report high quality rGO which is better than previously reported values. These results were confirmed by XPS measurements with reported changes in oxygen from 28% to 3.5% and carbon from 70% to 95.3% due to the reduction process. In an earlier study, Evlashin *et al.*, 2016, presented a method to produce reduced graphene oxide films for optical devices using a fibre laser with wavelength 1064 nm, fluence in the range 4 – 28 Jcm⁻¹, pulse duration 20 ns, frequency 10000 Hz and 50 µm diameter spot size. Raman spectroscopy showed that the peak of the D and G bands shifted from 1351 to 1342cm⁻¹ and 1581 to 1586cm⁻¹ respectively and that the ratio of ID/IG changed from 0.97 to circa 0.82. A weak 2D peak was observed to occur in the resultant rGO. These changes were explained as a function of the structural changes in the film with a reduction in the number of domains and the creation of greater number of smaller graphitic domains. Changes in the D band were attributed to local reduction of the GO surface caused by laser heat with resultant changes to the morphology of the surface. XPS analysis showed that at the lowest fluence of 4 Jcm⁻² the number of C–O bonds dropped by a factor of 2 whilst the C–C bonds showed a corresponding increase. Only slight changes were observed as the fluence was increased to 28 Jcm⁻².

Kumar *et al.*, 2016, used an Nd:YVO₄ pulsed laser, 355 nm, pulse duration 20 ns, 20 µm spot size, scan speeds 0.5 mms⁻¹ to 5.0 mms⁻¹ and laser power in range 130 mW to 376 mW to

irradiate GO films 35 mm diameter, 2.2 μm thick. For both GO and rGO, Raman spectroscopy highlighted D and G peaks at 1351 cm^{-1} and 1595 cm^{-1} respectively and a very weak 2D peak for the rGO at 2720 cm^{-1} . The ID/IG ratio increased slightly from 0.89 (GO) to 0.92 (rGO) which was attributed to the creation of defects and increased porosity during the laser induced thermal processing which created a roughening of the GO surface. At the optimum power of 244 mW, the at% oxygen was reduced from 22.3% to 7.9% as the scan speed was reduced, with a rapid reduction over the range 5.0 to 2.5 mms^{-1} . At a scan speed of 2.5 mms^{-1} the percentage reduction was from 33.4% to 7.2% as the laser power was increased with a similar rapid reduction over the power range 130 mW to 244 mW. Both observations confirmed the increased removal of oxygen containing functional groups at lower scan speed and higher laser power.

A continuous wave laser was used by Oh *et al.*, 2012, who reported on the development of a Laser Induced Backward Transfer (LIBT) technique to establish patterns of graphene and rGO directly transferred from GO layers onto PET substrates. The continuous wave laser had a wavelength 976 nm and power in the range 500 to 1000 mW and scan rate in the range 10 mms^{-1} to 50 mms^{-1} . A minimum power of 600 mW was required to create a continuous pattern of rGO. In their study lines of width 290 μm and spacing between lines of 140 μm were created.

Raman analysis of the GO and rGO showed the classical D (1350 cm^{-1}), G (1580 cm^{-1}) and 2D (2700 cm^{-1}) peaks. The ID/IG peak intensity ratio for the GO was 1.06 and this was reduced in the range 0.89 to 0.67 for increase in laser power at a constant scan speed. Correspondingly, the ratio was shown to increase with an increase in scanning speed at a constant power. The reduction in the ID/IG ratio indicated that the crystal defects were substantially reduced, and graphitization took place.

A high-power CO_2 laser with wavelength 10.6 μm , power in the range 9 W to 15 W and scan speed between 10 mms^{-1} and 500 mms^{-1} was used by Bhattacharjya *et al.*, 2018. to irradiate GO in a N_2 gas chamber. Raman results showed that the results were a function of the laser

power, the scan speed and distance between the irradiated lines. The ratio of ID/IG was observed to increase as the scan speed was increased with values in the range 0.2 to 1.0 (50% power and 0.1 mm between lines). At high scanning speed 500 mms⁻¹, 50% power and shifting pitch 0.5 mm only a slight 2D peak was observed but this was observed to increase with a reduction in the scan speed. At a scanning speed 10 mms⁻¹, 50% power and shifting pitch 0.1 mm the ratio ID/IG was circa 0.6. XPS results showed that with such a powerful laser the GO could be effectively reduced with the change in C1's from 46.9% (GO) to 98.4% with a corresponding reduction in the O1's from 50.2 % (GO) to 1.6 % (rGO). Compared to the reduction under ambient conditions the combination of the laser and the gas atmosphere these values represent the highest recorded reduction.

An early study that observed the impact of laser power was reported by Tao *et al.*, (2012), who used a continuous wave diode laser (532 nm, 12 mW) to create rGO channels in layers of different thickness GO for a range of laser power. Raman analysis showed that there was no band shift but that the D band was slightly broader and had an increased intensity peak (attributed to a decrease in the size of the graphene domains) for the reduced rGO. The ID/IG peak ratio changed negligibly from 0.97 to 0.96 which was attributed to the domain size decreasing after irradiation as well as removal of oxygen functional groups, but not necessarily resulting in the recombination of sp² hybridised carbon and the repair of defects.

The C1's spectra recorded using XPS showed C – C peak at 285.2 eV and this peak contributed 55.3%, the C=O peak was observed at 287.5 eV (37.6%) and O–C=O at 289.2 eV (7.1%). Irradiation resulted in a shift in the C – C binding energy to 284.7 eV with an increase intensity from 55.3% to 69.2%. Reductions were also observed in the C=O (3.7%) and O–C=O (6.7%) peaks. The intensity of the C=O peak changed dramatically from 37.6% to 3.7%. In addition, consideration of the recorded conductivity change, reported above, indicated there is strong evidence that some restoration of the sp² hybridised carbon has occurred, but as the XPS results provided no evidence of amorphous carbon, the spectra identified that a change in domain size was the most likely explanation of the consistent value in the ID/IG ratio.

Power changes were also studied by Guo *et al.*, 2012a, who used a femtosecond laser (780 ns, 120 fs, 80 Mhz) to tailor the bandgap in GO specifically for the direct fabrication of graphene-based microdevices. Raman spectroscopy showed that the ratio ID/IG was reduced with increasing laser power from 0.98 (GO) to 0.90 (10 mW) and 0.84 (23 mW) respectively. The decrease of the ID/IG ratio was considered an indication of graphitization which was confirmed by XPS. The C1's XPS spectra of pristine GO showed three peaks at 284.6, 286.6, and 288.5 eV, attributed to C-C (nonoxygenated ring carbon), C-O (hydroxyl and epoxy carbon), and C=O (carbonyl) bonds respectively. The content of carbon not bonded to oxygen increased with increase in laser power from 38% (GO) to 65% (10 mW) to 83% (23 mW), thereby confirming that a majority of the oxygen-containing groups were removed. XPS also confirmed a corresponding reduction in oxygen content as the power of the fs laser was increased. Hence changes to the channel bandgap could be effectively modulated by fs laser irradiation.

A LightScribe graphite oxide coated DVD was irradiated, using a laser wavelength 788 nm and max power 5 mW, by Strong *et al.*, 2012. The power of the laser was changed to give different measures of the laser intensity which was subsequently interpreted as grey scale images of different degrees of rGO reduction. The number of times the laser was scanned over the same section of the surface was also monitored. It was observed that both laser intensity and the number of passes over the surface significantly influenced the characteristics of the resultant rGO. Raman spectroscopy highlighted the characteristic D, G and 2D peaks in both graphite oxide and the laser reduced surface. The surface of the reduced GO was slightly exfoliated. The intensity of the D band at $\sim 1350 \text{ cm}^{-1}$ was unexpectedly observed to have a slight increase together with a narrowing of the band. These characteristics were considered due to a larger presence of structural edge defects, indicating an overall increase in the amount of smaller graphene domains and a decrease in the types of defects. The G band also narrowed but had a reduced peak intensity with a slight shift from 1585 to 1579 cm^{-1} . These results are consistent with the re-establishment of sp^2 carbons and a decrease in structural defects within the basal planes. The overall changes in the G band indicate a transition from an amorphous carbon state to a more crystalline carbon state. Following irradiation, the 2D peak intensity was

observed to increase significantly, again reflecting the successful reduction of the graphite oxide.

XPS showed that prior to laser reduction the C/O ratio was 2.6, corresponding to a carbon/oxygen content of ~72% and 28%. Following irradiation, the carbon content was enhanced to 96.5% and the oxygen content reduced to 3.5%, giving a C/O ratio equal to 27.8. The C1's spectra were resolved into three different carbon components: carboxyl, sp^3 carbons in the form of epoxide, and hydroxyl carbons, at the following binding energies: approximately 288.1, 286.8, and 284.6 eV, respectively. Spectral analysis showed a significant decrease in oxygen-containing functional groups and an overall increase in the C-C sp^2 carbon peak. The results confirmed that reduction using an infrared laser is viable.

A high-powered CO_2 laser with 2.0 W power and pulse density of $393.7 \text{ pulses cm}^{-1}$ was used by Ghoniem *et al.*, 2016, with a view to examining the use of rGO in inter-digitised supercapacitors. Raman spectrum of the laser reduced rGO film showed D, G and 2D bands at 1353 , 1570 and 2710 cm^{-1} and the derived values of I_{2D}/I_G and I_D/I_G ratios were 0.75 and 0.63, respectively. These results confirm that the high-powered CO_2 laser efficiently provided an excellent tool for recovering the sp^2 network graphitic structure of the GO film. This structural information is well correlated with the recorded high electrical conductivity, $2.73 \times 10^3 \text{ Sm}^{-1}$ of the laser rGO film. These values were observed to be better than those obtained by chemical reduction.

Deng *et al.*, (2016), reported a one-step laser scribing technology, using a 650 nm laser, to pattern large-scale multi-layer graphene like films on a number of substrates. They increased the laser power from low, through medium to high laser power (low power range 1.1 to 11.5 mW), medium laser power (71 to 116 mW), and high laser power (>172 mW). They observed three distinct regions of reduction which they termed growth, transition and etch regions corresponding to the increase in power. These are discussed more fully in Chapter 5 but in respect of Raman spectroscopy typical D, G and 2D peaks were observed at 1341 cm^{-1} , 1576 cm^{-1} and 2677 cm^{-1} respectively. At low power the I_{2D}/I_G intensity ratio was circa 0.6,

indicative of the existence of stacked graphene layers of laser scribed graphene whilst at medium power, the transition region, the I2D/IG intensity ratio reduced to circa 0.45, indicating an increase in the crystalline defects, whilst at high power the surface was ablated. Conductivity and resistance measurements confirmed the observation of three distinct zones. A fuller discussion of the outputs of this research have been discussed in Chapter 5 of the thesis.

The use of irradiated GO as a potential material for application in field effect transistors was studied by He *et al.*, 2016. They used a fs 780 nm wavelength, 120 fs pulse duration, 80 MHz repetition rate, 300 μ s exposure duration and power in the range 4 mW to 8 mW to reduce films of GO. XPS showed that for pristine GO, the carbon/oxygen atom ratio (C/O) was 1.94 which increased with laser power to 2.45 (4 mW) and 11.76 (8 mW). The O1's peak correspondingly reduced with an increase in laser power. The C1's spectra were deconvoluted into three peaks at 284.6, 286.6, and 288.5 eV, corresponding to C–C (nonoxygenated ring carbon), C–O (hydroxyl and epoxy carbon), and C=O (carbonyl), respectively. As laser power increased the C–C species increased from 45% to 63% (4 mW) to 78% (8 mW) with corresponding reductions in the C–O species circa to 15% and C=O species which reduced almost to zero. Hence the XPS results confirmed that the residual OCGs contents in the RGO patterns could be effectively controlled by tuning the laser power.

Yang *et al.*, 2018, investigated the laser reduction of GO powders using a pulsed UV laser with 355 nm wavelength at 5 fluences (0.153, 0.255, 0.357, 0.438 and 0.525 mJcm⁻²). The pulse repetition rate, scan speed and number of irradiated cycles were fixed at 100 kHz, 50 mms⁻¹, and 10 respectively. Raman spectra highlighted the usual D, G and 2D peaks at 1344 cm⁻¹, 1586 cm⁻¹ and 2669 cm⁻¹ respectively with no 2D peak observed for the GO powders. The powders had an ID/IG ratio of 0.77 and on irradiation the value of ID/IG increased from a value of 0.874 mJcm⁻² at a fluence of 0.153 to a value of 1.033 at a fluence of 0.357 mJcm⁻². The ID/IG ratio then reduced to a minimum of 0.922 at a fluence of 0.428 mJcm⁻² after which a further increase in fluence resulted in ablation of the powder with a subsequent increase in the ID/IG ratio to 1.23 at a fluence of 0.523 mJcm⁻². The reverse was true for the value of

I2D/IG which showed an increase from 0.05 at 0.153 mJcm⁻² to a peak value of 0.569 at 4.28 mJcm⁻² followed by a reduction down to 0.483 at 0.525 mJcm⁻². These results confirmed the optimum reduction at a fluence of 0.428 mJcm⁻². XPS results confirmed the reduction process with significant reduction in the oxygen containing bonds, significant increases in the carbon bonds and hence a significant increase in the C/O ratio (0.232 for GO powders to 0.722 at 0.153 mJcm⁻² to 1.86 at 525 mJcm⁻² on irradiation. The corresponding changes on oxygen were from 81.5% for GO down to 58% at 0.153 mJcm⁻² and 35% at 0.525 mJcm⁻², and for carbon bonds the percentages were 18.8% for GO powders up to 41.9% and 65.1% respectively.

Yung *et al.*, 2013, used a 248 nm excimer laser, 20 ns pulse width, 1 Hz and 200 μms⁻¹ scan speed, to irradiate tracks and circuits in spun cast GO on glass substrates. The spot size was circa 10 μm x 10 μm with a range of energy density 60 mJcm⁻² to 190 mJcm⁻². For a fluence range 0 to 100 mJcm⁻² Raman spectra of the GO film showed characteristic D (1351 cm⁻¹) and G (1590 cm⁻¹) peaks but no 2D peak. On irradiation the intensity of the G peak was greater than that of the D peak and the position of the peaks were shifted slightly to 1344 cm⁻¹ and 1569 cm⁻¹ respectively. A 2D peak emerged at 2700 cm⁻¹. The value of the peak intensities was reduced with an increase in laser energy but the change in the ratio of peak ID/IG was small. Using the area under the peaks in the equation after Cancado *et al.*, 2006, they showed that the crystalline size increased from 18.8 nm for GO to 29.7 nm for the rGO.

At the higher energy densities in the range 110 to 140 mJcm⁻² the Raman spectra showed very similar distributions. The relative strength between the D and G peaks remained unchanged but a significant 2D peak at 2700cm⁻¹ was observed.

2.8.2.4 Studies with changes to exposure duration

Chen *et al.*, 2014, used an ultrafast fs laser to reduce graphene oxides into micropatterns using direct laser writing. The laser had a 800 nm wavelength, 120 fs pulse width, 80 MHz repetition rate and was operated with exposure durations in the range 500 to 900 μs. A laser

power of between 3 mW and 8 mW was observed to produce uniform and continuous patterns of rGO. XPS results showed three peaks at 284.6, 286.6 and 288.5 eV, attributed to C–C (nonoxygenated ring carbon), C–O (hydroxyl and epoxy carbon) and C = O (carbonyl), respectively. For GO the content of carbon not bonded to oxygen was 45% and following fs irradiation the percentage of C–O and C = O species decrease the D peak significantly and the C–C percentage increased to 72%. Raman spectra of rGO at 15 sample sites showed similar spectra with two broad peaks at 1354 and 1599 cm^{-1} , corresponding to D and G bands respectively. The ID/IG intensity ratio for each sample was remarkably similar with a value 0.89, indicating a consistent degree of reduction.

Yang and Bock, 2016, used a KrF excimer laser (248 nm) using 300 mJ or 530 mJ beam energies at 10 Hz repetition for either 1 or 2 h to examine the reduction of GO solutions and subsequently the performance of GO films for supercapacitor applications. XPS analysis of the films showed a reduction of the C-O bonds from 50.7_{at} % to 11.2_{at} % with a corresponding increase in the C-C bonds from 28.9_{at} % to 61.0_{at} %. They also expressed their results as a CC/CO ratio where CC refers to the sum of C-Csp³ and C-Csp² bonds and CO applies to all combinations of carbon and oxygen atom bonds. They reported that the CC/CO ratio changed from 0.72 to 3.2 highlighting that the exposure time was a significant factor in the reduction process.

2.8.2.5 - Studies using two beam laser interference

Two-beam-laser interference was used for the simultaneous reduction, patterning and nanostructuring of graphene oxide on flexible substrates by Guo *et al.*, 2012b, to create a high performance humidity sensing device. A triple, Q-switched Nd:YAG laser with 10 ns pulse width and power in the range 0.1 mW to 0.3 mW with an exposure time of 10 s, was used to form channels of irradiated GO. XPS analysis of the GO and rGO showed changes in the O1's from 46% (GO) to 30% (0.15W) and 5.6% (0.3W) with a corresponding increase in the carbon

bonds from C-C=32%, C-O=56%, C=O=12% for GO to C-C=68%, C-O=23% and C=O 9% for rGO at a power of 0.15W and C-C=92%, C-O=9%, C=O=3% at the higher power of 0.3W. Such control of the oxygen groups using 2 beam interference offers added advantages for the production of large-area hierarchical graphene micro-nanostructures.

Micro-structured reduced graphene oxide films with unique superhydrophobicity were prepared by Jiang *et al.*, 2014, who used a frequency-tripled, Q-switched, single-mode Nd:YAG laser (wavelength of 355 nm, frequency 10 Hz, and pulse duration of 10 ns, together with a beam splitter to create furrows and grid structures using two beam laser interference. The resultant rGO had an increased C/O ratio from 2.2 (GO) to 10.2 (furrows) and 17.1 (grids). Corresponding O1's reduced from 31.5% to 9.0% to 5.5%. Raman analysis was inconclusive with no discernible difference between the GO and rGO. This was attributed to the gains in carbon being offset by the increase in defects. Two beam laser interference created the best reported superhydrophobicity.

2.8.2.6 - Thermal considerations

Three different thermal methods; low-temperature annealing TrGO, flame induced FrGO and laser reduction LrGO (DVD burner with 788 nm wavelength and 5 mW maximum power), were studied by Lazauskas *et al.*, 2014, to reduce layers of GO on glass. They observed the surface morphology, structural and chemical properties of the reduced layers and concluded that all techniques resulted in physical and chemical changes in the multi-layer GO. Thermal annealing and laser reduction produced more ordered graphene-like structure multilayer films but Raman analysis showed that the laser reduced graphene oxide had the lowest ID/IG ratio of 0.79 compared to that of GO at 0.97.

2.8.2.7 - Temporal evolution

Longo *et al.*, 2017, used graphite nanoplatelets in a modified Hummers method to produce GO which was deposited on polyethylene terephthalate (PET) substrates and reduced by

means of continuous Nd:YO4 laser, 532 nm wavelength, power 20 mW and exposure time 5 min. The uniqueness of these tests was the recording of the temporal evolution of GO reduction over the 5-minute duration at 50s intervals. Raman analysis showed that as the irradiation time increased the intensity of the D-band increased. This increase was related to the size of the in-plane sp^2 domains with more sp^2 s formed as the irradiation time increased. The ID/IG intensity ratio was observed to increase from 0.78 to 0.96, as a function of the laser exposure time but with the value almost constant at exposure times greater than 150s.

XPS analysis showed that the overall change in C1's and O1's was from 70.2% to 76.7% and 29.8% to 23.3% respectively but that the individual carbon species changed more significantly with the C–C species increasing from 51.3% to 78.0% and the C–O decreasing from 39.8% to 16.4%, thereby confirming reduction as a function of exposure time.

2.8.2.8 - Multi photon absorption

Li *et al.*, 2014, completed a study on the reduction and ablation of graphene oxide films using an fs laser system designed to induce multi-photon absorption (MPA). The laser had wavelength between 750 and 830 nm, instantaneous peak power 400 μ J per pulse, average power 4W, 90 fs, 10 kHz) with a digital micromirror device (DMD) to create 2D freeform patterns of reduced and ablated GO in GO sheets (3-5 microns thick).

Their experimental programme completed an extensive series of tests to first characterise the wavelength of the laser for optimum reduction and ablation. A series of 30 μ m by 30 μ m squares were systematically irradiated in the GO films using the two wavelengths (750 and 830 and 1000 pulse number) and step changes in the laser power from 10 mW to 90 mW. The results highlighted that the wavelength of 750 nm was far more efficient at reducing and ablating the GO. The 750 nm wavelength was used in subsequent studies that examined the optimum pulse number in the range 10^3 to 10^4 with a pulse energy 1.4 μ J. Raman spectroscopy showed that an increase in pulse number resulted in a reduction of the intensity of the D and G bands. 2D bands were difficult to observe attributed to the fact that multiple

layers of GO were used. For a pulse energy of 1.4 μJ the plot of ID/IG ratio versus pulse number was erratic with a minimum value of 0.937 at a pulse number of 4600. The ID/IG ratio was observed to reduce at higher pulse numbers due to the partial ablation of the GO surface. Many tests were required to reach this conclusion.

2.8.2.9 - Summary Table of Raman Spectra and XPS results of other researchers.

Section 2.8.2 has highlighted that a large volume of research has been associated with results analysed using Raman Spectroscopy and X-Ray Photoelectron. Details of the summary outputs of other researchers have been summarised in Tables 2.3 (Raman) and Table 2.4 (XPS).

Table 2.3 Summary of Raman Spectroscopy results of other researchers

Author	Raman Spectroscopy results
Arul <i>et al.</i> , 2016	ID/IG GO =1.0 rGO ns and fs 1.1. 1.3 for CW. I2D/IG fs almost no change, CW slight increase ns 6 fold increase at 0.12mjcm ⁻² with 40 overlapping pulses
Bhattacharjya <i>etal.</i> 2018	Function of scan peed, laser power and shifting pitch. ID/IG 0.2-1.1, ID/I2D 0.25-2.2
Bobrinetski <i>et al.</i> 2017	ID/IG GO 0.94, rGO 1.04 to 0.78, I2D/IG GO 0.3, rGO 0.1 to 0.4. 3 zones of reduction
Chen <i>et al.</i> 2014	ID/IG Little change at 15 sites of the same sample at 0.89
Deng <i>et al.</i> 2016	ID/IG increases with L to M laser power circa 0.35–0.7. I2D/IG reduces circa 0.6 – 0.45
Evlashin <i>et al.</i> , 2016	2016 D band shifts 1351-1342cm ⁻² . G band shifts 1581 to 1586cm ⁻² . ID/IG 0.97 – 0.82
Evlashin <i>et al.</i> , 2018	2018 ID/IG GO 1.03, rGO 0.22, I2D/IG 0.5.
Furio <i>et al.</i> , 2017	ID/IG rGO 0.63. I2D/G 0.75
Ghoniem <i>et al.</i> , 2016	2012a Bandgap ID/IG GO 0.98, rGO 10Mw 0.9, 23 Mw 0.84
Guo <i>et al.</i> , 2012 a	2012b No Raman measurements
Guo <i>et al.</i> , 2012 b	2016 No Raman measurements
He <i>et al.</i> , 2016	2011 GO ID/IG 1.03, rGO ID/IG 1.08. Crystalline size GO 4.3nm, rGO 4.1nm
Huang <i>et al.</i> , 2011	2016 D and G peaks show no discernible differences – down to gains in G band offset by additional defects
Jiang <i>et al.</i> , 2016	2018 No results
Kang <i>et al.</i> , 2018	2015 D and G peaks reduce with increase in pulse number
Konios <i>et al.</i> , 2016	2016 ID/IG 0.89-0.92. Weak 2D peak
Kumar <i>et al.</i> , 2016	2014 ID/IG GO 0.95. ns laser -Increased pulse no peak intensity increased, peaks narrowed and no appreciable band shift. ID/IG 0.79 – 1.0 in 120 pulses, 1.05 After 1200 pulses. ns ID/IG initially reduced up to 100 pulses but max at 0.85 at 400 pulses. Change of crystalline size 10 to 111nm.
Kymakis <i>et al.</i> , 2013	ID/IG GO 0.97, rGO 0.79.
Kymakis <i>et al.</i> , 2014	2014 Intensity od D and G bands reduced with increasing number of pulses with ID/IG values erratic in the range 0.841 to 1.067. Minimum value at 4600 pulses corresponding to a pulse energy of 1.4μJ. No 2D peaks.
Lasauskas <i>et al.</i> , 2014	2016 ID/IG GO 0.83, rGO 0.98. Possibly due to damage creating more defects
Li <i>et al.</i> , 2014	2017 Increase in irradiation time up to 150 secs then saturates. ID/IG GO 0.78, rGO 0.96.
Lin <i>et al.</i> , 2015	2012 ID/IG GO 1.04, rGO increased power constant scan speed 0.89 to 0.67, increased scanning speed 0.58 to 0.74.
Liu <i>et al.</i> , 2016	2013 ID/IG 0.79 – 1.0 in first 120 pulses (see Kymakis)
Longo <i>et al.</i> , 2017	2016
Oh <i>et al.</i> , 2012	2016 ID/IG 0.89 – 0.92
Petridis <i>et al.</i> , 2013	2010 ID/IG 0.17 in N ₂ , ID/I2D 2.0 – 1.0. Increase in laser power D band intensity reduced whilst 2D band increased.
Sokolov <i>et al.</i> , 2010	2013 High vacuum and N ₂ atmosphere. ID/IG and I2D/IG function of laser fluence and number of laser pulses. 3D plots of I2D/IG with wide range of values 0.1 to 0.5. ID/IG graphite oxide greater than 1 reduced to less than 1 on irradiation. La 18.2 – 31.5 nm. I2D/IG 0.1 to 0.5.
Sokolov <i>et al.</i> , 2013	2012 D band reduction, 2D band increase after laser irradiation
Spano <i>et al.</i> , 2014	2011 ID/IG 0.97 – 0.96 negligible. No band shift but D band slightly broader for rGO.

Strong *et al.*, 2012 2011 No difference in Raman analysis as a function of irradiated layers

Tao *et al.*, 2011 2013 Increase in power (7 – 50Mw) D band intensity increased and D and G bands narrowed with shift in intensities to shorter wavelengths. FWHM decreased as a function of laser power and dose rate. 2D band appeared at 30mW and increased in intensity to 50mW at which optimum reduction was observed.

Teoh *et al.*, 2012 2019 Shape of D and G peaks depends on crystalline size with narrower peak for larger crystalline size. ID/IG ratio decreased with decrease in scanning speed ($5\mu\text{ms}^{-1}$ to $1\mu\text{ms}^{-1}$). ID/IG ratio decreased with increase in laser power (3 – 13mW) 1. ID/IG ranged from 1.37 (GO) to 1.13 rGO. No 2D peak observed.

Trusovas *et al.*, 2013 2016 No Raman analysis

Wan *et al.*, 2019 2018 D, G and 2D peaks at 1344 cm^{-1} , 1586 cm^{-1} and 2669 cm^{-1} respectively with no 2D peak for the GO powders. Powders ID/IG 0.77 increased to 0.874 at fluence 0.153 mJcm^{-2} , 1.033 at 0.357 mJcm^{-2} , reduced to 0.922 at 0.428 mJcm^{-2} and increased to 1.23 to 0.523 mJcm^{-2} (ablation). I2D/IG increased from 0.05 at 0.153 mJcm^{-2} to 0.569 at 4.28 mJcm^{-2} down to 0.483 at 0.525 mJcm^{-2} .

Yang *et al.*, 2016 2013 Function of fluence up to 100 mJcm^{-2} D and G peak intensities reduced but peak intensity ID/IG remained almost the same. 2D peak developed at $80\text{-}100\text{ mJcm}^{-2}$. Slight shift 7cm^{-1} D and 21cm^{-1} for G. At higher fluence strong 2D peak emerged with 2D FWHM 64cm^{-1} . La increased from 18.8nm to 29.7.

Yang *et al.*, 2018 2010 ID/IG 0.83 – 0.89 due to decrease in size of reduced rGO domains. No band shift from 1354 cm^{-1} and 1599 cm^{-1} . Slight sharpening of D and G peaks

Yung *et al.*, 2013 2010 No band shift or broadening of peaks, D and G peak intensity reduced linearly with number of layers and intensity. ID/IG always greater than 1.

Table 2.4 Summary of XPS results of other researchers

Author	XPS findings
Arul <i>et al.</i> , 2016	Peaks of the C-O, C=O and COOH bonds normalised to the C-C peak for GO are 83%, 25% and 10% respectively. Corresponding rGO values for the ns laser are 16%, 10% and 5% respectively, values for fs laser are 59%, 20% and 3% and for the CW laser 15%, 8% and 5%. Hence CW and ns lasers able to convert sp ³ to sp ² with fs laser much less effective than ns laser.
Bhattacharjya <i>etal.</i> 2018	C/O ratios found between 60.4 and 9.8
Bobrinetski <i>et al.</i> 2017	No XPS analysis
Chen <i>et al.</i> 2014	C-C increased from 45% to 72% accompanied by significant reductions in C-O and C=O
Deng <i>et al.</i> 2016	No XPS analysis
Evlashin <i>et al.</i> , 2016	At 4Jcm ⁻² (lowest fluence) C-O bonds dropped by factor of 2 whilst C-C bonds showed corresponding increase. Fluence 28Jcm ⁻² only minor reductions and increases
Evlashin <i>et al.</i> , 2018	O1's reduced 28 – 3.5%, C1's increased from 70 – 95.3%
Furio <i>et al.</i> , 2017	No XPS taken
Ghoniem <i>et al.</i> , 2016	No XPS for rGO
Guo <i>et al.</i> , 2012 a	C-C GO 38%, rGO 10mW 65%, 23mW 83%
Guo <i>et al.</i> , 2012 b	GO O1's 46%, Power 0.15W 30%, 0.3W 5.6% GO C- C 32%. C – O 56%, C = O 12%, rGO Power 0.15W O 30%, C- C 68%. C – O 23%, C = O 9%, rGO Power 0.3W O 5.6%, C- C 92%. C – O 9%, C = O 3%
He <i>et al.</i> , 2016	C/O GO 1.94, rGO (4mW) 2.45, (8mW) 4.95. C-C GO 45%, rGO (4mW) 63.0%, (8mW) 78% C-O at 8mW down to 15%, C=O down to almost zero.
Huang <i>et al.</i> , 2011	37% weight loss at 220°C. C/O ratios from 38.1 to 8% were observed.
Jiang <i>et al.</i> , 2016	O1's GO 31.5%, TBLI 9.0%, Dual TBLI 5.5% C/O GO 2.2, TBLI 10.2, Dual TBLI 17.1.
Kang <i>et al.</i> , 2018	No detailed results as XPS resolution too low but able to show reduction in oxygen but not distinguish sp's
Konios <i>et al.</i> , 2016	Showed reduction of oxygen containing groups. Details in supplementary
Kumar <i>et al.</i> , 2016	No XPS analysis
Kymakis <i>et al.</i> , 2013	Carbon bonded to oxygen reduced from 61% to 16%
Kymakis <i>et al.</i> , 2014	No XPS analysis
Lasauskas <i>et al.</i> , 2014	No XPS analysis
Li <i>et al.</i> , 2014	C-C increased from 14% to 64%. C-O reduced from 56% to 25%
Lin <i>et al.</i> , 2015	C-C GO 46% increased to 61% when reduced. C-O from 50% to circa 10%
Liu <i>et al.</i> , 2016	C1's GO 70.2, rGO 29.8, C- C GO 51.3, rGO 78.0, C – O GO 39.8, rGO 16.4, C = O GO 7.3, rGO 4.5
Longo <i>et al.</i> , 2017	O1s peak decrease, considerable decrease in C-O/C=O
Oh <i>et al.</i> , 2012	C-O 61% to 16%
Petridis <i>et al.</i> , 2013	No XPS taken
Sokolov <i>et al.</i> , 2010	Oxygen content of GO 29%. C/O ratio 2.43. After irradiation C/O ratio may increase to 40 as a function of laser pulse and number of pulses. 3D plots of C/O with range of values 10 to 40.
Sokolov <i>et al.</i> , 2013	C1's 72% to 96.5%. O1's 38.0% to 3.5%. C/O 2.6 to 27.8
Spano <i>et al.</i> , 2014	C-C 55.3% to 68.2%, C – O 37.6% to 3.7%, C=O 7.1% to 6.8%
Strong <i>et al.</i> , 2012	C1's 64.5% to 71.5%, O1's 35.5% to 28.5%. C-C 55.3% to 68.2%, C-O 37.6% to 3.7%, C=O 7.1% to 6.7%
Tao <i>et al.</i> , 2011	No XPS analysis
Teoh <i>et al.</i> , 2012	C/O 2.46 to 3.35 as power increased 3 to 13mW. Percentage of CC bond to CO bond increased from 1.02 (GO) to 1.76 (LRGO 13 mW). C–C 23% to 49% (3mW) to 59% (13mW), C-O 27% to 6% to 1%, C=O 10% to 5% to 5%
Trusovas <i>et al.</i> , 2013	C-O 50.7 _{at} % to 11.2 _{at} %, C-C 28.9 _{at} % to 61.0 _{at} %. CC/CO 0.72 to 3.2, where CC is the refers to the sum of C-Csp ³ and C-Csp ² bonds and CO applies to all combinations of carbon and oxygen atom bonds.
Wan <i>et al.</i> , 2019	GO powders O1's 81.5%, C1's 18.8%, C/O 0.232. rGO Fluence 0.153 mJcm ⁻² , O1's 58.0%, C1's 41.9%, C/O 0.722, Fluence 0.375 mJcm ⁻² , O1's 41.8% , C1's 58.2%, C/O 0.1.39. Fluence 5.25 mJcm ⁻² , O1's 34.9%, C1's 65.1%, C/O 0.1.86.
Yang <i>et al.</i> , 2016	No XPS analysis
Yang <i>et al.</i> , 2018	C-C 44% to 61%. Reduction in oxygen observed
Yung <i>et al.</i> , 2013	No XPS analysis

2.9 Influence of temperature on the reduction process

This section highlights the importance of temperature on the reduction process. Firstly, in Section 2.9.1, aspects of temperature associated with the mechanisms of reduction are discussed whilst Section 2.9.2 presents a review of the previous literature associated with temperature and temperature modelling. This review highlights the processes associated with multi pulse irradiation are complex as changes in the absorption and heat transfer result in different thermal effects in the surface and lower layers which are difficult to quantify. The need for further modelling is identified.

2.9.1 *Photon Interaction with Matter and Photochemical and Photothermal Reduction*

The effects of photons incident on a GO surface have been characterised into two main groups; Photochemical interaction and photothermal interaction. Photochemical interaction occurs when the photon energy $E = h\nu$ is equal to or greater than the bond energy. Energy from these photons can transfer into electrons via the photoelectric effect directly breaking chemical bonds. This can expel functional groups from the lattice reducing GO. Photothermal interaction occurs when the photon energy $E = h\nu$ does not exceed the bond energy and so a photon can only promote an electron to a quantised vibrational energy state which is lower than the ionisation energy. This can be represented with a Jablonski diagram shown in Figure 2.14.

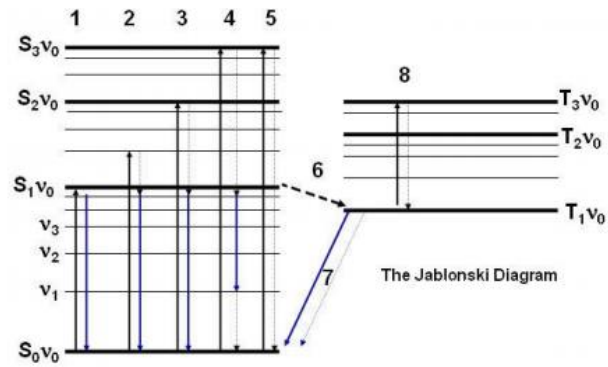


Figure 2.14 Jablonski diagrams show electron states and possible electron transitions between each state.

Here black solid lines represent electron promotion from one state to another, (this requires photon energy), blue lines represent photon emission and dotted lines represent heat producing mechanisms. Taking the second case in the diagram, light is absorbed by an electron in the ground state with enough energy to promote the electron to a metastable state between the first singlet state and second singlet state. This energy then vibrationally cascades as heat to the first singlet state and then is emitted as a photon as the electron drops back to the ground state. The heating produced in this manner gives thermal energy to the whole system and so with high power excitation ionisation and even plasma generation can occur.

Further to these two characterisations it is possible to break bonds directly with a laser that has a photon energy of less than the bond energy if the pulse is particularly intense as an electron can go through multiphoton absorption before being promoted to the next energy state or ionised. Pulses this intense can be produced from a mode locked laser where pulses produced can be femtoseconds or picoseconds in length.

Smirnov *et al.*, 2011, studied the reduction of graphite oxide in solution and in a film deposited on quartz using UV irradiation at ambient temperature. They observed that the threshold for transition between the photochemical and photothermal processes occurred at a photon

energy of 3.2eV. Similarly, Smirnov *et al.*, 2013, in a study of the effect of temperature on GO showed that the threshold temperature to create photothermal effects in GO was circa 77 °K and hence a combination of UV irradiation and temperature can effectively control the reduction process. The value of 3.2eV effectively corresponds to a laser wavelength of 390 nm and hence treatment by a laser with a wavelength smaller than 390 nm would mainly undergo a photochemical process; whereas for lasers with wavelengths larger than 390 nm, the photothermal process mainly accounts for the reduction of GO.

Arul *et al.*, 2016, in their comparison of laser performance led to the conclusion that the photochemical reduction of GO is not thermally mediated, and that the structural reorganization of the lattice requires heat deposition into the material. To create thermally mediated structural relaxation, it is required to have a laser pulse of duration longer than that of the electron-phonon equilibration time of the material. For GO, Zhou *et al.*, 2010, reported that the electron-phonon equilibration time is 0.37ps and hence any laser pulse duration less than this value will not be sufficient for the excited electrons to transfer their energy to the phonons and thereby heat the lattice. Hence the fs laser had an insufficient pulse duration to create such an energy transfer. Their findings agreed with those of Sugioka and Cheng, 2014, who confirmed that fs laser pulses were much less effective when compared to ns lasers at depositing heat in materials and hence only the ns laser provided photothermal reduction. Similarly, Zhang *et al.*, 2010, reported that thermal reduction may not occur using a femtosecond laser and that multiphoton absorption may account for the reduction with both photochemical and photothermal processes. Multi photon absorption was reported by Guo *et al.*, 2014, who developed a fs laser system with wavelengths of 750 and 830 nm, instantaneous peak power 400 μJ per pulse, average power 4W, pulse duration 90 fs and repetition rate 10 kHz to create 2D freeform patterns of reduced and ablated GO in GO 3 – 5 μm thick films. Pulse numbers of 750 and 830 and 1000 were used to irradiate 30 μm by 30 μm squares in the GO film with subsequent changes in laser power in the range. They observed that the laser with 750 nm wavelength was far more efficient at reducing and

ablating the GO. They explained the reduction process as system induced multi-photon absorption (MPA) and at high laser power high concentrations of free electrons lead to plasma mediated ablation.

Low wavelength laser sources, Bhattacharjya *et al.*, 2016, have low penetration depth and low reduction efficiency when compared to a continuous wave CO₂ laser with wavelength of 10.6 μm. The CO₂ laser with wavelength in the mid-IR region was able to convert electromagnetic energy into thermal energy with resultant high temperatures as a function of laser intensity.

There is a complex relationship between the irradiation of GO into heat and photothermal desorption of oxygen groups and the subsequent photothermal breakage of carbon bonds and the re-establishment of lattice frameworks. Upon initial excitation with nanosecond pulses the laser energy was converted into heat within the GO layer which results in a photothermal reduction of the G peaks due to desorption of the oxygen groups (hydroxyl and epoxides). As the irradiation is increased these thermal effects give way to photothermal breakage of the carbon bonds which re-establishes the lattice structure and reduces defects. The temperature changes that occur within the reduction process are exceptionally important and it has previously been reported that exothermic reduction of GO occurs at a temperature circa 200 – 230 °C and that oxidation and sublimation of the carbon backbone occur at circa 500 °C. Several researchers have attempted to describe the changes in temperature that occur within a GO layer due to irradiation from lasers with different characteristics. Some aspects of this modelling are now described.

2.9.2 *Review of Previous Literature on Temperature Modelling*

Different types of modelling approaches to predict the changes in temperature that occur during the reduction process have been used by several researchers. For example, Kymakis *et al.*, (2014), used a Finite Element Model (FEM) to solve the heat conduction equation to

provide a better understanding of the heat absorption and thermal effects within the layer and down to a PET substrate. Both longitudinal and vertical temperature distributions were predicted but they concluded that the numerical model over-predicted the temperature distribution and that the irradiation of GO may be considered as ablation/oxidation of the topmost layers and photothermal reduction by deoxygenation of the oxygen groups in the lower layers. Similarly, Zhou *et al.*, 2010, developed a finite element mathematical model to examine the heat transfer in layers of GO which were grown using an electrostatic layer-by-layer (LBL) technique on quartz substrate with each layer linked using polyethylenimine (PEI). They showed that the temperature on the surface of the GO was a function of the number of layers and that the temperature was rapidly reduced through the layers. Evlashin *et al.*, 2018, solved the heat transfer equation in cylindrical co-ordinates and showed that the temperature change was a function of the radial distance and that maximum temperatures of almost 2000 °K were predicted. It was anticipated that the maximum achievable temperature at the centre of the laser beam would be in excess of this value. All these studies indicated the difficulties associated with the changing values of the coefficients associated with heat transfer and suggested opportunities for further research.

Simulation of the temperature distribution in laser reduced GO layer was completed using the COMSOL Multiphysics software by Trusovas *et al.*, 2013. The mean laser power (pulse energy) and scanning speed (overlapping dose) were varied between simulations. The temperature distributions were calculated at the central point of the laser pulses for different depths into the layer. They showed that a similar distribution of the temporal change in temperature was observed at each location through the depth but with an increase in the peak value as the energy density was increased. After one pulse the highest simulated temperature greater than 1400 °K but the temperature rapidly reduced from the surface into the layer. The simulated temperature was a function of the time taken between overlapping pulses and the heating/cooling processes that occur and hence the way in which the pulses overlap is key to the generated temperature. Clearly, the development of the z-

scan approach is very much a function of the change in fluence due to the change in size of the overlapping pulses. It was considered appropriate therefore to attempt the development of a mathematical model to describe this process as part of this thesis and this is described in Section 3.2.

2.10 Literature Associated with the Wettability of Reduced GO Surfaces

The review of the literature has also highlighted that several researchers have given consideration to the application of rGO for surface coatings. Studies have been completed to examine the wettability of the surface as films with unique super hydrophobicity offer potential in future applications such as micro-droplet manipulation, anti-biofouling substrates, responsive switching and sensitive surface protection by the refined control of surface wettability. Generally, the surface wettability is governed by two factors: the chemical composition, and the surface topography. By controlling these two factors it is possible to tune the wettability, usually represented by the water contact angle (CA) with the surface.

Wettability may be defined as the propensity of a liquid to spread on a solid surface and when a droplet of liquid is deposited on a surface the shape changes to one of the forms shown in Figure 2.15.

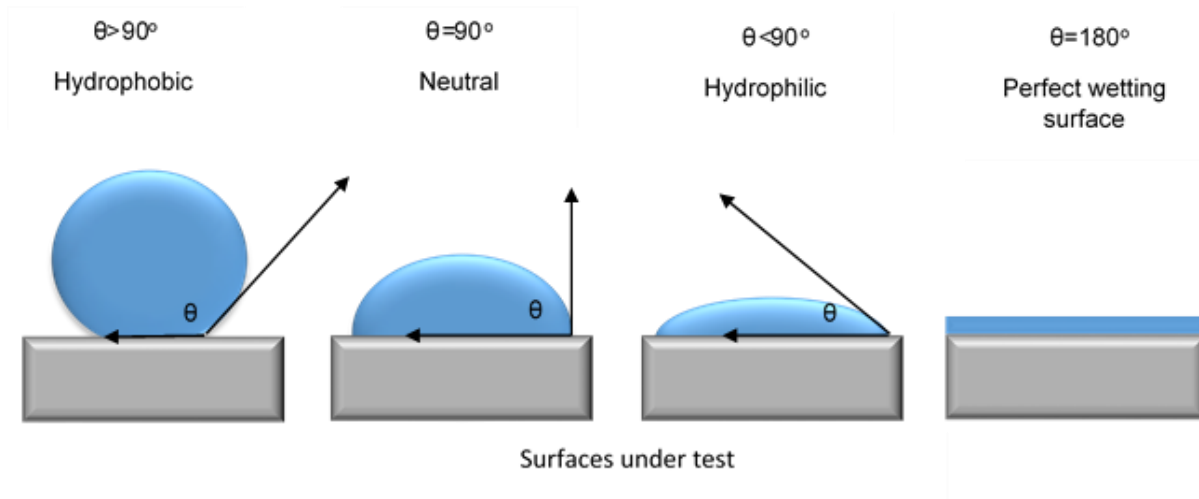


Figure 2.15 Droplets on solid surface with value of contact angle defining hydrophobic, neutral, hydrophilic and perfect wettability

The shape of the liquid surface is governed by gravity and the cohesion and surface tension forces which balance to achieve an equilibrium state. This corresponds to the minimum energy state governed by the three forces. The wettability of the surface may be defined by the contact angle (θ) made between the liquid surface and the solid surface and the resultant minimum energy state. The contact angle is governed by the characteristics of the liquid and the roughness of the solid surface, and, as shown in Figure 2.15, the wettability may be described as hydrophobic ($\theta > 90^\circ$), neutral ($\theta = 90^\circ$), hydrophilic ($\theta < 90^\circ$) and perfect ($\theta = 180^\circ$). Hence, in the application of surface coatings, it is desirable to create as near perfect wettability as possible and hence much research has concentrated on the creation of hydrophilic states. For such conditions, the equilibrium of forces is shown in Figure 2.16.

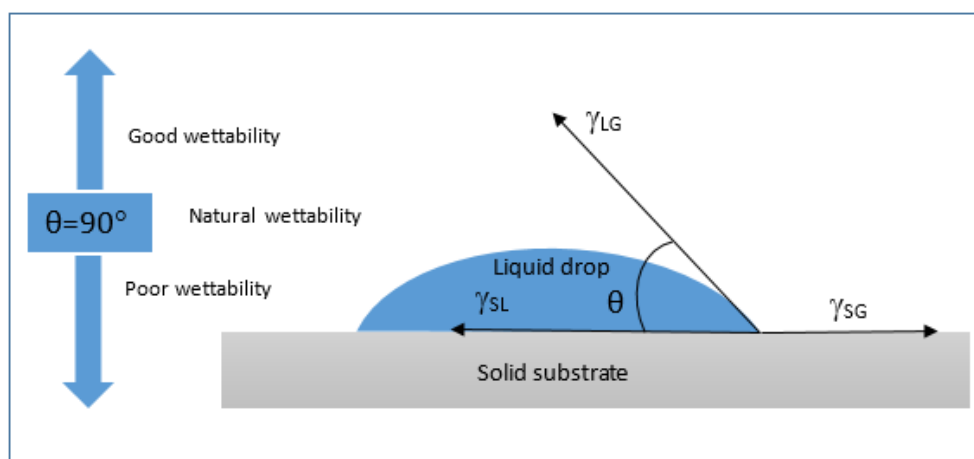


Figure 2.16 Single droplet on a solid substrate showing balanced solid/liquid, solid/gas and liquid/gas forces and values of contact angle classifying wettability

Photoreduction of GO provides the feasibility of manipulating both the chemical composition and surface topography simultaneously and researchers have used different reduction techniques to enhance the wettability of GO surfaces. For example, Bon *et al.*, 2011, used an Hg lamp of power 30 mWcm^{-2} to reduce GO and observed that changes in contact angle from a value circa 50° for GO to 68° and 73° for rGO were obtained as a function of the lamp exposure for one and three hours respectively. Microwave heating was used by Rasuli *et al.*, 2015, to examine changes to the wettability when graphene oxide was reduced by heating. This resulted in the removal of the oxygen containing groups with a corresponding increase in the contact angle from 29.7° (GO) to 69.9° (rGO). Graphene, graphite and graphene oxide surfaces were studied by Wang *et al.*, 2009, to establish the contact angle of each material using water. These showed wettability contact angles of 127° , 98° and 67° respectively thereby confirming that graphene and graphite are hydrophobic ($CA > 90^\circ$) whilst graphene oxide is hydrophilic ($CA \leq 90^\circ$).

Two beam laser interference induced (TBLI) reduction was used by Jiang *et al.*, 2014 who reported on the bioinspired fabrication of superhydrophobic graphene surfaces by TBLI

treatment of spin coated graphene oxide (GO) films on glass. This resulted in an ablation of the surface which together with the removal of abundant hydrophilic oxygen containing groups (OCGs) created superhydrophobic graphene films with two-dimensional features. They used a frequency-tripled, Q-switched, single-mode Nd:YAG laser (wavelength of 355 nm, frequency 10 Hz, and pulse duration of 10 ns) with beam splitter and mirrors to focus on the GO sheets to create a series of 1D periodically distributed grooved furrow structures with anisotropic super-hydrophobicity and, by turning the sample through 90° and repeating the laser irradiation, they created two dimensional grating structures with isotropic hydrophobicity - biomimetic graphene surfaces. Hence, the photoreduction method allowed the formation of hierarchical micro-nanostructures and the modulation of the chemical composition at the same time. The periodicity of the grated structures could be precisely controlled by changes to the angle of the 2 laser beams. The period was tuned from 1 to 4 μm and the resultant contact angle for the differently patterned surfaces varied within the range 120 to 153°. The initial CA was 70° and hence the periodicity had a significant impact on the wettability of the surface. Similarly, Wang *et al.* 2012, using a similar technique modulated the wettability of rGO in the range of ≈70° (pristine GO) to ≈ 157° (superhydrophobic surface). Similar grid patterns were also developed by Florian *et al.*, 2018, to examine the wettability of steel surfaces using an fs laser. They observed that the contact angle of water could be significantly enhanced and that the line-to-line spacing, grid size and the orientation of polarization were important parameters.

Little research has been completed on the change in contact angle of uniformly created large area rGO surfaces. Wei *et al.*, 2014, developed a model to examine the relationship between the wettability and the hydroxyl and epoxy oxygen containing groups and texture patterns in GO. The relationship between wettability and %hydroxyl was examined, and they observed a break point at 11% hydroxyl defined by the interacting range of hydrogen bonds with oxidized groups and water. They were able to model the wettability as a function of the groups and hence this allowed selective reduction to create hydrophilic conditions. The wettability

performance of GO surfaces using molecular dynamics was studied by Xu *et al.*, 2018, who showed that the contact angle of the GO increased from 70° to 82° with defect concentrations that increased from 0% to 10%. With an understanding of the defect properties of the surface they concluded that results provided a new method for controlling the wetting properties of GO.

The surface morphology, optical transmission and wettability of GO films was examined by Furio *et al.*, 2017, who created dropcast layers of GO on PET substrates which were irradiated using 3 techniques: 1) a 300W UV lamp for different durations, 2) a CO₂ laser with wavelength 10.6 μm, power 2W, scan velocity 100 mm s⁻¹, spot diameter 100 μm and laser power density 2.5 x 10⁴ Wcm⁻², with additional tests using wavelengths of 405 nm with power density 44 mWcm⁻² and 980 nm with power density 200 mWcm⁻², and 3) a LightScribe DVD/CD burner with wavelength 780 nm, power 5 mW, spatial resolution of 20 μm and power density 1.6 x 10³ Wcm⁻². The results showed that the laser reduced rGO resulted in a high contact angle of 132° and that the contact angle was a function of the duration of UV exposure, in the range 40° to 70°, and that laser scribing the UV reduced GO resulted in a further increase in the contact angle from 50° to 105°.

This component of the literature review has highlighted that there is scope to extend the research to examine the wettability characteristics of GO films when irradiated using pulsed lasers. This stimulated the study reported in Chapter 5, Section 5.6, which has examined the changes in the contact angle and surface roughness for films irradiated at different fluence values using the relationship between the characteristics of GO irradiated using an fs Nd:YVO₄ laser with wavelength 1064 nm.

2.11 Identified Knowledge Gaps Leading to Thesis Aims and Objectives

The literature review has highlighted by the following key points:

Firstly, the review has highlighted that the laser reduction of GO is a 'hot' research topic with a proliferation of the number of publications over the past 10 years. The advantages of laser reduced GO have been observed in μm patterning, the control of the surface morphology including the fabrication of 2D and 3D surfaces, and in the tuning of the electrical and chemical properties of the rGO.

It has been shown that a large number of lasers have been used by previous researchers. The Nd:YVO₄ laser with wavelength 1064 nm, 10 kHz and 4.8 ns used in this thesis compliments this research.

In general, it has been shown that pulsed nanosecond lasers are more effective than either continuous wave or femtosecond lasers in the production of high quality rGO. Kang *et al.*, 2016, showed that that kHz pulse trains were more effective than MHz pulse trains or a continuous wave laser. Hence the selection of laser type is a key feature of the reduction process.

The review has highlighted that in the laser reduction of GO the reduction process may be photochemical, photothermal or a combination of the two. The transition requires an electron-photon equilibrium of 0.37ps which corresponds to a photon energy greater than 3.2 eV. This translates to a laser wavelength of 390 nm. For wavelengths less than 390 nm the reduction process is mainly photochemical whilst at wavelengths greater than 390 nm the process is photothermal. In many cases the reduction process is a combination of both photochemical and photothermal reduction, for example, where the reduction process has involved two/multi photon absorption and laser induced thermal reduction. For the laser used in this study the reduction process was entirely photothermal.

Temperature changes are triggered by the reduction process and several researchers have attempted to develop temperature models to simulate potential changes in temperature and to relate these to the degree of reduction. Here the important factor is the absorption and resultant heat transfer of the irradiated beam into the GO layer. It has been shown that these processes are very much temperature dependent and, although several attempts have been made to describe the change in temperature within the reduced GO layer, there is scope for much further research.

To quantify the degree of reduction most researchers have used optical microscopy, changes to the conductivity and resistance of the irradiated GO, Raman spectroscopy, X-Ray photoelectron spectroscopy (XPS), Scanning Electron Microscopy, Atomic Force Microscopy and Powder X-Ray Diffraction. These techniques allow interpretations of the data. For example, in respect of Raman spectroscopy the use of the ID/IG and I2D/IG ratios has been prevalent. The review has highlighted a number of different trends with both increases, decreases and erratic changes recorded even when the same variables are tested. The general consensus with the application of ns lasers is that the ratio of ID/IG reduces for an increase in laser power and energy density but increases with an increase in scanning speed, see Bobrinetskiy *et al.*, 2017. Correspondingly the I2D/IG peak has usually been observed to increase for an increase in the degree of reduction although several researchers did not detect a 2D peak. A further measure that has commonly been used is an assessment of the change in crystalline size and distance between defects after Canacado *et al.*, 2006.

In terms of XPS the overall significant trend for almost all researchers is that the reduction in GO is accompanied by a reduction in the oxygen containing groups and an increase in the sp² carbon bonds.

Most researchers have expressed the degree of reduction as a function of fluence (energy density per unit area), but it has been shown that other researchers have related the degree

of reduction to the power of the laser or irradiation (unit energy per square metre per second or Power per metre squared). The different ways in which authors have presented their results make direct comparison difficult. In this study all results are expressed in terms of Fluence.

The overall thickness and the number of the GO layers has been observed as an important parameter and in the case of GO films, layer thickness is a function of the experimental process used to produce the GO and the concentration of the solution that is used to prepare the film. The review has highlighted that individual researchers have used a wide range in layer thickness in what appears to be an arbitrary selection process. As thickness governs parameter like conductivity and temperature change, there is again a difficulty with making comparative assessments.

Several authors have identified that the surface structure following irradiation was observed to be highly porous which could be attributed to the drastic expansion that occurs due to the removal of the oxygen containing groups (OCGs), see Lazauskas *et al.*, 2014, Strong *et al.*, 2012. They concluded that the expanded surface offered considerable potential for the development of sensors. Kymakis *et al.*, 2013, showed that the roughness of the GO surface was increased by irradiation but that the roughness was consistent irrespective of laser dose whilst He *et al.*, 2016, observed that the GO surface contained wrinkles which were smoothed by irradiation using an fs 780 nm laser. The channel depth after laser irradiation was seen to increase, this depth change was attributed to mass loss of OCGs and the emission of carbon species from the GO films.

Several researchers have identified zones of behaviour to explain their results, for example Deng *et al.*, 2016, used the terms 'growth, transition and etch regions' to describe changes in layer thickness corresponding to the increase in power. Similarly Bobrinetskiy *et al.*, 2017 used 3 stages of interpretation whilst Kang *et al.*, 2018, observed two patterns of material

behaviour as the laser power was increased due to the absorbed laser energy creating graphene like layers and due to a thinning of layer as a result of a smaller interlayer distance.

In summary several researchers support the argument for further research. For example, Bobrinetskiy *et al.*, 2017, identified that laser direct writing methods are most attractive as they both provide precise impurity-free control of the concentration ratio of carbon and oxygen atoms. Nevertheless, the direct laser induced 3D manipulation of graphene or GO films has not been implemented yet due to the complexity of the interaction between pulsed laser photons and carbon lattice. In addition, a review by Wang *et al.*, 2018 identified that 'the understanding of the interactions between laser beams and GO is still in its infancy' and hence much further research is ongoing whilst Wan *et al.*, 2018, reported that despite promising recent progress, there is still a huge scope to further tailor the surface and interface properties of GO through controllable photoreduction.

The end-product of much of the previous research has been the application of rGO in a range of devices. However, to find the correct characteristics of the rGO for each application it is usually necessary to complete a wide range of tests in which the governing variables are tested in sequence, for example step increases in fluence, scan rate and pulse duration, such that the most optimum reduction of the GO is obtained for each device. This is often extremely time consuming and expensive. For example, Evlashin *et al.*, 2018, completed over 8000 tests with changes to the pulse duration, pulse frequency and fluence.

To illustrate this key issue reference is made to Figures 2.17, and 2.18. These Figures, discussed more fully in Chapter 5, illustrate the published outputs of the research by Arul *et al.*, 2016, Figure 2.17 and Evlashin *et al.*, 2018, Figure 2.18, and serve to illustrate that to create such plots requires an extremely large number of tests.

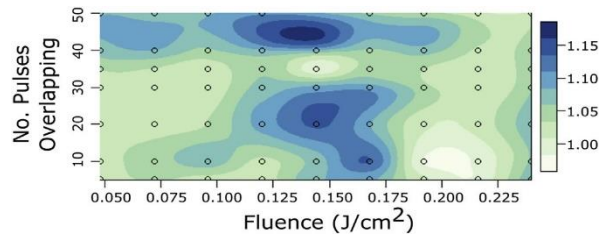


Figure 2.17 Plot of Raman ID/IG values as a function of the number of overlapping pulses and Fluence, after Arul *et al.*, 2016, © Elsevier

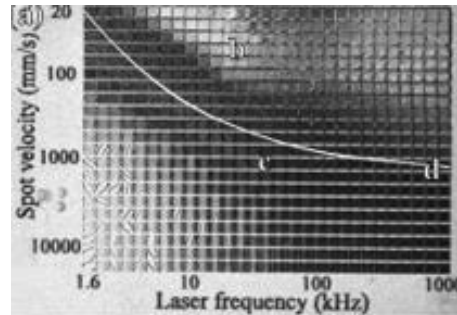


Figure 2.18 Grey scale degree of reduction of irradiated sample squares as a function of spot velocity and laser frequency, after Evalshin *et al.*, 2018, © WILEY

They each describe the relationship between 3 variables and hence the systematic and incremental changes in each parameter require a significant test programme. Such tests are time consuming and expensive. The concept of this thesis was to develop a methodology that would allow an examination of the reduction degree, from no damage to full ablation of the GO surface, using only one experiment. This was achieved by creating a z-scan pattern of irradiated GO film by moving the sample in both the x and z directions across the laser beam. The theory supporting the z-scan approach is presented in Chapter 3 and the results of the subsequent experimental programme of research are presented in Chapter 5.

In addition, it has been identified that there is a need for further research to better understand the influence of temperature on the reduction process. Hence an attempt has been made to study changes in temperature associated with the experimental results by the

development of a mathematical model. Similarly, a small number of researchers have attempted to relate the wettability of rGO samples to the degree of reduction and this study provides a further opportunity to evaluate the characteristics of the large area irradiated surfaces in terms of the relationship between wettability, roughness and the surface chemistry of the surface.

Theoretical considerations of the z-scan and temperature modelling are presented in the next Chapter.

Chapter 3: Theory

3.1 Z-Scan Theory

As stated in the introduction, the concept of the thesis was to develop a methodology that would allow an examination of the reduction degree, from no damage to full ablation of the GO surface, using only one experiment. To develop such a methodology the author had the idea to move a GO sample on a glass substrate, in both the horizontal and vertical planes, across a fixed laser beam. As the sample moves in the horizontal and vertical directions, the vertical distance between the laser beam and the sample will change and this results in a change in the spot size, and hence fluence. A schematic of the resultant change in spot size and the overlay of spots as the sample is moved is shown in Figure 3.1.

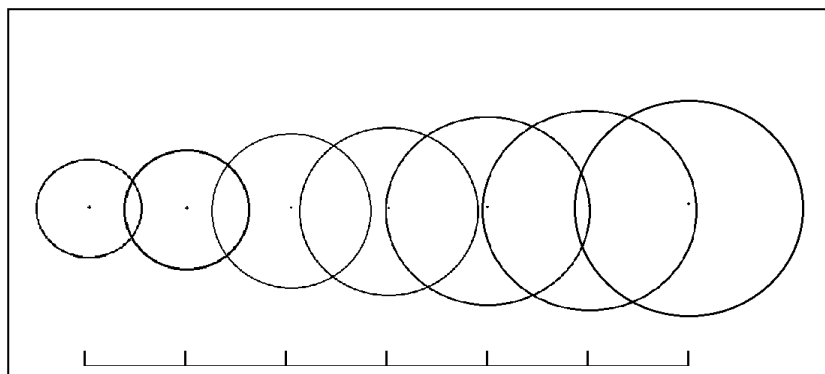


Figure 3.1 Schematic representation of zone of influence of overlapping spots as a sample is moved through a laser beam in the x and z directions

In such a case the fluence will reduce as the spot size is increased as the energy of the laser beam remains the same. The number of overlapping pulses, or scanning speed, will also influence the fluence distribution. The resultant pattern of damage has been termed a z-scan and the theory behind the Z-Scan was first proposed by Samad and Vieira (2006) who presented a method to calculate the surface damage threshold caused by the movement of a sample through a femtosecond laser beam with Gaussian distribution. In a similar way to

describe the extent of the ablation of a GO layer spin coated onto a glass substrate it is necessary to understand the characteristics of the laser beam and the relationship between these characteristics and subsequent damage. The characteristics of a Gaussian laser beam were outlined in Section 1.4 of the thesis and have been well reported, see Arnaud, 1976. The intensity of the laser beam $I(r, z)$ is given by the expression:

$$I(r, z) = \frac{2P_0}{\pi w(z)^2} e^{-\frac{2r^2}{w(z)^2}} \quad \text{eqn 3.1}$$

Where r is the radial component of the beam, z is the longitudinal component, P_0 is the laser power and $w(z)$ is the beam radius where $I = 1/e^2$. The peak intensity will occur when $r=0$ and is given by $I_p = 2I$

The beam radius at longitudinal distance z from $z=0$ is given by

$$w(z) = w_0 \left[1 + \left(\frac{\lambda M^2 z}{\pi w_0^2} \right)^2 \right]^{\frac{1}{2}} = w_0 \left[1 + \left(\frac{z}{z_0} \right)^2 \right]^{\frac{1}{2}} \quad \text{eqn 3.2}$$

where λ is the laser wavelength, M^2 is the beam quality factor and z_0 is the beam confocal parameter $\pi w_0^2 / \lambda M^2$.

Hence, for each longitudinal position z the intensity distribution is shown to be different with reducing peak intensity the further from the waist. For ablation to occur, the intensity has to be greater than a threshold intensity I_t . If distance $z = C$ defines the position at which the peak intensity becomes less than the threshold intensity for ablation, then position C defines the limit of the damage and for positions $0 \leq z \leq C$ there will be some damage. If $\rho(r)$ is defined as the radius at which the intensity equals that of the threshold intensity, $\rho(r)$ is termed the damage radius, and for values of $r \leq \rho(r)$ the surface will be damaged but for values of $r > \rho(r)$ there will be no damage.

Using the above equations, the threshold intensity may be expressed as;

$$I_1 = \frac{2P_0}{\pi\omega(z)^2} e^{-\frac{2r(z)^2}{\omega(z)^2}} \quad \text{eqn 3.3}$$

Which gives

$$r(z) = \sqrt{\frac{\omega(z)^2}{2} \ln \left[\frac{2 P_0}{\pi\omega(z)^2 I_1} \right]} \quad \text{eqn 3.4}$$

A plot of eqn. 4.4 yields a typical resultant z-scan pattern and is shown in Figure 3.2. Position A is at $\omega(0)$, the minimum spot size of the laser. Position B displays the maximum ablation diameter $\rho(z)$. Position C is the point where the peak intensity is less than the damage threshold and $\omega(z)$ shows where the beam intensity drops to e^{-2} of the peak value, which is considered the limit of reduction.

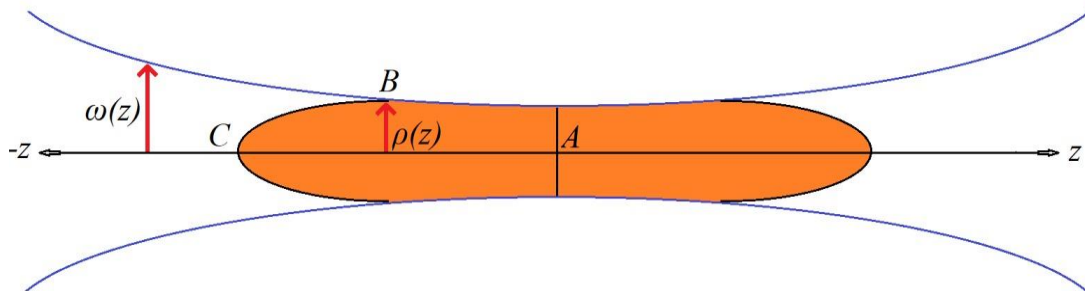


Figure 3.2 Typical z-scan pattern created when a sample is translated through a Gaussian laser beam in the x and z directions simultaneously.

Here, for ease of reference, the orange shaded pattern has been termed a z-scan which highlights the area over which some change will occur. The boundary of the z-scan therefore defines the extent of damage.

The maximum radius where damage occurs (ρ_{max}) may be established from equation

$$\rho_{\max} = \sqrt{\frac{1}{e\pi} \frac{P_0}{I_t}} \approx 0.342 \sqrt{\frac{P_0}{I_t}} \quad \text{eqn 3.5}$$

Where ρ_{\max} is the maximum damage radius, P_0 is the pulse power and I_t is the threshold intensity.

Rearranging gives;

$$I_t = \frac{P_0}{e\pi\rho_{\max}^2} \approx 0.117 \frac{P_0}{\rho_{\max}^2} \quad \text{eqn 3.6}$$

Equations 3.5 and 3.6 highlight that the maximum damage radius is a function of only two parameters: the laser power and the threshold intensity. Hence, if the maximum damage radius may be measured experimentally, the value of the threshold intensity may be established and subsequently used to control the area and pattern of ablation. Such an approach has the potential to improve the production of large area rGO and a programme of experimental measurement was made to find the laser threshold intensity and the resultant characteristics of the z-scan.

The novelty of using a z-scan in this way is that, with the use of Raman Spectroscopy, the distribution of laser fluence, defined as the laser energy per unit area, can easily be calculated at each location on the z-scan, thereby providing a means to select the optimum fluence to provide the required degree of reduction of GO to rGO for a particular application. The fluence at any location is given by equation 3.7.

$$F(r, z) = \frac{2E_0}{\pi w(z)^2} e^{-\frac{2r^2}{w(z)^2}} \quad \text{eqn 3.7}$$

Where $F(r, z)$ is the fluence at radial and longitudinal distance from the beam waist, E_0 is the laser energy and $w(z)$ is the beam radius. The equation also provides the means to establish the change in fluence as the focused Gaussian beam is moved in the x and z directions. Using

the above equations, a theoretical distribution of the fluence has been predicted and this is shown in Figure 3.3

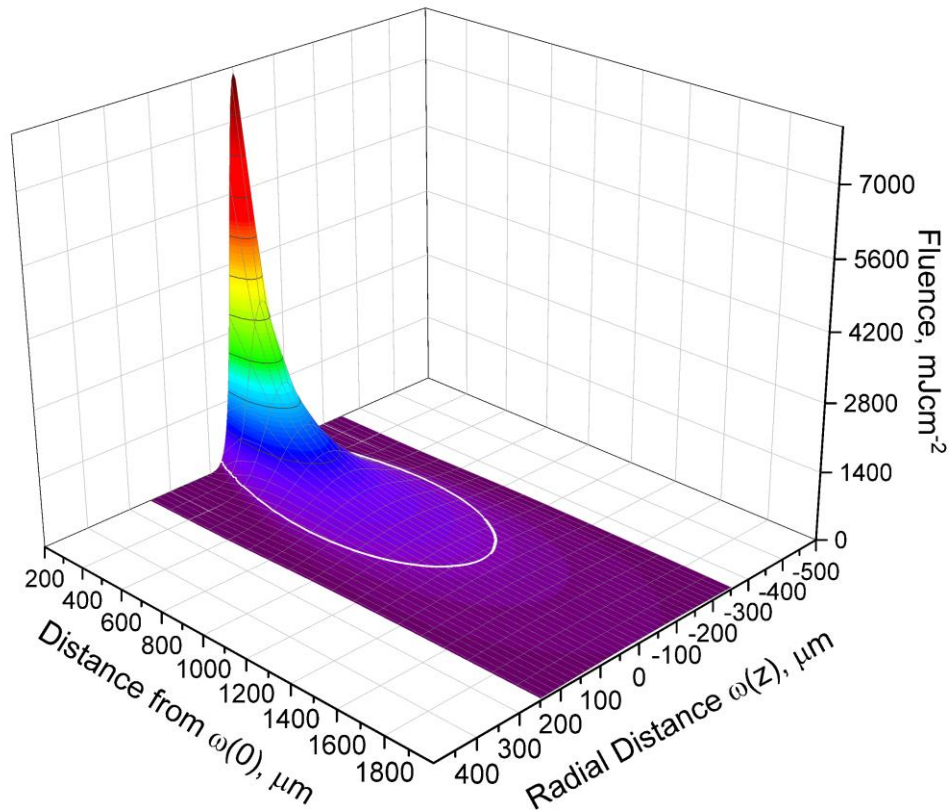


Figure 3.3 3D representation of the predicted fluence produced during a typical z-scan

These predicted distributions clearly show that extremely large values of Fluence occur at the centre of the beam but that the area over which they act is small. Hence it is usual to express values of fluence in terms of average fluence and such average theoretical values have been compared to the results of the z-scan experimental measurements presented in Chapter 5 of the thesis.

3.2 Temperature Modelling

As highlighted in the literature review, the photothermal reduction of GO films using a laser with nanosecond pulse duration is in part a function of the temperature rise created within the material. Due to the laser being pulsed, residual heat can remain in the sample between pulses and it is important to investigate the temperature of the sample as a result of multiple pulses as this will determine the highest temperature the sample will be exposed to.

The determining factors for temperature rise in GO from laser irradiation are the absorbed energy of the sample and this energy's distribution over its volume. The amount of laser energy absorbed is governed by the optical properties of GO; absorptivity and absorption coefficient which change dramatically if a phase transition occurs like that of GO being reduced. In order to estimate the temperature rise in the GO sample using a simple model the absorptivity and absorption coefficient will remain constant during the pulse and therefore phase changes are not accounted for.

A sample will reach its maximum temperature given the energy introduced due to a single pulse at the end of the pulse duration. After this the cooling of the surface begins which is governed by its thermal conductivity. It can be assumed in the following model that all absorbed energy results in heating and cooling begins after the pulse duration when the sample is at its maximum temperature.

Yakovlev, Shandybina and Shamova, 2019 produced a temperature model which was used to investigate the heating and cooling of a biological sample under pulsed laser conditions. It was assumed that the temperature distribution of the laser affected zone repeats the distribution of absorbed laser energy during the cooling of the sample when the pulse duration has ended. This causes a Gaussian temperature distribution over the laser spot which decreases exponentially through the surface in the direction of beam propagation, as given by equation 3.8.

$$T(r, d) = T_{max} e\left(-\frac{r^2}{\omega_z^2}\right) e(-\alpha d) \quad \text{eqn 3.8}$$

Where T_{max} is equal to the maximum temperature the sample experiences before cooling begins, α is the effective absorption coefficient of the sample, ω_z is the radius of the laser beam spot, r the radial distance from the beam centre and d the penetration depth into the sample. The maximum temperature can be found from equation 3.9.

$$T_{max} = \frac{\alpha AF}{c} \quad \text{eqn 3.9}$$

Here A is the absorptivity, C the heat capacity and F the laser fluence.

To consider the temperature at the surface of the sample where d is equal to zero eqn 3.8 can be simplified to become:

$$T(r) = T_{max} e\left(-\frac{r^2}{\omega_z^2}\right) \quad \text{eqn 3.10}$$

This then represents the temperature distribution on the surface of the sample before cooling begins. To establish the cooling of the sample the thermal conductivity equation given in equation 3.11 must be solved. Here κ is equal to the thermal diffusivity of the sample.

$$\frac{\partial T}{\partial t} = \kappa \frac{\partial^2 T}{\partial r^2} + \frac{1}{r} \frac{\partial T}{\partial r} \quad \text{eqn 3.11}$$

The radial temperature distribution is then given by

$$T(r, t) = \frac{T_{max} \omega_z^2}{(\omega_z^2 + 4\kappa \tau_p)} \exp - \left(\frac{r^2}{(\omega_z^2 + 4\kappa \tau_p)} \right) \quad \text{eqn 3.12}$$

Where τ_p is the time period of the laser and is equal to the reciprocal of the frequency. The temperature after multiple pulses can be given by equation 3.13.

$$T(N_p, r, z) = T_0 + \left[\frac{T_{max}\omega_z^2}{(\omega_z^2 + 4\kappa\tau_p)} \exp - \left(\frac{r^2}{(\omega_z^2 + 4\kappa\tau_p)} \right) \right] + \sum_{i=0}^{N_p} \left[\frac{T_{add}(r, z, \tau_p)\omega_z^2}{(\omega_z^2 + 4\kappa\tau_{pi})} \exp - \left(\frac{r^2}{(\omega_z^2 + 4\kappa\tau_{pi})} \right) \right]$$

eqn 3.13

Where N_p is the number of overlapping pulses, here the second term in this equation shows the temperature added from additional pulses where T_{add} gives the temperature after cooling before the next laser pulse and can be found in equation 3.14 after Bechtel, 1975.

$$T_{add}(r, z, t) = \frac{I(1-R)}{\sqrt{\pi K_t \rho c_p}} \exp \left[- \left(\frac{r}{\omega_z} \right)^2 \right] \int_0^t \left[\exp \left[\frac{- \left(\frac{t_s}{\tau} \right)^2 - \frac{z^2}{4\kappa(t-t_s)}}{\sqrt{(t-t_s)}} \right] \right] d t_s$$

eqn 3.14

Here I refers to the irradiance, R the reflectivity, K_t the thermal conductivity, ρ the density and c_p the specific heat capacity of the sample.

In this study the laser used had a pulse duration of 4.6 ns and a 10 kHz pulse repetition frequency i.e. the time period between pulses τ_p is 10^{-4} secs. Inserting such values into equation 3.14 shows that the cooling time is sufficiently long to return the GO surface back to ambient conditions as the duty cycle of the laser is only 0.0046 %. This therefore means that the second term in equation 3.13 tends to zero as the temperature of the sample after time τ_p has cooled to ambient conditions. The cooling of the sample after a laser pulse is displayed in Figure 3.5.

A Mathcad model was written to solve equation 3.14 and the following parameter values were inserted into the model:

Table 3.1 Parameter values for application into the temperature model.

Parameter	Notation	Value	Unit
Irradiance	I	1.904×10^{11}	Wm^{-2}
Reflectivity	R	0.33	-
Thermal Conductivity	K_t	1.6	$\text{Wm}^{-1}\text{K}^{-1}$
Density	ρ	1800	Kgm^{-3}
Heat Capacity	c_p	710	$\text{JKg}^{-1}\text{K}^{-1}$
Pulse Duration	τ	4.6	ns
Thermal Diffusivity	κ	1.252×10^{-6}	m^2s^{-1}

The results output from this model, together with a discussion of the research of others is presented in Section 5.7 of the thesis.

Chapter 4: Experimental Systems and Methods

4.1 Experimental System and Analysis

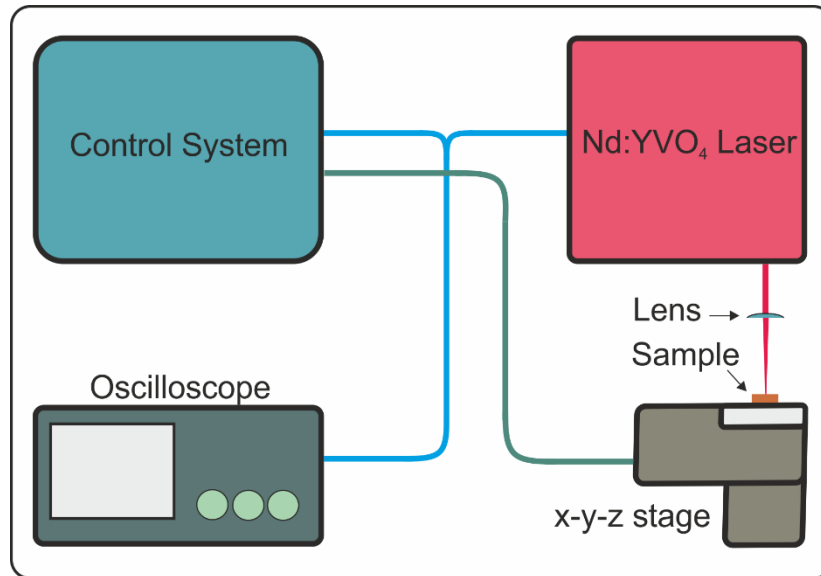


Figure 4.1 – Experimental system

As can be seen in Figure 4.1 the experimental system is comprised of four components; the control system drives the Nd:YVO₄ laser, which irradiates the sample held on an x, y, z stage after the light is focused by a lens. The oscilloscope is used to monitor the pulse train.

4.1.1 Lens

The lens used was a Thorlabs Mounted Geltech Aspheric Lens that was specified to have a 15.3 mm focal length. The lens was anti-reflection coated for 600-1050 nm.

4.1.2 Details of Laser

The laser used in the study was an Advanced Optical Technology Nd:YVO₄ Q-switched, diode pumped solid state laser with wavelength 1064 nm shown in Figure 4.2. The laser was used with an average power of 170 mW at 10 kHz pulse repetition frequency, a peak power of 3695 W, a pulse length of 4.6 ns, a pulse energy of 17 μ J and a minimum focal spot radius of 3.3 μ m when used with the Geltech aspheric lens. A Molectron PM150-190 power meter was used to measure the laser power while the energy per pulse was measured using a Molectron J9LP pulse energy meter. The temporal pulse shape was measured with an FND 100 infrared sensor photodiode and the wavelengths produced were measured with an AvaSpec ULS3648-USB2 spectrometer.



Figure 4.2 - Advanced Optical Technology Nd:YVO₄ laser and control unit (Photonics Media, 1999)

4.1.3 Optical Microscopy

Optical Microscopy (OM) was undertaken using a Leica DMCM microscope.

4.1.4 Stages

The main experimental programme used an ANT95XY series two-axis XY direct-drive nano positioning stage from Aerotech was used for control in the x and y dimensions with 25mm travel in each. This was used in conjunction with an ANT130V-5 single-axis lift direct-drive

nano positioning stage with 5 mm travel in the z dimension. The stages were controlled via G-code, the code for which can be found in Appendix I.

The preliminary tests were completed using three T-LS28M stages from Zaber Technologies oriented in x, y and z dimensions and were controlled with Labview.

4.1.5 Glass Substrates

The substrates were squares of length 25 mm and had a plan area of 625 mm². These were then sonicated for 10 minutes each with deionised water followed by isopropanol and then followed by acetone. Further ozone cleaning was completed for a period of 10 minutes.

4.1.6 Preparation of Graphene Oxide Films

An aqueous solution of GO was drop cast onto the glass substrates detailed above. After the GO had been deposited, the films were left to dry for 24 hours at room temperature followed by annealing at 70°C for 24 hours. This resulted in GO thickness between 4000-5000nm measured with the Dektak XT surface profiler. A total of 20 GO films were used in the study.

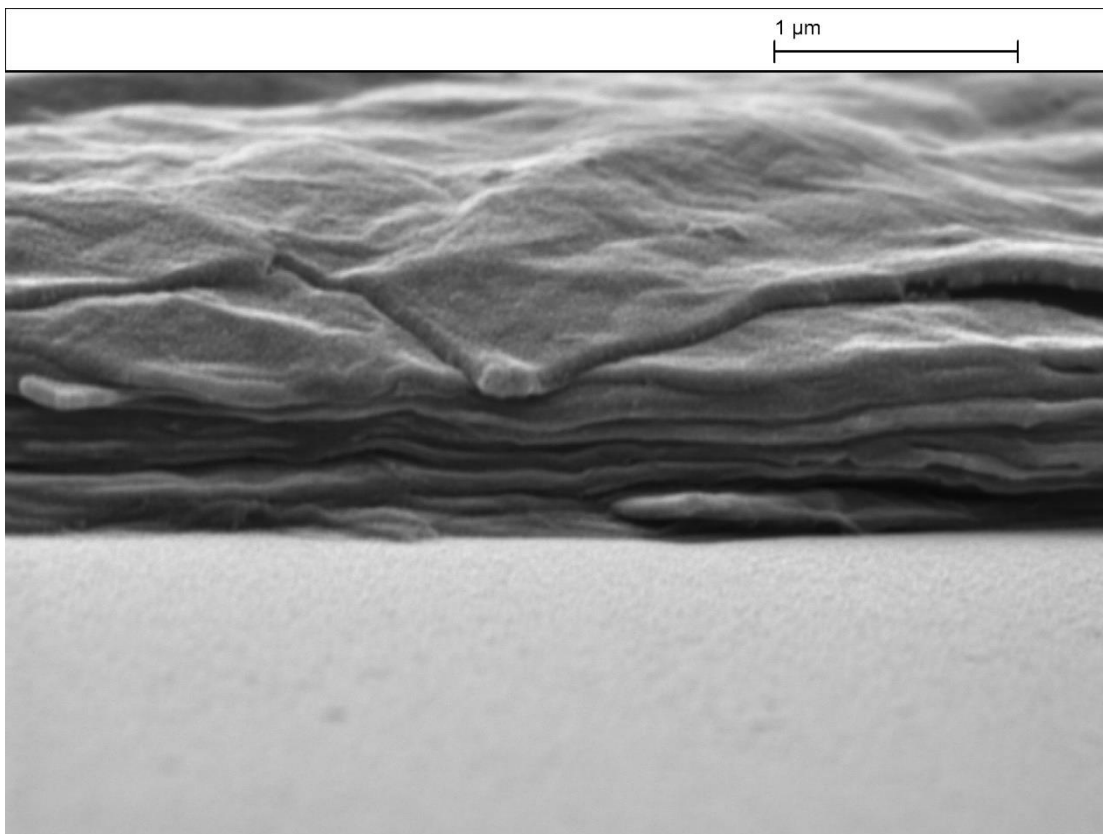


Figure 4.3 – Lamellae structure of GO after being drop cast from aqueous solution onto glass substrate as viewed from the side

A typical surface of the GO layers as recorded using the SEM is shown in Figure 4.3 which shows the layers of GO flakes with high aspect ratios stacked in lamellar structures on the glass substrate as viewed from the side.

4.1.7 Surface Profiler

Surface profiling was done using a BRUKER Dektak XT surface profiler, see Figure 4.4, which was used for step height measurements of GO films. The surface profiler takes measurements as a surface is moved relative to a contact stylus. The stylus used had a 12.5 μm tip radius and 3 mg of stylus force was used.

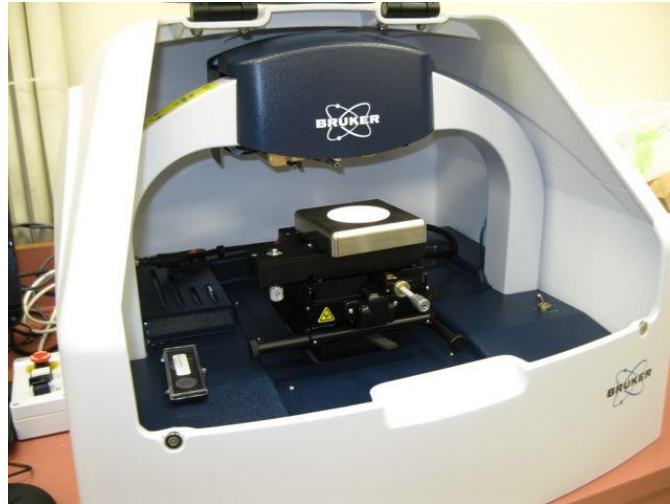


Figure 4.4 BRUKER Dektak XT surface profiler (Bruker, 2014)

4.1.8 Scanning Electron Microscope

Samples were characterised using a Zeiss EVO 60 scanning electron microscope (SEM). Surfaces are scanned with a focused electron beam in a raster scan pattern, the electrons interact with atoms in a sample and provide high resolution topographical information.

4.1.9 Raman Spectroscopy

A Thermo Fisher Scientific DXR II Raman spectrometer was used to gain information about the chemical composition of rGO samples, shown in Figure 4.5. The technique relies on the inelastic scattering of light from a monochromatic laser source which interacts with molecular vibrations and phonons of a sample. In this case a 532 nm wavelength was used with 1mW laser power and an estimated resolution of 5.5-8.3 cm^{-1} and 2.1 μm spot size.



Figure 4.5 - Thermo Fisher Scientific DXR II Raman spectrometer (ThermoFisher, 2019)

Preliminary work was completed using a Horiba XploRA Plus with a 532 nm laser, 1800 g^{-1} mm grating and 500 μW laser power.

Details of Raman spectroscopy are fully explained in section 2.5.3.

4.1.10 X-ray Photoelectron Spectroscopy

X-ray photoelectron spectroscopy (XPS) is a quantitative spectroscopic technique that measures the composition of the elements within the surface layers (0 – 10nm) of a material. X-ray beams are fired at the material with a subsequent release of electrons, the kinetic energy and number of electrons of which are measured.

XPS analysis was performed using a Thermo NEXSA XPS fitted with a monochromated Al ka (1486.7 eV) source and a dual neutralisation charge neutraliser. Analysis was performed at pressures below 10^8 Torr and data was analysed using CasaXPS version 2.3.19 software.

Details of XPS are fully explained in section 2.5.4.

4.1.11 Wettability

The wettability of a substance can be calculated based on intermolecular interactions with a liquid of known surface energy. A sessile drop method was used to measure the static contact angle of DI water. A CAG 100 contact angle Goniometer was used in this study and shown in Figure 4.6. Fuller details are presented in section 2.5.7.



Figure 4.6 CAG 100 contact angle goniometer

Chapter 5: Results and Analysis

Chapter 5 has been split into 3 sections: 1) System Characterisation 2) Z-Scan Studies and 3) Large Area Studies.

5.1 Initial System Characterisation

The equipment identified in Chapter 4 was used to establish the experimental system (Figure 4.1). This section details the calibration of the laser and stages followed by measurement of the surface characteristics of the GO layers.

5.1.1 *Uncertainty Calculation*

The uncertainty of the analysis instruments has been identified and plotted in the form of error bars onto each figure. Where multiple sets of data have been recorded manually the standard error for each repeat measurement has been calculated. In measurements where the standard error is calculated, and the uncertainty of the instrument error is known, the two values have been summed to produce the error bar. These are highlighted on each individual figure.

5.1.2 *Laser Characteristics*

Initial Testing on the Nd:YVO₄ laser had been completed but unfortunately due to unforeseen circumstances the laser pump diode burnt out and there was a period of 17 months prior to the acquirement and calibration of a new diode. The new pump diode had a critical current limit of 2.65 A and characterisation of the new diode is shown in Figure 5.1. The wavelength of the diode was dependent on temperature in an almost linear manner and, in the experimental programme, it was crucial that the diode output corresponded to an 808 nm

wavelength as this is the peak of the absorption cross section of the Nd:YVO₄ laser medium. From Figure 5.1 a temperature of 30°C was chosen on this basis.

The output power of the laser diode was studied as a function of input current for three different pulse repetition frequencies of 5, 10 and 20 kHz. Figure 5.2 shows that at a Peltier temperature of 30°C the relationship between the input current and output power for each repetition frequency was linear. As the fluence in this study was varied as a function of spot size the highest power available gives the largest range of fluence. During the calibration it was observed that some instability occurred at the 20kHz repetition rate and hence it was decided that a 10 kHz pulse repetition frequency would be used in the study.

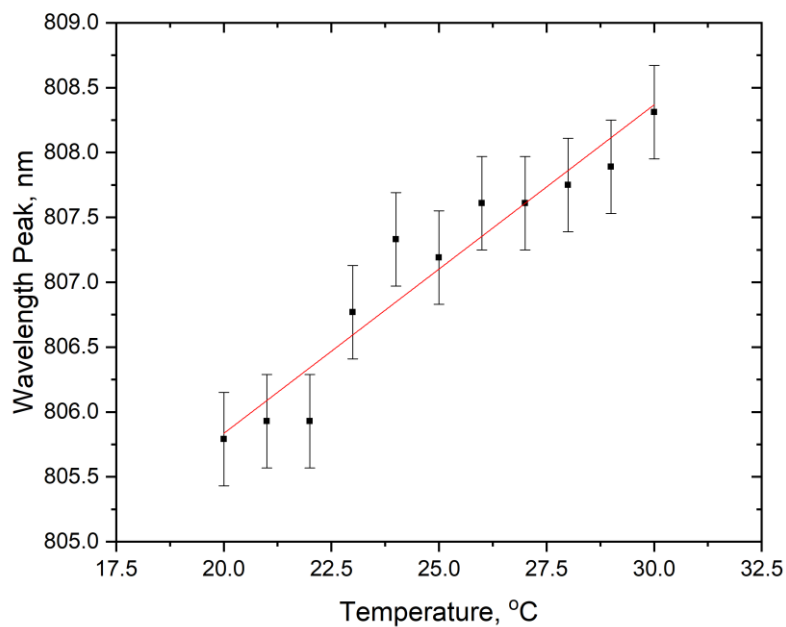


Figure 5.1 - Relationship between Diode Wavelength and Temperature.

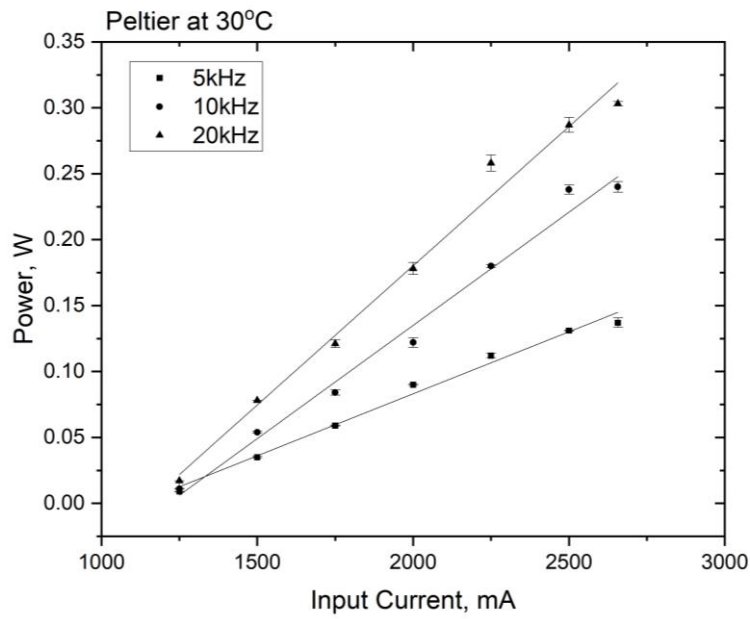


Figure 5.2 – Diode output power as a function of input current at 5, 10 and 20 kHz pulse repetition frequencies.

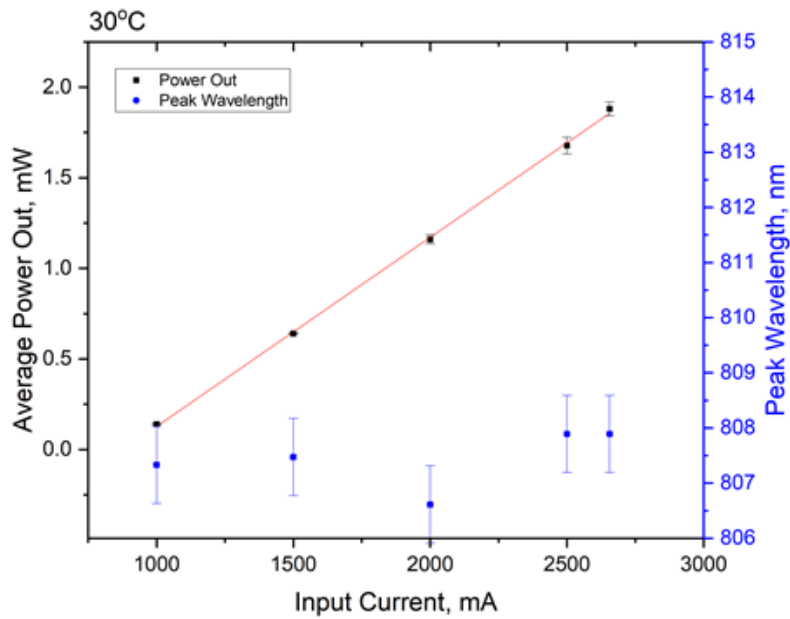


Figure 5.3 – Relationship between the average diode output power and wavelength as a function of input current

At a Peltier temperature of 30°C the relationship between average output power and current was almost linear and that the wavelength of the diode was almost constant with changes in the input current, see Figure 5.3. To confirm that the diode operated at the design wavelength of 808nm, the spectral response of the diode was recorded using an Avantes Starline AvaSpec-EVO spectrometer, the outputs from which are shown in Figure 5.4. This highlights that the operational wavelength of the diode was 808nm.

Following calibration, the pump diode was incorporated into the laser and again, using the AvaSpec spectrometer, the wavelength of the output from the laser was measured. This was to ensure that the characteristics of the laser produced the desired wavelength. The results are shown in Figure 5.5 which highlights that the output wavelength was indeed 1064 nm. In Figure 5.6 the measured relationship between spot size (ablation diameter) and the distance of the lens above the sample is shown. The results were recorded using software that defined the distance as a function of pixel size. The size of each pixel was 3 μm at the magnification used and hence due to this small size, no error bars have been included in Figure 5.6. Examination of Figure 5.6 confirms that the focal length of the focussing lens of the laser was 15.3 mm, as per the manufacturer's specification. This is important to the z-scan study, reported in Section 5.3, as the height of the laser is changed in the z-direction and this correspondingly results in a change in the fluence.

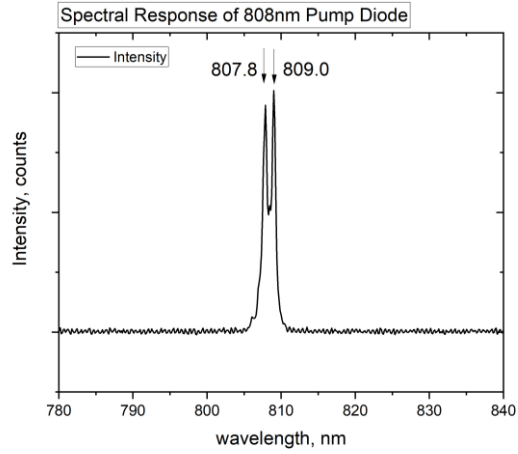


Figure 5.4 - Spectral response of pump diode.

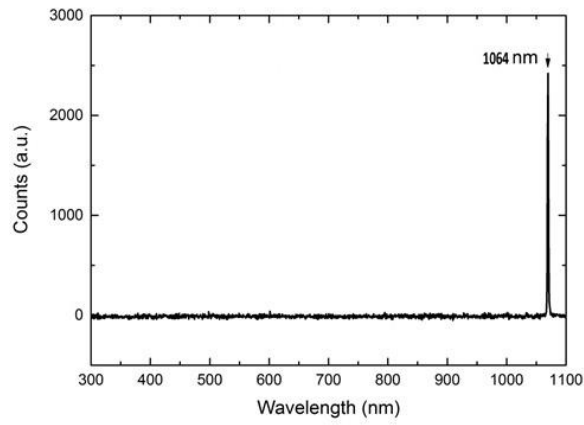


Figure 5.5 - Wavelength Output of Nd:YVO₄ laser

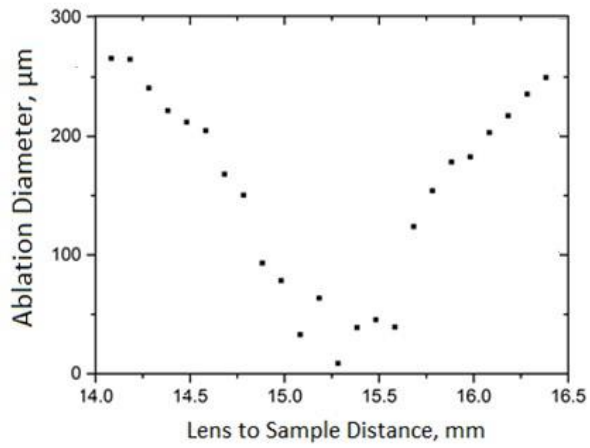


Figure 5.6 - Ablation diameter as a function of the vertical distance from the objective lens

5.1.3 Characteristics of the GO Layer

As stated in Section 4.1.6, the samples were created by drop casting a GO aqueous solution onto glass substrates in ambient conditions and left to dry. In order to ensure the samples had a minimum water content they were annealed at 70° C for 25 hours prior to their use. Prior to irradiation of the GO layers the characteristic thickness of five different samples, termed Set 1-5, were recorded using the Dektak surface profiler (see Section 4.1.7). To do this the graphene oxide was etched across the full width of the substrate in a track using ceramic tweezers. The resulting trench depth was then measured and the results of these five profiles are shown in Figures 5.7 and 5.8.

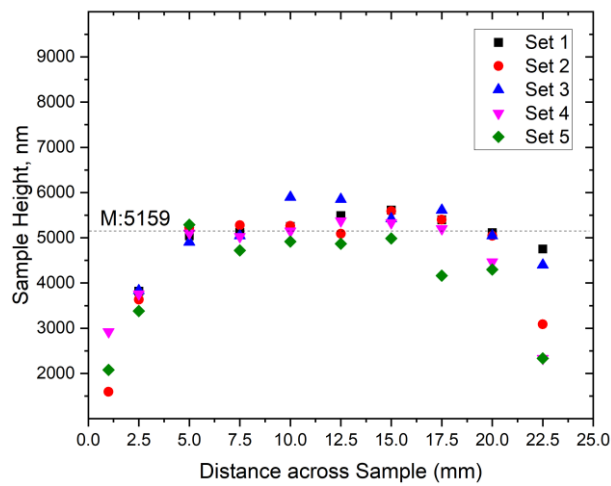


Figure 5.7 – Surface profiles of GO thickness across the sample at ambient temperature. M denotes mean value

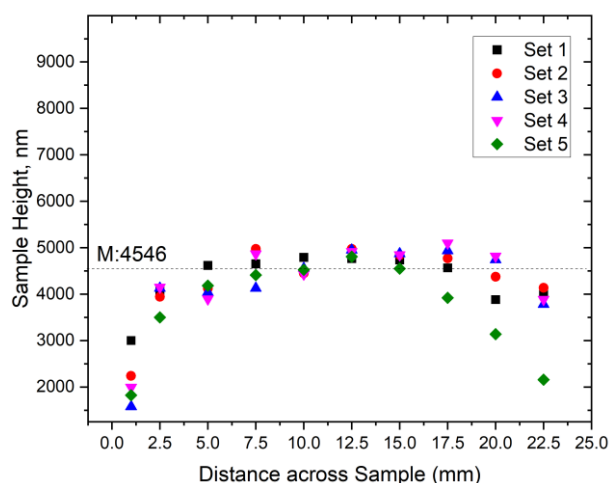


Figure 5.8 - Surface profiles of GO thickness across the sample after annealing. M denotes mean value.

It can be seen from Figures 5.7 and 5.8 that the thickness of the GO reduces at the edges which is due to a meniscus forming when the GO solution is drop cast onto the substrate. In order to avoid the meniscus effect the thickness of the sample was measured over the central 15 mm and this resulted in an average thickness for the ambient samples of 5159 μm which was subsequently reduced to 4546 μm following annealing. Hence, the average thickness of the GO layers was significantly reduced by annealing and this was attributed due to a reduction in the inter-layer spacing between layers due to the loss of water and gas from the sample on heating.

The literature has highlighted that the reduction of rGO is temperature dependant and studies have shown that GO reduction occurs at a temperature in the region of 200 – 230 $^{\circ}\text{C}$, see Sokolov et al., 2010. To find out the temperature at which the GO used in the study was likely to reduce, films of GO were placed between two metal plates with controlled temperature changes imparted into the layer. The relationship between layer thickness and temperature is shown in Figure 5.9 and it can clearly be seen that at a temperature of 210 $^{\circ}\text{C}$ there was a dramatic shift in the thickness of the GO layer, suggesting the onset of reduction

and the potential loss of water vapour and oxygen containing groups. Thus, the GO used in this study had similar characteristics to those previously reported.

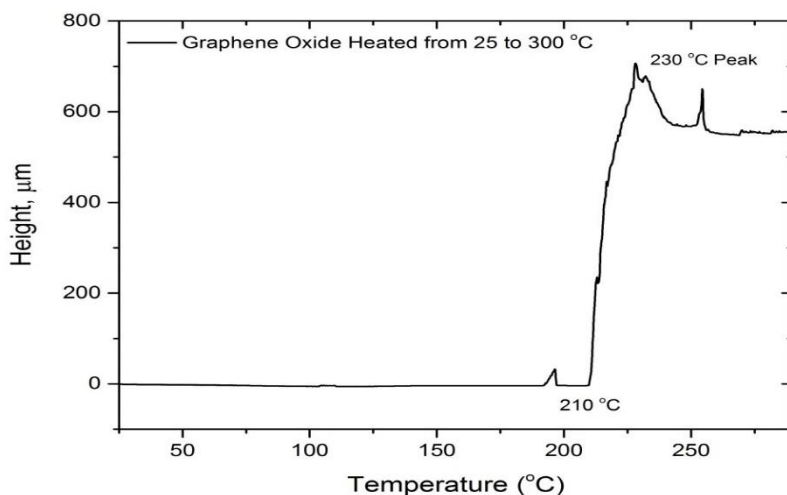


Figure 5.9. Relationship between thickness of the GO layer and temperature.

5.2 Reduction of GO

The relationship between fluence and the reduction of graphene oxide is extremely sensitive. Too low a fluence will not result in any reduction whereas too high a fluence will result in the complete ablation of the graphene oxide layer. The concept of the thesis was to develop an experimental methodology to describe a wide range in the degree of reduction of a GO sample using a procedure that involved the movement of the sample simultaneously in the horizontal and vertical directions. As a consequence, a series of visual tests were completed to examine the relationship between the fluence and the reduction of GO by changing the position of the laser in the vertical direction (spots) and translating the sample to move at different scanning speeds in the horizontal direction. The results of these tests are shown in Figures 5.10 to 5.12.

5.2.1 Creation of rGO Spots

Figure 5.10 shows a series of 6 tests, completed at 10 kHz pulse repetition frequency, 3800 mA diode current and 1000 pulses. Laser irradiated spots were created by firing the laser at the sample with the distance between the laser and the sample changed to create a range of fluences. Here the fluence was changed from 46 mJcm^{-2} to 85 mJcm^{-2} which corresponded to lens positions in the range 20150 to 20500 μm from its home position. The effective focal spot size was determined at I_0/e (Intensity/Euler No), where I_0 is the maximum intensity of the Gaussian beam. The spot size ranged from 163 to 131 μm . The fluence and spot size are referenced in Figure 5.10.

In Section 2.5 it was shown that the degree of reduction may be highlighted by a change in the surface characteristics with a transition from the brownish colour of GO with a gradual darkening through to black as the GO is irradiated, see Li et al., 2014. In Figure 5.10, the top left-hand spot highlights the largest effective spot size corresponding to the lowest fluence of 46 mJcm^{-2} . The dark region around the edges of the irradiated spot indicates partial reduction. The full black spot at 51 mJcm^{-2} indicates complete reduction. The images with a range of fluence from 57 mJcm^{-2} to 85 mJcm^{-2} show that the graphene oxide has been ablated through to the soda-lime glass substrate identified by the small grey dot in the centre of the spot. These results indicate that future tests should be completed at a fluence less than 51 mJcm^{-2} and that there is a relationship between the fluence of an Nd:YVO₄ 1064 nm wavelength laser and the degree of reduction.

Fluence mJcm^{-2}	46	51	57	65	75	85
Spot diameter μm	185	179	163	157	150	131



Figure 5.10. Irradiated spots on Graphene Oxide after 1000 Pulses at Different Fluences. 200x Magnification

5.2.2 rGO Tracks at Different Fluence

Tracks of rGO were created by moving individual samples at a constant speed across the focal spot of the lens. The vertical position of the lens was changed to obtain fluences in the range 9.89 mJcm^{-2} to 57.5 mJcm^{-2} . The samples were moved at a constant speed of 3 mms^{-1} to create the tracks and the results are presented Figure 5.11.

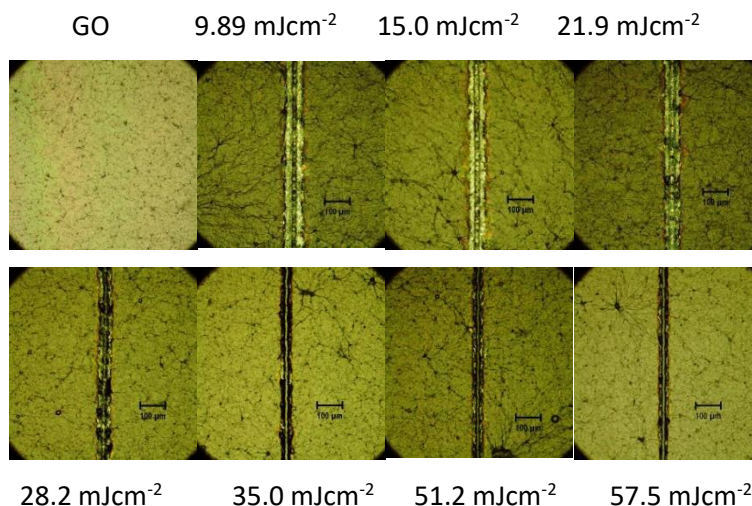


Figure 5.11. Tracks with Different Fluence at Constant Scanning Speed 3.0 mms^{-1} . 200x Magnification with the scale line representing $100 \mu\text{m}$

The top left-hand image of Figure 5.11 shows the unadulterated graphene oxide film whilst the adjacent track was created at a fluence of 9.89 mJcm^{-2} . The bottom right image corresponds to a fluence of 57.5 mJcm^{-2} and all values of fluence in between are shown for each individual image. Again, there is a transition in the colour of the irradiated surface

together with slight widening of the thickness of the line, see Oh et al., 2012. At a fluence of 21.9 mJcm^{-2} there is evidence of partial reduction with patchy regions of darkened material whilst at a fluence of 51.2 mJcm^{-2} the line is fully reduced and has sharpened edges, see He et al., 2016. These results again show that, for a constant scan speed, the degree of reduction is a function of the laser fluence.

5.2.3 Translation Speed

In order to develop the experimental methodology of the proposed z-scan, further tests were completed to investigate the importance of translation speed and here the sample was moved across the laser spot at different tracking speeds at a fluence of 35 mJcm^{-2} . In line with other researchers, see Kumar et al., 2016, tracking speeds of 0.05 , 0.1 , 0.5 , 1 and 5 mms^{-1} were used. The corresponding tracks are shown in Figure 5.12. The results identify that the scan speed has an important impact on the reduction process. At the lowest scanning speeds of 0.05 mms^{-1} and 0.1 mms^{-1} the track is ablated with the irradiation creating a surface transformation that extends well beyond the track width. This is due to the heating process at the surface releasing OCGs from the surrounding GO with the formation of a porous like surface, see Strong et al., 2012, Deng et al., 2016. As the scanning speed is increased the most optimum reduction is observed at the higher scan speeds of 1.0 mms^{-1} and 5.0 mms^{-1} . Based on these results, together with the track produced at a 3 mms^{-1} scanning speed shown in Figure 5.11, a scanning speed of 2 mms^{-1} was selected for the z-scan experiments.

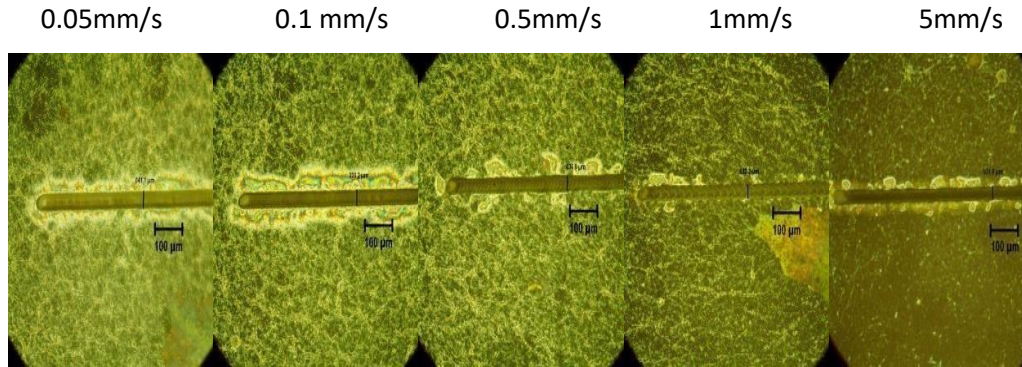


Figure 5.12 - Tracks Created at Different Translation Speeds after Irradiation at 10kHz Pulse Repetition Frequency and 35mJcm^{-2} . 200x Magnification, Scale line represents $100\mu\text{m}$

It is clear from the visual observation of the spots and stripes that changes in spot size and therefore fluence have a significant impact on the GO films ranging from complete ablation to unchanged GO. The previous literature has identified that there will be a fluence at which the reduction of oxygen containing groups and the recombination of sp^2 hybridised carbon will be maximised. The next phase of the research was to establish such optimum conditions by the development of the z-scan methodology.

5.3 Z-Scan Methodology and Experimental System

The original concept of the thesis was to create an experimental methodology to produce a wide range of fluence on the sample surface using a single sweep of the laser system by simultaneously translating the sample through x and z coordinates to create a pattern of reduction. To establish the location at which the degree of reduction is an optimum, the pattern requires that the range of fluence covers the full range of reduction from ablation in the focal plane through to locations where no reduction occurred. Such a system was successfully developed, and the resultant z-scan was analysed using Raman spectroscopy to identify the relationship between the resultant fluence and corresponding degree of reduction. The theory behind the z-scan was presented in Section 3.1 and the experimental methodology to create the z-scan is now described.

5.3.1 Experimental Z-Scan

To measure the z-scan produced from the experimental system, the sample was set up on a stage which translated at a speed of 2 mms^{-1} with the laser firing at a frequency of 10 kHz. The sample was then continuously moved across 10 mm in the x direction while simultaneously being moved 5 mm in the z direction through the focal plane of the laser. This resulted in the formation of a z-scan pattern in each of the GO films. The image shown in Figure 5.13 shows one half of a typical z-scan pattern using the experimental methodology. This highlights what has been produced after scanning through the laser beam focus to produce a graded rGO pattern. This pattern was observed using an Optical Microscope at 50x magnification and is typical of those recorded in the study. In this case the z-scan has the following characteristic measurements:

At point A, $z = 0$, the centre of the focal point of the laser at the start of the experiment, the intensity of the laser beam was sufficient to ablate all of the GO and the glass substrate was exposed. Here the value of ρ was a minimum and had a $3.8 \mu\text{m}$ radius.

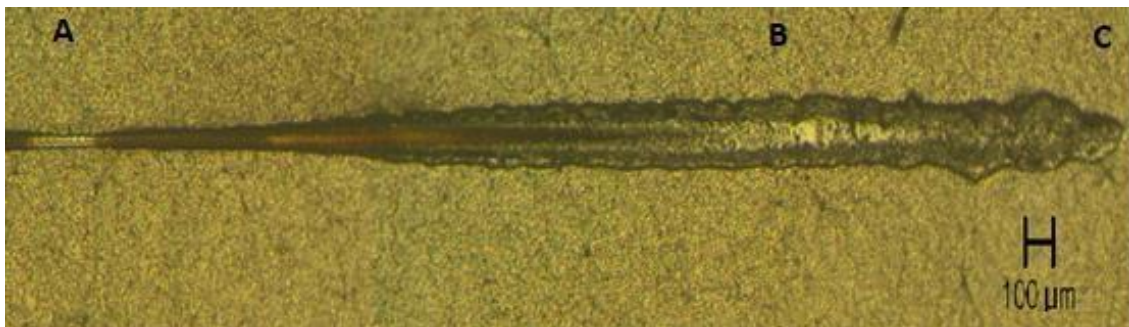


Figure 5.13. One half of a typical optical micrograph of z-scan (2 mms^{-1} , 10 Hz), 50x magnification

Point B is the site of ρ_{max} . This describes the site at which the damage radius was a maximum with a value of ρ_{max} equal to $100 \mu\text{m}$ at a z distance equal to $760 \mu\text{m}$.

Point C: The distance z at which for peak laser fluence falls below the damage threshold, with a value z equal to $1200\mu\text{m}$.

The area surrounding the damage area, shown in light brown, remained pristine GO. The damage boundary was observed to occur at a fluence of 13.8 mJcm^{-2} .

The characteristics of the z -scan were further explored using SEM and optical microscopy. Figure 5.14 (a – b) show two images of Point A in Figure 5.13 at $z=0$ but at different magnification. Figure 5.14 (a) shows two z -scan traces which highlight the scale and overall distribution but with little detail. In contrast Figure 5.14 (b) highlights that at ω_0 the graphene oxide has been ablated down to the glass and at the edges expansion has occurred detailing the lamella structure of the GO flakes.

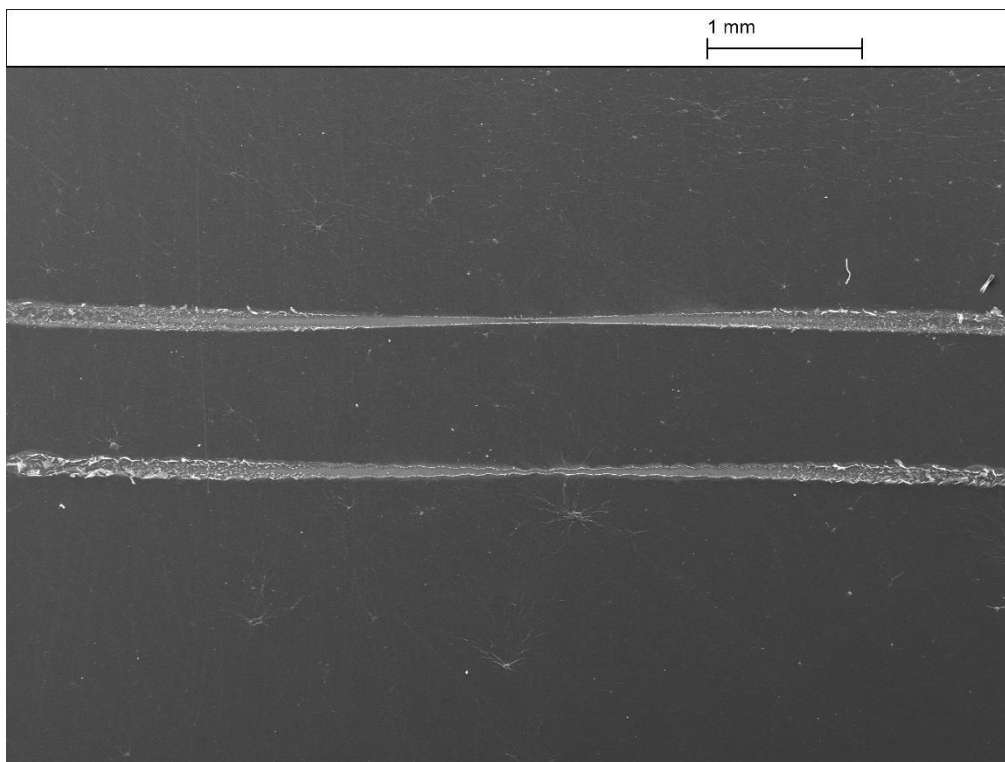


Figure 5.14 (a) - SEM image of z -scan at $z = 0$ with 1mm scale bar

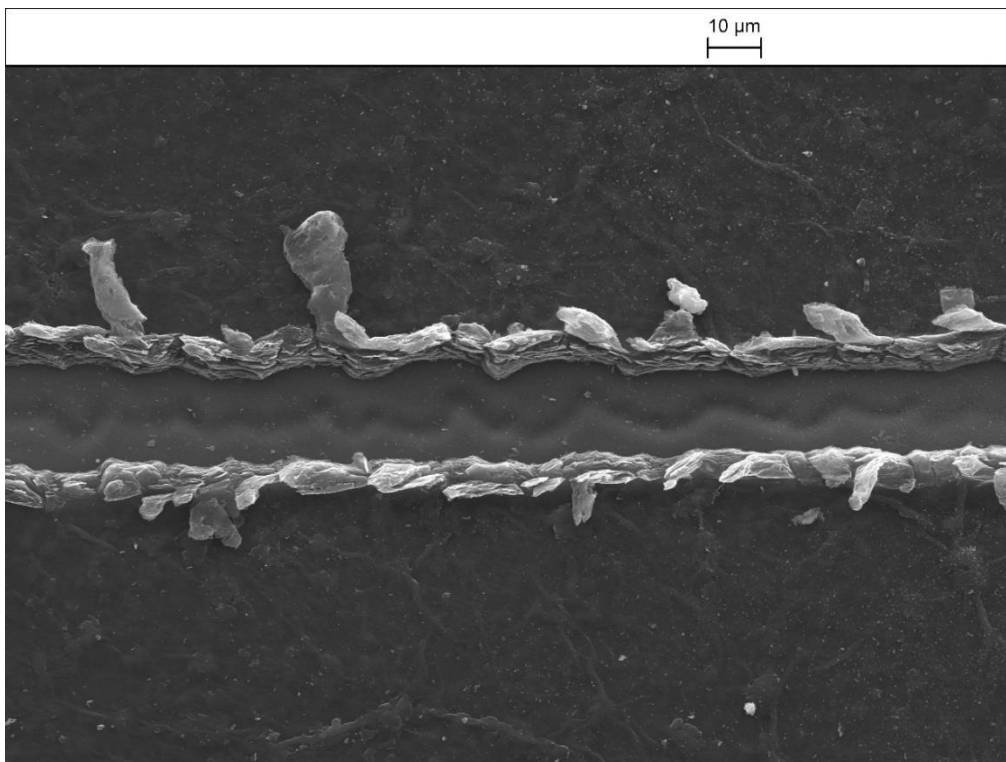


Figure 5.14 (b) - SEM image of z-scan at $z = 0$ with $10\ \mu\text{m}$ scale bar

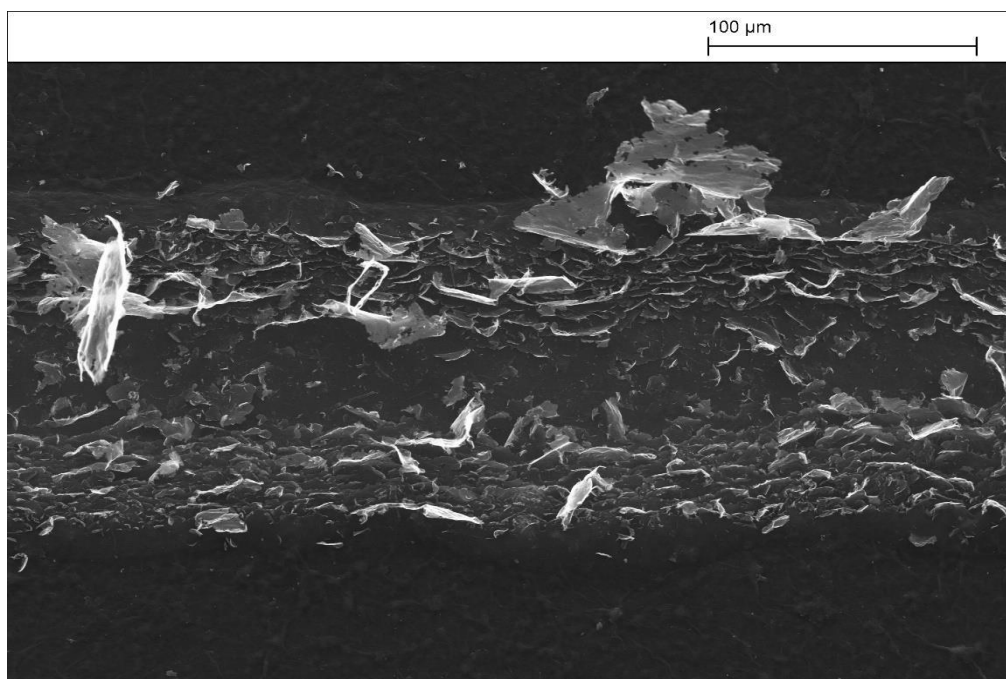


Figure 5.15. SEM image at the location, point B, Figure 5.13, where the damage radius is a maximum with ρ_{max} equal to $100\ \mu\text{m}$ and the z distance of $760\ \mu\text{m}$.

5.3.2 Measurements using Surface Profiler.

Figure 5.15 shows that the degree of reduction is graded across the irradiated z-scan where the damage radius is a maximum. To establish the way in which the surface profile changes a series of measurements were made using the Bruker DektakXT surface profiler to record the change in surface depth at different locations along the full length of the z-scan. Intervals of 300 μm were used from $z = 0 \mu\text{m}$ to $z = 1500 \mu\text{m}$. Typical sections are shown in Figures 5.16 (a-d). These figures show ablation down to the glass where the fluence is highest at the centre of the Gaussian beam with the expansion of GO on either side of the ablated zone where the fluence of the beam is insufficient to ablate the GO. There is a gradual transition in the surface profiles to that illustrated in Figure 5.16 (d) where the curve of the Gaussian beam profile is flattened as z increases and the fluence at the centre of the beam is not sufficient to ablate and only an expansion in the GO surface is observed.

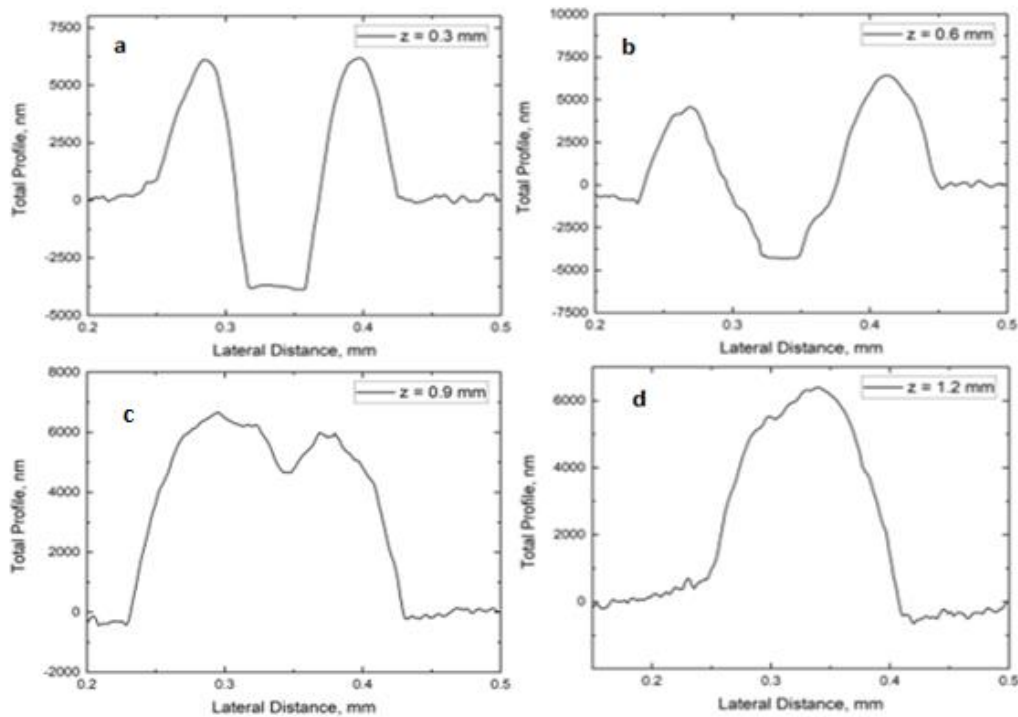


Figure 5.16 (a-d). Surface profiles showing the depth and expansion of the GO surface at different locations in the x direction from ω_0 with a) 0.3 mm, b) 0.6 mm c) 0.9 mm, d) 1.2mm.

These measurements at each cross section have been incorporated into a 3D image that describes the surface profile along the complete length of the z-scan. This is shown in Figure 5.17.

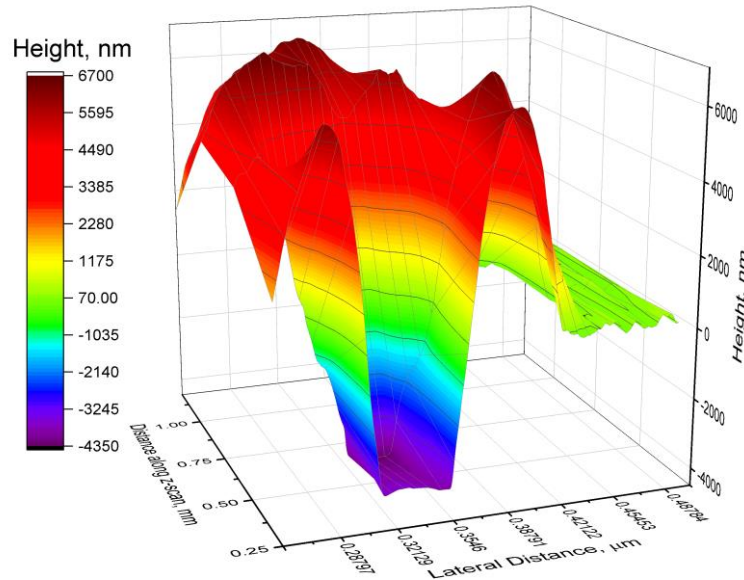


Figure 5.17 - 3D surface profile of z-scan

Taking 0 as the film height prior to irradiation it can be seen that close to ω_0 , towards the front of Figure 5.17, the laser power has ablated the GO down to the glass substrate at circa -5000 nm but laser heating of the surrounding GO has increased its height significantly. As the distance along z is increased the fluence lowers to below the ablation threshold while surface heating still occurs causing expansion between the GO layers leading to an increase in the film's overall height.

In addition, the profile along the z axis at $r=0$ has been plotted and is shown in Figure 5.18. This highlights that in zone A the GO surface is not damaged as the fluence is insufficient to cause any reduction of the GO surface. In zone B the surface rapidly expands at the fluence threshold of 13.8 mJcm^{-2} and the profile of laser fluence results in an expanded bank of irradiated GO which is in line with the findings of other researchers, see Strong et al., 2012,

Sokolov et al., 2013, Trusovas et al., 2013, Deng et al., 2016, who observed an expansion in the thickness of the GO layer upon irradiation. Subsequently the thickness of the layer reduces within zone C where the fluence is increased to the point where ablation occurs down to the glass substrate. Hence, prior to ablation, at the higher fluence values, the thickness of the layer is shown to reduce with the creation of a sunken depth within the irradiated surface, as observed by other researchers, see, for example, Tao et al., 2011, Yung et al., 2013 and Zhang et al., 2010.

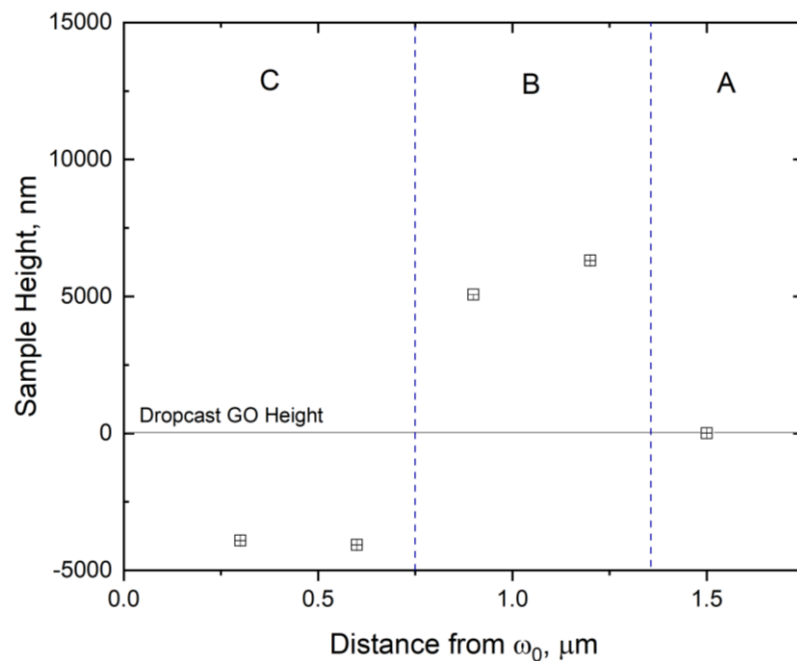


Figure 5.18 – Surface profile along the x axis at $r=0$ of z-scan.

5.3.3 Comparison of Experimental Results with Theoretical Distribution

The theory behind the z-scan was described in Section 3.1 and using the outputs from the theoretical model it is possible to compare the model outputs with the experimental pattern shown in Figure 5.13. To do this reference has been made to the damage boundary where the threshold fluence was equivalent to 13.8 mJcm^{-2} . This value has been plotted on the theoretical distribution shown in Figure 3.4 but repeated here as Figure 5.19. The threshold fluence of 13.8 mJcm^{-2} from the experimental results has been identified by the white line on

Figure 5.19. The experimental and theoretical extent of the damage show very similar distributions and hence it may be concluded that there is good agreement with the theoretically predicted fluence and experimental results. There is a slight deviation between the experimental results and theory in the region close to $z = \rho_{\max}$ as the theory is no longer applicable due to heat edge effects.

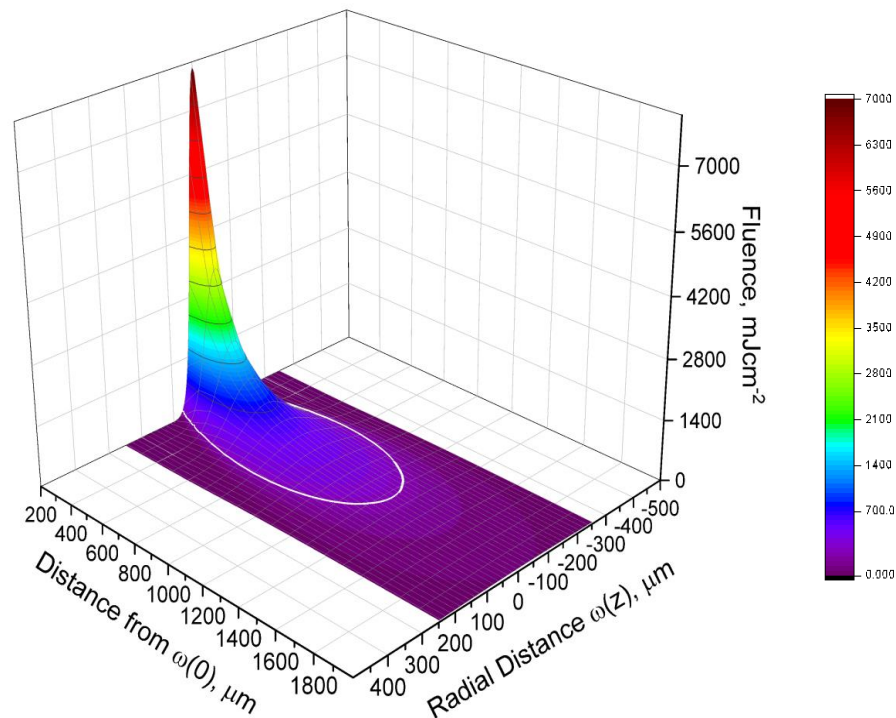


Figure 5.19 Predicted distribution of fluence with experimental limit of damage plotted as the white line at 13.8 mJcm^{-2} .

The above results highlight that the z-scan of GO reduction using a Gaussian beam produces a large fluence range and, in the case of the work in this thesis, the magnitude of fluence ranges from the highest fluence possible for the laser setup found at ω_0 , down through the range of fluence that causes reduction through to the damage threshold of the GO material and onto a fluence less than the damage threshold where no change occurs in the surface

characteristics. Using the experimental methodology outlined in the thesis it is possible to confidently calibrate the fluence incident on a sample as a function of its distance from a lens. Hence, based on the experimental data, the results highlight that the practical range of fluence to create rGO occurs within the range 20 – 50 mJcm⁻². Further tests have been completed to assess the quality of rGO using Raman spectroscopy and this research is described in Section 5.3.5.

5.3.4 Discussion of Surface Characteristics of Other Researchers

The thickness and the surface profile of irradiated surface have been studied by a large number of researchers as detailed in Table 2.2, Chapter 2. Many of these researchers reported a sunken depth in the GO surface whilst others reported an expansion and increase in porosity of the surface. In this thesis the z-scan pattern resulted in both an increase in the layer thickness and a sunken depth as a function of the laser fluence. Other researchers have also observed such changes. For example, Yung et al., 2013, used a 248 nm excimer laser, 20 ns pulse width, 1 Hz and 200 μms^{-1} scan speed, to irradiate tracks and circuits in spun cast GO on glass substrates. The spot size was circa 10 μm x 10 μm with a range of energy density 60 mJcm⁻² to 190 mJcm⁻².

The thickness of the GO layer, shown in Figure 5.20, was circa 40nm and for irradiated tracks at 15 μm spacing, the irradiated (sunken) depth in 10 μm wide tracks was between 18 nm and 25 nm, as a function of energy density. However, the edges of the tracks were much rougher attributed to steep temperature change accompanied by violent photothermal effects, but no profile measurements were reported. In contrast direct laser writing of reduced graphene oxide using a femtosecond-laser irradiation was reported by Kang *et al.*, 2018. Two lasers were used to examine the range of laser fluence and pulse repetition rate: a Ti:sapphire laser

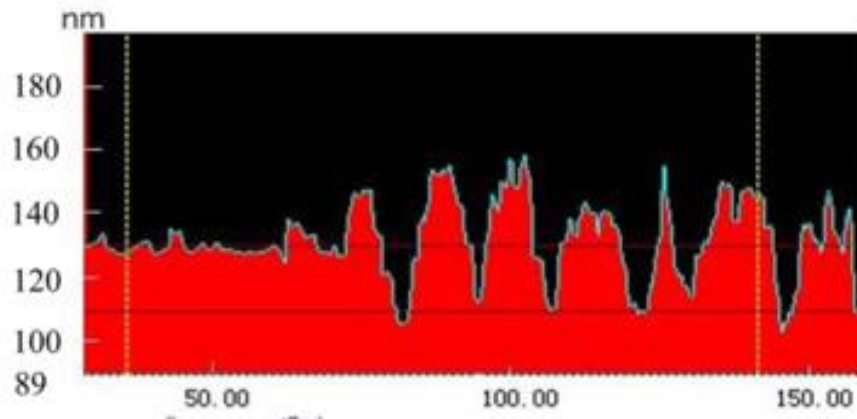


Figure 5.20 Irradiated tracks after Yung et al., 2013. X axis is 'Distance along layer μm ', Y axis is Layer thickness nm. © AIP Publishing

with wavelength 795 nm operated both in continuous-wave (CW) mode or in pulsed mode (11MHz repetition rate, and 300-fs pulse duration) and a Ti:sapphire laser with wavelength 794 nm operated at three repetition rates (76MHz, 10kHz and 250kHz) and three pulse durations (125 fs, 180 fs and 400 fs). Observations of the impact of increases in power using CW irradiation are shown in Figure 5.21. Images (a) to (d) highlight both changes to the irradiated spot size and in the degree of reduction. These contrast with the results presented in Figure 5.10 of the thesis which highlight similar trends. The results to the RHS of Figure 5.18

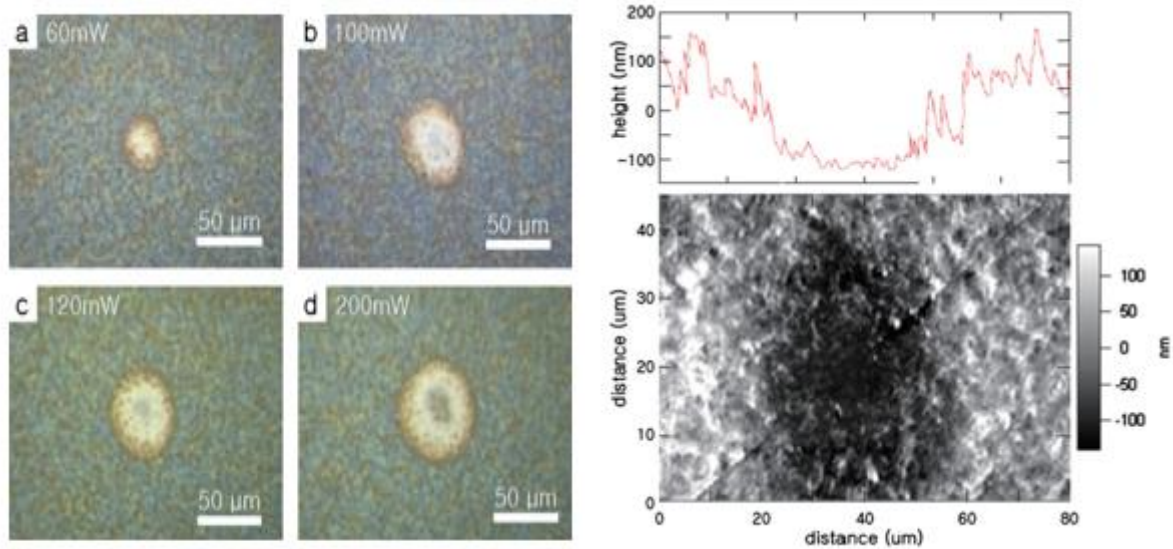


Figure 5.21 Changes in irradiated spot size with laser power and corresponding change in surface profile due to irradiation, after Kang *et al.*, 2018 Elsevier ©

indicate a similar distribution on the thickness of the GO layer with an expansion of thickness at the sides and a sunken depth in the centre of the spot.

Other researchers have only observed a sunken depth. For example, Wan *et al.*, 2019, studied the laser reduction of GO on glass substrates with changes to the laser power and scanning speed. They used an fs laser (780 nm, 50 Mhz) to reduce an array of rectangular spots each with different power (3 to 13 mW, corresponding fluence 1.9 to 8.3 mJcm⁻²) and scanning speed in the range 0.1 to 5 μms⁻¹. They observed that the thickness of the GO layer was reduced by the irradiation and was a function of the laser scanning speed and energy density. At energy densities greater than 37.5 mJμm⁻² the decrease in thickness was constant at circa 77nm (70% reduction) whilst at high scanning speed greater than 1μms⁻¹ there was no reduction in thickness. In Figures 5.16 – 5.18 of the thesis the z-scan results indicate similar changes in the sunken depth at high values of fluence and hence the power of the fs laser used by Wan was sufficient to create such reduced changes in depth. They observed a relatively smooth trend between the energy density and sunken depth, as shown in Figure

5.22. This illustrates that changes in thickness may be controlled using known laser characteristics and thereby provide the opportunity to tune 2D and 3D characteristics in GO, similar to the z-scan surface shown in Figure 5.17.

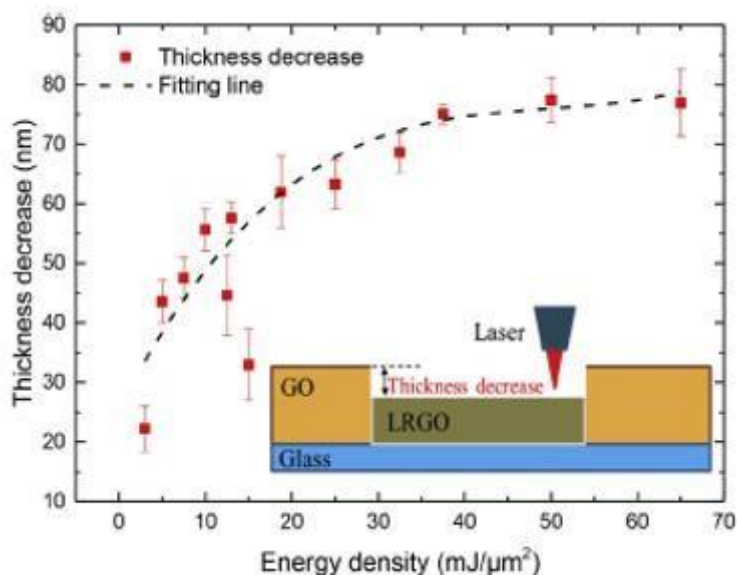


Figure 5.22 – Decrease in irradiated GO thickness as a function of energy density, after Wan et al., 2019. Elsevier ©

A highly relevant publication was reported by Deng et al., 2016, who used a 650nm laser, to pattern 2 mm thick multi-layer graphene oxide films, initially on glass but subsequently on a number of different substrates. They increased the laser power over 3 ranges: low 1.1 to 11.5 mW, medium 71 to 116 mW and high >172 mW. Correspondingly they observed three distinct regions of reduction which were classified by a change in thickness of the GO layer. The three regions are identified in Figure 5.23 a-c. At low power they observed an increase in the thickness of the GO layer with the formation of a loosely stacked structure. The increased thickness was termed the growth layer. As the laser power was increased there was a gradual reduction in the thickness of the laser scribed GO, termed the transition region, attributed to a combination of thickness growth and a reduction in thickness caused by a layer by layer gasification of the hydrogen and oxygen but not the carbon species. At high laser power a complete etching of the GO layer was observed with the removal of both oxygen and carbon

species. They observed that at low power the layer thickness increased approximately linearly whilst exponential damping was observed in the high power region. By comparison with Figure 5.16 and 5.17 of the thesis, there is good agreement with the patterns of reduction shown by Deng in Figure 5.23, thereby confirming that the z-scan approach is an effective way to produce a range in the degree of reduction using a single experiment.

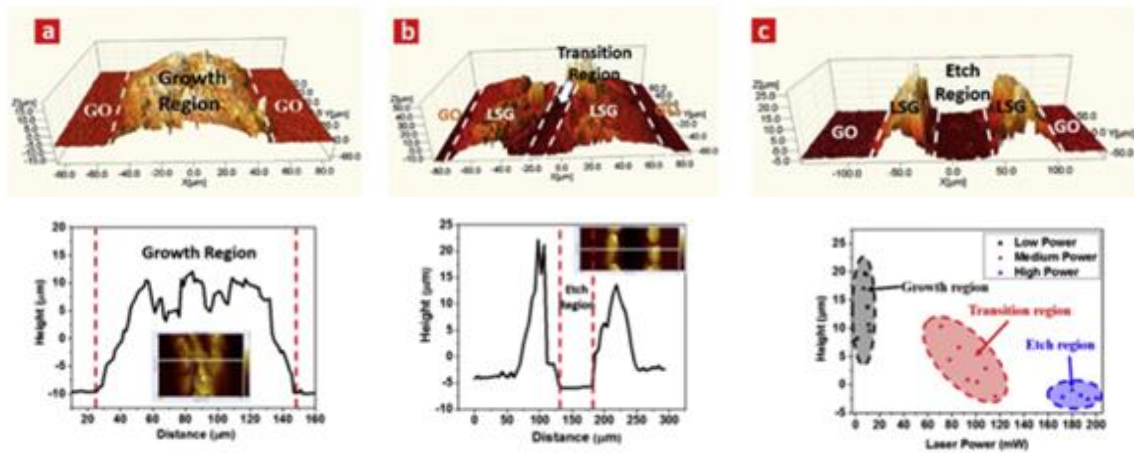


Figure 5.23 - Effect of laser power on rGO thickness showing three regions of reduction, after (Deng et al, 2016) Elsevier

5.3.5 Assessment of Z-Scan Degree of Reduction using Raman Spectroscopy

As explained in Sections 2.5.3 and 2.8.2 Raman spectroscopy has been extensively used to assess the degree of reduction and the quality of the rGO. The z-scan results identify that the maximum range of fluence occurs at point B in Figure 5.16, corresponding to the position of the maximum damage radius. Hence this transverse section was selected as the most appropriate to complete a Raman spectra analysis to quantify the degree of reduction. Figure 5.28 shows the Raman spectroscopy outputs for the GO layer and the corresponding spectra recorded across the section of the z-scan at incremental steps of 25 μm . These steps correspond to fluence values in the range 2.0 mJcm⁻² to 46.7 mJcm⁻² as shown in Figure 5.24. As expected, the results highlight Raman peaks around 1350 cm⁻¹ (D band) and 1580 cm⁻¹ (G band).

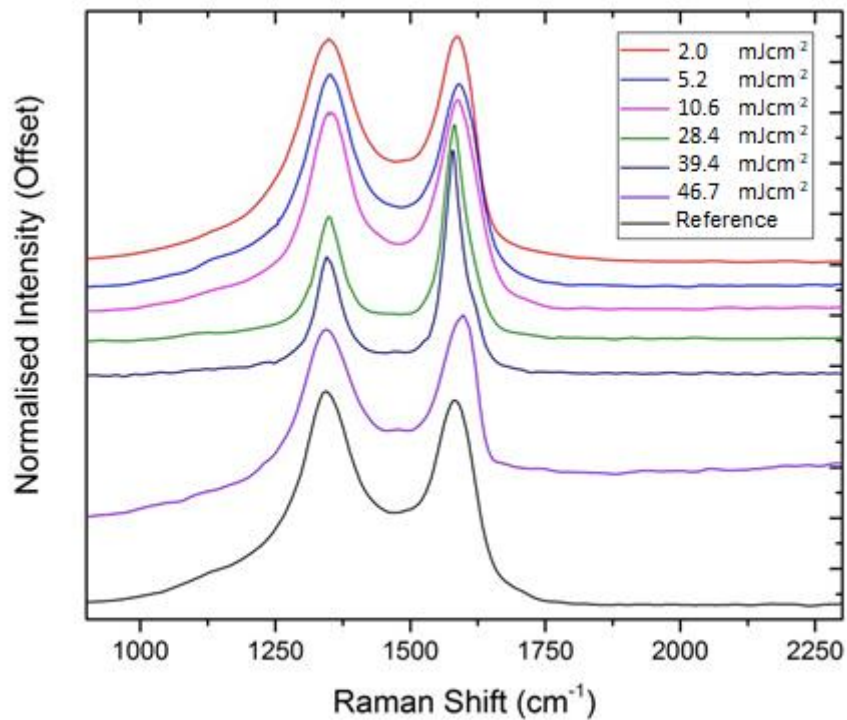


Figure 5.24 - Raman spectroscopy applied horizontally to the sample at location (b) from Figure 5.16

The peak intensities of the D and G spectra were observed to reduce as the fluence was increased and this may be attributed to oxidative burning which reduces layers from the GO sheet or a reduction in interlayer spacing due to the removal of water and oxygen functional groups among GO sheets.

The value of the peak ratio ID/IG has been commonly used to identify the degree of reduction, see Ferrari et al., 2006, as the ratio highlights the way in which the number of defects are changed accompanied by changes in the domain size. The relative intensity between the peaks of the Raman D and G bands is shown in Figure 5.25.

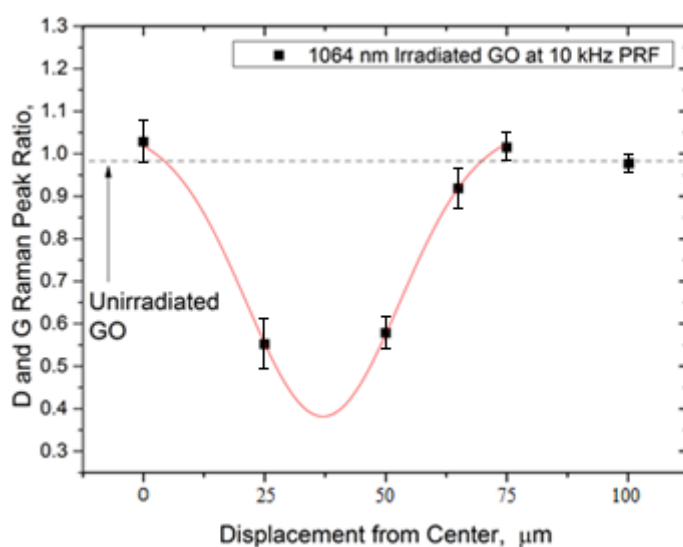


Figure 5.25 - Ratio of D and G peak intensities for Raman spectra at different positions across the z-scan. Fluence values at each displacement value are given in Table 5.1.

Corresponding fluence values for the above graph are shown in Table 5.1.

Table 5.1 - Fluence values corresponding to displacement from $z = 0$

Displacement, μm	Fluence, mJcm^{-2}
0	46.7
25	39.4
50	28.4
65	10.6
75	5.2
100	2.0

These results highlight that low values of ID/IG which indicate a high degree of reduction, say less than 0.8. may be observed from Figure 5.25 to occur at a fluence values in the range 20 mJcm^{-2} to 45 mJcm^{-2} . Hence these values represent the most optimum conditions for the effective reduction of the GO and hence it is possible to identify the locations within the z-scan at which these conditions occur. Subsequently further tests were completed to better examine the characteristics of the reduced GO at these fluence values. A series of large area tests were completed for this purpose and these are now described.

5.4 Large Area Results

From the z-scan experiments it was concluded that the optimum range of fluence for the reduction of the GO was 20 mJcm^{-2} – 45 mJcm^{-2} . To further examine the physical and chemical characteristics of GO samples irradiated at a range of fluence values, a number of large area samples were prepared by drop-casting a solution of GO onto 6 mm by 6 mm glass substrates using the same procedure as outlined in Section 4.1.6. To irradiate a uniform surface over the whole of the sample surface area the vertical position of the laser was adjusted in 6 incremental positions to create a series of fluence values in the range 23.9 mJcm^{-2} to 41.1

mJcm⁻². For each vertical position of the laser, the stages were set up to move at a constant speed of 2 mms⁻¹ and to raster the complete surface with a number of irradiated lines by the movement of the laser back and forth in the x-direction and avoiding overlap in the y-direction. Five repeat samples were prepared at each value of fluence. Hence a total of 30 samples were used in the analysis. The characteristics of the GO surface and irradiated GO at the above range of fluence, were evaluated using surface profiling, resistance measurement, Raman spectroscopy and X-ray photoelectron spectroscopy (XPS).

5.4.1 Surface Profile Measurements.

The surface profile of each GO layer and of the subsequent rGO was measured using the Dektak XT surface profiler described in Section 4.1.7. At each fluence 5 repeat tests were completed with the profile recorded in both the raster direction and perpendicular to the raster direction. Typical results are shown in Figure 5.26 which describes the surface profile prior to irradiation and Figure 5.27 which shows a typical profile after irradiation, in this case at a fluence of 41.1 mJcm⁻². Subsequently these results have been used to estimate the change in wettability of the irradiated surfaces as described in Section 4.1.11 of the thesis. Figures 5.26 – 5.27 clearly illustrate that the irradiation process has a significant impact on the roughness of the surface with the pristine GO being relatively smooth compared to the irradiated sample. These changes are created as a function of the expansion of the surface due to the release of water vapour and oxygen containing groups as the GO is reduced.

To assess the average roughness use was made of the Dektak Vision 64 software and all roughness results are shown on Figure 5.28. The error bars on this graph have been computed from the average of 5 samples for each point on the graph. In addition, the average roughness of the pristine GO was measured as 115±3 nm. Figure 5.28 highlights that there is little difference in the average roughness in both the raster direction and perpendicular to the raster direction indicating that the experimental methodology with a 50 µm spacing of the raster created a relatively uniform surface over the whole area of the sample. The relationship between average roughness and fluence is also shown on Figure 5.28 which highlights that

the magnitude of the fluence had little impact on the average roughness of the samples tested. There is no obvious trend in the data and values of average roughness were in the range 1036 nm to 1348 nm. This indicates an order of magnitude difference between the pristine GO and the irradiated GO.

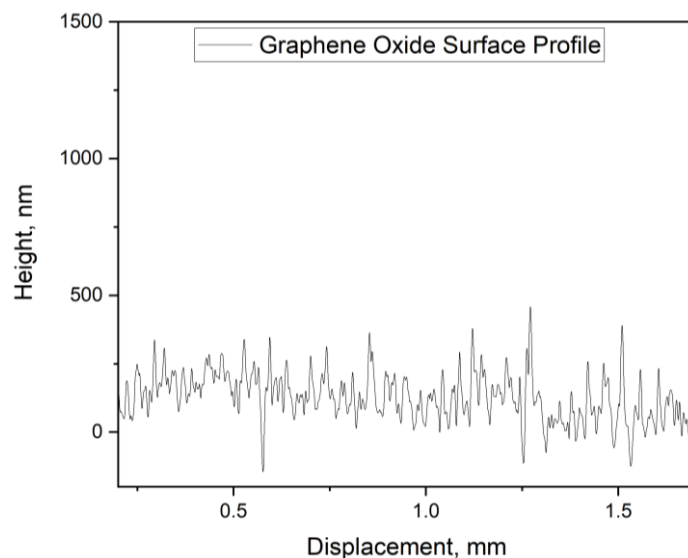


Figure 5.26 – Typical surface profile of drop-cast GO prior to irradiation. Displacement describes the distance across the sample

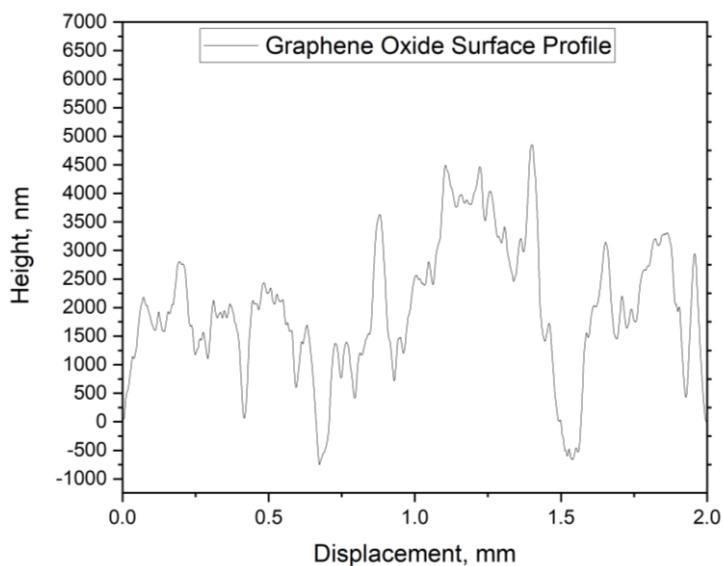


Figure 5.27 – Typical surface profile of a GO sample after irradiation at a fluence of 41.1 mJ/cm². Displacement describes the distance across the sample

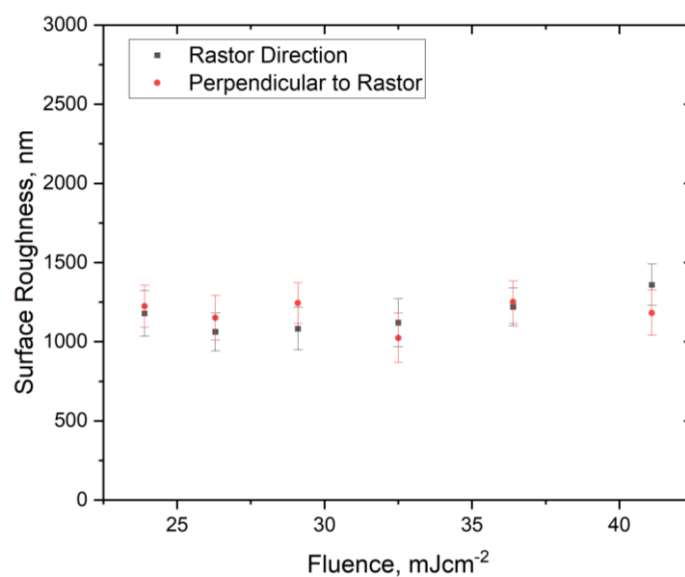


Figure 5.28 – Surface roughness of GO sample after raster irradiation showing roughness both parallel and perpendicular to the raster direction

5.4.2 Conductivity Measurements

The power of the laser has been shown to influence the characteristics of the laser reduced GO and a change in the conductivity of the irradiated GO has been used as a measure of this impact by many researchers, as detailed in Sections 2.5.2 and 2.8.1. In most studies the relationship between current (I) and voltage (V) across sections of irradiated rGO is measured. For increasing and decreasing voltage a linear relationship between I and V is commonly observed, the slope of which is equal to the electrical resistance (R). This allows the calculation of the sheet resistance (R_s) where;

$$R_s = \frac{(RW)}{L} \quad \text{eqn 5.1}$$

and W is the laser power and L is the distance over which the I/V measurements are made.

In this study a 2 point probe method was used to measure the change in the conductivity of the irradiated GO. The results are shown in Figure 5.29.

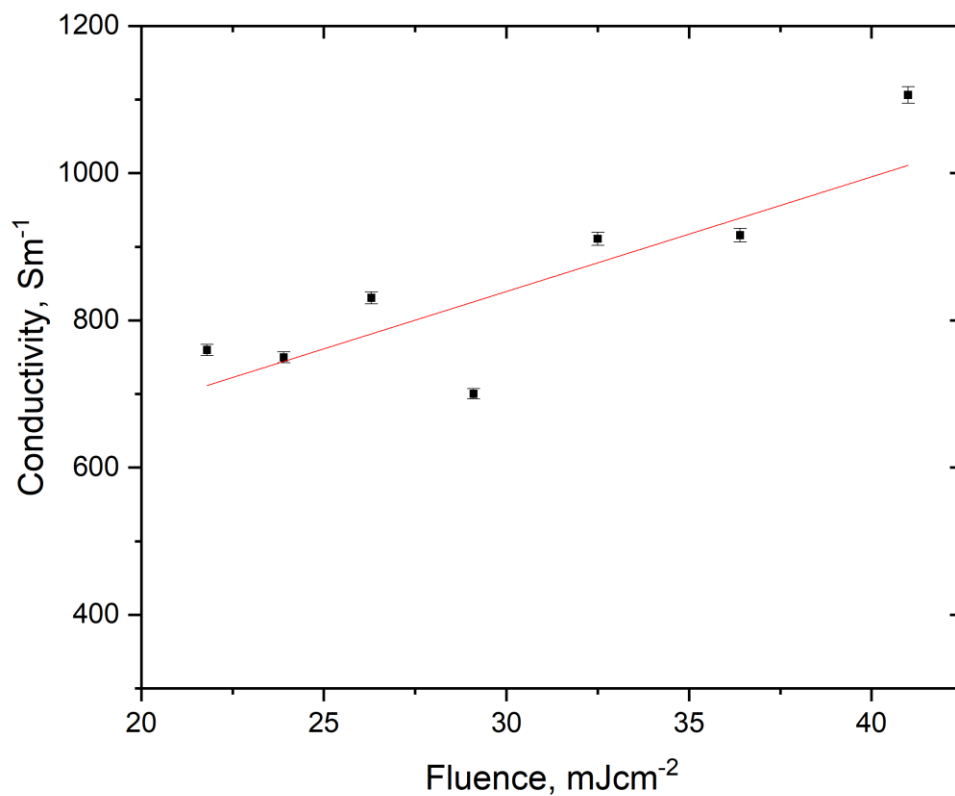


Figure 5.29 – Conductivity as a function of laser fluence

Figure 5.29 shows how the conductivity increased with fluence from a value of 760 Sm⁻¹ to 1100 Sm⁻¹ over the fluence range 23.9 mJcm⁻² to 41.1 mJcm⁻². The conductivity of the pristine GO was measured to be 5.5 Sm⁻¹. Hence the irradiation of the GO resulted in a huge increase in conductivity.

Similar results have been observed by many other researchers as detailed in Table 2.2, Chapter 2.

5.5 Raman Spectroscopy and XPS

5.5.1 Raman Spectroscopy

The analysis of the Raman results for the large area research were completed at Nottingham Trent University and the help of Dr Graham Hickman is gratefully appreciated and acknowledged.

Figure 5.30 shows the overall view of the results of Raman analysis of 6 rGO samples together with one GO reference sample. The results correspond to a range of fluence from 23.9 mJcm^{-2} to 41.1 mJcm^{-2} . The results at each fluence are shifted vertically to avoid overlap. It can clearly be seen that there are three identifiable peaks: D peak at 1355 cm^{-1} , G peak at 1585 cm^{-1} and the 2D peak at 2700 cm^{-1} . The plots showed that there was little translation in the D and G peaks but there was a slight narrowing of the peaks with increased fluence. The latter feature suggests an increase in the translation of sp^3 bonds to sp^2 bonds as the fluence is increased. To interpret the results, reference has been made to the application of the ID/IG integral ratio and the ratio I2D/G integral ratio. Plots of these identifiers are included Figures 5.30 and 5.31, respectively. In Figure 5.30, the 2D peak has been enhanced on the right-hand side.

Examination of the ID/IG integral ratio identifies two possible interpretations. Firstly, the results describe a 2-stage process whereby there is an overall reduction in the ratio up to a fluence of circa 35 mJcm^{-2} after which the value appears to saturate at a value of circa 0.75. The initial reduction may reflect a gradual removal of the oxygen containing groups as the fluence is increased which overrides the increase in defect formation due to the increase in the thickness as observed in Section 5.4.1, followed by an increase in the conversion of sp^3 bonds to sp^2 bonds which results in a lowering of the ID/IG ratio within the range of fluence 32.5 mJcm^{-2} to 36.4 mJcm^{-2} after which the transformation is saturated to yield a constant value circa 0.75. Secondly the reduction process may be described in three stages: a reduction from a value of 1.03 to a value of 0.85 over the range of fluence between 23.9 mJcm^{-2} and 26.3 mJcm^{-2}

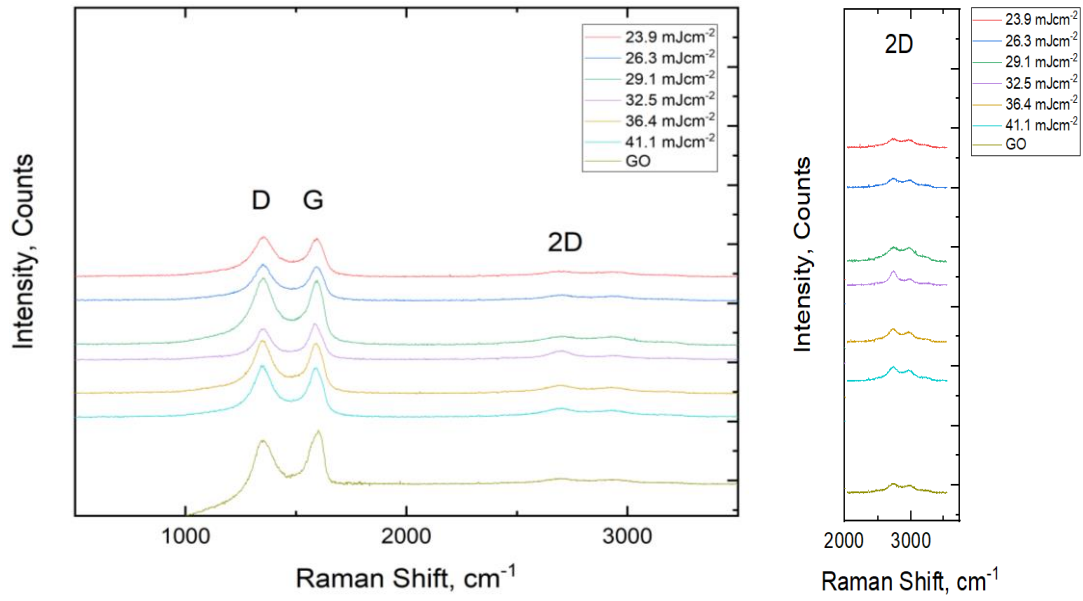


Figure 5.30 – Raman spectroscopy results showing D, G and 2D peaks of samples irradiated at fluence values in the range 23.9 mJcm⁻² to 41.1 mJcm⁻².

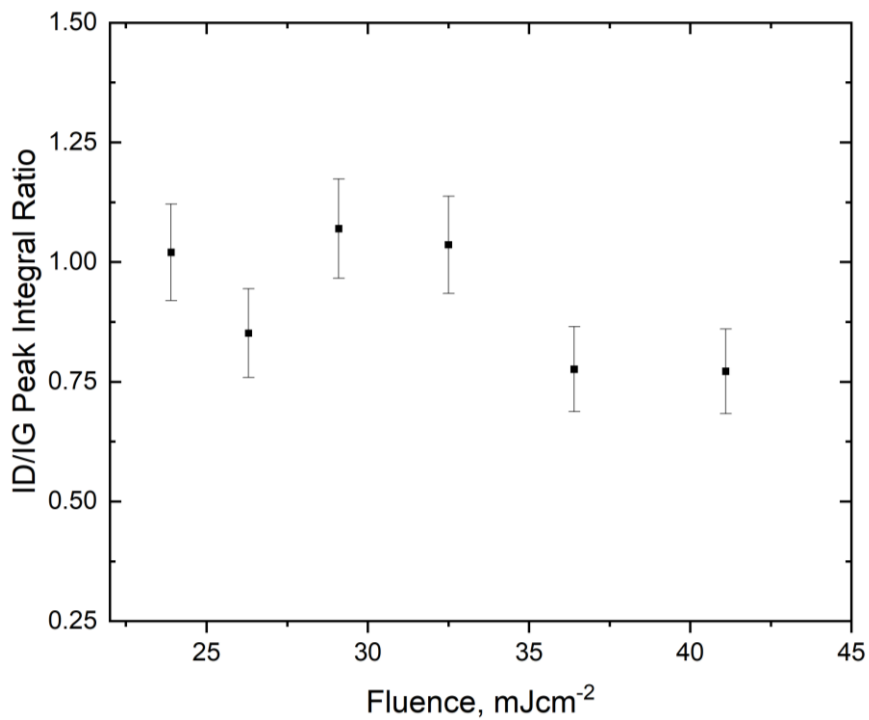


Figure 5.31 - Peak integral ratio of D and G Raman peaks corresponding to irradiation over the fluence range 23.9 mJcm⁻² to 41.1 mJcm⁻².

This decrease shows enough laser energy is supplied to remove defects or oxygen species from the GO lattice. A second stage highlights that as the fluence increases the value of ID/IG increases up to a value of 1.07 over the range 26.3 mJcm⁻² to 32.5 mJcm⁻² which may be attributed to an increase in GO thickness and the introduction of defects. Thereafter there is a gradual reduction in the value of ID/IG upto a fluence of 36.4 mJcm⁻² which coincides with the recombination of sp² hybridised carbon. This appears to reach a saturation at this latter fluence as the ID/IG ratio does not change for a further increase in fluence.

A further measure of the degree of reduction may be examined by calculating the change in crystallite size. Using the empirical expression, after Cançado *et al.*, 2011, shown here as equation 5.2 but repeated from Chapter 2, (see eqn 2.8 for details), where

$$La = (2.4 \times 10^{-10})\lambda^4(ID/IG)^{-1} \quad \text{eqn 5.2}$$

and La is the crystallite size, λ is the excitation wavelength of the Raman instrument, ID is the integrated area intensity of the D band, and IG is the integrated area intensity of the G band. Using this equation, the crystallite size was found to be 22 nm for GO which increased to a peak value of 49.6 nm for the reduced GO at a fluence of 36.4 mJcm⁻². These values confirm that graphene-like characteristics were observed in the reduced graphene oxide.

For optimum reduction, the value of I2D/IG should be as high as possible as this is an interpretation of recombination of sp² carbon hybridisation. The results outlined in Figure 5.31 may be interpreted in a similar way to those for the ID/IG ratio. The ratio for GO was measured at 0.22 and Figure 5.32 again highlights two possible interpretations of the results. Firstly, the overall trend may be interpreted as a gradual increase in the ratio up to a saturation value of 0.31 at a fluence of 32.5 mJcm⁻². This would indicate a gradual transition in the degree of reduction. The second interpretation relates to a 3 stage process of reduction. Firstly, the ratio is increased over the fluence range 23.9 mJcm⁻² to 26.3 mJcm⁻² which may be attributed to the loss of oxygen groups followed by a reduction in the ratio at a fluence of

29.1 mJcm⁻². This reduction may be associated with an increase in defects due to an expansion of the surface but this reduction is followed by a further increase in the ratio as the laser fluence is increased, possibly associated with an increase in the conversion of sp³ bonds to

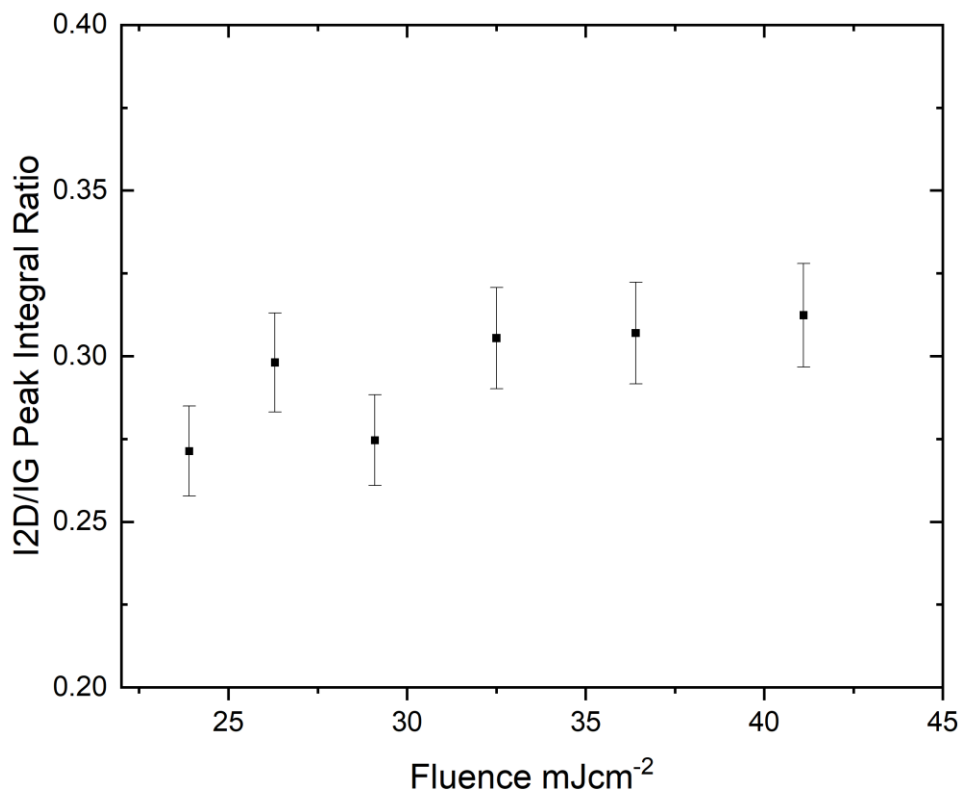


Figure 5.32 - Peak integral ratio for I2D/IG corresponding to irradiated samples at fluence values in the range 23.9 mJcm⁻² to 41.1 mJcm⁻².

sp² bonds. At values of fluence greater than 32.5 mJcm⁻² the ratio appears to saturate at a value of circa 0.31. These results are now referenced to the findings of other researchers.

5.5.2 Discussion of Raman Spectroscopy Results of Other Researchers

A major study was completed by Arul et al., 2016 who presented the results of a large scale test programme using the 248nm wavelength ns laser. Changes were made to the fluence and the scan speed, expressed as the number of overlapping pulses, and the Raman results were presented in a 2-D visual format included here as Figures 5.33 and 5.34 which show changes in the ID/IG and I2D/IG ratios for the range of overlapping pulses 5 – 50 and for fluence in the range 50 to 225 mJcm⁻². For optimum reduction it is desirable to locate the minimum ID/IG ratio and the maximum I2D/IG ratio. From Figure 5.33 there is a pocket of low ID/IG, of value circa 1.0, centred on a fluence of 140 mJcm⁻² and 35 overlapping pulses and from Figure 5.34 there is a maxima region of I2D/IG, of value circa 0.5, centred on a fluence of 120 mJcm⁻² at 40 overlapping pulses. The minimum ID/IG value reflected little change from that measured for the GO layer, and as all values of this ratio were greater than unity, Arul et al., explained this increase due to minor photoinduced defect formation.

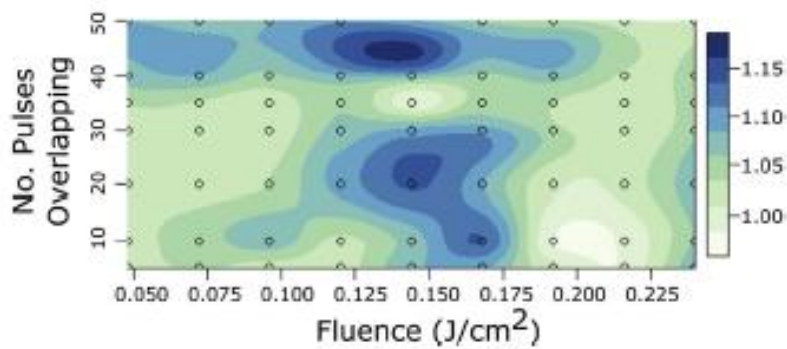


Figure 5.33 ID/IG peak intensity ratio for ns laser, after Arul et al., (2016). Elsevier ©

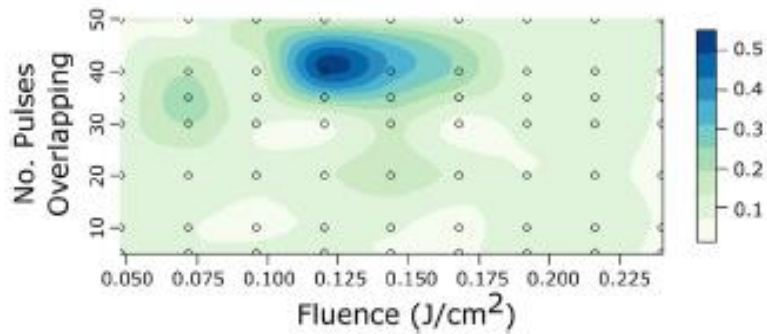


Figure 5.34. I2D/IG for ns laser, after Arul et al., (2016). Elsevier ©

They also observed that at a fluence 120 mJcm^{-1} and 40 overlapping pulses, the substrate type had a significant impact on the ablation characteristics of the GO. The results in Figures 5.33 and 5.34 were obtained for a PET substrate but the use of a stainless-steel substrate with high thermal conductivity resulted in less reduction whilst with no substrate in an ambient air environment the GO was fully ablated and pierced.

Tests were also completed to establish the damage threshold of the GO and it was observed that for 10 ns laser pulses the threshold was circa 10 mJcm^{-2} . The threshold fluence obtained by the author in this thesis was circa 13.8 mJcm^{-2} which is in relatively good agreement with that observed by Arul et al., 2016 but differences may be attributed to the characteristics of the GO (thesis value of ID/IG was 0.79 compared to a value of 1.0 measured by Arul), to differences in the laser wavelength and the type of substrate used in the thesis (silica).

A further major study was completed by Evlashin et al., 2018, who used an ns fibre pulse infrared laser of wavelength $1064 \mu\text{m}$ to reduce GO to rGO in ambient conditions. They completed over 8000 tests to examine the relationship between laser pulse duration (4 – 200ns), laser pulse frequency (1.6 t- 1000kHz), average laser fluence ($0.1 - 100 \text{ Jcm}^{-1}$) and laser scanning beam speed in the range 20 to 10000 mms^{-1} . Each variable was systematically changed, and Figure 5.35 identifies the relationship between the laser frequency and spot velocity for a large number of these tests. The degree of reduction is identified by the depth

of shading and the white line represents a good approximation to highlight the optimum conditions for reduction.

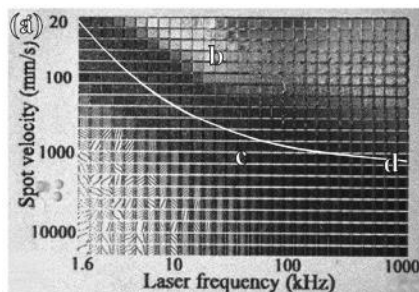


Figure 5.35. Relationship between degree of reduction, laser frequency and spot velocity after Evlashin et al. (2018). ©WILEY (2018)

A parameter termed Energy Fluence (EF) was used to analyse the results. EF is proportional to the frequency (f) and the energy of the pulse (E_{pulse}) and inversely proportional to the velocity of the laser spot (v) and the beam diameter (D), where

$$EF = f \times E_{\text{pulse}} / (v \times D) \quad \text{eqn 5.3}$$

Analysis of the optimum data (white line data) highlighted that the value of EF was almost constant. Unfortunately, it is not possible to directly compare the EF results reported by Evlashin et al., 2018, with the results presented in the thesis as changes in beam diameter and energy per pulse were made at the same time in the thesis methodology. However, in respect of Raman spectroscopy the work of Evlashin showed that the ID/IG ratio was in the range 0.97 to 0.22 (the lowest value recorded in the literature), the highest value of the I2D/IG ratio was 0.5 with crystallite sizes of 28nm for GO and a maximum of 88nm for rGO. Hence, their results covered the range of values obtained in this thesis.

Three distinct stages of reduction were reported by Bobrinetskiy et al., (2017), who used an fs laser, wavelength 515 nm, 280 fs pulse length and 500 kHz repetition rate, to create a grid of irradiated squares at 5nm spacing. Different values of energy per pulse (7 – 60 nJ) and

scanning speeds ($5 - 100\text{mms}^{-1}$) were used and the spot size was maintained under $5\ \mu\text{m}$. Raman spectroscopy and sheet resistance measurements showed that the degree of reduction was a function of both energy per pulse and scanning speed. The results were plotted to yield contours of ID/IG in the range 1.04 to 0.78, I2D/IG (0.1 to 0.40) and sheet resistance (200 to $1200\ \Omega\text{sq}^{-1}$). At a scanning speed of 20mms^{-1} the results are shown in Figure 5.36.

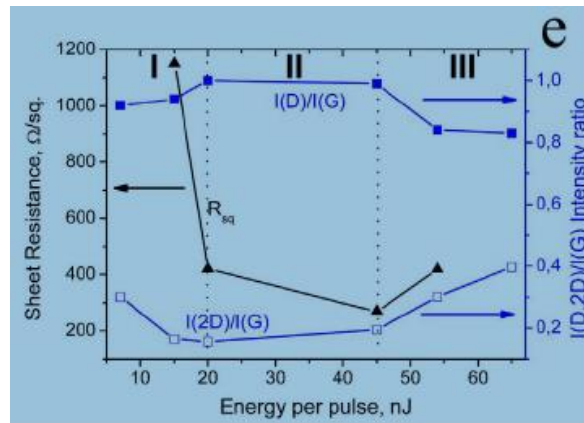


Figure 5.36 ID/IG ratio, I2D/IG ratio and resistance measurements as a function of laser energy per pulse, after Bobinskiy et al (2017) Elsevier ©

Three distinct stages of reduction were interpreted:

- Stage I Energy per pulse in the range 5 to 20 nJ
 ID/IG increased from 0.8 to 1
 I2D/IG reduced from 0.3 to 0.17
 Resistance significantly reduced from $1200+ \ \Omega\text{sq}^{-1}$ to $400 \ \Omega\text{sq}^{-1}$

The increase in ID/IG was attributed to the removal of the oxygen species and deletion of some weakly bonded carbon atoms resulting in the defect number increasing and hence the consequent increase in the ID/IG ratio. Stage I was entirely due to photochemical reduction.

- Stage II Energy per pulse in the range 20 nJ to 45 nJ
 ID/IG slightly reduced from 1 to 0.98

I2D/IG increased from 0.17 to 0.2

Resistance reduced from $400 \Omega\text{sq}^{-1}$ to circa $260 \Omega\text{sq}^{-1}$

Stage II resulted in more pronounced thermal effects giving rise to thermally mediated relaxation of the carbon lattice with an enhancement of crystalline properties of the layer and the generation and release of free oxygen or water vapour, accompanied by a reduction in the film thickness. Stage II was attributed to both photochemical and photothermal reduction processes.

Stage III Energy per pulse greater than 45 nJ.

ID/IG reduced from 0.98 to 0.82

I2D/IG increased from 0.2 to 0.4

Resistance increased from to $260 \Omega\text{sq}^{-1}$ to $400 \Omega\text{sq}^{-1}$.

Stage III described photothermal reduction only with the increased heat causing an explosive evaporation of gaseous species from reduced GO leading to ablation of the surface.

Figure 5.36 highlights a specific set of results at a scanning speed of 20 mms^{-1} and in many respects these results are similar to the results of the author in that, following Stage I, the results highlight a reduction in the ID/IG ratio and an increase in the I2D/IG ratio which confirm that the ns laser results of the author reflect photothermal reduction.

A fs laser (780nm, 50Mhz) was used by Wan et al., 2019 to reduce an array of rectangular spots each with different power (3 to 13mW, corresponding fluence 1.9 to 8.3 mJcm^{-2}) and scanning speed in the range 0.1 to $5 \mu\text{ms}^{-1}$. Raman spectra showed that the ratio of ID/IG, ranged from 1.37 to 1.13, as shown in Figure 5.37 with 2D representation in Figure 5.38.

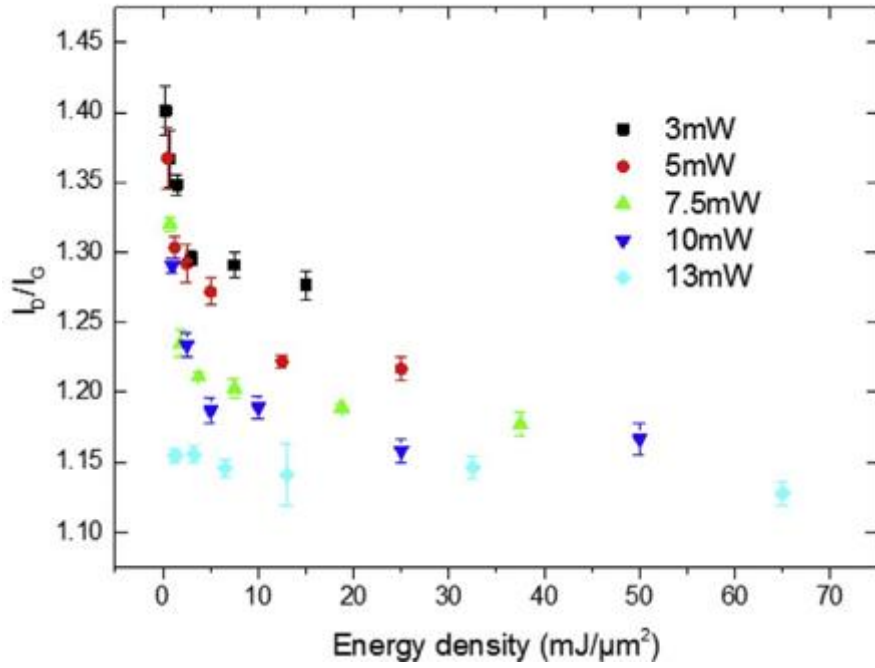


Figure 5.37 Results of ID/IG ratio after Wan et al., 2019. Elsevier ©

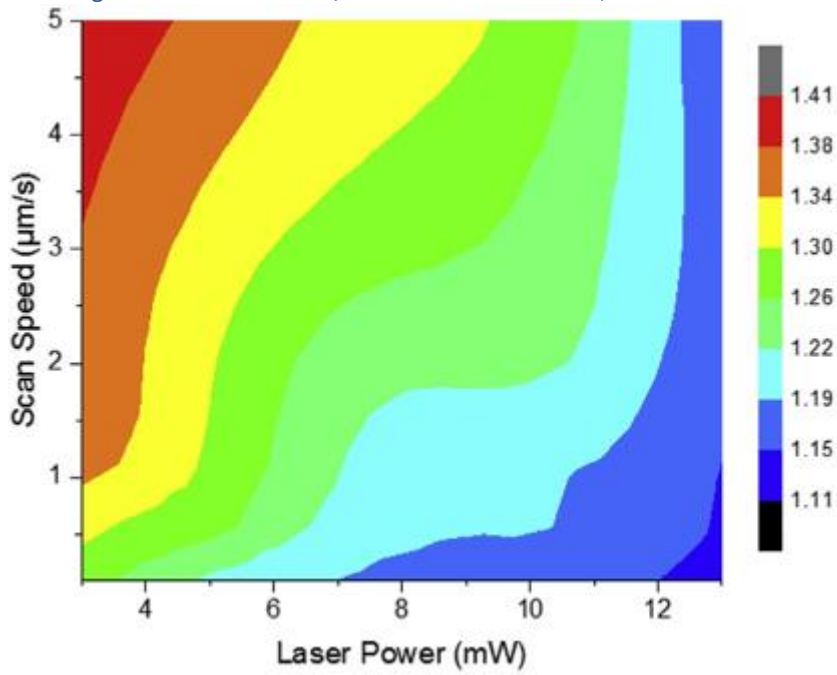


Figure 5.38 2D representation of ID/IG ratio results, after Wan et al., 2019. Elsevier ©

The ratio of ID/IG was, in general, observed to reduce for an increase in laser power and to increase with an increase in scanning speed. They reported their results using energy density $\text{mJ}/\mu\text{m}^2$ and at higher values of energy density, the ratio tended to a constant value circa 1.15. The decrease of ID/IG reflects fewer defects and an increase in the crystallite size. However, Wan et al 2019, reported the fs laser irradiation did not result in the development of a 2D peak at the expected 2700 cm^{-1} and suggested that the 780 nm fs laser reduction was localized and that the reduction was insufficient to create large planar sheets of graphene.

Kymakis *et al.*, 2014, used a one-step photoreduction pulsed laser process on spin coated GO films on PET substrates in air at room temperature. Two lasers were used: an fs laser, 800 nm wavelength of 800 nm, 100 fs and repetition rates 1 kHz and 80 MHz, and a ns laser with wavelength 248 nm, 30 ns and 10 Hz. Using the ns laser with a 20.1nm thick layer, as the pulse number increased the D and G peaks reduced in intensity and became narrower but with no appreciable band shift, as shown in Figure 5.39 (a), with the corresponding ID/IG ratio shown in Figure 5.39 (b).

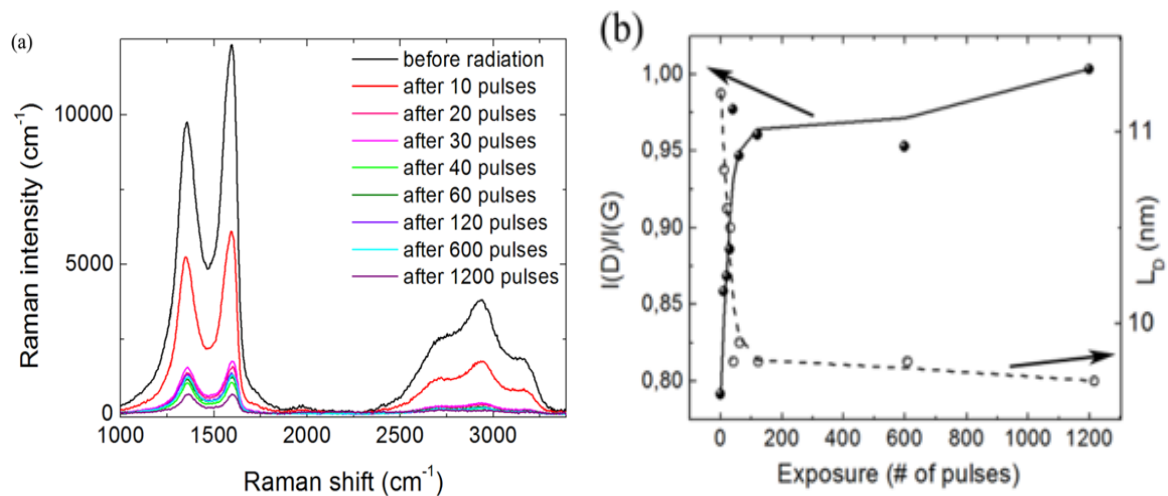


Figure 5.39(a) Raman spectra as a function of pulse number (b) ID/IG ratios, after Kymakis et al., 2013 and Petridis et al., 2013. ©WILEY (2018)

The peak intensity ratio, ID/IG, gradually increased from 0.75 for the GO to a value slightly greater than 1.0 at a pulse number of 400 as detailed in Figure 5.39 (b). An increase in the ID/IG ratio indicated disordering of graphite but ordering of amorphous carbon structures and hence the increase in the ID/IG ratio was a result of increasing ordering. The ID/IG was used to predict the average distance between defects, and, using the equation of Lucchese et al., 2010, Kymakis et al., showed that the distance between defects increased from 10 to 11 nm, as shown on Figure 5.39 (b). This suggested that there was a limit in GO lattice ordering and consequent oxygen removal and further reduction may take place due to thermal effects.

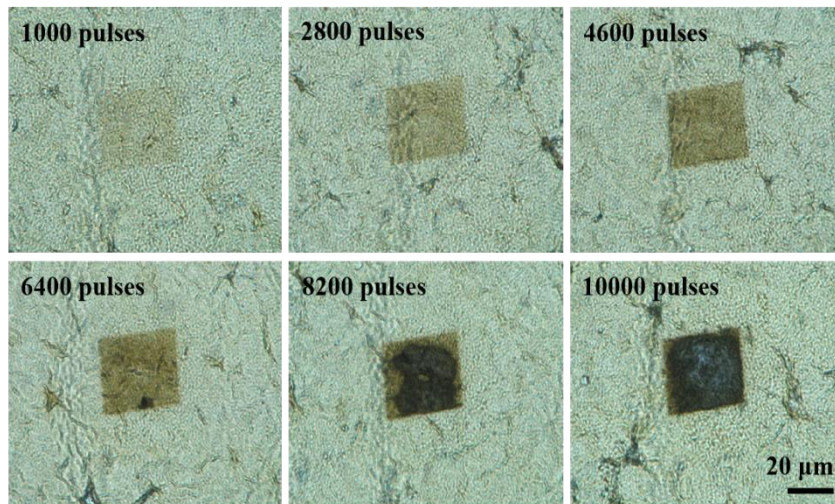
In contrast, for the fs laser (5.5mW, fs 100 and 20.1nm GO/PET) the ID/IG ratio was shown to reduce for pulse numbers up to 100 (due to non-thermal reduction) with a subsequent increase to a peak value at circa 0.85 corresponding to 400 pulses, attributed thermal reduction. Hence the pulse duration has a significant influence on the ratio of ID/IG which is due to the thermal mechanisms associated with fs and ns pulses.

An fs laser (wavelength between 750 and 830 nm, instantaneous peak power 400 μ J per pulse, average power 4W, 90 fs, 10kHz) was also used by Li *et al.*, 2014, to create 2D freeform patterns of laser reduced squares on GO sheets (3-5 microns thick).

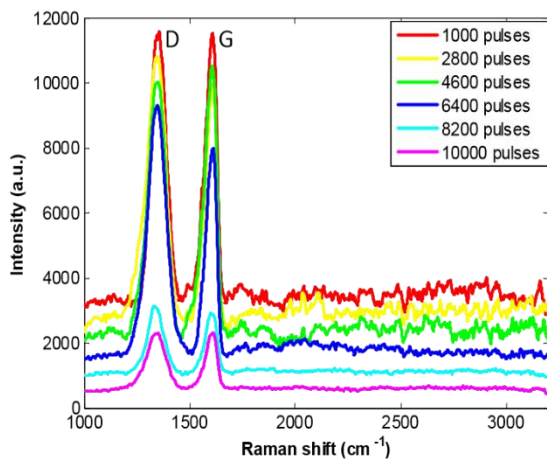
A series of 30 μ m by 30 μ m squares were systematically irradiated in the GO films using the two wavelengths (750 and 830 nm with 1000 pulses) and step changes in the laser power from 10mW to 90mW. The results highlighted that the wavelength of 750nm was far more efficient at reducing and ablating the GO. The 750nm wavelength was used in subsequent studies that examined the optimum pulse number in the range 1000 to 10000 with a pulse energy 1.4 μ J. The results presented by Li et al., 2014, are shown in Figure 5.40. The images presented in Figure 5.40 (a) highlight that as the pulse number was increased the reduction of the GO surface resulted in a change in colour with a

darkening of the surface. Corresponding Raman spectra and values of the ID/IG ratio are also shown in Figure 5.40 (b) and (c) respectively.

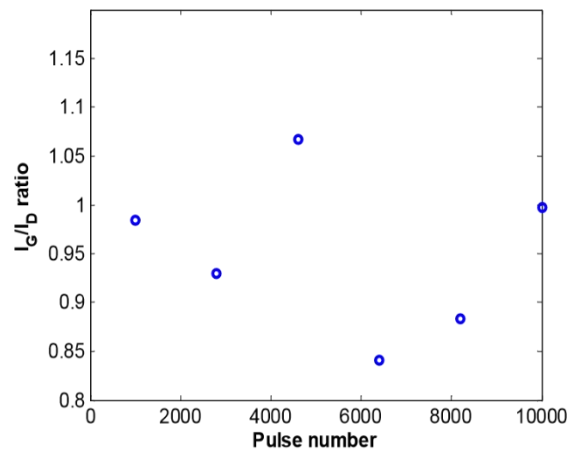
The Raman results show that an increase in pulse number resulted in a reduction of the intensity of the D and G bands. 2D bands were difficult to observe attributed to the fact that multiple layers of GO were used. The ID/IG ratio was erratic and for the first 2800 pulses the ratio increased from a value of 1.02 to 1.08 and then decreased sharply to a value of 0.93 at a pulse number 4600 followed by a sharp increase to a value of 1.19 at a pulse number 6400 and then a sharp reduction to a value of 1.0 at 10000 pulses. As a consequence, Li *et al.*, (2014), highlighted that the minimum value of 0.93 at 4600 pulses corresponded to optimum GO reduction at a pulse energy of 1.4 μJ . At higher pulse numbers it was observed that the surface of the GO was damaged and this resulted in the corresponding increase in the ratio ID/IG ratio. Similarly, they also observed that the optimum pulse number was a function of the pulse energy. Many



(a)



(b)



(c)

Figure 5.40 (a) Irradiated images at different pulse numbers, (b) Corresponding Raman spectra and (c) I_D/I_G ratios from the Raman data after Li et al.,(2014). ©Optical Society of America

researchers have highlighted similar patterns in the value of I_D/I_G relatively rapid increases and decreases in the value of I_D/I_G for a wide range of laser parameters and operational conditions. The results presented in this thesis follow a similar distribution in the values of I_D/I_G when changes are made to the laser fluence, as evidenced in Figure 5.31.

5.5.3 XPS analysis

The XPS analysis was completed at the EPSRC National Facility for XPS (Harwell XPS) and the help of Dr Mark Isaacs is gratefully acknowledged and appreciated.

The XPS analysis was completed on 8 sets of samples, each irradiated at a different fluence in the range 21.8 mJcm^{-2} to 46.0 mJcm^{-2} . The results for an original GO sample and for samples irradiated at 21.8 mJcm^{-2} , 29.1 mJcm^{-2} and 56.1 mJcm^{-2} are shown in Figures 5.41 to 5.44 respectively. The graphs have been deconvoluted to provide information about the chemical bonds in the surface of the samples. These include the sp^2 hybridised carbon-carbon bonds centred on 285.5 eV, the sp^3 hybridised carbon-carbon bonds centred on 285 eV, epoxide/hydroxyl carbon-oxygen bonds at 286.6 eV, carbonyl carbon=oxygenn bonds at 287.6 eV and carboxyl COOH at 286.6 eV. The results show that as the fluence is increased there is an increase in the sp^2 carbon hybridisation and simultaneous reduction of both the sp^3 carbon and the oxygen containing groups. Additional data for tests at other values of fluence is included in Appendix II.

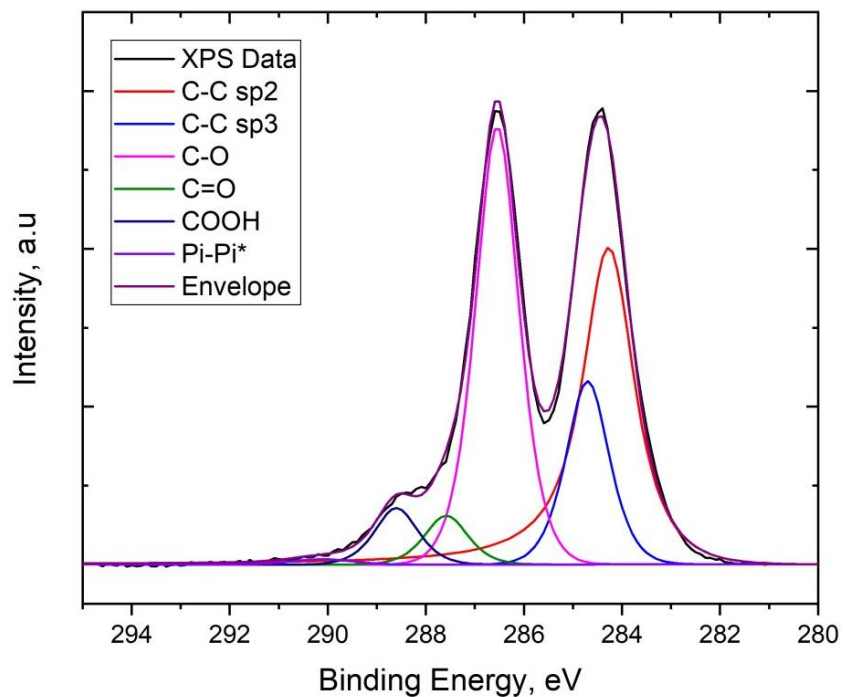


Figure 5.41 - XPS spectra of a GO sample used in the study

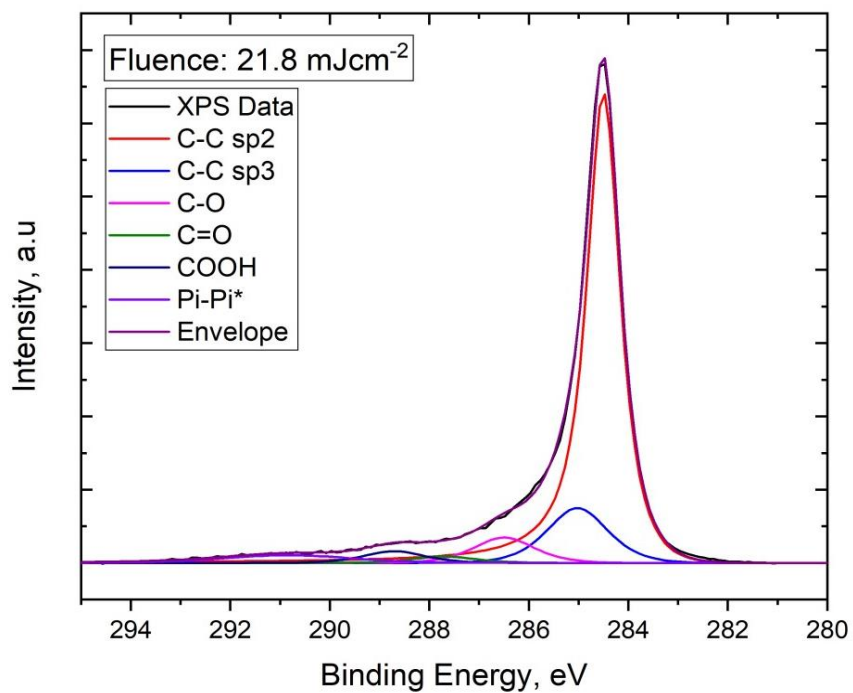


Figure 5.42 - XPS spectra of rGO after irradiation with a laser fluence of 21.8 mJcm⁻²

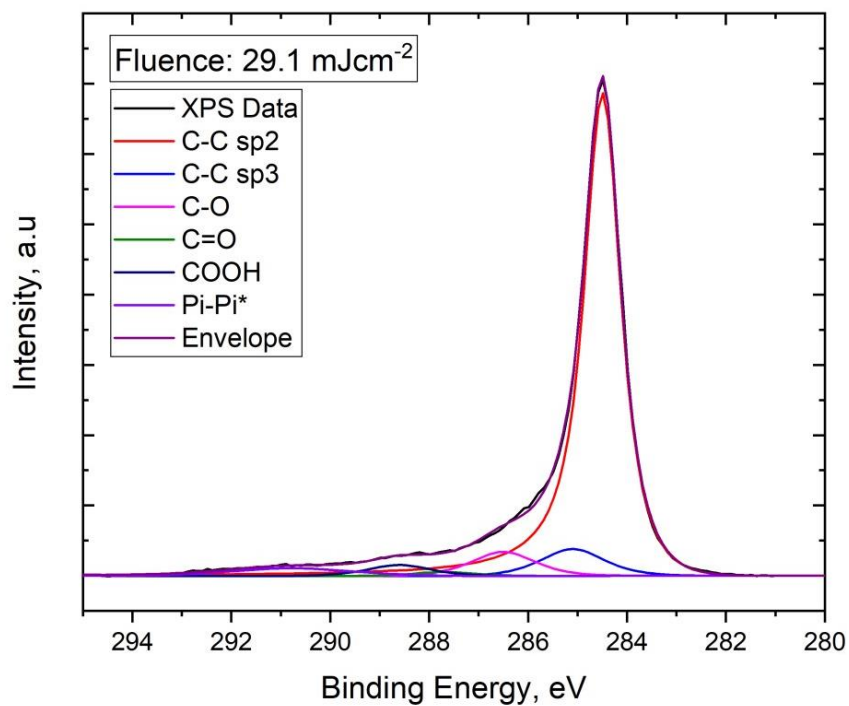


Figure 5.43 - XPS spectra of rGO after irradiation with a laser fluence of 29.1 mJcm⁻².

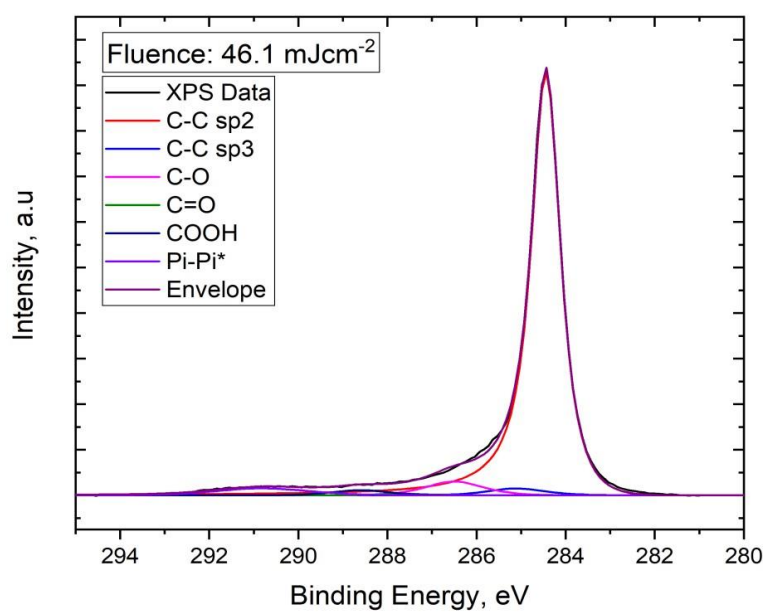


Figure 5.44 - XPS spectra of rGO after irradiation with a laser fluence of 46.1 mJcm⁻².

To illustrate the changes in more detail plots of the XPS spectra for the C-C sp^2 and C-C sp^3 along with the oxygen species O1's are shown in Figure 5.45 to 5.47 respectively. These again clearly show that as the fluence is increased there is a gradual increase in the sp^2 hybridisations and reduction in sp^3 hybridisations as well as a reduction in the oxygen containing groups.

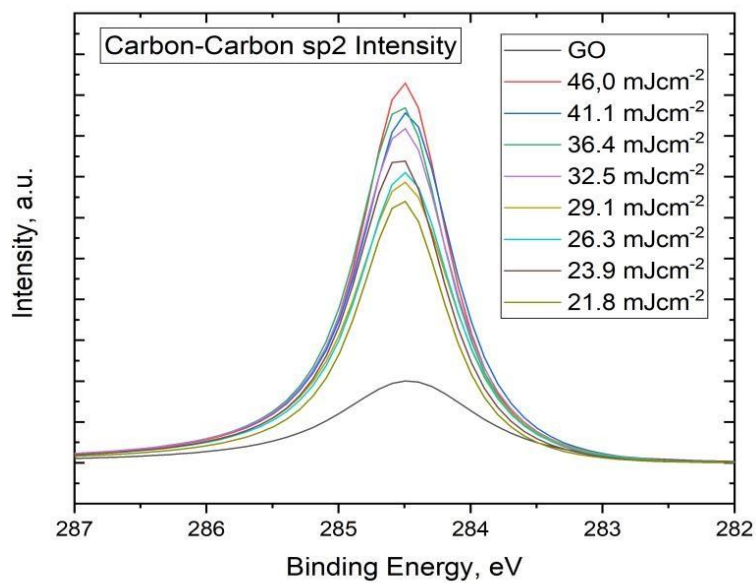


Figure 5.45 – XPS spectra of the C-C sp^2 hybridisation

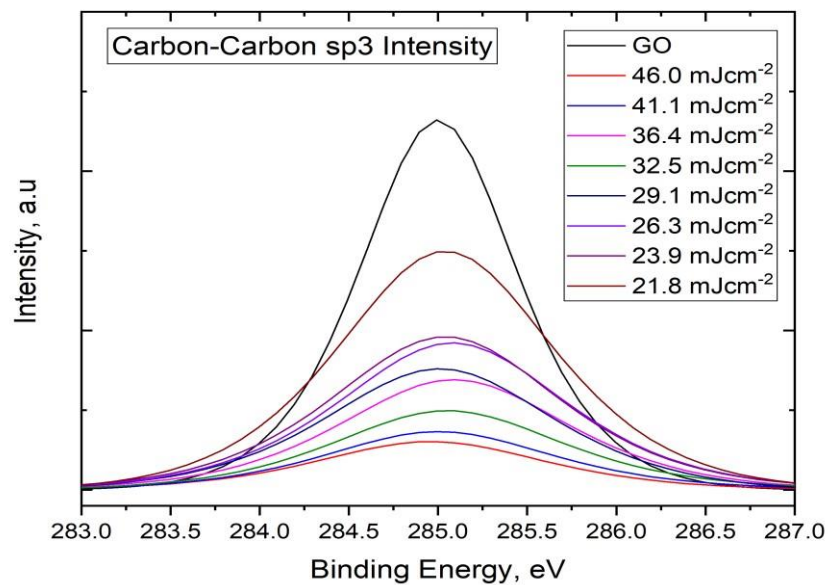


Figure 5.46 - XPS spectra of the C-C sp^3 hybridisation

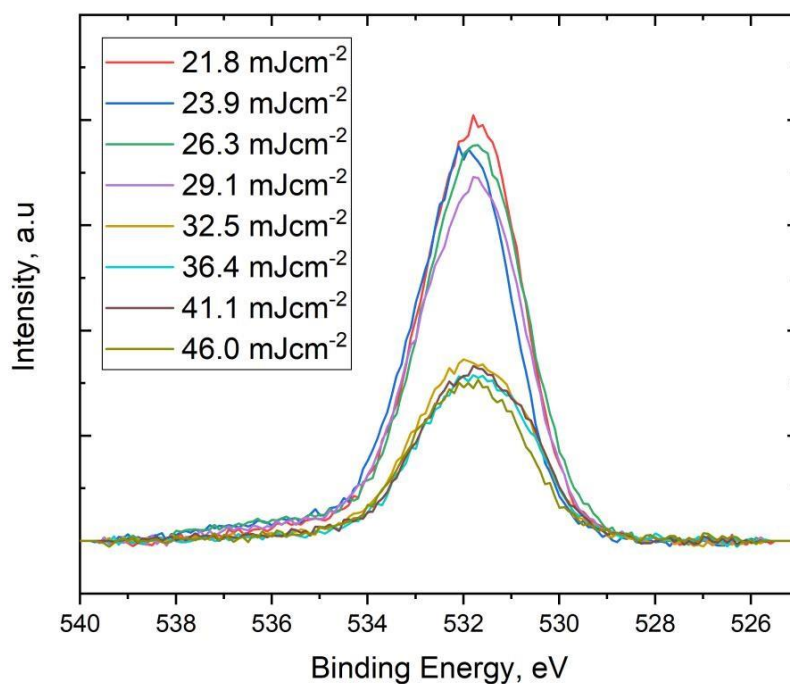


Figure 5.47 - XPS spectra of the oxygen species

Further examination of the change in the peak of the oxygen content is shown in Figure 5.48 which illustrates there is a gradual reduction in the oxygen content over the fluence range 21.8 to 29.1 after which there is a large reduction up to a fluence of ~ 35 mJcm^{-2} . At higher values of fluence the oxygen content appears to flatten out to a constant value. Figure 5.49 shows a corresponding increase in the carbon/oxygen peak ratio but with a significant increase in the range 29.1 to 36.5 mJcm^{-2} . The range of carbon oxygen peak ratio is from 3.5 at a fluence of 21.8 mJcm^{-2} to 13 at a fluence of 46.0 mJcm^{-2} . These results confirm that at a fluence in the range 30 – 35 mJcm^{-2} the degree of reduction is sufficient to transform the carbon and oxygen species with the reduced GO having graphene like characteristics. These values also illustrate that the irradiation process has removed the majority of the oxygen containing groups which confirm the results of the Raman analysis.

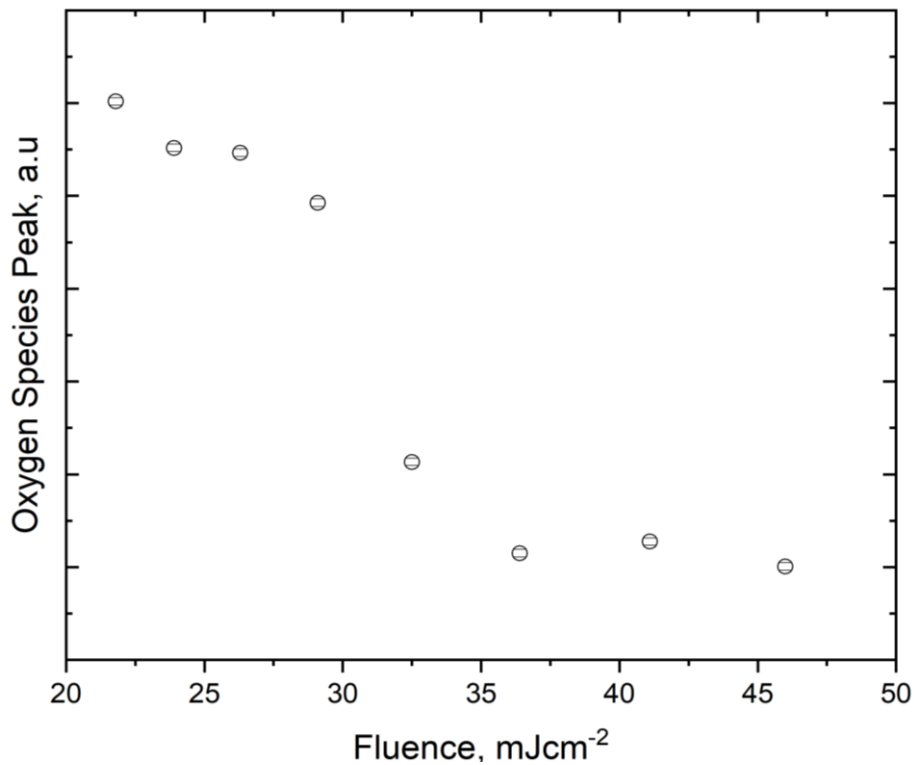


Figure 5.48 – Relationship between the oxygen species peak and fluence

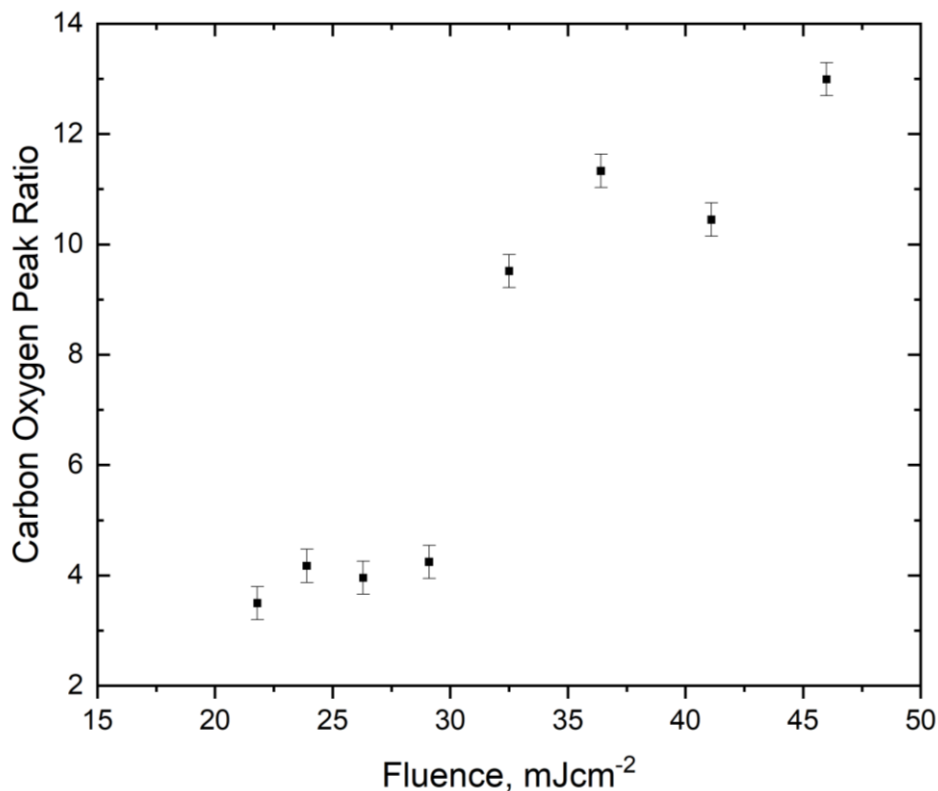


Figure 5.49 – Relationship between the Carbon/Oxygen peak ratios as a function of fluence

5.5.4 Discussion of XPS Results of Other Researchers

The literature review in Chapter 2 highlighted that a large number of researchers have used XPS in the interpretation of the chemical changes that occur when GO is irradiated. The majority of these researchers, as evidenced in Table 2.4, Chapter 2, have shown that significant changes occur in the carbon and oxygen species with an increase in the C-C species and a reduction in the oxygen species. The results presented in this thesis agree with the findings of these researchers and hence detailed descriptions of similar and repeated results have not been included in the thesis.

5.6 Results of Wettability Testing.

The background literature and description of wettability was presented in Sections 2.5.7 and 4.1.11 of the thesis. This highlighted that, in general, the wettability of a surface may be defined by the contact angle which is related to the roughness and chemical structure of the surface. To establish how the contact angle of the irradiated GO changed a series of tests were completed on samples that had been irradiated using the large area methodology at different fluences in the range 21.8 to 41.1 mJcm⁻¹. To measure the contact angle the procedure described in 4.1.11 was used whereby water droplets were dropped on top of the samples using a pipette and then measuring the contact angle of the droplet normal to the sample surface. Using a CAG 100 contact goniometer the resultant contact angle for each of the samples was recorded by the instrument manufacturers image analysis software.

The wettability tests were completed on large area irradiated samples, which were irradiated in the same way as described in Section 5.4 of the thesis. Tests were also completed at the same fluence values in the range of 21.8 to 46.0 mJcm⁻². The literature review highlighted that line spacing between the irradiated lines may be an important parameter and tests were completed for line spacings of 50 µm and 100 µm. A typical result at a fluence of 46.0 mJcm⁻² is shown in Figure 5.50 which highlights, in a similar way to tests at other values of fluence, that there was little difference in the contact angle results for different line spacing and that repeat results showed that the mean and standard deviation were 80.5 ° and 3.02 ° and 81.7 ° and 6.49 ° for the 50 µm and 100 µm spacing respectively. As the standard deviation for the 100 µm line spacing was higher a line spacing of 50 µm was selected for the series of tests to examine the relationship between the contact angle and fluence.

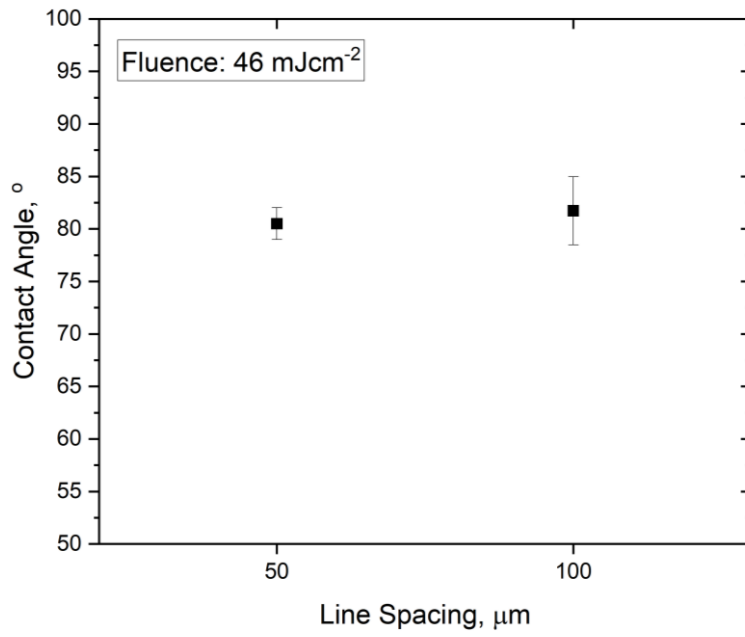


Figure 5.50 – Results of repeated tests to assess the relationship between contact angle and line spacing.

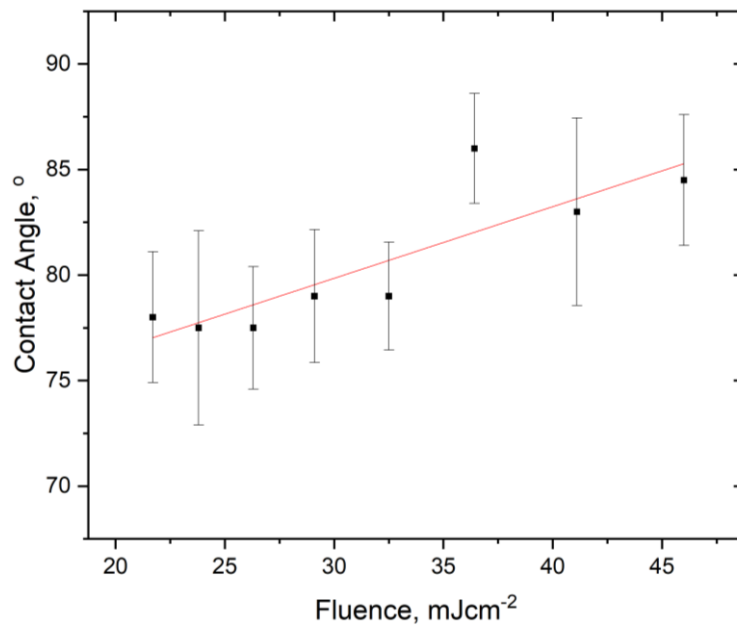


Figure 5.51 Relationship between contact angle and fluence

Measurements of the contact angle for a range of fluence values were widely spaced with values ranging from 78.0° at a fluence of 21.8 mJcm^{-2} to 84.6° at a fluence of 46 mJcm^{-2} . However, there is a general trend in the results that highlights that the contact angle increases as the laser fluence is increased. The change in contact angle with fluence, highlighted by the linear relationship shown in Figure 5.51, had a gradient of 0.34° per mJcm^{-2} .

5.6.1 Relationship Between Wettability and Surface Roughness

The literature review highlighted that the roughness of the GO surface is an important parameter in the interpretation of wettability. To assess this relationship from the experimental results reference is made to the surface roughness results presented earlier and repeated here for ease of analysis. Figure 5.52 has been reproduced here.

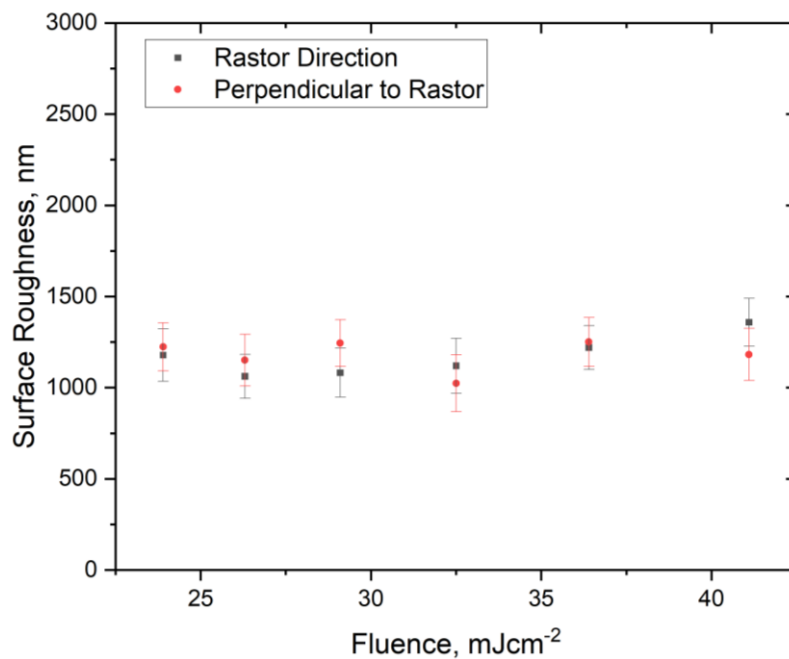


Figure 5.52 – Surface roughness of GO sample after raster irradiation showing roughness both parallel and perpendicular to the raster direction (repeat of Figure 5.37)

It was reported earlier that the results presented in Figure 5.52 confirmed that the roughness in both the horizontal and transverse directions to the raster movement was similar for all samples. It was concluded therefore that for the range of fluence used in the completed experiments, that the contact angle was independent of the surface roughness and therefore a function of other factors. The Raman spectra and XPS results confirmed a change in the chemical structure of the surface with the loss of oxygen containing groups and the conversion of sp^2 to sp^3 carbon bonds and hence it is concluded that one factor that these changes in the chemical structure are solely responsible for the change in contact angle.

5.6.2 Comparison of Wettability Results with Other Researchers

Bon *et al.*, 2011, recorded changes in contact angle from a value circa 50° for GO to 68° and 73° for rGO due to the exposure for one and three hours using Hg lamp of power 30mWcm^{-2} whilst Furio *et al.*, 2017, showed that using UV exposure the contact angle was a function of irradiation duration and resulted in a contact angle in the range 40° to 70° , and that laser scribing the UV reduced GO resulted in a further increase in the contact angle from 50° to 105° . For microwave heating reduced rGO, Rasuli *et al.*, 2015, reported an increase in the contact angle from 29.7° to 69.9° due to heating whilst Cai *et al.*, 2018, recorded the CA for rGO at 52° in ambient conditions. Hence the results in this thesis compare favourably with those of other researchers and are similar to those reported elsewhere.

The measured contact angles are low compared to other researchers who have completed biomimetic studies using two beam laser interference, for example Zhang *et al.*, 2012, and Jiang *et al.*, 2104. In these studies grids of irradiated rGO, shown in Figure 5.53 (a), are created with the result that contact angles as high as 155° may be produced for such surfaces, as recorded see Figure 5.53 (b). Hence from an rGO perspective the results in this thesis have highlighted that the fabrication of rGO materials with tunable wettability may be achieved

but in such situations the contact angles are relatively low and potentially of less value than the superhydrophobic surfaces created by others.

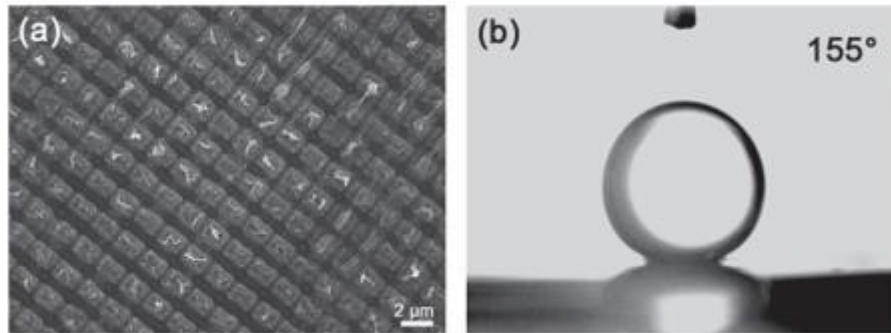


Figure 5.53 (a) Superhydrophobic grid surface and (b) resultant contact angle after Jiang et al., 2014. ©WILEY (2018)

5.7 Results of Temperature Modelling

5.7.1 Results from Model Predictions of Temperature

The basis of the theory used in the temperature modelling phase of the research was presented in Section 3.2 and a Mathcad model was used to solve the governing equation shown as equation 3.13, after Yakovlev *et al.*, 2019. The parameter values used in the model were also presented in Chapter 3 and solution of equation 3.31 showed that the influence in temperature of the overlapping pulses was minimal as the pulse duration, shown by the red dotted line on Figure 5.54 was significantly less than the repetition frequency of the laser pulses with the result that the surface was allowed to cool between pulses.

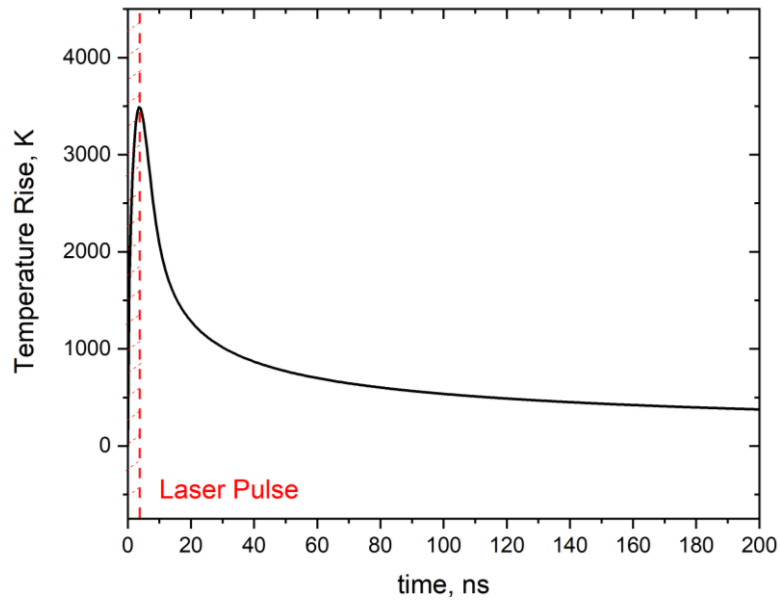


Figure 5.54 Predicted temperature on the surface of the GO with 1064 nm wavelength, 4.6 ns pulse duration and 10 kHz repetition frequency

Figure 5.55 highlights that the peak temperature at the centre of the laser beam may reach a value circa 3300 °C as a result of the high intensity of the Gaussian laser beam at the centre of the beam which rapidly diminishes with distance away from the centre of the beam. The results of tests by the author, shown in Figure 5.9, highlighted that the reduction of the GO used in the study occurred at a temperature of 210 °C. By examination of the temperature distribution from the theoretical predictions there is a rapid reduction in temperature to a value of circa 200 °C at a distance of 1.3 mm in z. Using the z-scan results from the experimental study the boundary of the z-scan, which defines the damage threshold which occurs at a temperature of 210 °C, the corresponding position on the z-scan at the boundary of reduction occurred at a z distance of 1.2 mm. This shows excellent agreement with the theoretical predictions.

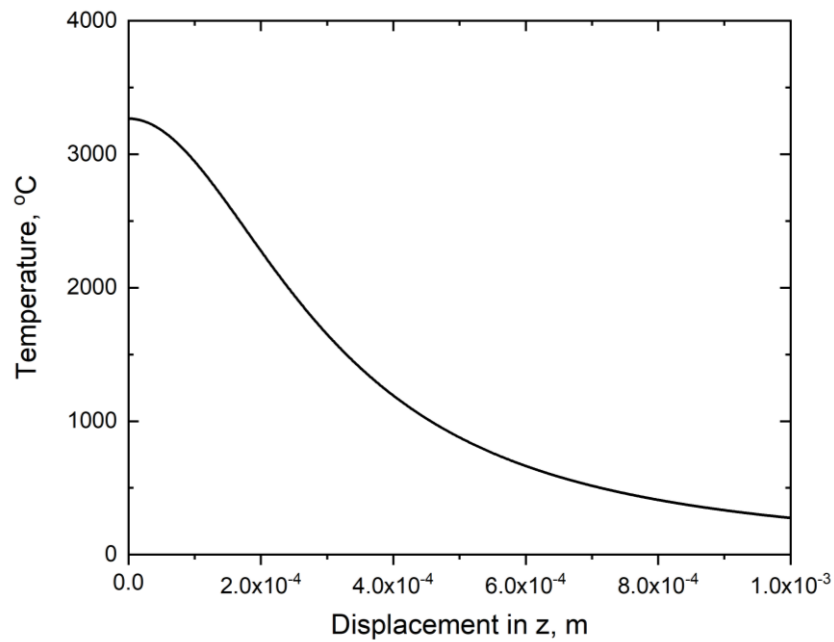


Figure 5.55 Distribution of temperature in the z-direction on the centreline of the sample

5.7.2 Review of Temperature Modelling Outputs Identified in the Literature

A Finite Element Model (FEM) was used to predict the temperature distribution due to irradiation of a GO layer on a PET substrate by Kymakis *et al.*, 2013. Simulations were completed for 100 spot pulses of 20 ns at a fluence of 17.5 mJ/cm² on a 20.1 nm thick GO film on PET. The model was developed to provide a better understanding of the heat absorption and thermal effects within the layer and down to the PET substrate. The temperature distribution was predicted for longitudinal distance (z axis) from the spot centre and vertically from the GO surface downwards. The dynamics of laser heating was considered as a typical three-dimensional heat-flow problem, which was simulated by the solution of the heat conduction equation.

The initial temperature of the surface was 20 °C and the incident laser heat flux was applied on the top surface of GO thin film. The film thickness was 20.1 nm and the PET layer thickness

9 μm . The resultant temperature distribution, effectively through the PET layer, is shown in Figure 5.56.

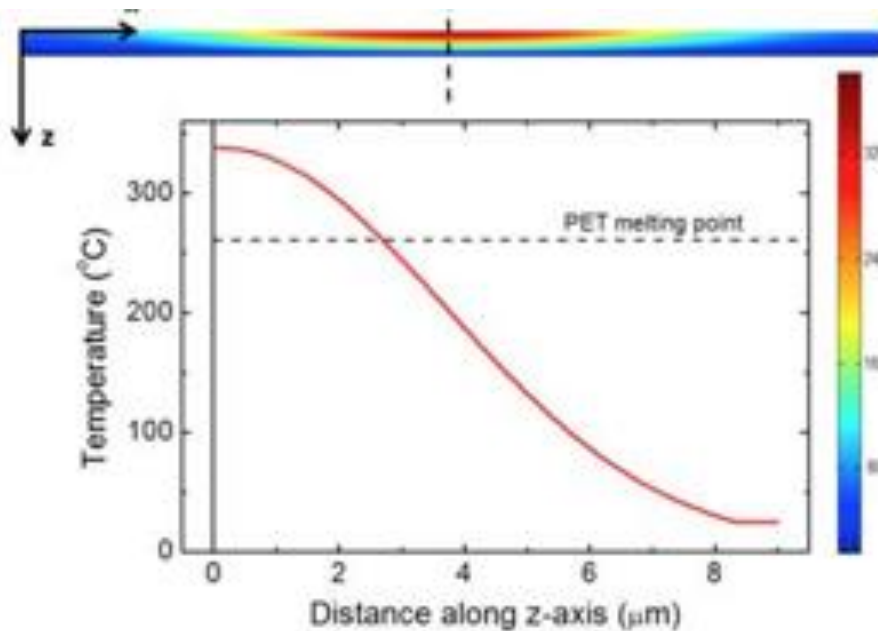


Figure 5.56 Predicted temperature distribution in a GO layer on a PET substrate, after Kymakis et al., 2013 ©Elsevier.

The temperature on the GO surface was circa 340°C and was observed to decrease through the depth of the layer. It is known that the removal of the oxygen containing groups from GO occurs at a temperature in the region of $200^{\circ}\text{C} - 230^{\circ}\text{C}$ and hence, from Figure 5.56, it is shown that this value would have been exceeded over a large area of the surface. Similarly, the temperature decay with depth (z-direction) would indicate that the PET substrate would also experience temperatures in excess of its melting point, circa 250°C , suggesting damage. No damage was observed and Kymakis et al., concluded that the numerical model over-predicted the temperature distribution and that the irradiation of GO may be considered as ablation/oxidation of the topmost layers and photothermal reduction by deoxygenation of the oxygen groups in the lower layers.

A similar FEM model was developed by Zhou *et al.*, 2010, to describe the heat transfer processes as a result of irradiation of a different number of GO layers. A continuous wave diode laser (wavelength 663nm, maximum output power of 80mW ($3.4 \times 10^9 \text{ Wm}^{-2}$ laser density at the sample surface), scan rate $15\mu\text{ms}^{-1}$ and beam diameter $3\mu\text{m}$) was used and the theoretical predictions were made by the solution of the heat conduction equations. In ambient conditions the energy losses due to radiation and convection were considered negligible and the surface of GO thin films was assumed adiabatic.

Results shown in Figure 5.57 show that the temperature at the surface was increased as a function of the number of layers with a temperature in excess of 500°C with 6 layers whilst for a single layer the predicted temperature was reduced to less than 100°C . These results were consistent with the experimental findings with the reduction of GO being very much layer thickness dependent.

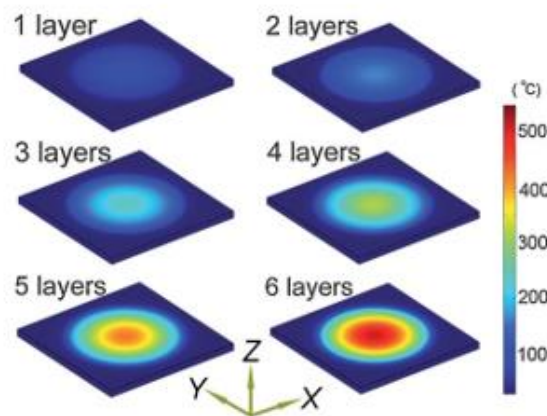


Figure 5.57 Predicted temperature distribution as a function of the number of GO layers, after Zhou *et al.*, 2010 ©WILEY (2018)

Solution of the heat transfer equation to estimate the temperature at the focal point of an ns fibre pulsed infrared laser of wavelength $1064\mu\text{m}$ was reported by Evlashin *et.al.*, 2018. The Beer Lambert law was used to describe the laser intensity distribution through the depth, and they predicted that the temperature increase corresponding to one pulse was 226K and

after 2 pulses was 700 K. This temperature is above the threshold for GO reduction and resulted in changes in the morphological properties of the surface and the absorption and heat transfer coefficients. Predicted radial profiles of temperature change are shown in Figure 5.58. This figure highlights that the temperature change is very much a function of the radial distance and that maximum temperatures of 2000 K were predicted. It was anticipated that the maximum achievable temperature at the centre of the laser beam would be in excess of this value and that an increase in temperature would occur due to the changes in the absorption of the laser power and heat transfer within the GO film leading to significant

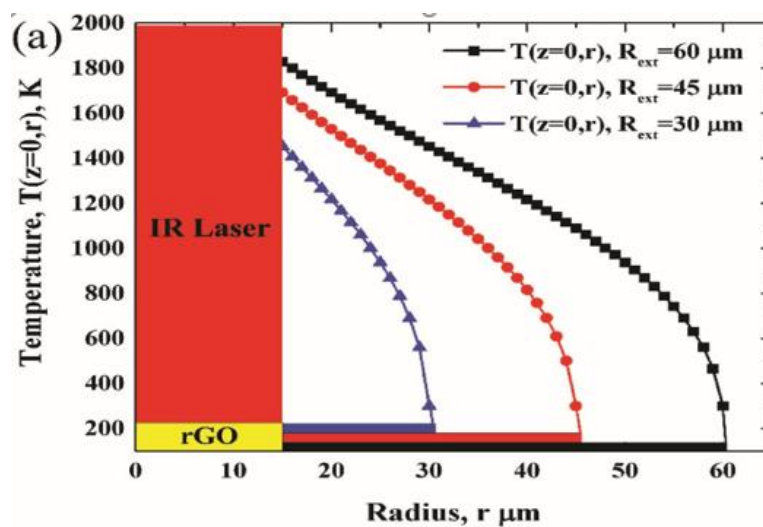


Figure 5.58 Temperature predictions in GO as a function of the radius from the laser beam centre, after Evlashin et al., 2018, © WILEY (2018)

temperature increase in the carbon structures. These predictions are supported by the mathematical modelling of the author.

Further, Evlashin et al., 2018, used Planck's radiation formula and showed that an increase in temperature to ≈ 3800 K, improved the quality of the rGO. They concluded that the complexities of modelling the temperature changes in laser reduced graphene oxide was extremely complex but that, with significant assumption, they were able to confirm that the

quality of the reduction process was a function of temperature and that predicted temperatures as high as circa 3800 Kelvin resulted in the production of high quality reduced GO.

The COMSOL Multiphysics software was used by Trusovas et al., 2013, to simulate the temperature distribution in a GO layer irradiated with a pulsed Gaussian beam of wavelength 1064 nm with changes to the mean laser power (pulse energy) and scanning speed (overlapping dose). They reported that the resultant change in temperature could be effectively described in terms of the product of pulse energy μJ x dose μJ . Simulations were completed with a 1200nm thick GO layer. The temperature distributions were calculated at the central point of the laser pulses for different depths into the layer. The simulated temperatures through the depth of the layer following one pulse is shown in 5.59.

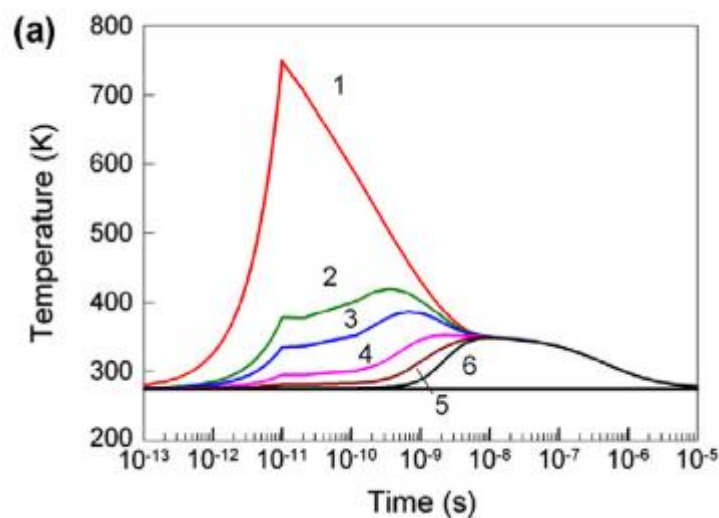


Figure 5.59 Temperature predictions in GO at a power of 50 mW highlighting the changes through the layer depth (1) representing the surface and (6) at 1200 nm. Trusovas et al., (2013) ©Elsevier

Figure 5.59 shows the highest simulated temperature corresponding to an input power of 50 mW is greater than 1400 K. Following the peak, the temperature is rapidly reduced from the

surface into the layer. Importantly, these simulations were conducted at a 100 kHz pulse repetition rate and the time interval between two pulses was longer than the graphene temperature settling through the depth. Therefore, the cooling time of the GO sheet was shorter than the interval between pulses. Thus, it was concluded that the accumulation of the heat between laser pulses was not present and hence the GO surface was heated to over 1400 °C during each pulse of the laser treatment. The modelling work of the author also confirmed the relationship between pulse duration and laser repetition rate is of significant importance.

Overall, the above results confirm that there is a wide range in the predicted surface temperature and of the way changes in temperature occur in both the radial direction from the laser beam centre and down into the thickness of the layer. The results of most studies highlight that the results are a function of the primary input variables and hence much further research would complement these existing findings.

5.8 Summary Comment Related to the Research of Others

In summary it is clear that a large number of researchers have been active in the laser reduction of graphene. In general, there is good agreement between the results presented in this thesis and that previously reported by other researchers. The overall findings of the research are summarised in the conclusions presented in the next chapter.

Chapter 6: Conclusions and Further Work

In recent years considerable research focus has been directed to graphene like materials that display properties that are similar to the excellent physical, chemical and mechanical characteristics of graphene. In this respect, one major research area is the reduction of graphene oxide (GO) and especially the laser reduction of graphene oxide. The research in this thesis has completed an experimental study of the properties and characteristics of laser reduced graphene oxide (rGO) using an Nd:YVO₄ laser with wavelength 1064nm, with a view to finding the optimum graphene like properties. These findings have been compared, with some success, to theoretical predictions.

The quality of the rGO, usually expressed in terms of the 'degree of reduction from no damage through to complete ablation', is a function of the characteristics of the GO and the type and mode of operation of the laser. Common analysis techniques to quantify the degree of reduction include an evaluation of the physical surface characteristics (profile, roughness, Scanning Electron Microscopy), electrical properties (conductivity) and changes in the chemical structure (Raman Spectroscopy, X-Ray Photoelectron Spectroscopy). These techniques together with recorded changes in wettability were used in the thesis.

Important laser variables include laser wavelength, power, pulse duration, repetition frequency and scanning speed. Commonly the laser fluence, defined as the laser energy per unit area on the surface has been used, and this is the case in this thesis.

An extensive volume of research has been reviewed which has highlighted that laser reduced GO has exceptional potential applications in electronics and ophthalmics. Each application requires the reduced GO to have a specific quality and characteristics. To find such characteristics most researchers have completed a large number of tests where the governing variables are systematically and incrementally changed. For example, Evlashin et al., 2018,

completed over 8000 individual tests. Such tests are time consuming and expensive. The concept of the thesis was to develop an experimental system in such a way that the same optimum information may be derived from a single test.

Hence, the primary aim of the thesis was to develop, construct and test an experimental system to create laser reduced graphene oxide films that encompassed the complete range of reduction, from no damage at the threshold fluence to complete ablation, in one experiment. This was successfully completed, and the resultant pattern of reduction was termed a 'z-scan'. This was achieved by simultaneously moving the sample through the laser beam in both the horizontal and vertical directions. Theoretical predictions of the z-scan pattern have been made and good agreement was observed between the experimental and theoretical predictions of the fluence at the boundary of the z-scan pattern. This defines the damage threshold, i.e. the fluence at which damage first occurs and the fluence at this threshold was 13.8 mJcm^{-2} .

A major feature of the z-scan was that significant changes to the surface profile and thickness of the GO layer were observed at different fluence values. These involved transverse sections across the z-scan having both expanded and sunken depths as a function of laser fluence. Other researchers also observed such phenomena with significant similarities. These were explained in terms of different zones of reduction as a function of the laser fluence. Two reduction mechanisms were identified as important: the conversion of the sp^3 to sp^2 carbon and the reduction of oxygen.

To further refine the importance of laser fluence the range of fluence values derived from the z-scan experiments were used to create a series of large area samples of irradiated GO. Tests at 6 individual values of fluence were used. These were created by positioning the focal point of the laser beam at different vertical heights above the GO surface and moving the beam over the surface using controlled forward and backward raster movement.

The roughness of these irradiated large area samples was enhanced by an order of magnitude when compared to that measured for GO but the roughness of the large area irradiated surfaces in both the direction of the raster and perpendicular to the raster did not show any significant change or trend.

The conductivity of the irradiated sample was shown to increase with increase in laser fluence in an almost linear way. This highlights an increase in reduction which was attributed the conversion of sp^3 to sp^2 carbon bonds and the loss of oxygen containing groups.

To better clarify the degree of reduction, analysis was completed using Raman spectroscopy and XPS. The Raman spectra demonstrated the usual D, G and 2D peaks and, in line with other researchers the reduction was interpreted by the ID/IG and I2D/IG ratios. As fluence was increased the relationship between the ID/IG ratio had an overall downward trend in the range 1.21 to 0.7 but could be classified into three regions as a function of the loss of oxygen containing groups, the conversion of sp^3 to sp^2 carbon bonds and a subsequent zone where the ratio remained constant at a minimum value of 0.7. This occurred at a fluence circa 35 mJcm^{-2} and the results suggest that for the particular GO samples and the experimental conditions used in the study, this value of fluence describes the fluence at which the rGO first achieves its optimum value. Examination of the I2D/IG ratio showed that there was a gradual increase from a value of 0.23 to 0.31 but in this case with a saturation value at a fluence circa 32 mJcm^{-2} . Hence it was concluded that the z-scan methodology creates an easily identifiable range in fluence that creates the optimal range of the degree of reduction, from zero damage to full ablation, and that at a fluence in the range 32 mJcm^{-2} to 35 mJcm^{-2} the optimum reduction for this setup is achieved.

Similarly, the XPS results recorded a significant change in the carbon and oxygen species in the GO and rGO. The oxygen content was shown to reduce significantly at a fluence of $\sim 35 \text{ mJcm}^{-2}$ with a flattening off at higher values of fluence to a constant value. A corresponding

increase in the C-C carbon occurred and the carbon/oxygen peak ratio increased significantly over the fluence range 29.1 mJcm⁻² to 36.5 mJcm⁻² with an overall increase in the ratio from 3.5 at a fluence of 21.8 mJcm⁻² to 13 at a fluence of 46.0 mJcm⁻². These results confirm that at a fluence in the range 30 – 35 mJcm⁻² the degree of reduction is sufficient to transform the carbon and oxygen species with the reduced GO having graphene like characteristics.

The relationship between temperature, timescale and chemical processes is clearly not yet fully understood. It would therefore be extremely helpful to develop in situ technologies to monitor the live changes in the temperature and chemical status as a sample is irradiated. Of particular interest, would be the impact of a pulsed laser system whereby the system could be monitored in real time.

Temperature changes were also identified as a major factor to influence the reduction process and a temperature model, based on the theory of Yakovlev et al., 2019, has been described. Application of the theory showed that the short pulse duration allowed the surface to cool between pulses but that the application of a laser beam with Gaussian distribution was observed to create significantly high values at the centre of the beam, as reported by Arul et al., 2019 and Trusovas et al., 2013. There was a rapid reduction in temperature in a radial direction away from the centre. The results of the thesis study have shown that the GO first reduced at a temperature of 210 °C which corresponds to the temperature at which the surface of the z-scan should show first signs of damage. Hence a comparison was made with the location of the boundary of the z-scan corresponding to the damage threshold and the position of the predicted temperature at 210 °C. Good agreement was observed. Subsequently, the temperature model showed that there was a rapid reduction of temperature from the surface down into the GO layer and this was attributed to changes in the absorption and heat transfer processes described in the model. Here the research completed by the author together with that of other researchers has identified that there is

considerable scope for further work to refine the understanding of the behaviour of temperature in the reduction process.

Tests were also completed to establish the wettability of the irradiated surface and it was observed that the wettability contact angle increased with increase in laser fluence. Values increased in an almost linear way, but values increased from 46 ° for GO to a maximum value of 84 ° for the rGO. These values compare well with the results of other researcher who have used similar irradiated surfaces but the improvements of wettability are small compared to those obtained using two beam laser interference, see Jiang et al., 2014, who achieved contact angle values of circa 155 °. What is important however is that the wettability is known to be a function of the surface roughness and the chemical composition of the surface. In this study it was shown that the contact angle was independent of roughness and hence the increases in contact angle observed for increases in laser fluence must be attributed to the changes in the chemistry of the surface. Hence there is a direct relationship between the wettability results and those obtained using Raman spectroscopy and XPS. For optimum reduction, based on the outputs of the surface chemistry analysis that identified a fluence in the range 32 mJcm⁻² to 36 mJcm⁻² the corresponding contact angle was circa 80 °.

In summary it was concluded that the experimental facility developed as part of this thesis was successfully used to create a one-step z-scan methodology. This technique provided an efficient and reliable one-step technique to establish the optimum range of laser fluence to create good quality rGO, supported by physical, electrical and chemical analysis of the results. Hence it is recommended that the z-scan approach could be adopted by other researchers to minimise the need for a large number of time consuming and expensive experiments to quickly obtain details of the important and optimum parameters for GO reduction.

References

- Allen M J., Tung V C and Kaner R B. (2010). *Honeycomb carbon: a review of graphene*. Chem. Rev., 110, 132–145.
- Arnaud J A. (1976). *Gaussian Beams*, In *Beam and Fiber Optics*, Academic Press, 50-161, doi: 10.1016/B978-0-12-063250-3.50008-0.
- Arul R., Reece N., Oosterbeek R N., Robertson J., Xu G., Jin J and Simpson M C. (2016). *The mechanism of direct laser writing of graphene features into graphene oxide films involves photoreduction and thermally assisted structural rearrangement*. Carbon, 99, 423–431. doi: 10.1016/j.carbon.2015.12.038.
- Bechtel J H. (1975). *Heating of Solid Targets with Laser Pulses*. Journal of Applied Physics, 46, 1585.
- Bi Y G., Feng J., Li Y F., Zhang Y L., Liu Y S., Chen L., Liu Y F., Guo L., Wei S and Sun H B. (2014). *Arbitrary Shape Designable Microscale Organic Light-Emitting Devices by Using Femtosecond Laser Reduced Graphene Oxide as a Patterned Electrode*. ACS Photonics, 2014, 1, 690–695. doi: 10.1021/ph500106f.
- Bhattacharjya D., Kim C H., Kim J H., You I K., In J B and Lee S M. (2018). *Fast and controllable reduction of graphene oxide by low cost CO₂ laser for supercapacitor application*. Applied Surface Science, 462, (2018), 353–361. doi: 10.1016/j.apsusc.2018.08.089.
- Bobrinetskiy I I., Emelianov A V., Smagulova S A., Komarov I A., Otero N and Romero P A. (2017). *Laser direct 3D patterning and reduction of graphene oxide film on polymer substrate*. Materials Letters, 187, (2017), 20–23.
- Bon S B., Piccinini M., Mariani A., Kenny J M and Valentini L. (2011). *Wettability and switching of electrical conductivity in UV irradiated graphene oxide films*. Diamond and Related Mater., 20, 871-874. doi: 10.1016/j.diamond.2011.04.013
- Cancado L G., Takai K., Enoki T., Endo E., Kim Y A., Mizusaki H., Jorio A., Coelho L N., Pantlago R and Pimenta M A. (2006). *General equation for the determination of the crystallite size L_a of nanographite by Raman spectroscopy*. Appl. Phys. Lett., 88, 3106-3109.
- Cancado L G., Jorio A., Martins Ferreira E H., Stavale F., Achete C A., Capaz R B., Moutinho M V O., Lombardo A., Kulmala T S and Ferrari A C. (2011). *Quantifying Defects in Graphene via Raman Spectroscopy at Different Excitation Energies*. Nano Lett., 11, 3190-3196. doi 10.1021/nl201432g.
- Chen X D., Liu Z B., Zheng C Y., Xing F., Yan X Q., Chen Y and Tian J G. (2013). *High quality and efficient transfer of large-area graphene films onto different substrates*. Carbon, 56, 271-278. doi: 10.1016/j.carbon.2013.01.011.
- Chen H Y., Han D D., Tian Y., Shao R Q and Wei S. (2014). *Mask-free and programmable patterning of graphene by ultrafast laser direct writing*. Chem. Phys., 430, (2014), pp. 13-17.
- Cote L J., Cruz-Silva R and Huang J X. (2009). J. Am. Chem. Soc., 131, 11027–11032.

Das, S R., Nian, Q., Cargill, A A., Hondred, J A., Ding, S., Saei, M., Cheng G J and Claussen J C. (2016). *3D nanostructured inkjet printed graphene via UV-pulsed laser irradiation enables paper-based electronics and electrochemical devices*. *Nanoscale*, 2016, 8, 15870. doi: 10.1039/c6nr04310k.

Deng N Q., Tian H., Ju Z Y., Zhao H M., Li C., Mohammad A M., Tao L Q., Pang Y., Wang X F., Zhang T Y., Yang Y and Ren T L. (2016). *Tunable graphene oxide reduction and graphene patterning at room temperature on arbitrary substrates*. *Carbon*, 109, (2016), 173-181. doi: 10.1016/j.carbon.2016.08.005.

Diez Betriu X., Alvarez Garcia S., Botas C., Alvarez P., Sanchez Marcos J., Prieto C., Menendez R and de Andres A. (2013). *Reduction mechanisms and optimization of conductivity in graphene oxide thin films*. *J. Mater. Chem., C*, 2013, 1, 6905. doi 10.1039/c3tc31124d.

Eigler S., Dotzer C and Hirsch A. (2012) *Visualization of defect densities in reduced graphene oxide*. *Carbon*, 50, 3666–3673.

Eda G., Fanchini G and Chhowalla M. (2008). *Large-Area Ultrathin Films of Reduced Graphene Oxide as a Transparent and Flexible Electronic Material*. *Nat. Nanotechnol.*, 3, 270–274.

Eda G and Chhowalla M. (2010). *Chemically derived graphene oxide: Towards large-area thin-film electronics and optoelectronics*. *Adv. Mater.*, 22, 2392–2415..

El-Kady M F., Strong V., Dubin S and Kaner R B. (2012). *Laser Scribing of High-Performance and Flexible Graphene-Based Electrochemical Capacitors*. *Science*, Vol 335, March 2012, 1326–1330. doi: 10.1126/science.1216744.

El-Kady M F and Kaner R B. (2013). *Scalable fabrication of high-power graphene micro-supercapacitors for flexible and on-chip energy storage*. *Nature Communications*, 4, 1475. doi: 10.1038/ncomms2446.

El-Kady M F and Kaner R B. (2014). *Direct Laser Writing of Graphene Electronics*, *ACS Nano*, 2014, 8 (9), 8725-8729. doi: 10.1021/nn504946k.

Evlashin S., Dyakonov P., Khmel'nitsky R., Dagesyan S., Klokov A., Sharkov A., Timashev P., Minaeva S., Maslakov K., Svyakhovskiy S and Suetin N V. (2016). *Controllable Laser Reduction of Graphene Oxide Films for Photoelectronic Applications*. *ACS Appl. Mater. Interfaces*, 2016, 8, 28880–28887. doi: 10.1021/acsami.6b10145.

Evlashin S., Svyakhovskiy S E., Fedorov F S., Mankelevich Y A., Dyakonov P V., Minaev N V., Dagesyan S A., Maslakov K I., Khmel'nitsky R A., Suetin N V., Akhatov I S and Nasibulin A G. (2018). *Ambient Condition Production of High Quality Graphene Oxide*. *Adv. Mater. Interfaces*, 2018, 1800737. doi: 10.1002/admi.201800737.

Ferrari A C., Meyer J C., Scardaci V., Casiraghi C., Lazzeri M., Mauri F., Piscanec S., Jiang D., Novoselov K S., Roth S and Geim A K. (2006). *Raman Spectrum of Graphene and Graphene Layers*. *Phys. Rev. Lett.*, 97, 187401.

Ferrari A C. (2007). *Raman spectroscopy of graphene and graphite: Disorder, electron phonon coupling, doping and nonadiabatic effects*. *Solid State Comms.*, 143, 47.

Ferrari A C and Basko D M. (2013). *Raman spectroscopy as a versatile tool for studying the properties of graphene*. *Nature Nanotechnology*, Vol 8, April. doi: 10.1038/NNANO.2013.46.

- Florian C., Skoulas E., Puerto D., Mimidis A., Stratakis E., Solis J and Siegel J. (2018). *Controlling the wettability of steel surfaces processed with femtosecond laser pulses*. ACS Appl. Mater. Interfaces, 10, 42, 36564–36571.
- Furio A., Landi G., Altavilla C., Sofia D., Iannace S., Sorrentino A and Neitzert H C. (2017). *Light irradiation tuning of surface wettability, optical, and electrical properties of graphene oxide thin films*. Nanotechnology, 28. doi 10.1088/1361-6528/28/5/054003.
- Gao X., Jang J and Nagase S. (2009). *Hydrazine and thermal reduction of graphene oxide: Reaction mechanisms, product structures, and reaction design*. J. Phys. Chem., C, 114, 2, 832–842.
- Gao W., Singh N., Song L., Liu Z., Reddy A L M., Ci L., Vajtai R., Zhang Q., Wei B and Ajayan P M. (2011). *Direct laser writing of micro supercapacitors on hydrated graphite oxide films*. Nat. Nanotechnol., 2011. 6. 496-500. doi: 10.1038/NNANO.2011.110.
- Ghadim E E., Rashidi N., Kimiagar S., Akhavan O., Manouchehri F and Ghaden E. (2014). *Pulsed laser irradiation for environment friendly reduction of graphene oxide suspensions*. Applied Surface Science, 301, 183-188. doi: 10.1016/j.apsusc.2014.02.036.
- Ghoniem E., Mori S and Abdel-Moniem. (2016). *Low cost flexible supercapacitors based on laser reduced graphene oxide supported on polyethylene terephthalate substrate*. J. Power Sources, 324, 272 – 281. doi: 10.1016/j.jpowsour.2016.05.069.
- Geim A K and Novoselov K S. (2007). *The rise of graphene*. Nat. Mater., 6, 183–191.
- Guan Y C., Fang Y W., Lim G C., Zheng H Y and Hong M H. (2016). *Fabrication of laser-reduced graphene oxide in liquid nitrogen environment*. Sci. Rep., 6, 28913.
- Guo L., Shao R Q., Zhang Y L., Jiang H B., Li X B., Xie S Y., Xu B B., Chen Q D., Song J F and Sun H B. (2012a). *Bandgap tailoring and synchronous microdevices patterning of graphene oxides*. J. Phys. Chem., C, 2012, 116, 3594.
- Guo L., Jiang H B., Shao R Q., Zhang Y L., Xie S Y., Wang J N., Li X B., Jiang F., Chen Q D., Zhang T and Sun H B. (2012b). *Two-beam-laser interference mediated reduction, patterning and nanostructuring of graphene oxide for the production of a flexible humidity sensing device*. Carbon, 50 (4) (2012), pp. 1667-1673.
- Guo L., Zhang Y L., Han D D., Jiang H B., Wang D., Li X B., Xia H., Feng J., Chen Q D and Sun H B. (2014). *Laser-Mediated Programmable N Doping and Simultaneous Reduction of Graphene Oxides*. Adv. Optical Mater., 2, 120–125. doi: 10.1002/adom.201300401.
- Han D D., Zhang Y L., Liu Y., Liu Y Q., Jiang H B., Han B., Fu X Y., Ding H., Xu H L and Sun H B. (2015). *Bioinspired Graphene Actuators Prepared by Unilateral UV Irradiation of Graphene Oxide Papers*. Advanced Functional Materials, 25(28), 4548–4557. doi: 10.1002/adfm.201501511.
- He Y., Zhu L., Liu Y., Ma J N., Han D D., Jiang H B., Han B., Ding H and Zhang Y L. (2016). *Femtosecond Laser Direct Writing of Flexible All-Reduced Graphene Oxide FET*. IEEE Photonics Technology Letters, 1041-1135, 2016. doi: 10.1109/LPT.2016.2574746.
- Huang L., Liu Y., Ji L C., Xie Y Q., Wang T and Shi W Z. (2011). *Pulsed laser assisted reduction of graphene oxide*. Carbon, 49 (7) (2011), 2431-2436. doi: 10.1016/j.carbon.2011.01.067.

Ibrahim K H., Irannejad M., Hajialamdari M., Ramadhan A., Musselman K P., Sanderson J and Javus M. (2016). *A novel femtosecond laser-assisted method for the synthesis of reduced graphene oxide gels and thin films with tunable properties*, Adv. Mater. Interfaces, 3, (14), (2016), 1500864.

Jang H., Park Y J., Chen X., Das T., Kim M S and Ahn J H. (2016). *Graphene-based flexible and stretchable electronics*. Adv. Mater., 28, 4184–4202

Jiang H B., Zhang Y L., Han D D., Xia H., Feng J., Chen Q D., Hong Z R and Sun H B. (2014). *Bioinspired Fabrication of Superhydrophobic Graphene Films by Two-Beam Laser Interference*. Adv. Funct. Mater., 2014, 24, 4595–4602. doi: 10.1002/adfm.201400296.

Ju H M., Huh S H., Choi S H and Lee H L. (2010). *Structures of thermally and chemically reduced graphene*. Mat. Lett., 64, 3, 357-360.

Kang S Y., Evans C C., Shukla S., Reshef O and Mazur E. (2018). *Patterning and reduction of graphene oxide using femtosecond-laser irradiation*. Optics and Laser Technology, 103, (2018), 340–345.

Kang J., Shin D., Bae S and Hong B H. (2012). *Graphene transfer: key for applications*. Nanoscale, 4, 5527. doi: 10.1039/c2nr31317k.

Komarov I A., Struchkov N S., Levin D D., Silakov G O., Danelyan E E., Orlov M A., Schervin S N., Bogachev V V and Lagodenko N K. (2019). *Laser reduction of graphene oxide thin films for nanoelectronic application*. Proc. Int. Conf. on Micro and Nano-Electronics, 2018, Vol110221A. doi: 10.1117/12.2521802

Konios D., Petridis C., Kakavelakis G., Sygletou M., Savva K., Stratakis E and Kymakis E. (2015). *Reduced Graphene Oxide Micromesh Electrodes for Large Area, Flexible, Organic Photovoltaic Devices*. Adv. Funct. Mater. 2015. doi: 10.1002/adfm.201404046.

Konios D., Kakavelakis G., Petridis C., Savva K., Stratakis E and Kymakis E. (2016) *High efficient organic photovoltaic devices utilizing work-function tuned graphene oxide derivatives as the anode and cathode charge extraction layer*. **J. Mater. Chem., A**, 3, 21428-21433. doi: 10.1039/C5TA06096F.

Kudin K N., Ozbas B., Schniepp H C., Prud'homme R K., Aksay I A and Car R. (2008). *Raman Spectra of Graphite Oxide and Functionalized Graphene Sheets*. Nano Letters Vol 8, No 1, 36–41.

Kumar P., Subrahmanyam K S and Rao C N R. (2011). *Graphene produced by radiation-induced reduction of graphene oxide*. Nanoscience, 10, 04n05, 559. doi: 10.1142/S0219581X11008824.

Kumar P. (2013). *Scalable green synthesis of 2D atomic sheets: A matter of laser flash*. RSC Advances. doi 10.1039/C3RA41149D.

Kumar R., Savu R., Joanni E., Vaz A. R., Canesqui M. A., Singh R K., Timm R A., Kubota L T and Moshkalev S A. (2016). *Fabrication of interdigitated micro-supercapacitor devices by direct laser writing onto ultra-thin, flexible and free-standing graphite oxide films*. RSC Advances, 6(88), 84769–84776. doi:10.1039/c6ra17516c

Kumar R., Singh R K., Singh D P., Joanni E., Yadav R M and Moshkalev S A. (2017). *Laser-assisted synthesis, reduction and micro-patterning of graphene: Recent progress and applications*. Chemistry Reviews, Vol 342, 34-79. doi.org/10.1016/j.ccr.2017.03.021.

Kymakis E., Petridis C., Anthopoulos T D and Stratakis E. (2014). *Laser-Assisted Reduction of Graphene Oxide for Flexible, large-area optoelectronics*. IEEE Journal of Selected Topics in Quantum Electronics, Vol 20, No 1. doi: 10.1109/JSTQE.2013.2273414.

Kymakis E., Savva K., Stylianakis M M., Fataakis C and Stratakis E. (2013). *Flexible Organic Photovoltaic cells with in-situ nonthermal photoreduction of spin coated graphine oxides*. Adv. Funct. Mater., 23, 2742-2749. doi: 10.1002/adfm.201202713.

Lazauskas A., Baltrusaitis J., Grigaliunas V., Guobiene A., Prosycevas I., Narmontas P., Abakeviciene B and Tamulevicius S. (2014). *Thermally-driven structural changes of graphene oxide multilayer films deposited on glass substrate*. Superlattices and Microstructures, 75, (2014), 461–467. doi: 10.1016/j.spmi.2014.08.006.

Lee W C., Lim C H Y X., Shi H., Tang L A L., Wang Y., Lim C T and Loh K P. (2011), ACS Nano 2011 , 5 , 7334 – 7341

Li X., Ren H., Chen X., Liu J., Li Q., Li C, et al. (2015). *Athermally photoreduced graphene oxides for three-dimensional holographic images*. Nat. Commun., 6, 6984. doi: 10.1038/ncomms7984 (2015).

Li Y C., Yeh T F., Huang H C., Chang H Y., Lin C Y., Cheng L C., Chang C Y., Teng H and Chen S J. (2014). *Graphene Oxide based micropatterns via high-throughput multiphoton-induced reduction and ablation*. Optics Express, 22, 16. doi: 10.1364/OE.22.019726.

Lin T N., Chih K H., Yuan C T., Shen J L., Lin C A J and Liu W R. (2015). *Laser-ablation production of graphene oxide nanostructures: from ribbons to quantum dots*. Nanoscale, 2015, 7, 2708, doi: 10.1039/c4nr05737f.

Liu J M. (1982). *Simple technique for measurements of pulsed Gaussian-beam spot sizes*. Optics Letters, Vol 7, No 5, May.

Liu Y Q., Zhang Y L., Liu Y., Jiang H B., Han D D., Han B., Feng J and Sun H B. (2016). *Surface and Interface Engineering of Graphene Oxide Films by Controllable Photoreduction*. The Chemical Record, Volume 16, Issue 3, June, 1244–1255.

Liu W., Song M S., Kong B and Cui Y. (2017). *Flexible and Stretchable Energy Storage: Recent Advances and Future Perspectives*. Adv. Mater., 29, 1603436. doi: 10.1002/adma.201603436.

Longo A., Verucchi R., Aversa L., Tatti R., Ambrosio A., Orabona E, et al. (2017). *Graphene oxide prepared by graphene nanoplatelets and reduced by laser treatment*. Nanotechnology, 28, 22, 224002.

Lucchese M M., Stavale F., Martins Ferreira E H., Vilani C., Moutinho M V O., Capaz R B., Achete C A and Jorio A (2010). *Quantifying ion-induced defects and Raman relaxation length in graphene*. Carbon, Vol 48, 1592-1597.

Martins Ferreira E H., Moutinho M V O., Stavale F., Lucchese M M., Capaz R B., Achete C A and Jorio A. (2010). *Evolution of the Raman spectra from single, few, and many-layer graphene with increasing disorder*. Phys. Rev., B, 82, 125429.

Mukherjee R., Thomas A V., Krishnamurthy A and Koratkar N. (2012). *Photothermally Reduced Graphene as High-Power Anodes for Lithium-Ion Batteries*. ACS Nano, 6(9), 7867–7878. doi: 10.1021/nn303145j.

Muttaqin., Nakamura T., Nishina Y and Sato, S. (2016). *Chemical surface modification of graphene oxide by femtosecond laser pulse irradiation in aqueous suspensions*. Journal of Materials Science, 52(2), 749–759. doi:10.1007/s10853-016-0368-8.

Novoselov K S., Falko V L., Colombo L., Gellert P R., Schwab M G and Kim K. (2012). *A roadmap for graphene*. Nature, 490, 192-200.

Novoselov K S., Geim A K., Morozov S., Jiang D., Zhang Y., Dubonos S A., Grigorieva I and Firsov A. (2004), Science, 306, Oct, 666–669.

Obeng Y and Srivathanan P. (2011). Graphene: Is it the future for semiconductors? An overview of the material, devices and applications. The Electrochemical Society, Interface, Spring 2011.

Oh J S., Kim S H., Hwang T., Kwon H Y., Lee T H., Bae A H., Choi H R and Nam J D. (2012). *Laser-Assisted simultaneous patterning and transferring of graphene*. J. Phys. Chem., C, 117, 663-668. doi: 10.1021/jp309382w.

Papazoglou S., Petridis K., Kymakis E., Kennou S., Raptis Y., Chantzandroulis S and Zergioti I. (2018). *In-situ sequential laser transfer and laser reduction of graphene oxide films*. Applied Physics Letters, 112, 183301. doi: 10.1063/1.5021862.

Pei S and Cheng H M. (2012). *The reduction of graphene oxide*. Carbon 50, 3210-3228. doi: 10.1016/j.carbon.2011.11.010.

Petridis C., Lin Y H., Savva K., Eda G., Kymakis E., Anthopoulos T D and Stratakis E. (2013). *Post-fabrication, in situ laser reduction of graphene oxide devices*. Applied Physics Letters, 102, 093115, (2013). doi: 10.1063/1.4794901.

Petridis C., Konios D., Stylianakis M M., Kakavelakis G., Sygletou M., Savva K., Tzourmpakis P., Krassas M., Vaenas N., Stratakis E and Kymakis E. (2016). *Solution processed reduced graphene oxide electrodes for organic photovoltaics*. Nanoscale Horizons. doi: 10.1039/C5NH00089K.

Rasuli R., Mokarian Z., Karimi R., Shabanzadeh H and Abedini Y. (2015). *Wettability modification of graphene oxide by removal of carboxyl functional groups using non-thermal effects of microwave*. Thin Solid Films. doi: 10.1016/j.tsf.2015.06.002.

Samad R E and Vieira N D. (2006). *Geometrical Method for Determining the Surface Damage Threshold for Femtosecond Laser Pulses*. Laser Physics, Vol 16, No 2, 336-339.

Senyuk B., Behabtu N., Martinez A., Lee T., Tsentelovich D E., Ceriotti G., Tour J M., Pasquali M and Smalyukh I I. (2015). *Three-dimensional patterning of solid microstructures through laser reduction of colloidal graphene oxide in liquid-crystalline dispersions*. Nature Communications, 6, 8157. doi: 10.1038/ncomms8157.

Singh R K., Kumar R and Singh D P. (2016). *Graphene oxide: strategies for synthesis, reduction and frontier applications*. RSC Adv., 6, 69, 64993-65011. doi: 10.1039/C6RA076268.

- Smirnov V A., Arbuzov A., Shul'ga Y M., Baskakov S., Martynenko V., Muradyan V and Kesova E I. (2011). *Photoreduction of graphite oxide*. High Energy Chem, 45, (1), (2011), 57-61.
- Smirnov V A., Denisov N N and Alfimov M V. (2013). *Photochemical Reduction of Graphite Oxide*. Nanotechnologies in Russia, 8, 1–2, 1–22. doi: 10.1134/S1995078013010151.
- Sokolov, D.A., Shepperd, K.R., Orlando, T.M. (2010). *Formation of graphene features from direct laser-induced reduction of graphite oxide*. J. Phys. Chem. Lett., 1, 18, 2633–2636.
- Sokolov D A., Rouleau C M., Geohegan D B and Orlando T M. (2013). *Excimer laser reduction and patterning of graphite oxide*. Carbon, 53, 81-89. doi 10.1016/j. carbon.2012.10.034.
- Spano S F., Isgro`G., Russo P., Fragala M E and Compagnini G. (2014). *Tunable properties of graphene oxide reduced by laser irradiation*. Appl. Phys. A., (2014), 117, 19–23. doi 10.1007/s00339-014-8508-y.
- Stobinski L., Lesiak B., Malolepszy A., Mazurkiewicz M., Mierzwa B., Zemek J., Jiricek P and Bieloshapka I. (2014). *Graphene oxide and reduced graphene oxide studied by the XRD, TEM and electron spectroscopy methods*. Journal of Electron Spectroscopy and Related Phenomena, 195, 145-154.
- Stratakis E., Eda G., Yamaguchi Y., Kymakis E., Fotakis C and Chhowalla M. (2012). *Free-standing graphene on microstructured silicon vertices for enhanced field emission properties*. Nanoscale 4, 3069–3074.
- Strong V., Dubin S., El-Kady M F., Lech A., Wang Y., Weiller B H and Kaner R B. (2012). *Patterning and Electronic Tuning of Laser Scribed Graphene for Flexible All-Carbon Devices*. ACS Nano, 6, 2, 1395–1403. doi: 10.1021/nn204200w.
- Stylianakis M M., Sygletou M., Savva K., Kakavalakis G., Kymakis E and Stratakis E. (2015), *Photochemical Synthesis of Solution-Processable Graphene Derivatives with Tunable Bandgaps for Organic Solar Cells*. Adv. Opt. Mater., 2015. doi: 10.1002/adom.201400450.
- Subrahmanyam K S., Kumar P., Nag A and Rao C N R. (2010). *Blue light emitting graphene-based materials and their use in generating white light*. Solid State Commun., 150, 1774.
- Sugioka K and Cheng Y. (2014). *Ultrafast lasers--reliable tools for advanced materials processing*. Light Sci. Appl., 3, (4), (2014), 149.
- Tahir A A., Ullah H., Sudhagar P., Teridi M A M., Devadoss A and Sundaram S. (2016). *The Application of Graphene and Its Derivatives to Energy Conversion, Storage, and Environmental and Biosensing Devices*. The Chemical Record, 16, 3, June, 1591–1634. doi: 10.1002/tcr.201500279.
- Teoh H F., Tao Y., Tok E S., Ho G W and Sow C H. (2012). *Direct laser-enabled graphene oxide–reduced graphene oxide layered structures with micropatterning*. J. Appl. Phys., 112, 64309.
- Thekkekara L V., Jia B., Zhang Y., Qiu L., Li D and Gu M. (2015). *On-chip energy storage integrated with solar cells using a laser scribed graphene oxide film*. Appl. Phys. Lett., 107, 3, 031105. doi: 10.1063/1.4927145Tao

- Tao Y., Varghese B., Jaiswal M., Waag S., Zhang Z., Oezylmaz B., Loh KP., Tok E S and Sow C H. (2012). *Localized insulator-conductor transformation of graphene oxide thin films via focused laser beam irradiation*. Appl. Phys. A., (2012), 106, 523–531. doi: 10.1007/s00339-011-6710-8.
- Tian H., Chen H Y., Ren T L., Li C., Xue Q T., Mohammad M A., Wu C., Yang Y and Wong H S P. (2014). *Cost-Effective, Transfer-Free, Flexible Resistive Random Access Memory Using Laser-Scribed Reduced Graphene Oxide Patterning Technology*. Nano Lett., 2014, 14, 3214–3219. doi: 10.1021/nl5005916.
- Trusovas R., Ratautas K., Rac̃iukaitis G., Barkauskas J., Stankevič̃ien I., Niaura G and Maz̃eikien R. (2013). *Reduction of graphite oxide to graphene with laser irradiation*. Carbon, 52, 574–582. doi: 10.1016/j.carbon.2012.10.017.
- Trusovas R., Raciukaitis G., Niaura G., Barkauskas J., Valisis G and Pauliukaite R. (2016). *Recent advances in laser utilisation in the chemical modification of graphene oxide and its applications*. Adv. Optical Mater., 4, 37-65, doi: 10.1002.adom.2015000469.
- Tuinstra F and Koenig J L. (2007). *Raman spectrum of graphite*. J. Chem. Phys., 53, 1126–1130.
- Viskadouros G., Konios D., Kymakis E and Stratakis E. (2014). *Direct laser writing of flexible graphene field emitters*. Applied Physics Letters, 105, 203104. doi:10.1063/1.4902130.
- Voiry D., Yang J., Kupferberg J., Fullon R., Lee C., Jeong H Y, et al., (2016). *High-quality graphene via microwave reduction of solution-exfoliated graphene oxide*. Science, 353, 6306, 1413-1416.
- Wan Z., Streed E W., Lobino M., Wang S., Sang R T., Cole I S., Thiel D V and Li Q. (2018). *Laser-reduced graphene: synthesis, properties, and applications*. Adv. Mater. Technol., 1700315. doi: 10.1002/admt.201700315
- Wan Z., Wang S., Haylock B., Kaur J., Tanner P., Thiel D., Sang R., Cole I S., Li X., Lobino M and Li Q. (2019). *Tuning and sub processes in laser reduction of graphene oxide by adjusting the power and scanning speed of the laser*. Carbon, 141, Jan, 2019, 83-91. doi: 10.1016/j.carbon.2018.09.030.
- Wang J N., Shao R O., Zhang Y L., Guo L., Jiang H B., Lu D X and Sun H B. (2012). *Biomimetic Graphene Surfaces with Superhydrophobicity and Iridescence*. Chem. Asian J. 2012, 7, 301–304. doi.org/10.1002/asia.201290000.
- Wang J., Gao W., Zhang H., Zou M., Chen Y and Zhao Y. (2018). *Programmable wettability on photocontrolled graphene film*. Sci. Adv., 4, eaat7392, Sept.
- Wang S., Zhang Y., Abidi N and Cabrales L. (2009). *Wettability and Surface Free Energy of Graphene Films*. Langmuir, 25, 18, 11078–11081. doi: 10.1021/la901402f.
- Wang S C., Ouyang X Y., Feng Z W., Cao Y Y., Gu M and Li X. (2018). *Diffraction photonic applications mediated by laser reduced graphene oxides*. Opto-Electronic Advances, Vol 1, No 2. doi: 10.29026/oea.2018.170002.
- Wei N., Lv C. and Xu Z. (2014). *Wetting of Graphene Oxide: A Molecular Dynamics Study*. Langmuir, 30, 3572-3578, doi: 10.1021/la500513x.

Xu K., Zhang J., Hao X., Zhang C., Wei N and Zhang C. (2018). *Wetting Properties of Defective Graphene Oxide: A Molecular Simulation Study*. *Molecules*, 23, 1439. doi:10.3390/molecules23061439

Yakovlev, E., Shandybina, G., & Shamova, A. (2019). Modelling of the heat accumulation process during short and ultrashort pulsed laser irradiation of bone tissue. *Biomedical optics express*, 10(6), 3030–3040. <https://doi.org/10.1364/BOE.10.003030>

Yang D., Velamakanni A., Bozoklu G., Park S., Stoller M., Piner R D., Stankovich S., Jung I., Field D A., Ventrice Jr. C A and Ruoff R S. (2009). *Chemical analysis of graphene oxide films after heat and chemical treatments by X-ray photoelectron and Micro-Raman spectroscopy*. *Carbon*, 47, 145–152. doi:10.1016/j.carbon.2008.09.045.

Yang C R., Tseng S F and Chen Y T. (2018). *Laser-induced reduction of graphene oxide powders by high pulsed ultraviolet laser irradiations*. *Applied Surface Science*, 444, (2018), 578-583. doi: 10.1016/j.apsusc.2018.03.090.

Yang D and Bock C. (2016). *Laser reduced graphene for supercapacitor applications*. *J. Power Sources*, 337, 73–81. doi: 10.1016/j.jpowsour.2016.10.108

Yin Z Y., Sun S Y., Salim T., Wu S X., Huang X., He Q Y., Lam Y M and Zhang H. (2010). *Organic photovoltaic devices using highly flexible reduced graphene oxide films as transparent electrodes*. *ACS Nano*, 4, 5263-5268. doi 10.1021/nn1015874.

Yung K C., Liem H., Choy H S., Chen Z C., Cheng K H and Cai Z X. (2013). *Laser direct patterning of a reduced graphene oxide transparent circuit on a graphene oxide thin film*. *J. App. Phys.*, 113, 244903. doi 10.1063/1.4812233.

Zhang Y L., Guo L., Wei S., He Y Y., Xia H., Chen Q D., Sun H B and Xiao F S. (2010). *Direct imprinting of microcircuits on graphene oxides film by femtosecond laser reduction*. *Nano Today*, 5, (1), 15-20. doi:10.1016/j.nantod.2009.12.009.

Zhang Y L., Chen Q D., Jin Z., Kim E and Sun, H B. (2012b). Biomimetic graphene films and their properties. *Nanoscale*, 4, 16, 4858. doi:10.1039/c2nr30813d

Zhang Y L., Guo L., Xia H., Chen Q D., Feng J and Sun H B. (2013). *Photoreduction of Graphene Oxides: Methods, Properties and Applications*. *Adv. Optical Materials*, doi: 10.1002/adom.201300317.

Zhao Y., Han Q., Cheng Z., Jiang L and Qu L. (2017). *Integrated graphene systems by laser irradiation for advanced device*. *Nano Today*, 12, 2017, 14–30. doi: 10.1016/j.nantod.2016.12.010.

Zheng X R., Lin H., Tang T S and Jia B H. (2017). *Laser trimming of graphene oxide for functional photonic applications*. *J. Appl. Phys.*, D, 50, 7, 074003. doi: 10.1088/1361-6463/aa54e9.

Zheng X., Jia B., Chen X and Gu M. (2014). *In-situ third-order nonlinear responses during laser reduction of graphene oxide thin films towards on-chip nonlinear photonic devices*. *Adv. Mater.*, 26, 2669-2703. doi 10.1002/adma.210304681.

Zhou Y., Bao Q., Varghese B., Tang L A L., Tan C K., Sow C H and Loh K P. (2010). *Microstructuring of Graphene Oxide Nanosheets Using Direct Laser Writing*. *Adv. Mater.*, 2010, 22, 67–71. doi: 10.1002/adma.200901942.

Appendix I

Sample of G-code input for Aerotech stages.

```
G00 G90 X0 Y0 Z0
G91 F0.5 X11 Y44 Z0
G91 Z4
G91 Z-4
G01 F0.5 X10 Z5
G00 G90 Z0
G00 G90 X0 Y0
G00 G90 X0 Y0 Z0
G91 F2 X16.5 Y50.5
G91 Z3.9
Repeat 30
G01 X-6
G01 Y-0.100
G01 X6
G01 Y-0.100
END Repeat
G00 G90 Z0
G00 G90 X0 Y0 Z0
G91 F2 X23.5 Y50.5
G91 Z4.0
Repeat 30
G01 X-6
G01 Y-0.100
G01 X6
G01 Y-0.100
END Repeat
G00 G90 Z0
G00 G90 X0 Y0 Z0
G91 F2 X16.5 Y43.5
G91 Z4.1
Repeat 30
G01 X-6
G01 Y-0.100
G01 X6
G01 Y-0.100
End Repeat
G00 G90 Z0
G00 G90 X0 Y0 Z0
G91 F2 X23.5 Y43.5
G91 Z4.2
Repeat 30
G01 X-6
G01 Y-0.100
G01 X6
G01 Y-0.100
End Repeat
G00 G90 Z0
G00 G90 X0 Y0 Z0
```

Appendix II

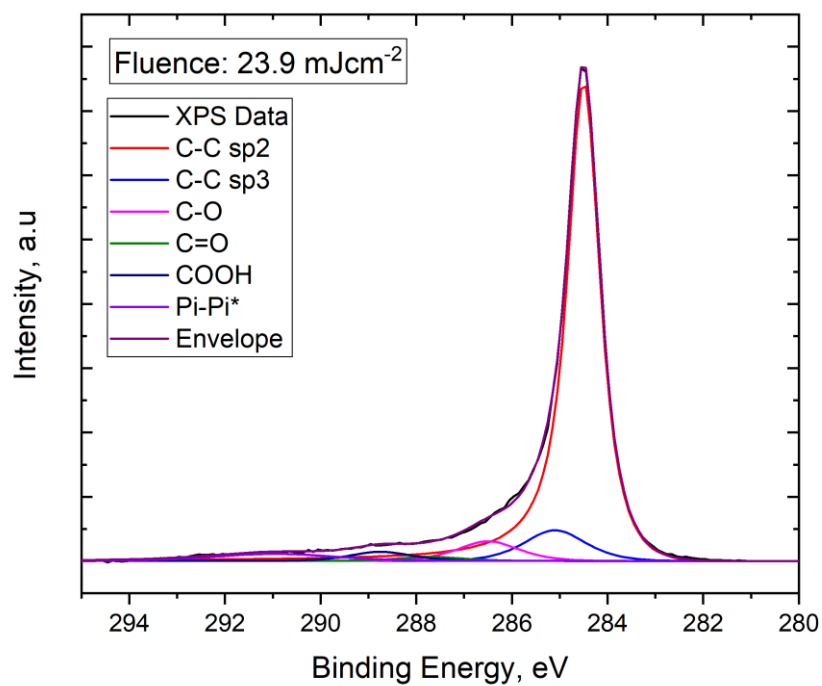


Figure A1 - XPS spectra of rGO after irradiation with 23.9 mJcm⁻² fluence

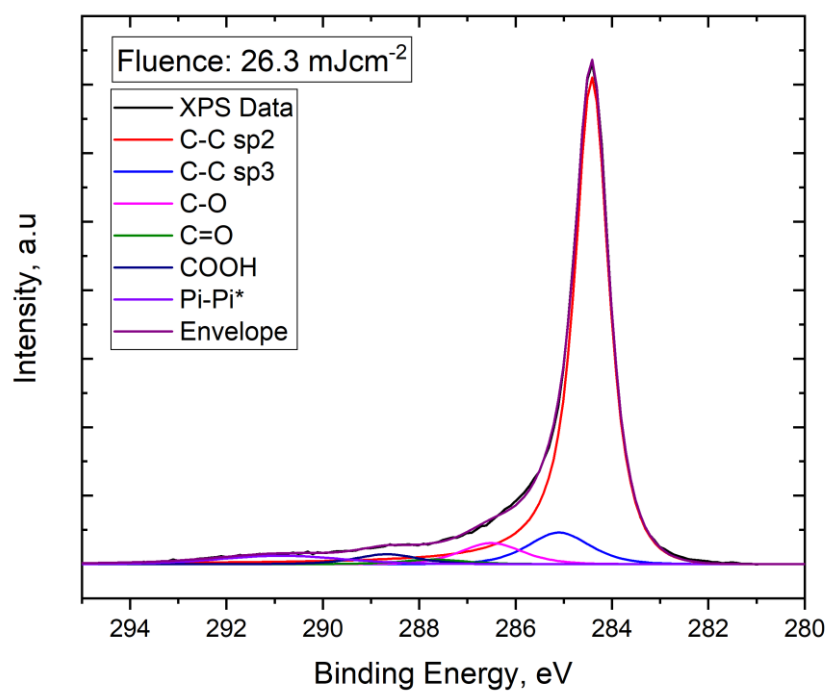


Figure A2 - XPS spectra of rGO after irradiation with 26.3 mJcm⁻² fluence

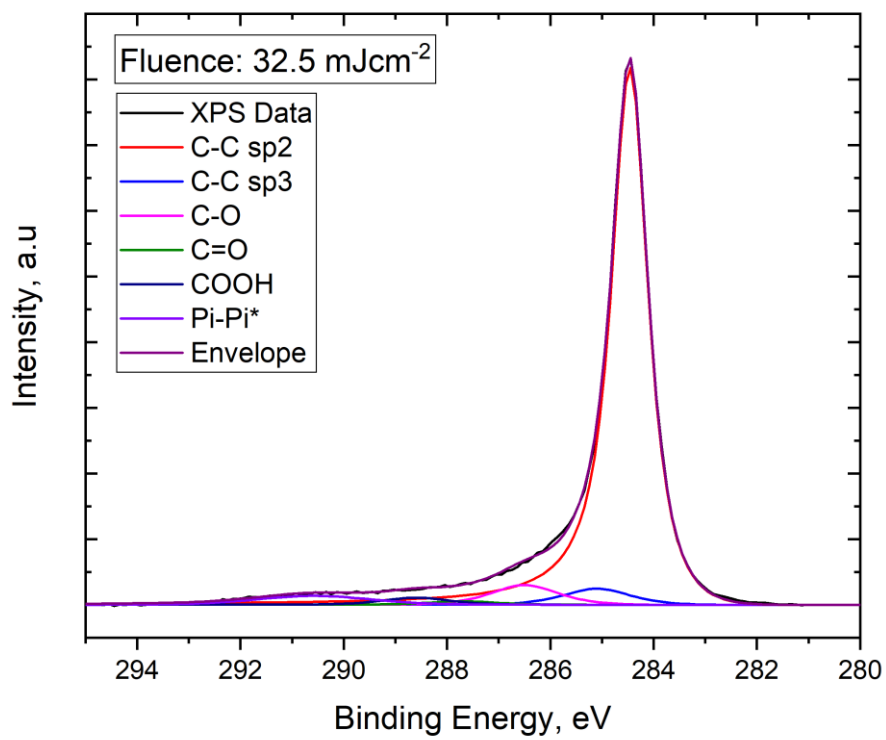


Figure A3 - XPS spectra of rGO after irradiation with 32.5 mJcm⁻² fluence

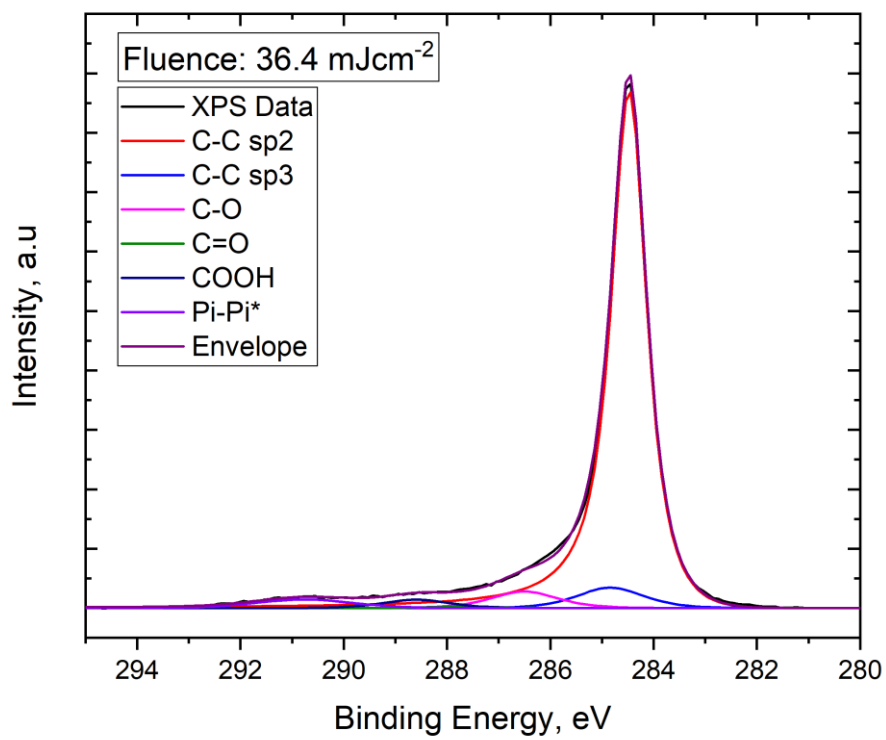


Figure A4 - XPS spectra of rGO after irradiation with 36.4 mJcm⁻² fluence

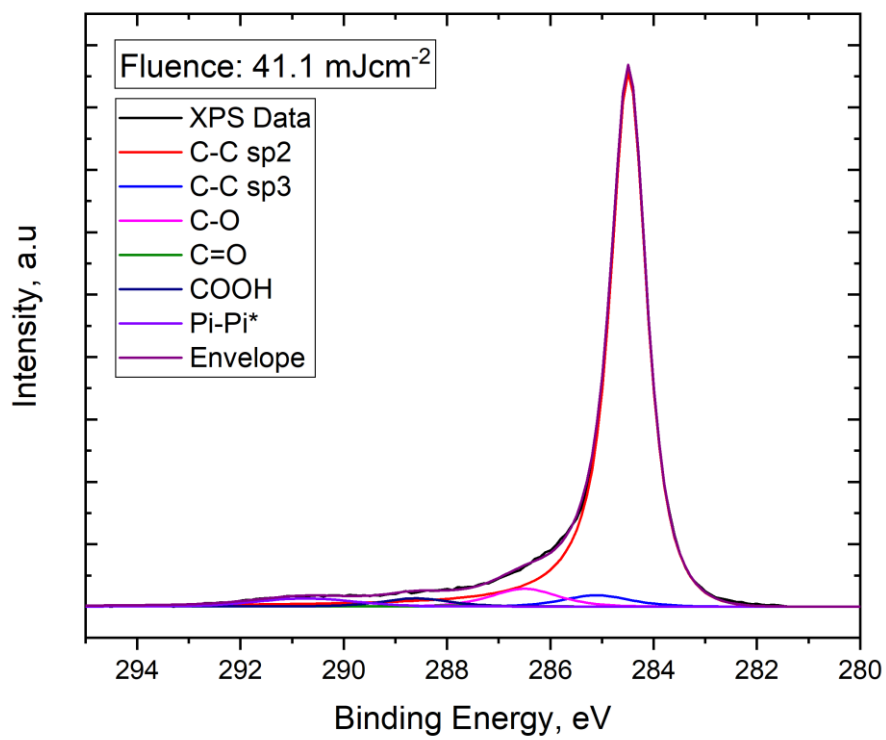


Figure A5 - XPS spectra of rGO after irradiation with 41.1 mJcm⁻² fluence